

UNIVERSITÀ DEGLI STUDI DI MILANO

Scuola di Dottorato in Fisica, Astrofisica e Fisica Applicata

Dipartimento di Fisica

Corso di Dottorato in Fisica, Astrofisica e Fisica Applicata

Ciclo XXXVIII

Design and study of the IRIS 10 T Energy Saving dipole Magnet for Accelerators: ESMA

Settore Scientifico Disciplinare FIS/01

Supervisore: Professor Lucio Rossi

Coordinatore: Dr Stefano Sorti

Candidato: Lorenzo Balconi

Matricola: R13951

ORCID: 0009-0004-3497-9082

Anno Accademico 2024/2025

Commission of the final examination:

External Referee:
Professor Yifeng Yang

External Member:
Professor Marina Putti

Internal Member:
Doctor Stefano Sorti

Final examination:

Date: 13 January 2026

Università degli Studi di Milano, Laboratorio Acceleratori e Superconduttività Applicata (LASA), Segrate (MI), Italy

Il meglio è l'inimico
del bene.

Abstract

The research and development of new superconducting materials is progressively refining the manufacturing of a new class of conductors: REBCO tapes. Although REBCO was discovered in 1987, tape manufacturing suitable for magnet windings has only recently been optimized. REBCO tapes belong to the class of High Temperature Superconductors (HTS), a class of materials which remain superconducting at temperatures higher than liquid nitrogen, in contrast to classical Low Temperature Superconductors (LTS) that require liquid helium refrigeration. This capability has the potential to transform superconducting magnet technology by enabling a wide range of applications in medical, energy, and societal domains beyond particle accelerators. The possibility of operating at higher temperatures simplifies infrastructure and improves thermal efficiency, yielding substantial energy savings and making the technology more sustainable. However, manufacturing challenges as sudden localized performance drops and unforeseen defects occurrences as well as the early stage of understanding of these conductors make a reliable application a challenging quest.
The objective of this thesis is to set an initial milestone toward a new generation of superconducting dipole magnets by exploiting REBCO tapes to realize a complete HTS technological demonstrator. Within the IRIS project, funded by the NextGeneration EU (PNRR), the Energy Saving Magnet for Accelerators (ESMA) was conceived to reach a peak central field of 10 T and to operate cryogen-free at 20 K, thus yielding more than competitive conductor performance with respect to classical LTS while delivering an estimated energy saving relative to operation at 4.2 K of roughly a factor five. The project is a collaboration with industry, ASG Superconductors, for magnet construction and co-design.
This thesis addresses the challenges of designing an HTS dipole magnet, beginning with the electromagnetic configuration while accounting for the mechanical constraints of using tape rather than round wire or cable. The procured tape was extensively characterized through electrical and mechanical measurements to provide insight for the design phase and to build in-house expertise at the LASA laboratory. After completing the integrated electromagnetic, mechanical, and thermal design, the operation of the magnet was studied with dedicated analyses aimed at optimizing charging procedures while respecting thermal limits, critical since ESMA will also serve as a variable field user facility at INFN Genova. Quench dynamics and AC losses were investigated in collaboration

with Little Beast Engineering, to prepare an intervention or mitigation strategy in case of quench and to confirm a reliable operation. Lastly, an experimental campaign was carried out to design, manufacture, and test small HTS windings to validate handling and winding procedures, to study tape behavior under realistic processing, and to confirm the design assumptions used for ESMA.

Sommario

Il processo di ricerca e sviluppo di nuovi materiali superconduttori ha progressivamente rifinito la procedura di produzione di una nuova classe di conduttori: i nastri di REBCO. Nonostante la scoperta del REBCO risalga al 1987, la produzione di nastri adatti all'avvolgimento di magneti è stata ottimizzata solo recentemente. I nastri REBCO appartengono alla classe dei superconduttori ad alta temperatura (HTS), in quanto mantengono le loro proprietà superconduttrici a temperature superiori a quelle dell'azoto liquido, a differenza dei superconduttori a bassa temperatura (LTS), che richiedono l'utilizzo di elio liquido. Questa caratteristica ha il potenziale di trasformare la tecnologia dei magneti superconduttori, aprendo la strada a un'ampia gamma di applicazioni negli ambiti: medico, energetico e in altri settori di interesse sociale, oltre al campo specifico degli acceleratori di particelle.
La possibilità di operare a temperature più elevate semplifica le infrastrutture e migliora l'efficienza termica, da cui ne risulta un notevole risparmio energetico che rende questa tecnologia più sostenibile. Tuttavia, le difficoltà di fabbricazione, come interruzioni improvvise e difetti imprevisti, unite alla comprensione ancora prematura del comportamento e delle caratteristiche di tali conduttori, rendono complessa la loro applicazione a casi reali.
L'obiettivo di questa tesi è quello di porre un primo traguardo verso una nuova generazione di magneti dipolari superconduttori, sfruttando le potenzialità dei nastri REBCO per realizzare un dimostratore tecnologico HTS completo. Questo lavoro si inserisce nell'ambito del progetto IRIS, finanziato da NextGeneration EU (PNRR), ed ha come obiettivo la realizzazzione di un Energy Saving Magnet for Accelerators (ESMA), un magnete progettato per raggiungere un campo centrale massimo di 10 T e operare a 20 K senza refrigeranti liquidi, ottenendo allo stesso modo prestazioni del conduttore competitive rispetto ai magneti LTS classici e un risparmio energetico stimato di circa un fattore cinque rispetto al funzionamento a 4.2 K. Il progetto è frutto di una collaborazione con l'industria, in particolare con ASG Superconductors, per la costruzione e la co-progettazione del magnete. Questa tesi affronta le sfide legate alla progettazione di un magnete dipolare HTS, a partire da una configurazione elettromagnetica che consideri i vincoli meccanici derivanti dall'uso di nastri invece che di fili o cavi rotondi. Il nastro fornito è stato poi ampiamente caratterizzato attraverso misure elettriche e meccaniche, al fine di fornire indicazioni utili per la fase di progettazione e sviluppare competenze

interne presso il laboratorio LASA. Completata la progettazione, elettromagnetica, meccanica e termica, il funzionamento del magnete è stato analizzato mediante studi volti a ottimizzare le procedure di carica, nel rispetto dei limiti termici, aspetto cruciale poiché ESMA serivirà da infrastruttura sperimentale a campo variabile presso i laboratori INFN di Genova. La dinamica del quench e le perdite in corrente alternata (AC losses) sono state investigate in collaborazione con Little Beast Engineering, per definire strategie di intervento o mitigazione in caso di quench e garantire un funzionamento sicuro del magnete. Infine, è stata condotta una campagna sperimentale per la progettazione, la realizzazione e il test di piccoli avvolgimenti HTS, con l'obiettivo di validare le procedure di manipolazione e avvolgimento, studiare il comportamento del nastro in condizioni operative realistiche e confermare le ipotesi di progetto adottate per ESMA.

Contents

Abstract vii

Sommario ix

List of Figures xiii

List of Tables xix

1 Introduction 1
- 1.1 Superconducting Dipole Magnets 2
  - 1.1.1 Technical Superconductors 6
  - 1.1.2 REBCO 10
  - 1.1.3 State of art about HTS magnets 14
- 1.2 Challenges in HTS magnets 19
  - 1.2.1 Screening currents and magnetization 19
  - 1.2.2 Mechanical issues 21
  - 1.2.3 Quench in HTS magnets 23
  - 1.2.4 NI and MI magnets 25
- 1.3 IRIS project 27
  - 1.3.1 ESMA 30
- 1.4 Organizational note 32

2 Electromagnetic design of ESMA 33
- 2.1 Coil Geometry and Layout Analysis 33
  - 2.1.1 Analytical point-like current sources 36
  - 2.1.2 Finite dimension current sources 38
  - 2.1.3 Cloverleaf comparison 41
- 2.2 Winding technology 43
  - 2.2.1 Insulated cable 43
  - 2.2.2 Non Insulation and Metal as Insulation 46
- 2.3 Final Electromagnetic Design 52
  - 2.3.1 Preliminary Configuration 52
  - 2.3.2 Final electromagnetic optimization 55

2.3.3 Effect of residual permittivity 61
2.3.4 Fringe field 64
2.3.5 Towards an Accelerator Design 69
2.4 Summary and achievements 71

3 HTS tape electrical measurements 73
3.1 Critical current measurements 73
3.1.1 Temperature, field and angle dependencies 77
3.2 Superficial defects 83
3.3 Internal splices 95
3.3.1 Enhanced flat joint 106
3.4 Summary and achievements 115

4 Thermo-Mechanical design of ESMA 117
4.1 Thermal design 117
4.1.1 Thermal conductivity measurements 122
4.2 Mechanical design 132
4.2.1 Thermal contraction measurements 135
4.2.2 Uniaxial compressive load test 138
4.2.3 Peeling 143
4.3 Design of the magnetic measurement system 145
4.4 Summary and achievements 150

5 ESMA operation 151
5.1 Charging time optimization 151
5.1.1 Nonlinear Optimal Control 152
5.1.2 ESMA case study 154
5.2 Quench analysis of ESMA 157
5.2.1 Preliminary quench considerations 158
5.2.2 Single coil quench analysis 159
5.2.3 ESMA single coil discharge 173
5.2.4 Full quench analysis 181
5.3 AC losses 191
5.4 Summary and achievements 195

6 Small-scale HTS coils: design and test 197
6.1 First winding and test experiences 197
6.2 Small-scale NI racetrack coils 209
6.2.1 Small racetrack coils design 209
6.2.2 Small racetrack coils LN_2 test results 213
6.3 Summary and achievements 217

Conclusions 219

Bibliography 223

List of Figures

1.1 Illustration of ESMA final design 1
1.2 Perfect dipole rapresentation 3
1.3 Sector dipole representation 4
1.4 LHC dipole 6
1.5 Type-II superconductors 7
1.6 Ic measurement criteria 8
1.7 Operational Margins 9
1.8 Structure of YBCO 11
1.9 Critical surface of YBCO 12
1.10 Structure of REBCO 13
1.11 Tapestar® measurement of a 4 mm HTS tape 14
1.12 Performances and unit length for HTS tape manufacturing 15
1.13 FeatherM2 HTS insert for EuCARD2 16
1.14 32 T magnet from NHMFL and NOUGAT 16
1.15 Non-Insulated 45 T solenoid 17
1.16 Commonwealth Fusion Systems toroidal field model coil 18
1.17 Commonwealth Fusion Systems toroidal field model coil - quenched 18
1.18 Screening current induced field and stress 20
1.19 Sample of a striated HTS tape. 21
1.20 Winding examples 22
1.21 Cloverleaf coil geometry 23
1.22 Electrical scheme of NI or MI windings 26
1.23 IRIS technological poles 28
1.24 IRIS work packages 29
1.25 Ground level of the new IRIS building 30
1.26 Green Superconducting Line 30

2.1 Coil layout options 34
2.2 Coil layout optimization problem 36
2.3 Coil layout optimization problem - Mixed configuration 39
2.4 Helmholtz-like coil versus mid-plane layout 40

2.5 Helmholtz-like coil versus mid-plane layout 40
2.6 Plot of the ratio B_2/B_1 as a function of the Helmholtz coil width. 41
2.7 Cloverleaf and Helmholtz configuration compoarison 42
2.8 Insulated cable cross section 45
2.9 ESMA - QLASA simulation 46
2.10 Preliminary ESMA cross-section 47
2.11 Non-insulated cable cross section 48
2.12 Charging of NI configuration 49
2.13 Charging of MI configuration 50
2.14 Iron pole optimization concept 53
2.15 Cross section of the preliminary design of ESMA with iron pole 54
2.16 Rendered image of the preliminary design of ESMA with iron yoke 54
2.17 Field quality trend within the GFR at different magnetic fields 55
2.18 Magnetic field of ESMA along z-axis 56
2.19 ESMA electromagnetic layout 57
2.20 Field quality within GFR 58
2.21 ESMA margins 59
2.22 Charging behavior of ESMA 60
2.23 Relative permeability analysis - μ_r=1 61
2.24 Relative permeability analysis - μ_r=1.5 62
2.25 Relative permeability analysis - center of GFR 63
2.26 Relative permeability analysis - corner of GFR 64
2.27 Map of INFN Genova laboratory 65
2.28 Magnetic field values level plot for fringe field studies 65
2.29 Magnetic field screening of ESMA 66
2.30 Misplacement forces analysis of ESMA within the iron shield 67
2.31 3D RAT model of the magnets inside INFN Genova laboratory 68
2.32 HTS magnet designs for future particle accelerators 69

3.1 SnIn crucible with silicone brushes 74
3.2 Sample holder for I_c measures in LN_2 74
3.3 Ic measurement - FFJ 12 mm 77 K self field 75
3.4 Probability distribution function of tapestar data for a specific spool 76
3.5 Probability distribution function of tapestar data and measured data 76
3.6 I_c measures at 20 K, variable field parallel to c-axis 77
3.7 Tapestar equivalent estimated I_c 79
3.8 Transport current and Tapestar measurement comparison 79
3.9 I_c measures at 4.2 K and 20 K, variable field at four different angles - FFJ-3273 81
3.10 I_c measures at 4.2 K and 20 K, variable field at four different angles - FFJ-3483 82
3.11 Inclusion on FFJ 12 mm HTS tape 83
3.12 Probability distribution function of inclusions on HTS tapes 84
3.13 Inclusion removal process and leftover imprint 85
3.14 Inclusion leftover imprint showing REBCO layer 86
3.15 Inclusion sample test result over time 87

3.16 Inclusion sample test result over multiple thermal cycles 88
3.17 Measurement set up for testing defects under external pressure 89
3.18 Representative scheme for disc springs 89
3.19 Inclusion tests under external compressive load - part 1 91
3.20 Inclusion tests under external compressive load - part 2 91
3.21 Defect before compressive load test 93
3.22 Defect after compressive load test 93
3.23 Indent caused by superficial defect on HTS tape after compressive load test 94
3.24 Fujifilm Prescale test on superficial defects 94
3.25 Pressing tool for resistive splices on HTS tapes 96
3.26 Fujifilm Prescale pressure profile of the splicing tool 97
3.27 Splice geometries for a two tape HTS cable 98
3.28 Manufactured bridge joint on a double tape HTS cable 99
3.29 Manufactured lap joint on a double tape HTS cable 100
3.30 Manufactured flat joint on a double tape HTS cable 101
3.31 Flat joint measurement 101
3.32 Lap joint measurement 102
3.33 Bridge joint measurement 102
3.34 electrical models for lap and bridge joints 103
3.35 Bridge joint breakdown 103
3.36 Improved joint manufacturing set up 104
3.37 Mechanical simulation of the displacements for the resistive splices tool 105
3.38 Improved resistive splice manufacturing tool 105
3.39 Enhanced flat junction 107
3.40 Current redistribution in enhanced flat joint 108
3.41 Parametric study on the cutting angle for the enhanced flat joint 109
3.42 Alternative cutting geometry for the enhanced flat joint 110
3.43 Voltage-current simulated curves for the enhanced flat joint 111
3.44 Sample of enhanced flat junction 112
3.45 Enhanced flat joint measure 112
3.46 Enhanced flat joint probability distribution function 114
3.47 Enhanced flat joint breakdown 114

4.1 Overview of ESMA thermal design 118
4.2 Power map of the cryocoolers of ESMA 120
4.3 ESMA coils thermal and electrical scheme 121
4.4 HTS stacks for thermal conductivity measurement 123
4.5 PLA mold for thermal conduction measurements sample preparation 124
4.6 PLA mold under external applied pressure 124
4.7 Wax-impregnated sample for thermal conductivity measurements 125
4.8 Winding tension to radial stress evaluation 126
4.9 Thermal conductivity measurements set-up 127
4.10 Themal conductivity measuremet results - wax impregnated sample 130
4.11 Themal conductivity measuremet results - dry sample 130

4.12 Themal conductivity measuremet results - dry and wax samples 131
4.13 ESMA forces analysis 132
4.14 Structural design of ESMA 133
4.15 ESMA final assembly 134
4.16 Thermal contraction measurements set up 136
4.17 Cross section of HTS tapes showing dog-bone effect 138
4.18 Fujifilm Prescale imprints of HTS tapes 139
4.19 Uniaxial compressive stress test on 4 mm tapes 139
4.20 Fujifilm Prescale MS film imprint left by a stack of 20 HTS tapes 141
4.21 Fujifilm Prescale HS film imprint left by a stack of 20 HTS tapes 141
4.22 I_c values for 12 mm wide tapes after applying a 100 MPa compressive load 142
4.23 I_c values for 4 mm wide tapes after applying a 100 MPa compressive load 143
4.24 Visual representation of peeling test set up 144
4.25 ESMA magnetic measurement system 146
4.26 Hall probe sensors position on magnetic field profile 147
4.27 Sensitivity analysis for ESMA magnetic measurement 149

5.1 Optimal control applied on ESMA charging 157
5.2 Position of the heater on one racetrack coil of ESMA 160
5.3 The current redistribution around a hot-spot or defect. 161
5.4 Different current distributions in MI coils. 162
5.5 Normal zone voltage and the heater power as a function of time. 163
5.6 Temperature profiles in the first 5 s of a simulated quench event. 164
5.7 Current densities profiles in the first 5 s of a simulated quench event. 165
5.8 Evolution of T and J for a single ESMA coil during a quench - part 1. 166
5.9 Evolution of T and J for a single ESMA coil during a quench - part 2. 167
5.10 Temperature profiles as a function of time for the entire quench simulation. 168
5.11 Current density profiles for the entire quench simulation. 169
5.12 Voltage profile over the whole coil for the entire quench simulation. 169
5.13 Normal zone V and ΔJ_θ for different delay times. 170
5.14 Hot-spot and average coil T for different delay times. 171
5.15 Quench simulation results with circuit breaker opened at 1.16 s 172
5.16 ESMA single coil fast discharge simulation results 174
5.17 Map of temperature and current density during a fast discharge 175
5.18 ESMA single coil slow discharge simulation results 176
5.19 Map of temperature and current density during a slow discharge 177
5.20 Current flowing in different types of dump resistors 178
5.21 ESMA single coil simulation results with different dump resistors 179
5.22 ΔJ in a single coil of ESMA for different dump resistors 180
5.23 V and T time evolution for the full ESMA magnet quench simulation 182
5.24 Full ESMA magnet quench simulation results 183
5.25 T and the longitudinal current density map at t = 0.601 s 184
5.26 Resistive power in different parts of the ESMA dipole 185
5.27 T and the longitudinal current density map at t = 0.434 s and t = 0.670 s 186

5.28 T and the longitudinal current density map at t = 0.783 s and t = 0.852 s 187
5.29 T and the longitudinal current density map at t = 1.511 s 188
5.30 T map for each coil as function of time during a quench of ESMA. 189
5.31 J map for each coil as function of time during a quench of ESMA 190
5.32 Results of the AC losses analysis for the ESMA dipole - R_c = 0.024 Ω·mm^2 191
5.33 Results of the AC losses analysis for the ESMA dipole - R_c = 0.092 Ω·mm^2 192
5.34 Results of the AC losses analysis for the ESMA dipole - R_c = 1.92 Ω·mm^2 193

6.1 Small circular coils - Design and NI winding 198
6.2 Winding process of small circular coils 199
6.3 Voltage-current measured curves for C1 NI coil. 200
6.4 small circular NI coils transient behavior 202
6.5 Breakdown of C2 NI circular coil 203
6.6 Small circular coils - Insulated winding 203
6.7 Insulation test on C1- wax small coil 204
6.8 Rendered and real images of the first HTS ractrack coil 205
6.9 Improved manual winding machine 206
6.10 Simulation results for the firts HTS racetrack coil 207
6.11 Measurement results of the first HTS racetrack coil in LN_2. 208
6.12 Improved design of the HTS small racetrack coil 209
6.13 Improved HTS small racetrack coils - completed 210
6.14 Simulation results for the improved HTS small racetrack coil 211
6.15 Winding machine from Saes improved to wind HTS 212
6.16 In-line current lead soldering on SAES winding machine 213
6.17 Transfer function of the flux density in the center for both coils. 214
6.18 Voltage differences across the turns pack for both racetrack coils 215
6.19 Measured transient behavior for the two small HTS racetrack coils 215
6.20 Stacked racetrack configuration 216

List of Tables

1.1	ESMA final design paramaters	31
2.1	Legend of the symbols	35
2.2	Optimization parameters for insulated winding	44
2.3	ESMA shielding summary	67
2.4	Forces on MA.RI.S.A. caused by iron shield of ESMA	68
2.5	Design features of HTS designs for future particle accelerators	70
3.1	Lift factor from 77 K self field to 20 K, 15 T field parallel to c-axis	80
3.2	Disc springs properties - M8	90
3.3	Disc springs combinations and compression	92
3.4	Inclusion sizes measured under external compressive load	92
3.5	Disc springs properties - M6	96
3.6	Brazing alloys and flux used in joints campaign	97
4.1	Parameters for radial stress estimation	125
4.2	Heat power input - thermal conductivity measurements	129
4.3	Thermal contraction set up calibration	137
4.4	Thermal contraction set up calibration	137
4.5	Compressive stress test samples	140
4.6	Nominal Hall probe positions	145
4.7	Uncertainties on magnetic measurement system	147
4.8	Uncertainties on ESMA structure	148
5.1	ESMA Model parameters and optimization weights	156
5.2	Material properties for preliminary quench analysis	158
6.1	Bruker HTS tape specifications	200
6.2	Critical current values of small circular NI coils	201
6.3	Critical current values of small circular NI coils	204
6.4	Small round coils properties	205
6.5	First HTS racetrack coil key design parameters	206
6.6	FFJ HTS tape characteristics used to wind the first HTS racetrack coil	207

6.7 Measured I_c values for the first HTS racetrack coils in LN_2. 208
6.8 Small racetrack coil design parameters 210
6.9 FFJ HTS 4 mm adopted tape characteristics 211

CHAPTER 1

Introduction

This thesis focuses on advancing the research and development of High Temperature Superconductors (HTS) in the area of high-field dipole magnets for future particle accelerators. The purpose is to set the first milestone toward a new generation of superconducting dipole magnets, by exploiting the potential of the so-called REBCO tape superconductors by realizing a complete HTS technological demonstrator. To this aim the project IRIS, within the Italian PNRR, has funded the construction of an Energy Saving Magnet for Accelerators (ESMA), with its final design anticipated in Fig. 1.1. In this chapter a brief introduction will be given to asses the differences and challenges of HTS REBCO tapes with respect to traditional Low Temperature Superconductors (LTS), together with brief description on superconducting magnets and a complete overview about the IRIS project. In addition, all Chapters in this thesis are summarized.

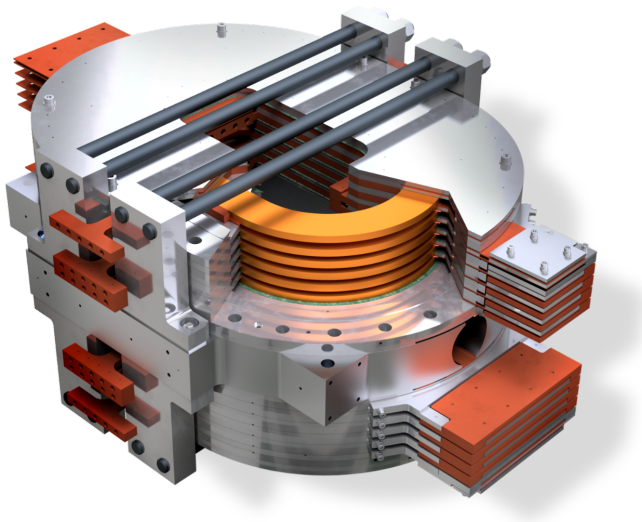


Figure 1.1: Illustration of the final design of the High Temperature Superconducting (HTS) dipole magnet demonstrator for the PNRR-IRIS project named ESMA.

1.1 Superconducting Dipole Magnets

The first successful liquefaction of helium gas, occurred in 1908 by K. Onnes [1], enabled the access to cryogenic temperatures making it possible to discover the phenomenon of superconductivity, which was first observed in 1911 by Onnes himself [2] who measured a sudden drop in the electrical resistivity of mercury when cooled down below 4.15 K. Soon after, more superconductors were discovered and defined as a class of materials which once cooled down below a characteristic temperature known as critical temperature T_c, undergo a phase transition that allows them to carry an electric current with zero resistance.
In parallel, particle accelerators have been developed to probe the fundamental interactions of matter by studying collisions between high-energy particles. To this purpose particle are accelerated in beams to speeds approaching that of the light. One common strategy to achieve this is to do build a circular collider, making the particles running in a loop while keeping on accelerating them. To keep the orbit, a transverse magnetic field is needed, specifically the bending of the beam is achieved through a dipolar field given by dipole magnets. The higher the energy E, the higher is the field B needed to keep the the particles in the same orbit of radius ρ as described by:

$$E[GeV] = 0.3 \cdot B[T]\rho[m] \tag{1.1}$$

The energy of the interacting particles is a critical parameter, as it determines both the types and the amount of particles produced in the collisions. The goal for high energy physics is therefore to reach the highest possible energy. With this in mind, the opportunity of carrying an electrical current with zero resistance has meant for the particle accelerator community to obtain the possibility to overcome the limit in generating magnetic field imposed by traditional cooper winding with an iron yoke, which, due to iron saturation, are almost superiorly limited to a 2 T maximum field. Moreover, beside the costs of cryogenics, holding zero resistance means to dissipate no power therefore making the superconducting technology able to set the way towards a more efficient and a more sustainable magnet manufacturing technology. This technological advancement has culminated with the realization of the currently most powerful circular collider: the Large Hadron Collider (LHC) at CERN. LHC accelerates protons with a maximum collision energy of 14 TeV, which are kept in a 27 km circular orbit by 1232 superconducting dipole magnet, each generating a field of 8.33 T [3]. LHC is currently undergoing the final phase of its upgrade to become High Luminosity (HiLumi) LHC [4], which is aimed at enhancing the number of collision event per second per cross section in the interaction region - namely luminosity - from $1 \cdot 10^{34} cm^{-2} s^{-1}$ to $5 - 7 \cdot 10^{34} cm^{-2} s^{-1}$.
Looking beyond LHC, feasibility studies for a future particle collider have started with the two most promising research lines to be the Future Circular Collider (FCC) with its two stages dedicated to electrons (FCC-ee) and hadrons (FCC-hh), aiming at a circumference of 90.7 km and a targeted ultimate energy of 100 TeV for protons [5], and the MUon COLlider (MUCOL) with the ambition to be the first muon accelerator aiming for a collision energy of 10 TeV within a circumference of 10 km. In both cases the designed value for the dipolar magnetic field needed to reach the ultimate collision energy is cur-

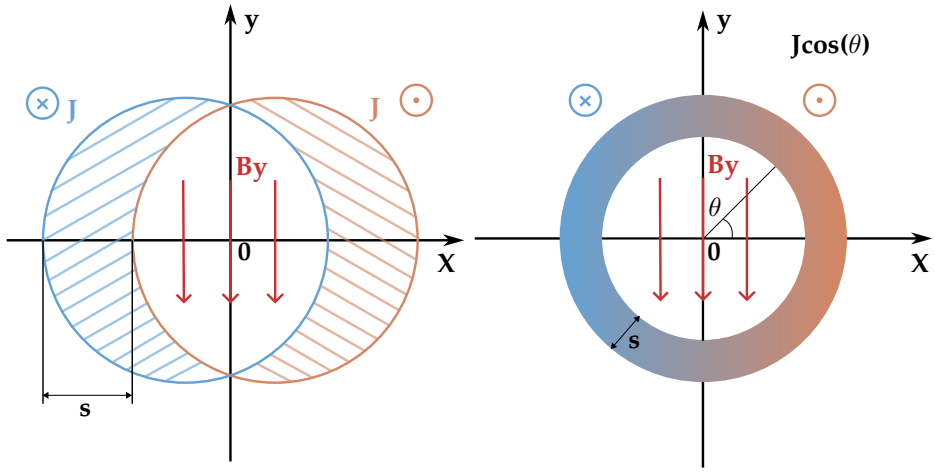


Figure 1.2: Cross-section of windings to produce a perfectly uniform transverse field B_y. In orange it is pictured the current density J coming out of the paper plane, in blue the fraction directed towards the paper plane. In the left picture it is showed the layout resulting from the partial intersection of two homogeneous current distribution equal circles carrying J in the opposite direction, namely nested circles, with their centers separated by a distance s. In the right picture it is sketched a ring shaped section of thickness s carrying a non-homogeneous current distribution varying as cosine of the angle θ.

rently assumed to be 14 T for both the FCC-hh and MUCOL ring [6].
An accelerator dipole magnet, in addition to the designed magnetic field necessary to have the particle beam fit within the curvature radius of the machine, needs to come with a high field homogeneity. In the specific case of dipoles, a perfectly uniform dipolar field can be achieved using geometries by means of a layout consisting in the partial intersection of two equal circles carrying a homogeneous current distribution J in the opposite direction, known as the nested circles configuration, or from a ring-shaped conductor carrying a current density $J(\theta)$ varying with a cosine function [7]. These configurations are illustrated in Fig. 1.2 and both lead to a field expression where only the transverse component of the field B_y is present and equal to:

$$By = -\frac{\mu_0 \cdot J \cdot s}{2} \tag{1.2}$$

where J is the module of the current density and s is respectively the distance between the two intercepting circles and the thickness of the ring carrying the $J(\theta)$ current density. When manufacturing these layouts, the current density J must be carried by a cable that exits the plane of the paper and returns on the other side of the aperture to complete the loop. This process must be repeated as many times as necessary to fill the intended cross-sectional area. Since the same cable is used for all turns of the magnet, it is challenging to achieve both ideal dipole configurations, as the cable carries a constant current density and has a constant cross-sectional area. However, by combining elements from both layouts, one can naturally converge to the well-known sector dipole design (Fig. 1.3), which approximates the ideal current distribution through an ad hoc arrangement

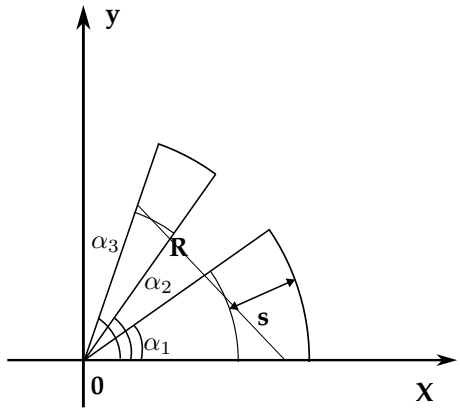


Figure 1.3: Cross-section of a sector dipole magnet with two distinct sectors defined by the three angles α_1, α_2 and α_3.

of coil blocks. However, simplifying the layout to have a sector dipole brings impurity to the field quality inside the aperture, which causes the field to deviate from the ideal one. Therefore, it is fundamental to have a description of the field inside the aperture itself, which is the region where the particle beam flows inside the accelerator.
The analytical description of this field can be derived starting from the expression of B generated by the elementary unit of the coil, which is given by the current line defined by the Biot-Savart law:

$$B(r,\theta) = \frac{\mu_0 I}{2\pi(re^{i\theta} - \rho e^{i\phi})} \tag{1.3}$$

where r and θ refers to the radial and angular position where the field is evaluated, while ρ and ϕ identify the current line radial and angular position. Since the region considered is the one inside the aperture, i.e. where $r < \rho$, the eq.1.3 can be expanded in series to obtain:

$$\begin{aligned} B(r,\theta) &= By + iBx \\ &= 10^{-4} B_{ref} \sum_{n=1}^{\infty} (b_n + ia_n)(cos((n-1)\theta) + isin((n-1)\theta)) \left(\frac{r}{R_{ref}}\right)^{n-1} \end{aligned} \tag{1.4}$$

where:

$$\begin{cases} bn = \frac{10^4}{B_{ref}} \cdot \frac{\mu_0 I}{2\pi R_{ref}} \left(\frac{R_{ref}}{\rho}\right)^n cos(n\phi) \\ an = \frac{10^4}{B_{ref}} \cdot \frac{\mu_0 I}{2\pi R_{ref}} \left(\frac{R_{ref}}{\rho}\right)^n sin(n\phi) \end{cases} \tag{1.5}$$

Here the complex exponential have been made explicit and the equation has been described in terms of the coefficients bn and an which are named field units. Indeed, these coefficients are dimensionless elements that quantify the amount of the nth field component in unit of 10^4 with respect to the main field component B_{ref} within the analyzed

magnetic field. Specifically, bn represents the normal field components, while an the so-called skew field components which are the same as the normal ones but rotated clockwise by a $pi/(2n)$ degree angle. The normalization is applied with respect to a reference radius R_{ref} - which is usually taken to be $2/3$ of the magnet aperture - and to the main field component B_{ref} which depends on the magnet which is being built. In the case of a dipole magnet B_{ref} would be the dipolar component, i.e. the one corresponding to $n = 1$. For quadrupoles, sextupoles, and $2n$-poles, the n-index will grow correspondingly.
The field described by the series expansion in eq. 1.4, can then be integrated on a specific cross section to have the analytical expression of a specific magnet, under the assumption that the evaluation is performed far enough from the coil ends such that the B_z component may be neglected. In the specific case of a sector dipole, with reference to Fig. 1.3, the integration of eq. 1.4 between R and $R + s$, as well as 0 and α_1 gives:

$$\begin{cases} bn = \frac{1}{n(n-2)} \cdot \frac{R_{ref}^{n-1} sin(n\alpha_1)}{(s \cdot sin(\alpha_1))} \cdot \left(\frac{1}{R^{n-2}} - \frac{1}{(R+s)^{n-2}} \right) \cdot 10^4 \quad if\ n\ odd \\ bn = 0 \quad if\ n\ even \\ an = 0 \quad \forall\ n \end{cases} \tag{1.6}$$

where the coefficients an and bn for n odd are set to zero by the symmetry of the problem. It is remarkable to notice that calculating B resulting only from the main component b_1 results in:

$$B_y = -\frac{2\mu_0 Js \cdot sin(\alpha_1)}{\pi} \tag{1.7}$$

which quite resembles the result reported in eq. 1.2 and as well does not depend on the coil aperture R. However, this is not the only contribution since, as described by the solution in eq. 1.6, all normal components for odd n are non-zero. To set the higher-order components to zero one first step is to fix the angle of the sector α_1 such that the first permitted unit, i.e. b_3, is fixed to zero. It can be easily verified that this happens for $\alpha_1 = 60°$. Instead of b_3, α_1 can be chosen to nullify another term such as b_5 if set to $36°$ or b_7 if set to $25.7°$, however with one sector only one component can be compensated for. To further enhance the field quality it is necessary to introduce more degrees of freedom. One common way to act in this direction consists into adding an additional block to the sector coil design as showed in Fig. 1.3 and to fix α_2 and α_3 such that the first permitted unit, i.e. b_3, is fixed to zero. The expression for the units describing the field generated by a sector dipole with two sectors then becomes:

$$bn = \frac{1}{n(n-2)} \cdot \frac{R_{ref}^{n-1}(sin(n\alpha_1) - sin(n\alpha_2) + sin(n\alpha_3))}{s \cdot (sin(\alpha_1) - sin(\alpha_2) + sin(\alpha_3))} \cdot \left(\frac{1}{R^{n-2}} - \frac{1}{(R+s)^{n-2}} \right) \cdot 10^4 \tag{1.8}$$

where now the three degrees of freedom offered by the three angles α_i allows for three superior harmonics to be set to zero. One solution in this case is offered by the triplet: $\alpha_1 = 43.2°$, $\alpha_2 = 52.2°$ and $\alpha_1 = 67.3°$. The process can be reiterated by adding another block until the target field quality is reached. For the main dipoles of LHC this optimization has brought to the cross section in Fig. 1.4 For a complete and exhaustive explanation about field harmonics and analytical expression of the magnetic field inside

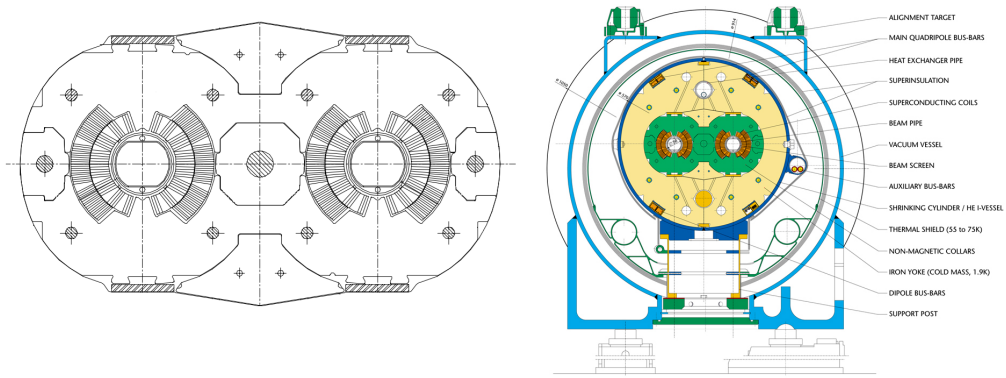


Figure 1.4: Representation of the cross section of the double aperture main LHC dipole magnet (left, adapted from [8]). Scheme of the main LHC dipole magnet installed inside the LHC accelerator together with the labeled components necessary for this implementation [9].

the aperture of a magnet, refer to [10].
In addition to the coil layout itself, accelerator magnets involve many other complexities. Some challenges are directly related to the conductor, such as the risk of a sudden loss of superconducting properties, a phenomenon known as a quench, and the need for a robust mechanical support structure. These will be discussed later on in this thesis. Other aspects to take into account concern the integration of the magnet into a complex system like a particle accelerator, as illustrated in the right picture of Fig.1.4. This includes ensuring compatibility with the vacuum vessel, beam pipe, power supply, and cryogenic system, as well as providing radiation protection and ensuring reliable operation. However, these aspects are beyond the scope of this thesis.

1.1.1 Technical Superconductors

In the previous section (1.1) a superconductor was defined as a material that undergoes a phase transition to zero electrical resistance when cooled below T_c. A further classification in superconductors can be introduced considering their behavior in presence of a magnetic field. Specifically, when a type-I superconductor below T_c is exposed to a magnetic field, it generates a resistance-less current on its surface to fully shield the magnetic field. Therefore, the magnetic field inside the material decreases exponentially with a characteristic length λ called penetration length and is eventually set to zero. This phenomenon is known as the Meissner-Ochsenveld effect [11]. However, there is a limit in the magnetic field, called critical field B_{c1}, beyond which the material is no longer able to shield the field and the superconductivity is lost. Typical values of B_{c1} below which type-I superconductivity may exists are in the range of $10^{-3} \sim 10^{-2}$ T. The class of type-I superconductors includes mainly elemental metals such as mercury, lead, and aluminum. On the other hand, certain materials known as type-II superconductors, still exhibit superconducting properties beyond B_{c1}. These materials are typically alloys such as: Nb-Ti, Nb_3Sn and REBCO (Rare-Earth Barium Copper Oxide). Once the applied magnetic field exceeds B_{c1}, they enter the so-called vortex-state, in which superconduc-

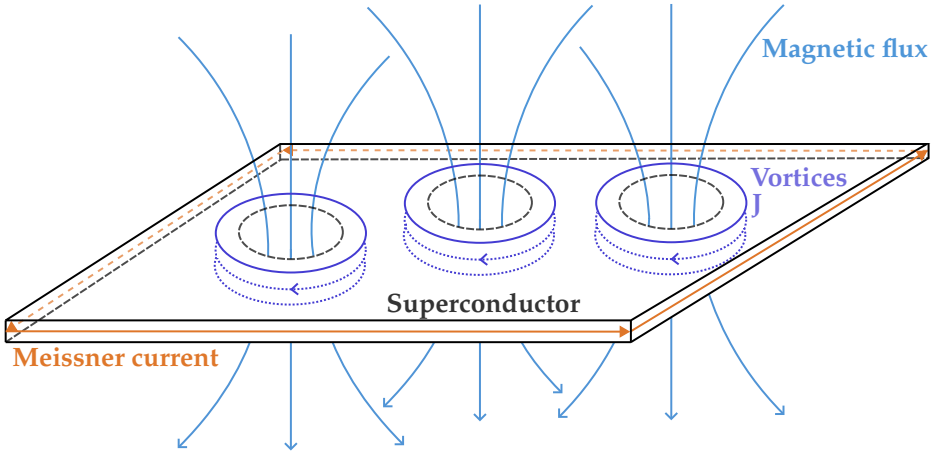


Figure 1.5: Schematic representation of type-II superconductivity where quanta of magnetic flux are able to penetrate the material through vortices of superconducting currents.

tivity persists while the magnetic field partially penetrates the conductor. This penetration, sketched in Fig. 1.5, occurs in the form of vortices of superconducting current generating a quantum of magnetic field called fluxon, equal to $\phi_0 = h/2e = 2.07 \cdot 10^{-15}$ Wb, an effect known as the Abrikosov effect [12]. This state can withstand much higher magnetic fields, up to a second critical field, B_{c2}, typically in the range of: $10 \sim 10^2$ T. The vortices are located on micro-structural defects of the material, an effect known as flux pinning. Pinning centers may be generated naturally or artificially created and optimized to efficiently lock in place fluxons. The force required to detach a vortex from its pinning center, is called pinning force. Indeed, when a transport current is fed to the material it applies a Lorentz force to the vortices. When the force exceeds the pinning force, the vortices start to move resulting in dissipation due to the Faraday-Neumann-Lentz law, eventually resulting in the material to become normal conducting. This places a third and final critical value above which the superconducting state is lost: the critical current density Jc.

The critical current is the most practical of the three parameters and it is therefore widely used to characterize and map the superconductor properties in order to define the material working area of parameters called critical surface. Once set the temperature and the external magnetic field a superconducting sample can be powered until it loses its superconducting properties, to fix a point within the critical surface. Generally, working conditions closed to a critical parameter lead to a small tolerable values of the other two. To this purpose, the most adopted criteria to define when the transition has occurred are: the electric field, the offset, and the resistivity criteria [13]. The electric field criterion is the most common one and consists in setting a threshold value for the electric field so that above and below the sample is considered respectively normal and superconducting. The threshold values used are 10 and 100 $\mu V/m$ corresponding to a critical value usually referred to as Ic_{10} and Ic_{100}. To this aim, while the sample is powered, the voltage across a defined length is measured via a voltmeter through voltage taps. Around

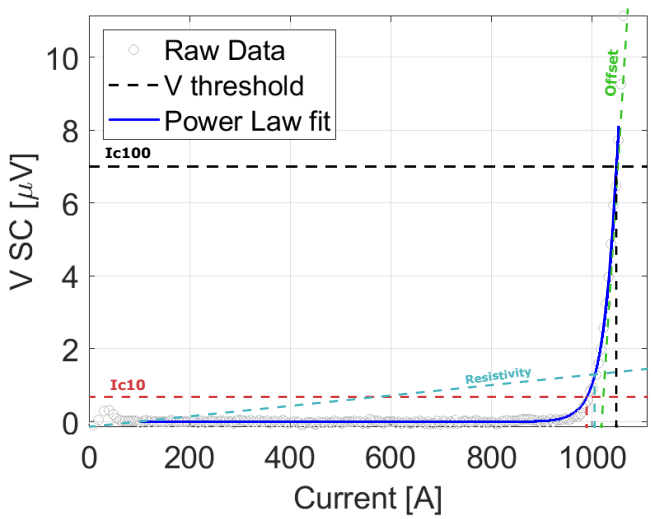


Figure 1.6: Voltage-current curve of a real experimental critical current measurement where the Ic_{100} criterion has been used for Ic determination. The gray circles are the experimental data, while the blue curve is the result of the fitted power law. Every other criteria and possible outcomes have been superimposed, and labeled on the picture.

the critical value Ic, the transition may be modeled using a power law:

$$V = E_{th10/100} \cdot d_{taps} \cdot \left(\frac{I}{I_{c10/100}} \right)^n \tag{1.9}$$

where E_{th} is the threshold value for the electric field, d_{taps} is the distance between the voltage taps, and I is the current flowing in the sample when the voltage V is measured. To achieve a measurement of Ic_{10} or Ic_{100} the experimental data have to be fitted to the power law model expressed in eq.1.9 using the corresponding threshold for the electric field. Moreover, the fit would give the exponent n which defines the steepness of the voltage growth around the critical value. The so-called n-values are typically in the range of $25 \sim 40$. The second criterion is the resistivity criterion which consists into setting a resistivity threshold ρ_{th}, which is typically equal to 10^{-13} Ωm or 10^{-14} Ωm. In this second case the critical current is given as the interception between the power law and the linear Ohm's law having ρ_{th} as its steepness. Finally, the offset method gives the critical current as the value at which the tangential line starting from the current-voltage power law crosses zero voltage. A visual representation of the three methods is available in Fig. 1.6.

In order to design a superconducting magnet it is necessary to select a superconductor that has all critical values high enough to allow the material to sustain both the transport current and the generated magnetic field at the highest possible working temperature. Moreover, the material needs to be processed with a metal matrix and have a manufacturing technology that enables the production of continuous unit lengths of at least hundreds of meters. Among almost ten thousand of materials exhibiting superconduct-

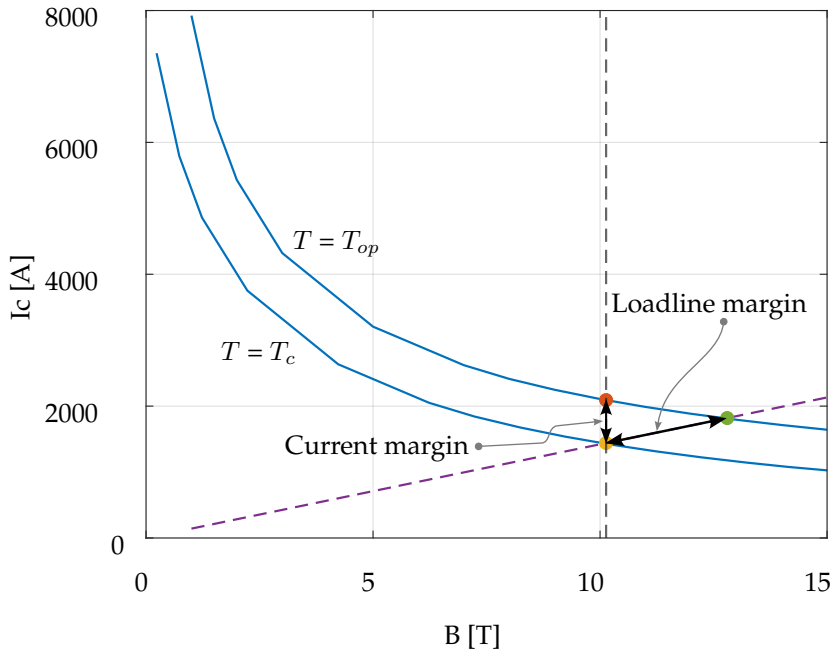


Figure 1.7: Critical curves representing the values of I_c as function of the magnetic field B for a real case study of a HTS magnet. In the graph is labeled what is commonly referred to as current margin and loadline margin with respect to the operating conditions identified by the yellow-dot. Temperature margin is given by the difference of the operating temperature T_{op} and the critical temperature T_c at the operating conditions.

ing properties, up to now only six respect the requirements to be used inside a magnet and are called technical superconductors.

Technical superconductors can be further classified in two categories, based on the critical temperature limit, respectively called: Low-Temperature Superconductor (LTS) and High-Temperature Superconductors (HTS). LTS includes classical superconducting materials as Nb-Ti, Nb_3Sn, and MgB_2, having Tc respectively of 9 K, 18 K, and 39 K. These materials, excepts for MgB_2 which may operate also at slightly higher temperatures, are bounded to liquid He temperatures, i.e. 4.2 K or 1.9 K for superfluid He, for cryogenics, to fully exploit the properties of the materials. On the other hand HTS includes the class of REBCO, $Bi_2Sr_2CaCu_2O_{8-x}$ and $Bi_2Sr_2Ca_2Cu_2O_{10-x}$ commonly called BSSCO 2212 and 2223. The difference with respect to LTS is the possibility to operate at 77 K using liquid nitrogen, given the Tc of REBCO being $\sim$ 90 K, and those of BSSCO 110 K and 95 K respectively for 2223 and 2212. However, to become competitive with LTS the working temperature shall be decreased, still giving the possibility of avoiding liquid helium for cryogenics, which is constantly increasing in cost per liter, currently around 30 €/L [14], and introducing an energy saving factor by simply increasing the working temperature. Overall, the choice of the superconductor is strictly related to the desired parameters of a

particular design. In the specific case of a superconducting magnet, the central magnetic field is the main target. Once the magnetic field is set, the operating temperature and current are chosen so that the conductor works below the critical surface. The operating current is typically chosen with an appropriate safety margin. Such margins are represented in Fig. 1.7 and are conventionally quantified in terms of the residual amount of a specific critical value under operational conditions which may ultimately lead the coil to the loss of its superconducting properties, that is, a quench event. This margin commonly targets the current and can be defined as the loadline margin or current margin, whether the margin itself is calculated as the distance between the operational point and the critical curve in the $Ic - B$ plane or as the relative fraction with respect to the critical current value at the operational field, respectively. This way of defining safety margins is mainly empirical. Instead a more physical approach involves the critical temperature and consists in calculating the value of T_c in operational condition and quantifying how many degrees the coil needs to be heated up from the operating temperature in order to reach the critical value. This provides a more direct interpretation of the energy required to quench the magnet at its most critical point.

1.1.2 REBCO

Among the available technical superconductors, specifically within HTSs, the family of materials which has achieved the highest performances in terms of I_c at high fields and temperatures of tens of degrees kelvin is the one of REBCO (Rare Earth Barium Copper Oxide). The formulation of the material can be expressed as $REBa_2Cu_3O_{7-\delta}$ where the Rare-Earth (RE) is commonly replaced by Yttrium, leading to YBCO. However, other elements such as Gadolinium (Gd), Neodymium (Nd), Samarium (Sm) may be used and all ultimately lead to a superconductor with a $Tc \sim 92$ K. REBCO belongs to the cuprate family, which is characterized by a layered perovskite crystal structure, as illustrated in Fig.1.8. With reference to the picture, the copper-oxide (CuO_2) plane is identified by two crystallographic axes called a-axis and b-axis, whereas the direction orthogonal to the CuO_2 layers is referred to as c-axis. Cuprates superconductors are generally considered to be quasi-two-dimensional materials with their superconducting properties determined by electrons moving within weakly coupled CuO_2 layers, determining an intrinsic anisotropy of these materials. Indeed, the in-field behavior of REBCO is different from traditional LTS conductor. Since the superconducting state is present primarily within the CuO_2 planes, when a magnetic field is parallel to the c-axis, the mixed state occurs, causing circulating currents on each of these planes. On the other hand, between the planes the currents are not present, resulting in relatively weak flux pinning. However, when the field is orthogonal to the c-axis, the size of a vortex is much larger than the thickness of the superconducting layers. Therefore, the field can harmlessly penetrate between the layers [16], granting a much higher tolerance to the magnetic field. The effect is evident when the critical surface is observed. To this purpose, an example of the critical surface of commercially available YBCO is graphed in Fig.1.9 at two different temperatures. This anisotropy introduced by CuO_2 planes, imposes that the material must be produced such that the c-axis orientation remains coherent overall the whole

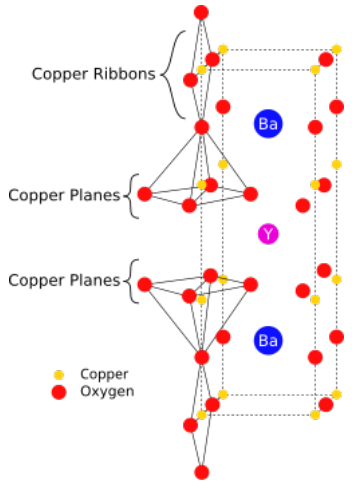


Figure 1.8: Microscopic structure of the YBCO lattice [15].

superconductor, in order to allow the current flow between the planes. Moreover, an orientation between crystallites is needed. A misorientation between ab-planes impedes current flow as described by the relation:

$$J(\theta) = J_0 e^{\theta/\theta_c} \tag{1.10}$$

where J_0 is the critical current density in the ideal case of perfectly aligned crystalline boundaries, θ is the actual angle between the planes and θ_c is the threshold angle, beyond which the critical current density begins to drop exponentially. In the specific case of REBCO, θ_c is the order of $3° - 5°$, therefore requiring also an in-plane texturing to align the ab-planes.

The discovery of YBCO as a bulk superconducting material occurred in 1987 [17]. However, given the above-mentioned challenges due to the precise biaxial texture required throughout the whole length to avoid a degradation of the critical current, the processing and manufacturing optimization has been achieved and greatly developed only in the last decade. Specifically, the manufacturing process has converged to the realization of a coated conductor, which consists of a multi-layer tape architecture. The tape shape to now is an unavoidable constraint introduced by the necessity of granting a biaxial texture. A HTS tape consists of several layers deposited on a mechanically strong substrate, as illustrated in Fig. 1.10. The thickness of the different layers varies depending on the manufacturer, except for the copper and a possible custom finish which may vary depending on the user requests and applications. The width of the produced tape is generally 12 mm, smaller widths are mechanically or laser slit from the 12 mm.

The substrate layer works as a mechanical support and is typically made with C-276 Hastelloy® or a nickel alloy. The thickness varies between a minimum of 30 μm and up to 100 μm, and the material properties contribute to the mechanical strength of the tape having, in the case of Hastelloy®, an ultimate tensile stress strength of $\sim$ 700 MPa and a Young's modulus of $\sim$ 200 GPa [18]. Higher thicknesses result in a more robust

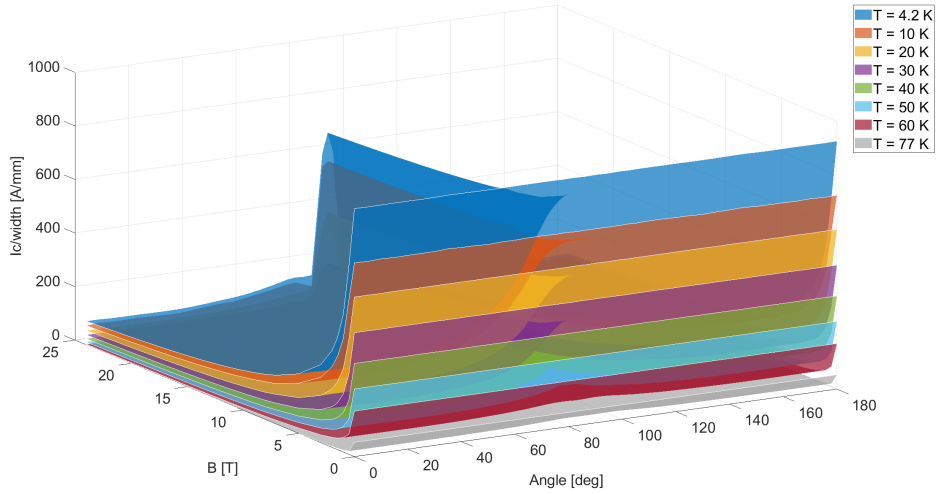


Figure 1.9: Critical surface at different temperatures of commercially available HTS YBCO tape. On the z-axis is graphed the value of I_c normalized on the tape width as a function of the angle with respect to the c-axis and the applied magentic field.

conductor, but reduce the overall current density across the tape cross section, that is the engineering current density (J_{eng}). The substrate then needs to be covered by a buffer layer in order to accomplish an orientated growth of REBCO on its surface. One way to achieve the texture is RABiTS technique (Rolling Assisted Bi-axially Textured Subtrates [19]). With this technique, a cube texture is created in a Nickel-Tungsten (NiW) substrate by a rolling and recrystallization process. Afterwards, several epitaxial buffer layers are needed to provide a lattice-matched surface to grow the HTS layer.
The texture may also be provided via Ion Beam Assisted Deposition (IBAD) [20]. In this case a bi-axially textured MgO layer is grown on a polycrystalline Hastelloy® tape. Several other buffer layers are needed to enable replication of the low angle grain structure of the substrate in YBCO and protect it from chemical contamination. The superconducting layer itself could then be deposited following a physical route, implying the use of a Pulsed Laser Deposition (PLD) or an Electron Beam Deposition (EBD), or a chemical route via a Metal-Organic Deposition (MOD) or a Metal-Organic Chemical Vapor Deposition (MOCVD). Ultimately, a silver layer of 2 to 4 μm, is deposited for protection against environmental degradation, to facilitate current injection and to act weakly as a stabilizer. In absence of potential custom finishes such as pre-tinning of the tape, the last layer consists in copper, which is electro-deposited on the tape, covering all the previous layers and enclosing the tape. The thickness may vary between 0 and 20 μm per side, additional copper may come with depositing issues resulting in a much less homogeneous layer. This last layer is fundamental for thermal and electrical stabilization of the tape in case of quench. With this last layer, the final YBCO tape is complete and could be afforded in a range of overall thicknesses between a minimum of 50 μm and a maximum

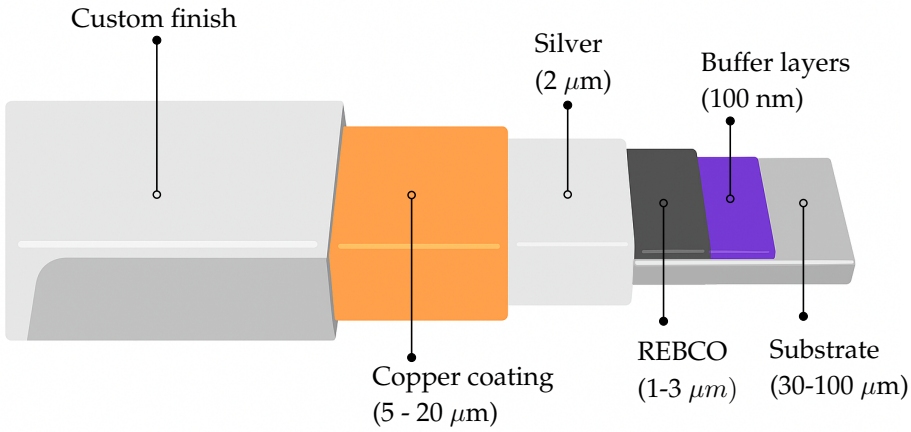


Figure 1.10: Multi-layer structure of a coated conductor REBCO tape. Buffer layer thickness may change depending on the producer.

of $\sim$ 150 μm, and 2 mm to 12 mm wide.
Although the production phases are established, the manufacturing process itself is extremely complicated to control. Therefore, producing unit lengths of HTS the order of kilometers with constant high performances is yet to be achieved. Since manufacturing is acknowledged to be unstable, an online quality control system is often installed in the production chain to control the performance of the HTS tape. The system has been developed from Theva and is called Tapestar® [21]. The system carries out a non-destructive measurement of I_c at 77 K and self-field, continuously on the newly produced tape to qualify its performances. The measure is acquired in liquid nitrogen (LN_2) via an array of hall probes sensing the magnetization field induced on the superconducting tape. The sensors have an active area of $\sim$ 0.01 mm^2 and placed 0.6 mm apart from each other, therefore granting a millimeter resolution. The external magnetic field applied in the direction paralel to the c-axis is supplied by a copper coil generating 8.0 mT/A, and field homogeneity of about 5% along the tape width. Ultimately, the field produced by the induced superconducting currents is measured by hall probes and correlated to the critical current value [22]. In order to scale up this value and meet the demands for a superconducting dipole magnet which requires a specific performance at operational conditions, a set of lift factors has been found. One of the most commonly used is the conversion between the 77 K self-field Tapestar® measure and the expected performance at 20 K, 20 T transversal field which is $\sim$ 1. A real Tapestar® measurement of a FFJ 4 mm YBCO tape is reported in Fig.1.11 and shows the trend of the I_c value as a function of the position within the overall length of the tape. From the graph, it is straightforward

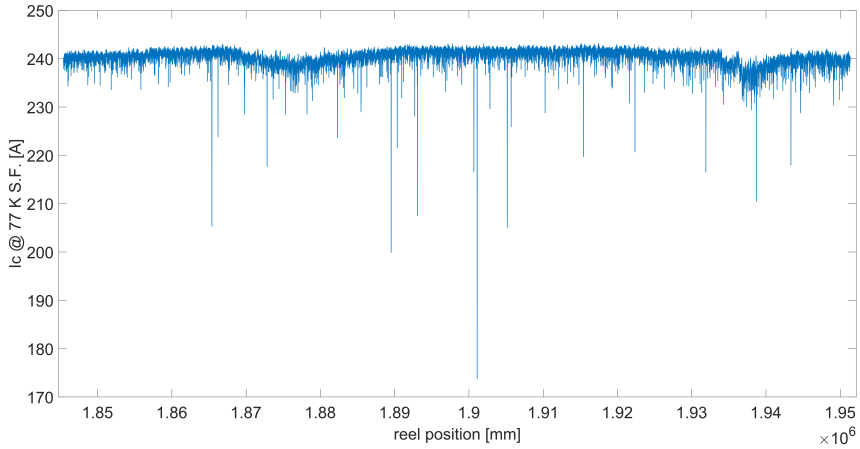


Figure 1.11: Tapestar® measurement of a 4 mm HTS tape from Faraday Factory Japan (FFJ) showing the value of I_c overall the length of the whole HTS tape spool.

to notice that while the average value of I_c could be set around 240 A, the measurements performed every few millimeters are able to spot local defects occurring during the production, which, in the worst case, produce an expected performance drop in the middle of the spool of about 25%, specifically down to $\sim$ 180 A. This is a direct result of the unstable production process, which forces the manufacturer to interrupt the fabrication in case a more severe defect is detected. For this reason, the available tape unit length, as well as its cost per meter, is strictly correlated to the required performances from the user. Specifically, the cost and feasibility of obtaining a tape that meets demand depend on whether the requirements target an acceptance threshold on local defect, which can be often interpreted as a constraint on a minimum value of I_c or more a relaxed criteria like average critical current.
This difference in the feasibility of procuring the desired tape is resumed in Fig.1.12, where it can be observed that while the average produced unit length is about 400 m and may go up to 600 m, the available length is halved if the requirements set an acceptance constraint on the minimum value of I_c. Both a high value for minimum I_c, which means there are almost no defects, and a spool length approaching 600 m would mean both a challenging task for the manufacturer and a dramatic increase in the conductor cost per meter which would likely be excessive to bear for the magnet designer. Indeed, managing the optimization between the unit length, keeping satisfactory performances, and a not excessive cost of the tape itself, is still an open challenge and the solution is to be taken specifically for each magnet design.

1.1.3 State of art about HTS magnets

Given the extreme potential of HTS REBCO tapes, ambitious designs focused on exploiting the high critical values of this conductor have been proposed with the aim of realizing high-field magnets. One of the first projects concerned the conceptual design

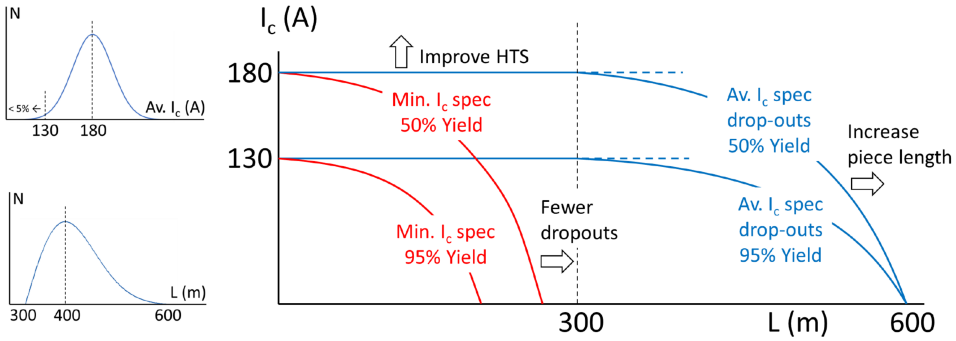


Figure 1.12: Statistical distribution of the average I_c properties (top left picture) and average unit length without (bottom left) of the produced HTS tape from Faraday Factory Japan (FFJ). The right picture shows the trend of the unit length which can be produced with respect to the required performances from the user.[23]

of a HTS insert named FeatherM2[24], within the framework of the European Collaborative Accelerator R&D-2 (EuCARD2) [25]. The magnet is reported in Fig.1.13 and is designed as an aligned block insert with a 40 mm aperture, which is capable of producing a 5 T field at 4.2 K in a standalone powering. However, its real purpose as an insert is to enhance the field produced by the FRESCA2 [26] Nb_3Sn dipole magnet, increasing the central magnetic field up to 16.9 T, always at liquid helium temperature (LHe) of 4.2 K. The aligned block takes advantage of the high tolerance of the HTS tape in the direction parallel to the c-axis, thus enabling the insert to work and efficiently produce a magnetic field even when submerged in a background of 13 T. The coil has been wound using a particular cable, derived from HTS tape, named Roebel [27] which has been insulated and subsequently impregnated.
Superconducting magnets targeting higher fields have then been developed, although the aim has been shifted to a mechanically simpler problem with respect to a dipole, that is, a solenoid design. To this purpose, two superconducting solenoids have achieved a central magnetic field of $\sim$ 32 T: the superconducting solenoid at the National High Magnetic Field Laboratory (NHMFL) in Tallahassee [28] and the magnet built for the French project ANR NOUGAT at CEA [29], both pictured in Fig. 1.14. The aim of the 32 T project at NHMFL was to build an all superconducting user magnet capable of generating 32 T in a cold bore of 32 mm, using REBCO coated conductor in addition to a traditional outsert in Nb-Ti and Nb_3Sn. The insert consists of six double-pancake modulus, engineered to generate a magnetic field of 17 T in a background field of 15 T generated by the outsert at 4.2 K. The magnet has been dry-wound with non-insulated conductors and insulated stainless steel co-wind and ultimately successfully tested. The second example comes with almost the same premises, since the magnet for the NOUGAT project was designed as a 10 T HTS solenoidal insert intended to operate in a 20 T background generated by a resistive, 170 mm bore outsert magnet, for a target field in the center of 30 T within a 38 mm cold bore aperture at 4.2 K. The insert consists in nine double-pancakes which

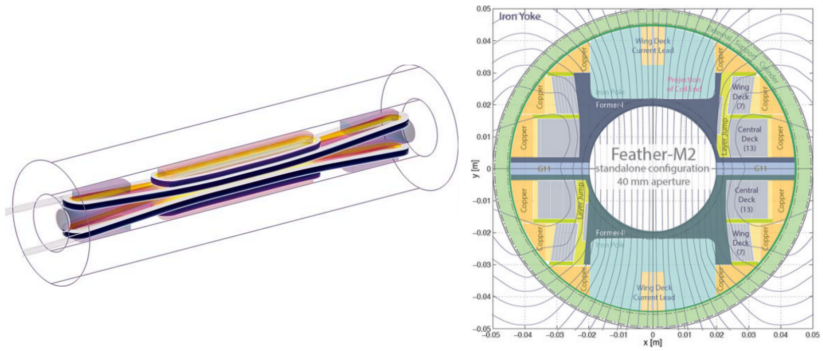


Figure 1.13: The left picture shows the 700 mm long coils of the prototype magnets FeatherM2, while on the right picture it is represented its detailed cross section (reprinted from [24][25]).

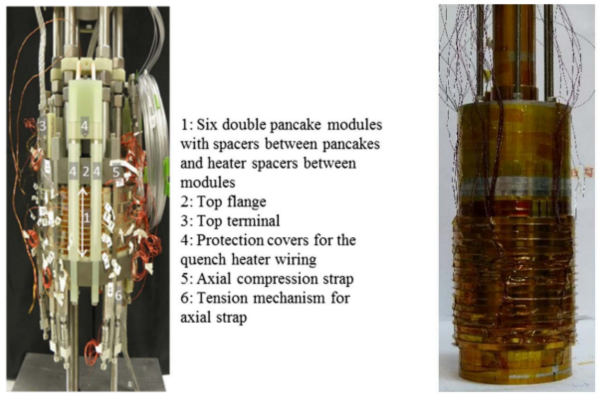


Figure 1.14: HTS insert for the high field 32 T solenoid at NHMFL (left picture) and for the NOUGAT project (right picture). (reprinted from [28],[30]).

have been wound with the Metal-as-Insulation (MI) technique, meaning that the HTS tape has been dry-wound together a non-magnetic steel tape without any insulation. A more in-detail discussion about this winding technique will be dealt with later in this chapter. The coil has been successfully tested and reached a central field of 32.5 T, with 14.5 T generated by the HTS insert.

Beyond the high magnetic field achieved by the above-mentioned HTS insert for both the solenoids at NHMFL and CEA, a HTS insert named LBC (Little Big Coil) has been designed and manufactured at the University of Seoul to generate a magnetic field of 14.4 T inside a 31.1 T resistive background magnet to obtain a magnetic field of 45.5 T in LHe [31]. The design had to be constrained to the very narrow bore of 37 mm of inner diameter, so that inner and outer winding diameters were set to be 14 mm and 34 mm respectively. This has necessarily imposed the windings to be made of single pancakes wound with a single tape. The tape has been dry-wound without any kind of insulation, a technique known as non-insulated (NI) windings which is to be discussed together with MI later on in this chapter. The whole insert, which is detailed in Fig. 1.15,

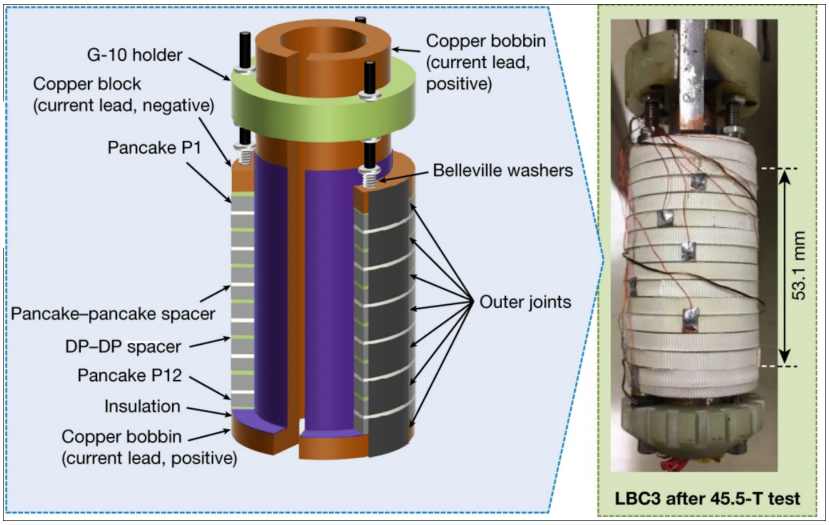


Figure 1.15: Construction design of LBC HTS insert for the 45.5 T solenoid at the University of Seoul together with the manufactured HTS magnet. (Adapted from [31]).

was finally realized with 12 coils with both inner and outer resistive joints to electrically connect adjacent pancakes. The magnet has then been tested and successfully reached the extraordinary central field of 45.5 T. However a quench event occurred, irreversibly compromising almost every coil except for two which completely survived. Although, it is significant to notice how the quench did not produce a macroscopic burn, but instead caused cracks in the superconducting REBCO layer which could be detected via a scanning electron microscope.

One last coil to complete this state of the art summary for HTS magnets is the toroidal field model coil engineered and tested by Commonwealth Fusion Systems (CFS) and illustrated in Fig. 1.16. The Toroidal Field Model Coil (TFMC) is a superconducting test coil designed for the experimental fusion reactor SPARC by CFS. This underlines the importance that HTS materials has meant not only for the accelerator and material scientist community, but also for the fusion plasma research, where the specifications of the magnetic confinement machines (Tokamak) are very demanding. The TFMC has represented the first large-scale HTS coil, with an approximate size of 3 m and a peak field of 20 T. Moreover, it is the first high-field prototype to work at 20 K, thus truly exploring the operational temperature beyond the limits of traditional LTS. The coil has been built with a total of 270 km of REBCO, wound with a non-insulated stack of around 200 tapes, organized in 16 pancake of 16 turns, each set in a grove of stainless steel. However, even in this last case, although the coil had been successfully tested, a quench event occurred causing lethal damage to the whole coil. The burn damage suffered by the coil is showed in Fig. 1.17. These last two ambitious projects, ended with a critical quench event, have clearly stated the need for a way of handling the quench problem in high-field HTS magnets.

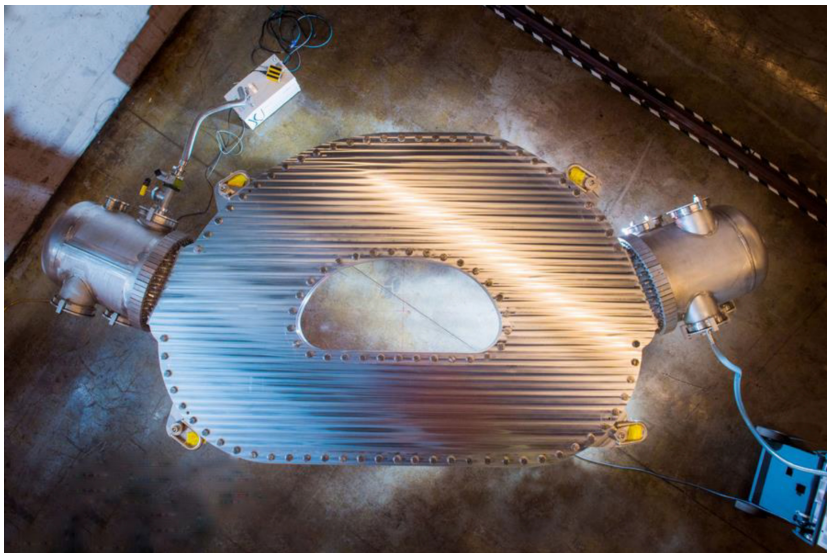


Figure 1.16: Completed toroidal field model coil manufactured by CFS, before testing. (Reprinted from [32]).



Figure 1.17: Post mortem close-up picture of the quench induced damages in the toroidal field model coil at CFS. (Reprinted from [33]).

1.2 Challenges in HTS magnets

As discussed in Sect. 1.1.2 and Sect.1.1.3, the HTS production has reached at satisfactory level, such that working prototypes could be built and tested. This has also been made possible thanks to the investments performed by fusion research programs, associations, and start-ups, which have greatly contributed to the advancement of HTS manufacturing and supply chains. These efforts have improved production efficiency and scalability, while increased demand has driven down costs, facilitating a technological diffusion also for other research purposes or industrial applications such as accelerator magnets or electrical machines. However, this technology comes with many challenges that are yet to be solved, due to its maturity still not being comparable with traditional LTS. To this purpose, the following section will cover the most common challenges which are commonly encountered when approaching a magnet design with HTS materials.

1.2.1 Screening currents and magnetization

HTS materials are bounded to their tape geometry by the manufacturing procedure. The wide and uninterrupted surface of the tape therefore offers the right conditions for superconducting screening currents to develop when the magnetic field is changing, simply due to Faraday law:

$$\oint_{\delta S} \mathbf{E} \cdot d\mathbf{l} = -\int_{S} \frac{\delta \mathbf{B}}{\delta t} d\mathbf{S} \tag{1.11}$$

where t is the time, $\mathbf{E}$ and $\mathbf{B}$ are the electric field and magnetic field vectors and $d\mathbf{l}$, and $d\mathbf{S}$ are respectively the tangent vector of the closed loop circuit integration and the surface vector. The main effects introduced by the screening currents are the Screening Current induced magnetic Field (SCF) and the Screening Current induced Stress (SCS), which could both be visualized in Fig.1.18.
The SCF is responsible of causing field distortion and temporal drift. In a typical pancake stack layout $\mathbf{B}_{tot}$ may deviate from the nominal magnetic field $\mathbf{B}_n$ due to SCF by a quantity $\mathbf{B}_s$ as described by:

$$\mathbf{B}_s = \mathbf{B}_{tot} - \mathbf{B}_n \tag{1.12}$$

Given this, the spatial distribution of $\mathbf{B}_s$ can introduce harmonic errors, which may not be allowed in accelerator magnets or other applications demanding magnetic fields with a spatial homogeneity the order of a unit and temporal stability. On the other hand, the result of the Lorentz force related to the high parallel field generated by the magnet and the screening currents is responsible for the SCS which are non-uniformly distributed since they depend on the direction of the induced current which is by definition a closed loop. This results in stresses which tend to pull the HTS tape in opposite direction as showed in Fig.1.18.
One example were the effect of the SCF has been quantitatively estimated in a HTS coil wound with 4 mm tape and designed for Nuclear Magnetic Resonance (NMR) [35]which has been tested in a background field generated by an LTS and a Bi-2223 outsert magnet. The measured central field was found to be 2% lower than the nominal value of 30.6 T at 265.6 A plus an overshooting of 2-5 A. A similar effect has been measured on another

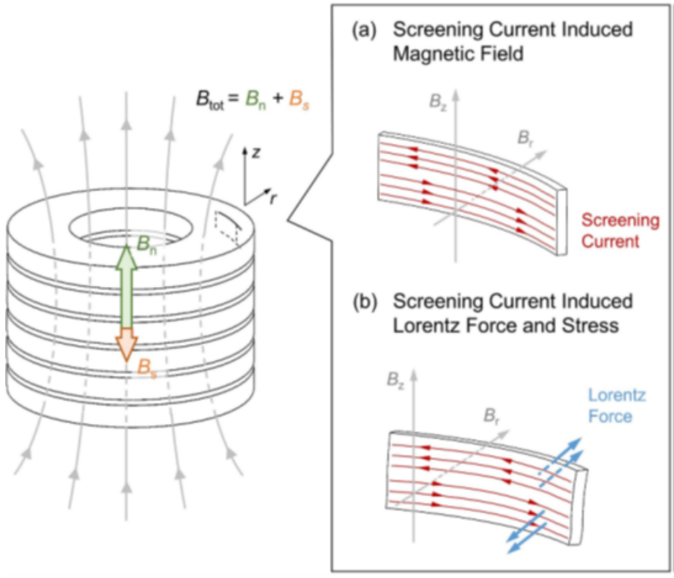


Figure 1.18: Effect of the induced screening current into a HTS tape, in terms of magnetic field deviation and induced stress on the conductor. (Reprinted from [34]).

coil for NMR, named H800 [36], which showed a similar central field reduction by 3.1% at 190.0 A and 2.9% at 217.5 A compared to the designed values. In this second case percentage were slightly higher due to the fact that the tape used to wind H800 was 6 mm wide. For what concerns the phenomenon of SCS, this has been confirmed quantitatively by direct measurements of the hoop strains in small pancake were the effect was strong enough to produce ripples on conductors' edges as well as delamination of the REBCO layer from the buffer layer [34]. Specifically, in the just mentioned case of H800, the coil has been severely damaged after a quench even and the peak hoop stress computed via SCS ranged between 680 and 940 MPa. The same cause has been attributed to cause the damages detected after the quench of the 45.5 T magnet at the University of Seoul [31]. To this aim the tape itself might not be enough to withstand these kind of stresses. Mechanical reinforcement could be integrated, but might not be sufficient to protect the conductor.
In LTS magnets, the effect of the screening currents induced fields and stresses is minimized by the application of twisted multi-filamentary conductors. However, in high-packed pancake coils made from REBCO tape twisting becomes practically challenging. Although, some attempts are being developed with partial twisting, or full transposition resulting in the superconducting cable design of: Viper [37], the above-mentioned Roebel used in EuCARD2 [27], the Symmetric Tape Round (STAR) [38] and the Conductor on Round Core (CORC®) [39]. Moreover, for what concerns the filamentization of the conductor, striated HTS tapes are being developed by engraving the tape itself with laser, mechanically scribing it or building the tape itself on a striated substrate[40]. When a striated coated conductor is subject to a time varying magnetic field, induced

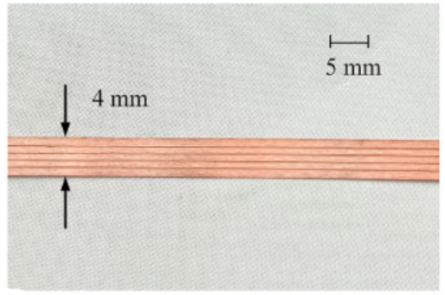


Figure 1.19: Sample of a striated HTS tape. (Reprinted from [34]).

screening currents will generate overall the conductor width, coupling the filament via the resistive matrix, and within the striation. Therefore, the filamentization will only become effective after the decay of the coupling currents, giving a ratio of the overall hysteresis energy loss Q_h between the filamentized tape and an equivalent standard HTS conductor, assuming full decoupling, of [40]:

$$\frac{Q_{h,filamentized}}{Q_{h,non-filamentized}} = \frac{1}{N} \tag{1.13}$$

where N is the number of filaments. This practice however is yet to be applied to high procurements of HTS tape due to its processing cost, yield, and scalability, thus still far from meeting large market demands.

1.2.2 Mechanical issues

Another challenge directly related to the tape shape, regards the constraints imposed by the degrees of freedom of tape when it is to be bent in space. Indeed, the tape can be easily bent on its short side, the so-called easy-way, but it requires long length to accommodate a curvature on the long side, in the so-called hard-way. To this purpose, the coil geometry which could be wound using HTS tape is much more bounded to flat coils, such as racetracks or circular pancakes, making the design of accelerators magnet much more challenging on the mechanical and manufacturing side. Indeed, as discussed in Sec. 1.1, superconducting magnets for accelerators achieving a field quality the order of the unit, often relies on the cos θ winding layout which consists in placing the conductor around the beam-pipe and closing the winding on the other side by climbing over the aperture, as showed in Fig.1.20. This method strictly implies an hard-way bend if carried out with a tape, and therefore would require a dedicated feasibility study on the winding technology. However, the tape shape does not necessarily mean that every out-of-plane winding geometry is excluded, although they would not come without significant complications. To this aim, one example of coil geometry which could trespass the beam-pipe using a tape instead of a cable, is represented by the cloverleaf design [41], illustrated in Fig.1.21. The design is based on diluting the hard-way bend on a much longer path, without elongating the coil extremities too much.

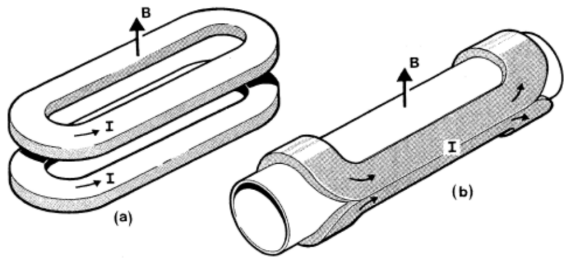


Figure 1.20: In the picture a flat coil design made with racetracks for a dipole magnet is represented in picture (a), whereas on the right side (b) it is sketched a geometry requiring an out-of-plane winding to climb over the beam-pipe. (Reprinted from [7]).

Other mechanical constraints are imposed on the tape, as a result of the chemical structure of the HTS layer. Indeed, this brittle ceramic composite is deposited on a metallic substrate which can grant mechanical robustness, however, thresholds are still present such as a minimum bending radius and a maximum allowed strain. In particular, the Hastelloy® substrate, allows the tape to bear a tensile stress of around $600 - 700$ MPa in static conditions, and a corresponding strain value of ~ 0.5 % before irreversibly degrading [42]. The criterion used to determine whether a degradation has occurred is related to the performance of the HTS tape. Specifically, the threshold is conventionally set to loss in transport current performances up to 95 %, meaning that if the conductor loses more than 5 % of its nominal I_c value under the same conditions, the conductor has suffered a degradation. With the same criterion, mechanical studies have been performed on the minimum bending radius achievable in a winding without degrading the HTS tape, resulting in a range of values between 5 and 8 mm. These values depend on the layer thicknesses within the tape, possible external coatings, and also on the orientation of the superconducting layer with respect to the winding, i.e.: facing the mandrel or pointing outward [43][44]. The HTS tape is also sensitive to high temperature, having a threshold set to a maximum of ~ 200 °C [45].
One further limitation is set by the multi-layer structure of the tape. Indeed, the coated structure is particularly sensitive to delamination. The term delamination describes the phenomenon of detachment of the layers from each other, which is particularly critical when occurring between the superconducting layer and the substrate or copper layer. The delamination strength of YBCO coated conductors under transverse tensile stress shows indeed a low delamination resistivity of less than 15 MPa [46]. Such a phenomenon considerably reduces the properties of the superconducting layer, since the possibility of tearing layers of CC apart would result into an irreversible damage of the conductor. To this purpose a widely used technique in magnet design and manufacturing to provide good mechanical stability, which is the impregnation, would likely backfire when considering a winding performed with HTS tape. Indeed, if the radial stress generated during the cooling process, or due to Lorentz forces when the magnet is energized, exceeds the delamination limit of the conductor, since the conductors themselves are rigidly bonded to each other, cracks or delamination are likely to occur,

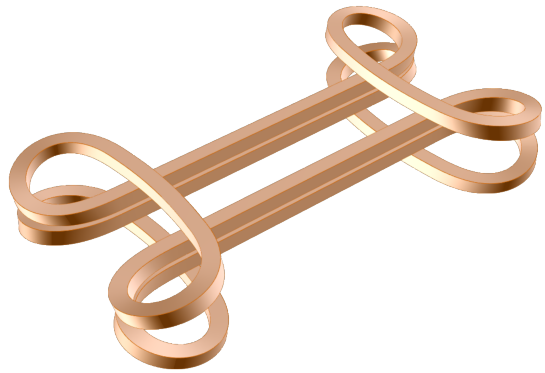


Figure 1.21: Illustration of a cloverleaf coil design for a dipole magnet.

threatening the operation. One possibility is trying to adapt the impregnation or to develop a novel impregnation technology to avoid delamination. On the other hand, as described in Sec. 1.1.3, another possibility is to make windings without impregnation, namely dry windings.

1.2.3 Quench in HTS magnets

The advantage given by HTS of reaching higher fields also means dealing with higher energy and consequently more catastrophic quench events, as seen in the case of LBC or the more severe damage of TFMC from CFS where the coils could not be protected. For this aim a novel paradigm to quench, different from what has traditionally been conceived for LTS magnet, needs to be developed. To date, the detection and mitigation of thermal runaway, also known as a quench event, in HTS remains a not yet fully resolved issue. A quench may occur when the superconductor heats up locally such that it exceeds the Current Sharing Temperature T_{cs}, which is defined as the temperature above which the superconductor can no longer conduct the entire transport current with zero resistance. Beyond this point, the portion of the current that exceeds the capacity of the superconductor is carried by the surrounding stabilizing material, usually copper, leading to the formation of a region with finite electrical resistance. If the local temperature continues to increase and surpasses the critical temperature, the superconducting material completely loses its superconducting properties, forcing all the current to flow through the resistive matrix. Therefore, a normal zone is created and could be defined as a resistive zone including a temperature range between T_{cs} and T_c.
When the length of the normal zone within a superconducting tape or cable becomes sufficiently large, the resulting heating may exceed the cooling capacity of the system. This heating surplus leads to the expansion of the normal zone and, ultimately to a local hot-spot which may result in the failure of the conductor. On the other hand, if the generated heat is effectively dissipated and remains below the cooling capacity, the system could recover, and the conductor would return to its superconducting state. To prevent

irreversible damage, it is essential to detect or prevent, the thermal runaway promptly, allowing the current to be safely diverted or eventually shut down the magnet before the situation escalates. To this purpose a Minimum Quench Energy (MQE) can be defined as the smallest amount of energy required to initiate a self-sustaining propagating normal zone, serving as an indicator of the thermal stability of the conductor, a concept closely related to the already introduced temperature margin. Moreover, to enhance this stability, part of the cross-sectional area of the conductor is composed of copper or aluminum stabilizer, as discussed in the REBCO manufacturing chain in Sec.1.1.2.
To avoid the coil suffering lethal damage following a quench event, quench detection and protection systems have been developed. In particular, the most traditional and implemented one consists in measuring the voltage across the conductor. Indeed, under normal operating conditions, due to superconductivity, no or very low voltages are present, so that when an unexpected voltage is detected it might indicate a formation of a normal zone and consequently the magnet protection system is triggered. In small cables or coils characterized by low self-inductance, a simple shutdown of the power supply may be sufficient to safely interrupt current flow and protect the magnet. However, in large-scale accelerator magnets, the stored magnetic energy is the order of MJ and requires active system to handle its dissipation. In such cases, one solution consists in redirecting the energy to an external dump resistor, which is integrated in the circuit and switched in upon quench detection. Moreover, to prevent localized overheating and to ensure a uniform energy deposition, an additional protection strategy involves intentional heating of the entire conductor pack above T_{cs}. This is achieved by activating heaters embedded within the coil windings, named quench heaters, to initiate a controlled transition of the entire coil, thus allowing the magnetic energy to be deposited over a larger volume, minimizing the damage due to a local hot-spot. An alternative approach to quench heater is the Coupling Loss Induced Quench (CLIQ) system [47], which consists in heating the magnet through coupling losses.
Considering now the specific case of REBCO CCs, due to their high critical temperature, they show a significant temperature margin, with a consequently high thermal stability. Moreover, under cryogenic conditions, the specific heat capacity of the materials composing the HTS tape increases rapidly with temperature, resulting in a MQE that can be up to three orders of magnitude greater than that of LTS. Therefore, HTS magnets are expected to exhibit significantly higher stability. On the other hand, in the event of a quench, the normal zone propagates very slowly with respect to LTS, since the energy required to heat up and quenching the nearby material is higher [48][49]. A slower normal zone propagation velocity means to reach localized higher temperature and a more critical damage following a quench event. For this reason the quench is also more difficult to detect before the conductor is damaged since, for the same voltage detection threshold, the peak temperature reached in the HTS conductor is higher than in the LTS. This implies that a classical detection and discharge quench detection in HTS conductors yields a delayed response, thus representing a challenge for protection systems. To this aim other quench detection systems are being investigated, as the use of optical fibers to detect a local increase of temperature [50], but are still to be perfected for a real implementation. Quench detection and protection remain an open challenge for HTS magnet

and could open the path to a new designing paradigm, which could take advantage of the high thermal stability of HTS magnets and pursue the ambitious goal of making the magnet not quenching at all.

1.2.4 NI and MI magnets

Given the challenges of quench detection and protection given by the high thermal margin of the HTS tape, a winding technology that foresees no or controlled insulation between superconductive tapes, may be employed to realize a more robust winding design. The concept of using metallic insulation in superconducting coils was first proposed and patented by Bailey in 1988 [51]. This concept then evolved, ultimately leading to two main research lines considering a winding technology considering only the tape and no insulation at all, known as No-Insulation (NI) [52], or including a metal band co-winding as a method to increase the turn to turn resistance, known as Metal-as-Insulation (MI) [30]. No-Insulation (NI) and Metal-as-Insulation (MI) winding technologies represent a turning point in the design of superconducting magnets with respect to conventional insulated coils. Indeed, traditional magnets rely on electrical insulation to maintain controlled current paths, whereas the removal or replacing of the insulation with a conductive but resistive metallic layer, allowing for current sharing between turns. This enables the coil to bypass localized quenched regions by passing through the resistive matrix to the next superconducting turn, thus distributing heat more uniformly and reducing the risk of damage. As a result, the aim of these technologies is to provide an intrinsic form of protection, thus proposing a solution to the design and operation of protection systems, which have been proven to be an open point for HTS magnets. Although the physical principle is prior to the development of HTS technology, it finds in REBCO the ideal case to be applied since every current sharing between the turns is a source of heat which could lead to a quench in case the coil holds a critical stability as for LTS magnets. Indeed, REBCO tapes are characterized by a higher thermal stability and temperature margins than LTS. This unique feature enables the use of MI/NI technologies to improve quench protection and magnet reliability, especially in applications concerning high stored magnetic energies. Given the high thermal stability, removing the turn-to-turn insulation, allows the current to bypass local resistive zones through radial paths, thus minimizing the risk of localized overheating. However, this phenomenon occurs both in cases of manufacturing local defects, partial degradation, or early presence of normal zone as well as when powering the magnet and changing the central field. To describe this last case, the overall winding could be simply modeled with a parallel R-L circuit as shown in Fig.1.22, where R_R represents the finite radial resistance resulting from the cumulated contribute of every turn-to-turn contact resistance, whereas R_{HTS} and L_{HTS} represent, respectively, the resistance of the azimuthal path of the superconducting winding and its self-inductance. Due to the presence of a conductive radial path, when the magnet is ramped up, or down, although the contribute of the superconductor to the impedance is zero, a current divider is created between the non-zero voltage rising from the inductance and a radial resistive path. This causes the magnet to show an exponential charging time behavior and a finite charging time con-

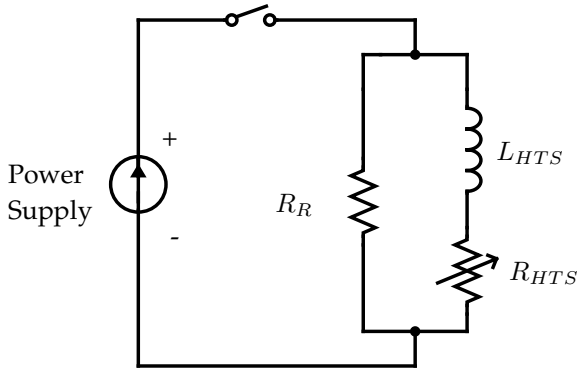


Figure 1.22: Parallel R-L circuit modeling the overall behavior of MI or NI coils where R_R represents the total radial resistance, and R_{HTS} and L_{HTS} the resistance and the inductance of the superconducting winding respectively.

stant such as in standard R-L circuits, which can be described as:

$$I = I_{op} \cdot e^{-t/\tau} = I_{op} \cdot e^{-t/(R_R/L_{HTS})} \tag{1.14}$$

where the charging time constant is expressed by the ratio between the radial resistance and the self-inductance of the magnet. However, this simple lumped model is not sufficient to describe the more complex dynamic current behavior which could occur in case of local quenches and, to this purpose, more sophisticated methods needs to be developed. Anyhow, a critical parameter in MI or NI magnets is the turn-to-turn contact resistivity R_{ct}, often found in $\mu\Omega \cdot cm^2$, which governs both the transient response of the coil and its self-protection capacity. The value of R_{ct} is critically dependent from the winding method, the winding tension and the surface of the tape itself and might slightly vary even if the manufacturing process is kept the same [30]. Typically, this value may range from a few tens of $\mu\Omega \cdot cm^2$ for NI coils, up to about 1000 $\mu\Omega \cdot cm^2$ for MI windings. The value of R_{ct} can be measured once the winding is complete directly from the characteristic charging time constant of the magnet by means of an exponential fitting. The value of R_{ct} indeed, is directly related to R_R via:

$$R_r = \sum_{i=1}^{N_{turns}-1} \frac{R_{ct}}{A_i} \tag{1.15}$$

where A_i is the contact area between the ith and $i^{th}+1$ turn. To this aim, a characterization of R_{ct} is essential to understand the behavior of MI and NI windings, although its value may vary over time due to changes in mechanical pressure, oxidation layers, or cooling conditions. For instance, the surface oxidation which might affect the tapes during mechanical cycling, can act as thin, yet highly resistive interfaces between turns, introducing unpredictability in the long-term behavior of the magnet [53]. The value of R_{ct} is directly related to the ease with which the current can take an alternative path other than the superconductive one. On one hand low values of R_{ct}, typical in NI coils, make the design extremely robust, thus able to withstand currents more than 10% higher

than the nominal break-down value measured in the short sample limit [52]. This gain has been widely confirmed by experiments in liquid nitrogen. Lower gains, approaching the short-sample limits, are to be expected at higher currents and lower temperatures. On the other hand, low contact resistance means high charging time values and high stresses which can potentially be caused by current redistribution when bypassing large defects or extended normal zone.

1.3 IRIS project

The IRIS project [54][55] aims at realizing an Innovative Research Infrastructure on applied Superconductivity (IRIS) which has been funded in 2022 by the Italian Minister for University and Research (MUR). This plan is set within the framework of the Next Generation Europe, a program that the European Union has formulated to compensate for the debilitation left from the pandemic caused by the corona virus. A fundamental part is the Recovery and Resilience Facility plan, which in Italy is called PNRR (Piano Nazionale di Ripresa e Resilienza). In this frame the Italian MUR has opened a call in early 2022 with which IRIS has been funded as a top class research infrastructure. However, the PNRR has a very strict timeline and requires that all tenders must be adjudicated by the end of 2023, thus making the IRIS a very ambitious and demanding project. IRIS is a research infrastructure distributed over six poles across all Italy represented in Fig. 1.23 and counts on seven institutes:

- National Institute of Nuclear Physics (INFN), which is present on the poles of Frascati (LNF, National Laboratory of Frascati near Rome), Genoa, Milan and Salerno;
- National Research Counsil (CNR), the largest research institution in Italy,–through its SPIN Institute, devoted to superconductivity. SPIN is active in IRIS in the pole of Genova, Naples and Salerno
- Università degli Studi di Genova (Genoa)
- Università degli Studi di Milano (Milan)
- Università degli Studi di Napoli Federico II (Naples)
- Università degli Studi del Salento (Lecce)
- Università degli Studi di Salerno (Salerno)

Each of the six poles already hosts laboratories conducting research in superconductivity, cryogenics, or accelerator instrumentation. Within the IRIS project, these facilities are being upgraded and assigned specific roles, promoting complementarity and collaboration across the network. The scope of IRIS is to have an infrastructure in Italy capable of facing the great challenge posed by the development of superconducting magnets and related technologies for next generation colliders for particle physics as the Future Circular Collider (FCC) or the Muon Collider (MuCol) [56] [57] [6]. In addition to its focus



Figure 1.23: The six technological poles involved in the IRIS project throughout Italy.

on particle physics, IRIS is also structured to increase the societal application of superconductivity, particularly regarding green energy and medical technologies. Another key goal of IRIS is the training of the next generation of scientists and engineers in superconductivity for the above-cited applications. To achieve its goals, IRIS is organized into nine Work Packages (WP), summarized in Fig. 1.24 and described below:

- WP1 (Milan–LASA): Project management and coordination
- WP2 (Frascati): Magnetic measurement laboratory
- WP3 (Genoa): Superconducting cable and material laboratory
- WP4 (Milan–LASA): Superconducting magnet laboratory
- WP5 (Naples): Advanced instrumentation laboratory
- WP6 (Lecce): Laboratory for superconductivity and magnetism
- WP7 (Salerno): Test facility for large magnets and superconducting lines
- WP8: Green superconducting line demonstrator
- WP9: Energy saving HTS magnet demonstrator

The LASA Laboratory in Milan serves as the hub, providing both technical leadership and logistic coordination. A Steering Committee and Project Office ensure compliance with the PNRR stringent timelines and fiscal constraints. The infrastructure is expected to be fully operational by 2025 and maintained until at least 2035. WP1, which is based in the laboratory LASA of Milan, regroups all common activity for management, coordination and dissemination for the whole project. In addition, the main experimental hall, which currently hosts the facilities for the cryogenic testing of superconducting

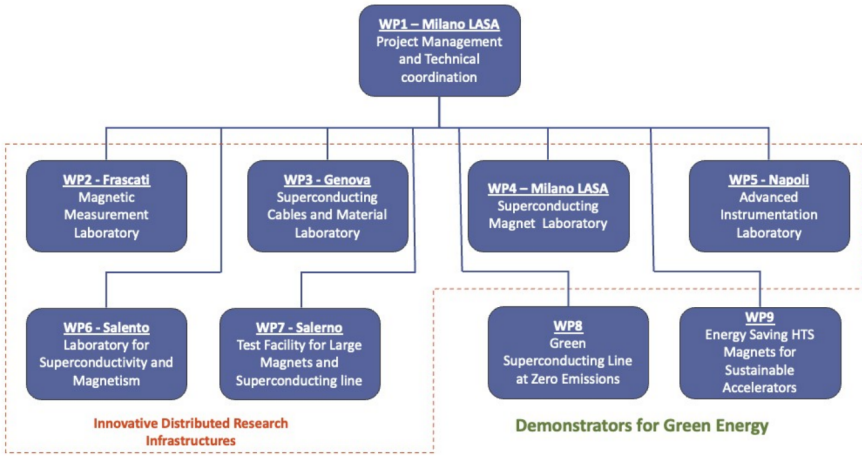


Figure 1.24: IRIS work packages organization scheme.

magnets, will undergo significant upgrades. These will include the installation of a large Variable Temperature Insert (VTI) capable of testing coils in a 8 T superconducting solenoid SOLEMI [58] (SOLEnoid MIlan), even at temperatures above that of liquid helium. The facility will also be equipped with a newly developed, remotely controlled cryogenic distribution system, and a high-performance power converter for superconducting magnets, producing up to 10 kA at $\pm$ 40 V (or 30 kA at $\pm$ 20 V). The quick test in vertical cryostat at operational conditions of models and prototype magnets is a critical tool for fast feedback on design and manufacturing. Additionally, rapid prototyping of magnet components will be employed to accelerate development cycles. The upgraded infrastructure will be accessible to external laboratories, external collaborations, and industrial partners. Moreover at Milan-LASA pole, the project IRIS includes the construction of a new building to create a facility devoted to the a new Superconducting Magnet Laboratory (SML) for development of models and prototypes of the next generation superconducting magnets. This new infrastructure for superconducting magnet construction is located at the LASA site and foresees the construction of a $\sim$ 600 m^2 hall, and other technical services necessary for magnet prototyping. To this purpose, the ground level of the building will host the tooling necessary for magnet constructions, such as a winding machine with vertical axis and double movement (covering all coil topology, single cable and multiple tapes), press system for high pressure polymerization, special ovens for vacuum impregnation and for Nb_3Sn coils heat treatment. The ground level scheme of the new building with machines locations is represented in Fig.1.25.

Within IRIS, WP8 and WP9 are dedicated to the design and realization of two technological demonstrators: a Green Superconducting Line (GSL - WP8) [59] and a full-HTS Energy Saving superconducting dipole Magnet for Accelerators (ESMA - WP9). GSL is designed to be a 130 m long cable intended to demonstrate electrical power transmission using MgB_2 superconducting cable, cooled by 20 K He gas. The design aims at manufacturing a cable which can transport a current of 40 kA at an operating voltage of 25

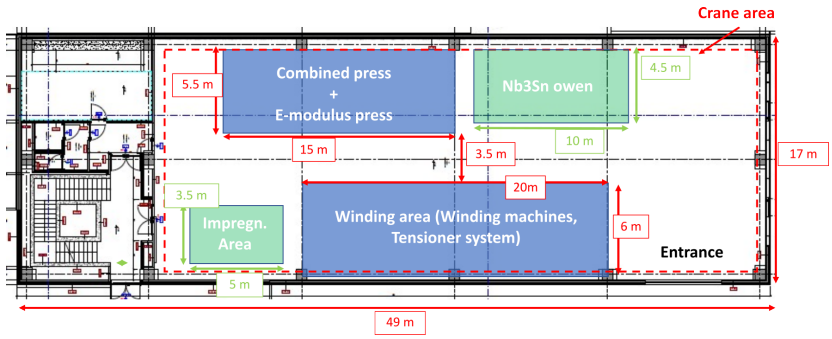


Figure 1.25: Ground level scheme of the new IRIS building including the positioning of new machines.

kV in a flexible cryostat, for a total power transmission of 1 GW. The current design of the GSL power transmission cable is represented in Fig. 1.26. The second technological

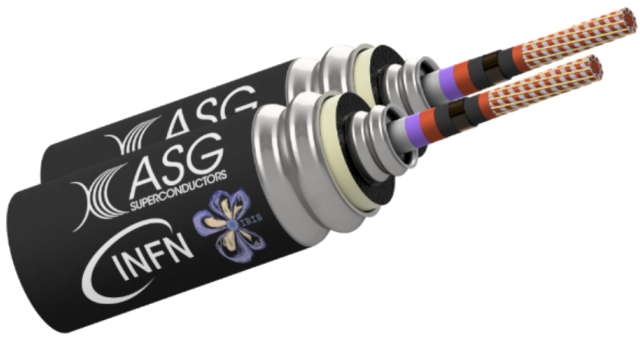


Figure 1.26: Visual representation of the Green Superconducting Line technological demonstrator. (Adapted from [59]).

demonstrator is focused on HTS technology and is the central objective of this thesis. It will be briefly introduced in the next section and is described in depth throughout this manuscript. The tender for the manufacturing of both technological demonstrators of WP8 and WP9 has ended with the work being is awarded to ASG Superconductors (Genoa, Italy).

1.3.1 ESMA

The purpose of the second IRIS demonstrator (WP9) is to realize a full-HTS dipole magnet (ESMA), which could direct the future technological development to a new generation of superconducting magnets for accelerators and societal application. Indeed, in literature and among state-of-the-art prototypes, a working high field dipole magnet fully built in HTS and exploiting their potential to operate at temperature above the range of

LHe is still not present. To this aim, the project ESMA was conceived fostering a one meter long dipole magnet targeting a maximum central field of 10 T magnetic field within a room-temperature rectangular bore of 80 mm $\times$ 50 mm, operating at 20 K cryogen-free, i.e. without liquid coolant. The magnet was to be realized only with REBCO tape conductors and granting a field quality of $\pm$ 1.5% in a box-shaped region of 50 mm $\times$ 30 mm $\times$ 400 mm centered coherently with the center of the dipole. The higher operating temperature of HTS eliminates the need to use liquid helium, which has been traditionally used in particle accelerators up to now. This leads to a dramatic reduction in the energy consumption, up to a factor of 5 to 10 with respect to the present baseline, which relies on superfluid helium at 1.9 K cooling. The power savings are huge, at least 200 MW or 1.5 TWh of energy saved per year, with a large impact on sustainability of future large accelerator infrastructure. As for WP8, the manufacturing of ESMA has been entrusted to ASG Superconductors.
The project has been ongoing for 3 years now and is about to be realized, although some technological challenges forced the design to shift from its original scope. ESMA now consists of a double set of 6 racetrack coils per side, operating at 20 K and producing a central magnetic field of maximum 10 T in a cold bore of 70 mm in diameter and granting a Good Field Region (GFR) of $\pm$ 1.5% in a space of 50 mm $\times$ 30 mm $\times$ 350 mm. The final design parameters of ESMA are summarized in Table 1.1. A graphic visualization of the actual design status is reported on the first page of this chapter (Fig.1.1). The design process which ultimately led to this result, as well as the technological challenges which forced the initial project to be modified, will be discussed in depth in the following chapters. Moreover, it is fundamental to state that ESMA will not serve just as a technological demonstrator to state the maturity of the HTS technology for high field dipole magnet, since it will be installed at INFN-Genova to provide background field for superconducting material tests.

Maximum central Field B_0	T	10
Free aperture diameter	mm	70
GFR dimensions	mm	H50$\times$V30$\times$L350
GFR uniformity	N/A	$\pm$ 1.5 %
Operating temperature	K	20
Maximum current	A	1150
Total number of coils	N/A	12
Number of turns per coil	N/A	350

Table 1.1: ESMA final design paramaters

1.4 Organizational note

The present thesis is structured in six chapters, aimed at providing a comprehensive overview of the studies carried out on the ESMA magnet, together with complementary analyses dedicated to achieve a deeper understanding of HTS tapes. In particular:

Chapter 1, Introduction: This chapter provides the fundamental concepts of superconductivity relevant to the design of superconducting dipole magnets. The composition and manufacturing processes of HTS materials are described, followed by an overview of existing HTS magnets. The chapter concludes with a presentation of the IRIS project, outlining its main objectives and future perspectives.

Chapter 2, Electromagnetic design of ESMA: This chapter focuses on the electromagnetic design of ESMA) It outlines the design process leading to the final configuration, including the coil geometry, spatial arrangement, winding technology, and cable composition, and concludes with a fringe field analysis supporting the final installation of the magnet at INFN Genova.

Chapter 3, HTS tape electrical measurements: This chapter presents the experimental campaigns and corresponding test results carried out to characterize the electrical properties of the HTS tape. In particular, it includes: critical current measurements, analysis of surface defects, and a preliminary investigation of internal splice design, focusing on optimizing their geometry and electrical resistivity.

Chapter 4, Thermo-Mechanical design of ESMA: This chapter outlines the thermal and mechanical design of the ESMA magnet, developed by ASG Superconductors with support from analyses performed at LASA laboratory. The design addresses the combined challenges of high magnetic fields, strong Lorentz forces, and cryogen-free operation. The mechanical structure and MI winding layout are discussed, highlighting their roles in ensuring stability, protection, and structural integrity under operational stresses.

Chapter 5, ESMA operation: This chapter focuses on the operational behavior of the ESMA magnet. Particular attention is given to challenges arising from the MI winding technology of twelve racetrack coils, including heat generation from radial current flow during ramping and the resulting impact on thermal stability and facility operation. The chapter also addresses quench dynamics, proposing methods to optimize charging within defined temperature limits and analyzing the effects of rapid discharge events.

Chapter 6, Small-scale HTS coils: design and test: This chapter presents the first HTS coil winding experiments performed at the LASA laboratory. The campaign aimed to identify suitable winding techniques for the HTS tape, validate numerical models with experimental data, and assess process repeatability to ensure robustness of both design and fabrication. The chapter outlines the winding approaches adopted, the design and fabrication of prototype coils, and the results of liquid nitrogen testing.

CHAPTER 2

Electromagnetic design of ESMA

The design and manufacturing of the Energy Saving Magnet for Accelerators (ESMA), funded by the IRIS project, has started with the management and positioning of the conductor in space, aimed at developing a coil layout which could fulfill all specified requirements, thus initiating the formulation of the electromagnetic design. The magnet layout had to be studied in order to grant a field quality within the nominal Good Field Region (GFR) at every field level between 2 T up to the maximum central field of 10 T. One major constraint in completing this task has been the total amount of conductor, since the design had to be carried out using HTS REBCO tape from Faraday Factory Japan (FFJ) up to a maximum consumption of 15 km, fixed by a previous study on a preliminary configuration. Given these premises the coil geometry, their layout in space, the winding technology and the cable composition leading to the final electromagnetic design, as well as a fringe field analysis for the final positioning at INFN Genova, have been assessed and will be described throughout this chapter.

2.1 Coil Geometry and Layout Analysis

The electromagnetic design of ESMA, specifically concerning coil geometry and layout study, in addition to the constraint regarding the total amount of the conductor, had to deal with the the requirements imposed by the manufacturing process managed by ASG Superconductors. As a result, the design criteria needed to accommodate scalability toward industrial production. Given that the requirements of the magnet are met, a simpler geometry is to be preferred to a more complicated one even if the latter is demonstrated to be more efficient. Consequently as a resulting compromise between industrialization and scalability of the coil manufacturing, and an optimized layout minimizing the cost while providing a more uniform GFR, the coil geometry and layout has focused mainly on flat coils with an emphasis on maximizing uniformity among coils to facilitate production. Moreover, given the strict timelines imposed by the PNRR, the project required a design that could be efficiently realized, minimizing the risks of unexpected complication during the winding process. In this context, a flat coil geometry was clearly the most suitable option, as it offered a more practical and less mechanically demanding alternative to more complex configurations, such as saddle coils or layouts requiring the superconducting tape to undergo hard-way bends, despite the performance advantages

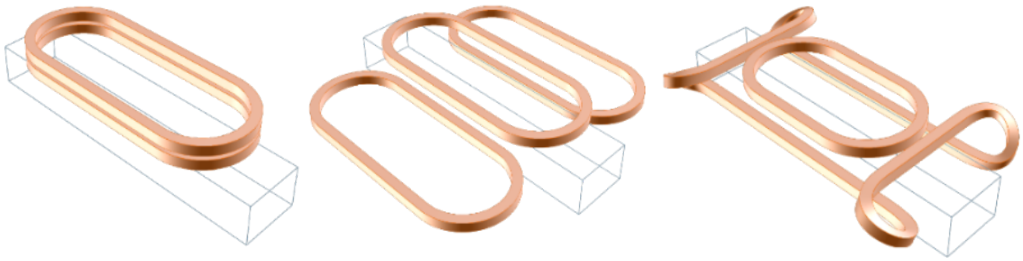


Figure 2.1: Geometrical coil layouts investigated for the electromagnetic design of the ESMA dipole, only the top pole is shown schematically. Starting from the left: Helmholtz-like, mixed solution where midplane coil is added, and cloverleaf ends. The free bore envelope of ESMA is traced.

of the latter. Given this premises, the problem of the electromagnetic design of ESMA has started with the optimization of its cross-section. In particular, since the total amount of tape was a hard constrain fixed to 15 km, the process started with finding the most efficient way to generate magnetic field in the center using only flat geometries, given the same amount of conductor. To this purpose, the process of optimizing the design of the cross section of the dipole had to take into account - as a first order consideration - a former decision about the spatial disposition of the coils. The choice had to be done between: a double pancake Helmholtz coil configuration, positioning the coil on the mid-plane or a mixed option considering both elements. The problem of designing the cross section of the dipole had to deal with the constraint of not climbing over the nominal aperture, i.e. reaching the nominal values of field value and quality by using simple racetracks. Indeed, the dipole will be realized with a 12 mm wide HTS REBCO tape which, as described in , as described in Sect. 1.2, cannot easily be bent the hard way, therefore making the classical cosine-θ a challenging option, especially in a context of strict timelines such the one of the PNRR. In order to avoid dealing with this issue, flat geometries are mandatory. One solution to build a dipole magnet consists in placing a double pancake of coils right over, and under, the aperture, thus realizing a Helmholtz-like configuration. Another way to approach the problem is based on the fact that the major contribution to the central field is given by a set of coils placed on the mid-plane, since they are nearer to the center with respect to the Helmholtz-like option, thus considering a layout with only a pancake coil placed on the mid-plane. Moreover a mixed configuration of both the Helmholtz and mid-plane coils will be assessed. However, it is mandatory to notice that since the coils on the mid-plane are planar, they cannot be closed on the other side of the aperture like the upper coils would do in the Helmholtz configuration, therefore an opposite contribution arises by closing the coils on the same side of the aperture.

In order to state the relative efficiency of these configurations, fixing the amount of conductor used, and to decide in which direction proceed with the optimization, a first simple analytical calculation considering point-like current sources has been set up to state which coil set is giving the greater contribution to the field in the center of the aperture. Then the comparison has been explored in detail by considering the finite

dimensions of the current sources and comparing the field generated in the center by both the Helmholtz and the mixed configuration. Indeed, ESMA will target the central field with a higher priority with respect to field homogeneity, which is still far from being comparable to the one of accelerator magnets, above all if one also considers the deviations introduced by screening currents in such wide, non-twisted and non-multifilamentary conductors. To this purpose, a comparison concerning only the efficiency in field generation has been studied. One last comparison, at the end of this section, will disclose the possibility of having a cloverleaf non-planar coil in this study to investigate whether a significant higher efficiency could be achieved in exchange for a more difficult winding procedure and mechanical analysis. All the main configuration investigated in this section are illustrated in Fig.2.1.

Let us first consider the geometry of the problem: the central nominal aperture of ESMA being 0.08 m $\times$ 0.05 m, plus an estimated 1 cm thickness of thermal insulation volume around the aperture for a total occupied area of 0.1 m $\times$ 0.07 m. The coils have then been placed as packs of double pancakes separated by a distance equal to s = 0.005 m as near as possible to the useful central aperture: i.e. at a distance a = 0.05 m. The closure of the mid-plane coil will be place at the variable distance b in order to quantify the effect of the negative contribution. The set of double pancake Helmholtz coils, are placed - as well - as near as possible to the area near the aperture, at a sufficient height to be closed on the other side of the aperture without climbing over it: i.e. at a distance c = 0.035 m and $c^\star$ = 0.035 m + s. In order to center the mid-plane double pack of coils on the mid-plane itself, they must be put at a height of $\pm$ $s/2$ with respect to the mid-plane. Exploiting the intrinsic symmetry of the problem, only a quarter of the actual geometry is being considered throughout this whole section. For the purpose of this demonstration squared coils of width $w = t$ are considered. A sketch of the problem set up is shown in Fig.2.2 and the main quantities discussed in the next paragraphs are summarized in Tab. 2.1.

Label	**ESMA Case study [m]**	**Description**
a	0.05	Distance of the coils from the center of the aperture
b	0.2	Mid-plane coil internal spacing
c	0.035	Distance of the lower coil of the Helmholtz double pancake from the mid-plane
c*	0.040	Distance of the upper coil of the Helmholtz double pancake from the mid-plane
s	0.005	Coil spacing
t	0.012	Tape width
w	0.012	Width of a single squared current source
$\hat{W}$	$\geq w$	Helmholtz coil width
J	N/A	Current density
B_{y0}	N/A	Magnetic field at the center of the aperture

Table 2.1: In this table a summary of the principal quantities considered in this problem is reported

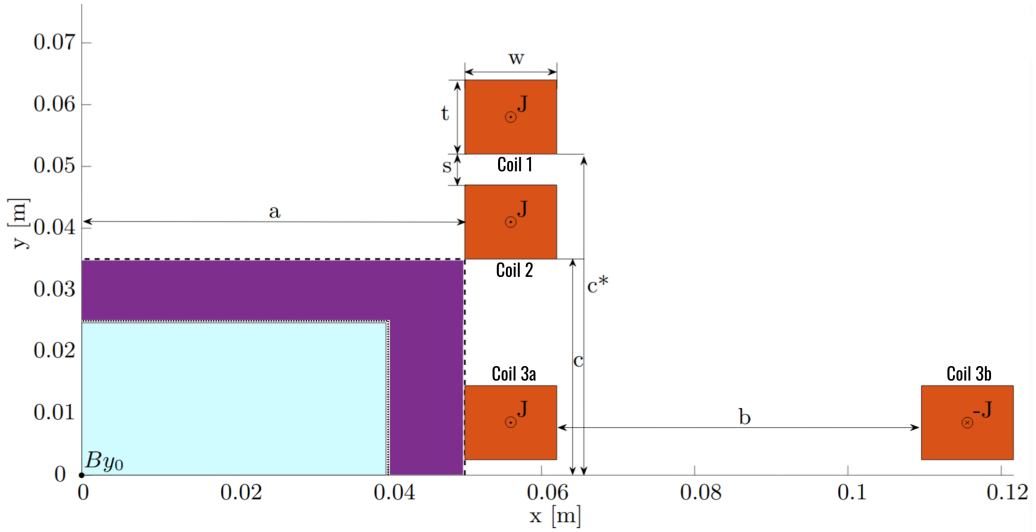


Figure 2.2: Scheme of the geometry of the problem: the operational aperture is here sketched in in light-blue, the insulation volume thickness in purple while the coils are represented in orange. The current density *J* is also indicated together with its sign with respect to the cross section plane.

2.1.1 Analytical point-like current sources

Given the geometry of the problem, the first question that must be answered is that of stating which set of coil is giving the highest contribute to the central field, using the same amount of conductor. It is worth noticing that given the symmetry of the problem with respect to both y- and x-axis, the conductor used to build a racetrack coil on the mid-plane, is equivalent to that needed to build a double pancake in the Helmholtz-like layout. Indeed, the first comparison will be performed by confronting the Helmholtz-like geometry, with respect to displacing the conductor on the mid plane. To this aim, the relative contribution to the central dipole field By_0 is computed by considering the ratio of the central field produced by the upper set of coils B_{top} with respect to that of the mid-plane coils B_{bot}. Before proceeding with the calculation an approximation has been done for the sake of obtaining an easily understandable result: the coils are modeled as point-like current sources carrying the same current I in modulus and placed at the center of the coil section. With reference to Fig.2.2, the coils are numbered from 1 to 3, starting with the coil in the highest position *c** and proceeding counterclockwise. The mid-plane coil is labeled as coil 3a for the main contribution and coil 3b for its return leg. For every coil, from 1 to 3 then the Biot-Savart law for the By_0 field in the center and normalized with respect to the current I can be written:

$$\frac{B_y}{I} = \frac{\mu_0}{2\pi} \cdot \frac{cos\theta}{r} \tag{2.1}$$

where r is the distance between the center of the aperture and the position of the current source and θ is the angle between r and the horizontal axis. Eq.2.1 can then be applied for the point-like current source related to the coils from 1 to 4 as follows:

$$\frac{By_{01}}{I} = \frac{\mu_0}{2\pi} \cdot \frac{a + \frac{w}{2}}{\left(a + \frac{w}{2}\right)^2 + \left(c^* + \frac{t}{2}\right)^2} = \frac{\mu_0}{2\pi} \cdot \frac{A}{A^2 + C^{*2}} \tag{2.2}$$

$$\frac{By_{02}}{I} = \frac{\mu_0}{2\pi} \cdot \frac{a + \frac{w}{2}}{\left(a + \frac{w}{2}\right)^2 + \left(c + \frac{t}{2}\right)^2} = \frac{\mu_0}{2\pi} \cdot \frac{A}{A^2 + C^2} \tag{2.3}$$

$$\frac{By_{03_a}}{I} = \frac{\mu_0}{2\pi} \cdot \frac{a + \frac{w}{2}}{\left(a + \frac{w}{2}\right)^2 + \left(\frac{s}{2} + \frac{t}{2}\right)^2} = \frac{\mu_0}{2\pi} \cdot \frac{A}{A^2 + \left(\frac{s}{2} + \frac{t}{2}\right)^2} \tag{2.4}$$

$$\frac{By_{03_b}}{I} = -\frac{\mu_0}{2\pi} \cdot \frac{a + b + w + \frac{w}{2}}{\left(a + b + w + \frac{w}{2}\right)^2 + \left(\frac{s}{2} + \frac{t}{2}\right)^2} = -\frac{\mu_0}{2\pi} \cdot \frac{A + B}{(A + B)^2 + \left(\frac{s}{2} + \frac{t}{2}\right)^2} \tag{2.5}$$

where A, B, C, C* have been introduced to simplify the equations and are respectively defined as: $A = a + w/2$, $B = b + w$, $C = c + t/2$ and $C^* = c^* + t/2$. Moreover, the last two equation, eq.2.4 and eq.2.5, can be further simplified by neglecting the term $(s/2 + t/2)^2$ which is small compared to A^2 and $(A + B)^2$:

$$\frac{By_{03_a}}{I} = \frac{\mu_0}{2\pi} \cdot \frac{A}{A^2 + \left(\frac{s}{2} + \frac{t}{2}\right)^2} \sim \frac{\mu_0}{2\pi} \cdot \frac{1}{A} \tag{2.6}$$

$$\frac{By_{03_b}}{I} = -\frac{\mu_0}{2\pi} \cdot \frac{A + B}{(A + B)^2 + \left(\frac{s}{2} + \frac{t}{2}\right)^2} \sim -\frac{\mu_0}{2\pi} \cdot \frac{1}{A + B} \tag{2.7}$$

Once having the contribution to the central field given by every coil from 1 to 3, the sum between eq.2.2 and eq.2.3 as well as between eq.2.6 and eq.2.7 has been computed in order to evaluate the ratio between the contribute of coil 1 and 2 to the central field with respect to that of coil 3 and 4. The result of the ratio is the following:

$$\frac{By_{01} + By_{02}}{By_{03_a} + By_{03_b}} = \frac{B_{top}}{B_{bot}} = \frac{A(2A^2 + C^2 + C^{*2})}{(A^2 + C^2)(A^2 + C^{*2})} \cdot \frac{A^2 + AB}{B}$$

In the limit case where $B \longrightarrow \infty$ (i.e. no opposite contribution from the closure of the mid-plane coil 3b), the ratio tends to:

$$\frac{B_{top}}{B_{bot}} = \frac{A^2(2A^2 + C^2 + C^{*2})}{(A^2 + C^2)(A^2 + C^{*2})} \tag{2.8}$$

The ratio expressed by eq.2.8, computed with the values of this problem, is equal to $\sim$1.07, thus stating that the pair of Helmholtz coils provide a higher contribution to the central field with respect to the coils on the mid-plane even for the ideal case of no opposite contribution coming from the closure of the mid-plane coil.
Let us consider again the ratio expressed in eq.2.8. In order to retrieve a general condition to distinguish cases where a set of racetracks in Helmholtz-like configuration will prove to be more efficient with respect to a set of mid-plane coil and vice-versa, one can assume to put $C = C^* = \mathcal{C}$, where $\mathcal{C}$ could be equal to a generic height, being, for instance, the average height of the two upper coils in the above-discussed problem. With this simplification, it is possible to rewrite eq.2.8 as:

$$\frac{B_{top}}{B_{bot}} = \frac{2}{1 + \frac{\mathcal{C}^2}{A^2}} \tag{2.9}$$

where it is straightforward to state that the ratio tends to favor the Helmholtz configuration whenever $C^2/A^2 < 1$. The results can be directly interpreted by fixing the coil thickness equal to the coil width, i.e.: $w = t$. Under this assumption, the condition highlights that a Helmholtz-like configuration is more efficient at generating magnetic field than a flat coil positioned on the mid-plane whenever $c < a$, that is, when the aperture has a rectangular aspect ratio with the base larger than its height. The opposite condition applies when the aspect ratio is inverted, corresponding to a taller and narrower aperture. The limiting case is a square aperture, for which the two contributions are equal.

2.1.2 Finite dimension current sources

To verify the results of the previous section, the exact field generated in the center of the aperture by a finite-dimension conductor carrying a uniform current density J is computed. Indeed, the field generated by such a conductor, normalized over the uniform current density J in the center of the aperture - i.e. in the point (x,y) = (0,0) - can be calculated analytically starting from the local expression of the Biot-Savart law for an infinitesimal current element $Jdxdy$ integrated over the rectangular cross section of the coil:

$$By_0 = \int_{a_1}^{a_2} \int_{c_1}^{c_2} \frac{\mu_0}{2\pi} \cdot \frac{Jcos\theta}{r} \cdot dxdy \tag{2.10}$$

where a_1, a_2, are the x-coordinates of the basis left and right corners respectively and c_1, and c_2 the correspondent y-coordinates of the bottom and upper basis. The integral can be solved via an integration by parts, resulting in:

$$\begin{aligned} \frac{By_0}{J} =& \frac{\mu_0}{2\pi} \left(a_2 \left(\text{atan}\left(\frac{c_2}{a_2}\right) - \text{atan}\left(\frac{c_1}{a_2}\right)\right) + a_1 \left(\text{atan}\left(\frac{c_1}{a_1}\right) - \text{atan}\left(\frac{c_2}{a_1}\right)\right) + \right. \\ & \left. \frac{c_2}{2} \ln\left(\frac{a_2^2 + c_2^2}{a_1^2 + c_2^2}\right) - \frac{c_1}{2} \ln\left(\frac{a_2^2 + c_1^2}{a_1^2 + c_1^2}\right)\right) \end{aligned} \tag{2.11}$$

With eq.2.11 the calculation performed in the previous section under the assumption of point-like current sources can be repeated with the exact solution for the 2D problem concerning racetrack coils. In particular, the result for the ratio B_{top}/B_{bot} of the upper coil versus the mid-plane configuration can be computed for different values of b, making it possible to observe the trend of the ratio as a function of the mid-plane coil aperture. The results are graphed in Fig.2.4 and it can be readily noticed how the ratio changes from about ~ 1.5 for a realistic b-value of 200 mm to ~ 1.1 for higher values of b, according to what has been found previously. For this specific problem, the pair of coils in the Helmholtz-like configuration has proven to perform better than the equivalent set of coil placed on the mid-plane.

Once set the Helmholtz-like configuration to be more efficient than the mid-plane layout, the mixed option, i.e. considering both a top coil and one on the mid-plane, is compared using a similar approach to the Helmholtz-like arrangement.To this aim, the efficiency of the configuration with conductors placed both on the mid-plane and on the top is evaluated in comparison to the Helmholtz-like layout, where mid-plane conductors are

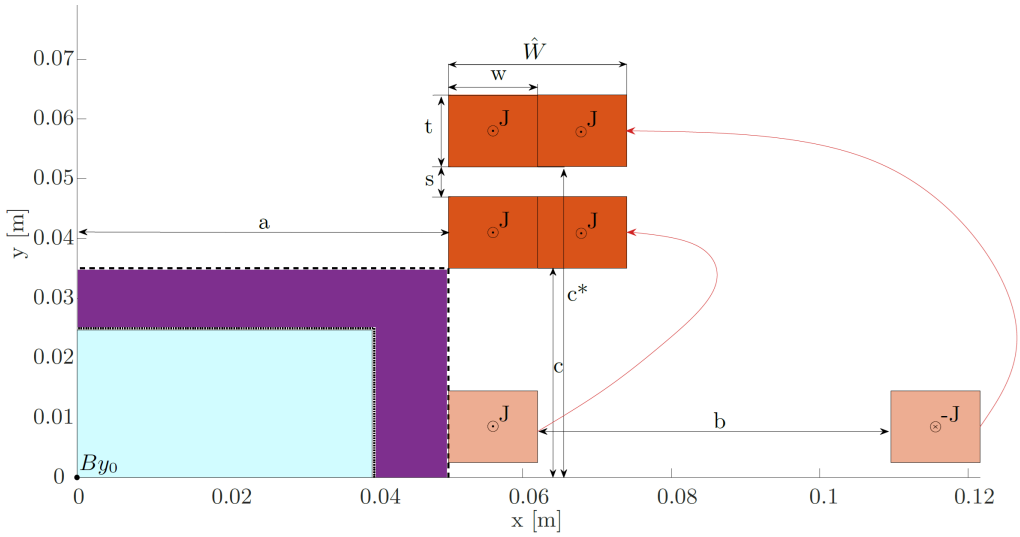


Figure 2.3: Scheme of the geometry of the problem where the mid-plane coil is moved to increase the thickness of the upper coils. The procedure is schematized by the red arrows. The orange coils represent now the new configuration and the set of the first two upper orange squares and the semi-transparent ones on the mid-plane represent the previous set-up.

gradually added to the top coils so that the total conductor length is kept constant. The scheme of this second set up and the changes from the previous one is sketched in Fig.2.3. To quantify the relative efficiency, once again the ratio between the field in the center of the aperture of this new configuration where only the Helmholtz coils are present, called B_2, with respect to the overall field produced by the previous configuration, now called $B_{top} + B_{bot} = B_1$ has been computed as a function of the mid-plane coil internal spacing and the result are graphed in Fig.2.5. Even in this second case, the relative efficiency of the Helmholtz configuration is proving to perform better both in the case of a realistic internal displacement of $\sim$ 0.2 m where the ratio equals $\sim$1.2 and in the ideal case of $b \longrightarrow \infty$ where the ratio stays in favor of the Helmholtz set-up.
To complete this comparison and to set the problem towards a real case, the relative efficiency of the two cases will be assessed, allowing the cross section of the coils to vary. To this purpose the above-explained procedure of transferring the conductor from the mid-plane to the top coils will be iterated until the increase of the thickness of the upper coils is such that the Helmholtz-like configuration cease to be favorable. One may define a step as the increase of the upper coil thickness by a pair of squares of current equivalent to those on the mid-plane, i.e. $w \times t$. To this purpose the ratio B_2/B_1, for a fixed mid-plane internal displacement b of 0.2 m, has been evaluated for many steps to produce the plot in Fig.2.6 where the ratio B_2/B_1 has been evaluated as a function of the upper set of coil thickness. It is important to notice that in the ratio, for the nth step, the field B_2 is produced by a set of upper coil of thickness $n \times w$, whereas B_1 is produced by a set of upper coil of thickness $(n-1) \times w$ and a single pair of square current sources on the mid-plane. With reference to the plot in Fig.2.6 it can be observed that, within the chosen

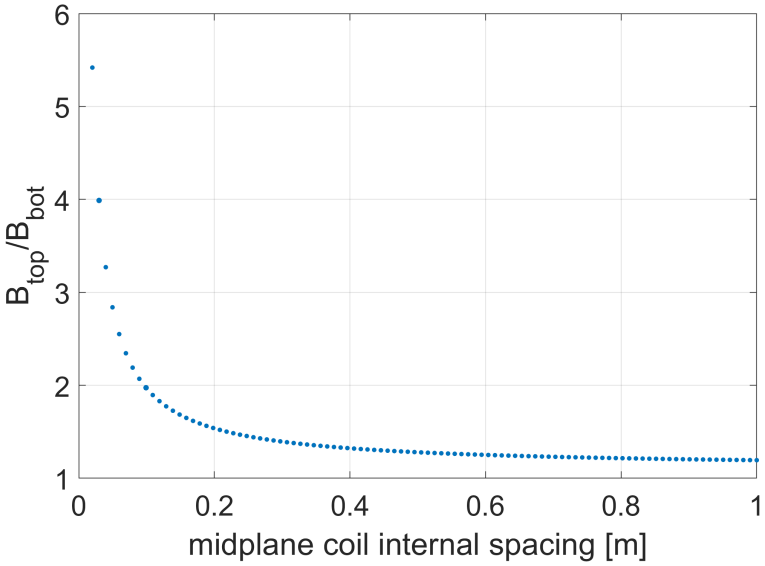


Figure 2.4: Trend of the ratio B_{top}/B_{bot} as a function of the internal spacing of the coil on the mid-plane

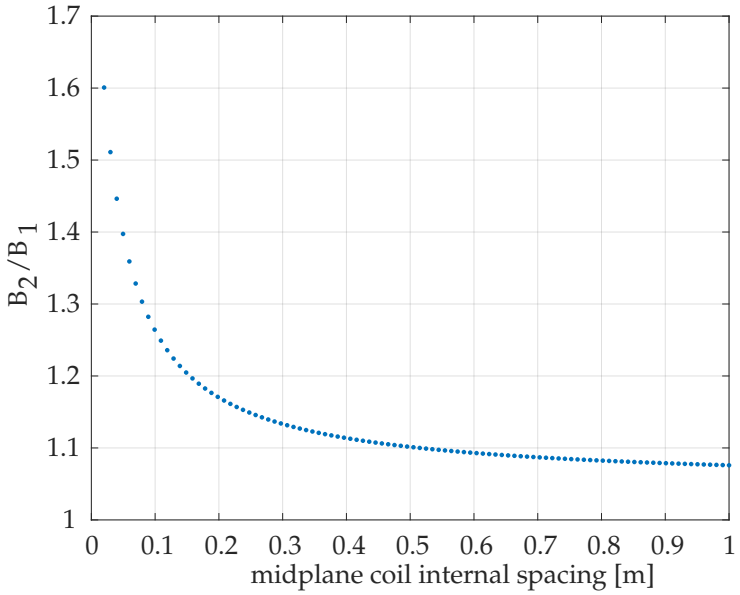


Figure 2.5: Plot of the ratio B_2/B_1 as a function of the internal spacing of the coil on the mid-plane

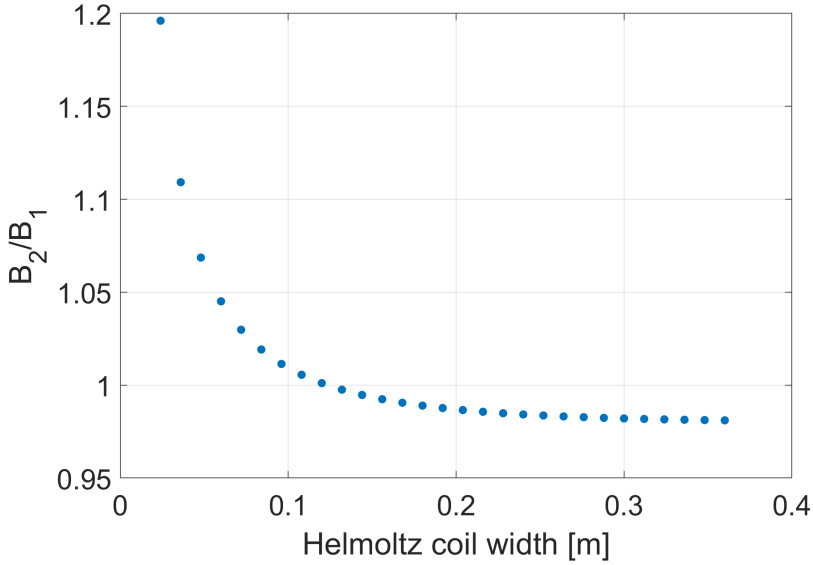


Figure 2.6: Plot of the ratio B_2/B_1 as a function of the Helmholtz coil width.

configuration, the process of increasing the thickness of the upper set of coil ceases to be favorable around 0.1 m. However, even trying to go further, around the point where the ratio starts to be less than one, the difference between the two configurations is the order of the percent. For this reason, a Helmholtz-like configuration was chosen for the ESMA dipole.

2.1.3 Cloverleaf comparison

A racetrack coil is the simplest feasible geometry which can be wind using superconducting tapes. However, in order to deal with the hard-way bend necessary to climb over the aperture and place the conductor on the mid-plane, as introduced in Sec. 1.2.2, a novel geometry named cloverleaf has been developed. A sketch is represented in Fig. 1.21. The principle behind this winding geometry to place racetrack coil in the mid-plane and avoiding the hard-way bending necessary to climb over the aperture by winding a cloverleaf path at the heads of the coils, thus creating four solenoid-like coils. A top racetrack completes the winding to reach the required field. This last configuration is pictured in the rightmost part of Fig. 2.1.
On one hand, placing the conductor on the mid-plane is the most efficient way of producing field within the aperture of a magnet, on the other hand manufacturing a cloverleaf winding is really challenging, especially for thicker coils. Moreover, the principle of diluting the hard way bend at the heads of the coil requires more conductor compared to traditional winding techniques, in particular if referred to short magnets where the ratio between the conductor used for the straight parts becomes comparable with the quantity needed for the clover-ends. A comparison between the Helmholtz configuration and a

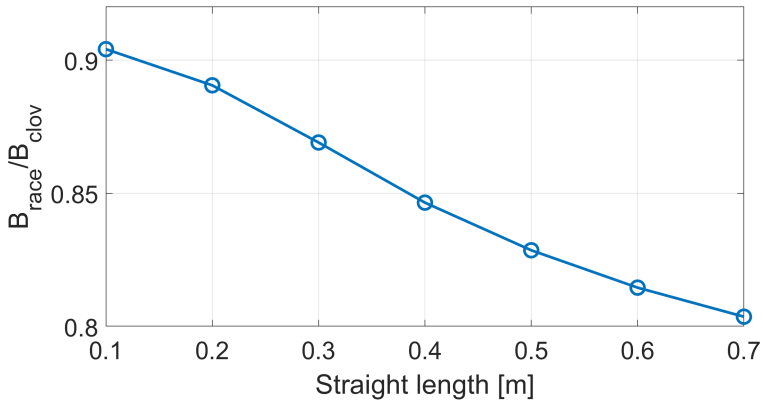


Figure 2.7: Ratio between the field generated in the center of the aperture by two coils in a Helmholtz configuration (B_{race}) with respect to a layout where part of the conductor is kept on the midplane as a cloverleaf coil (B_{clov}) as a function of the coil straight section length.

cloverleaf layout has been carried out, as usual at constant amount of conductor. The peculiar shape of the conductor and the head-effects of a cloverleaf required an intrinsic 3D calculation which has been carried out using RAT [60] to model the problem. The ratio between the central field produced by the two configurations, named respectively B_{Helm} and B_{clov}, has been calculated and results are plotted in Fig. 2.7., as a function of the straight section length of the coil. As expected, the longer the magnet, the more efficient is the cloverleaf, because the fixed amount of tape consumption in the heads has less weight: however, since ESMA has longitudinal GFR dimension of 400 mm, the cloverleaf configuration is only 15% more efficient in usage of conductor. This 15% advantage, also according with the future manufacturer of the dipole, does not justify the severe construction complexity and the risk of a cloverleaf, a concept not yet proven. Moreover, the coils should be thicker to reach the targeted 10 T and the cloverleaf would either become relatively less efficient if made thinner, or mechanically more complicated if thicker. Therefore, both for high efficiency and simplicity of fabrication, together with the absence of strict boundaries on the field quality, the Helmholtz configuration proved to be the best option for ESMA.

2.2 Winding technology

The configuration which proved to be the most efficient among those concerning flat coils is the Helmholtz-like layout. Before proceeding to the optimization of the magnet cross section and consequently to the full 3D problem, to provide a design which could meet the target parameters for the highest central field and the field uniformity across the GFR, the problem of choosing the winding technology must be assessed. With winding technology, comes the definition of the cable cross section and, therefore, of the engineering current density J_{eng} with which the expected performances of the ESMA dipole could be evaluated. In the following sections, three possible outcomes will be disclosed: a traditional insulated design, a non-insulated winding, and a metal-insulated winding. Every option will be evaluated in terms of field generation efficiency, quench protection, and charging time constant. Moreover, since ESMA is foreseen to be conduction-cooled at 20 K, the possibility of considering the co-winding of multiple tapes to form a high-current cable, thus minimizing the magnet inductance, will have a strong impact on the thermal design, mostly related to the resistive section of the current leads. In order to minimize the heat dissipation of the current leads, thus preserving the thermal budget of the cryocoolers, the analysis on the winding technology has been performed considering a co-winding of two tapes in a face-to-face configuration, i.e. with their superconducting layers facing each other. To further reduce the tape to just one would mean, mostly for the insulated and metal-insulated design, to have no redundancy at all which could compensate for a possible local defect occurring on the tape, thus leading to a less robust design. The conductor consists in a total of 15 km of 12-mm-tape REBCO coated conductor with a required minimum I_c of 500 A at 20 K, 15 T, at any field angle. This last value has been considered to calculate the margins in this preliminary analysis.

2.2.1 Insulated cable

Once the Helmholtz configuration was chosen as layout for the ESMA dipole, the cross-section of the magnet has been optimized in order to minimize the conductor while respecting the design goals. This preliminary optimization of the cross section has been performed using a constrained gradient-based optimization algorithm implemented with the built-in function *fmincon()* [61] in MATLAB. The algorithm could act on the geometrical parameters of the coil cross section expressed in Eq. 2.11, which have all being constrained to be greater than zero or such as the resulting coil width would be non-negative, giving as output the produced magnetic field with which a cost function is evaluated. The output design was given by the minimization of the following quadratic cost function:

$$\begin{aligned} Cost =& k \cdot \left(\frac{By_0 - By_{0target}}{B_{Res}} \right)^2 + \\ &+ l \cdot \left[\left(\frac{By_{corner} - By_0}{B_{quality}} \right)^2 + \left(\frac{By_{bot} - By_0}{B_{quality}} \right)^2 + \left(\frac{By_{top} - By_0}{B_{quality}} \right)^2 \right] + \\ &+ (1 - k - l) \cdot \left(\frac{L}{L_{targ}} \right)^2 \end{aligned} \tag{2.12}$$

where By_0 is the dipolar field generated by a rectangular area carrying a constant J_{eng} as described by Eq. 2.11. The cost function is divided into three terms dedicated the main targets of ESMA: cental field, field uniformity, and conductor usage. The first part is focused on achieving the target field specified by $By_{0target}$ with a precision of B_{res}, the second part probes the field in the three most critical points of the aperture, namely the vertices of the rectangle formed by 1/4 of the nominal aperture, always via Eq. 2.11. These values, specified by By_{corner}, By_{bottom}, and By_{top} are compared with the central field and weighted over the targeted uniformity specified by $B_{quality}$. Lastly, the third term is responsible for the conductor consumption, penalizing every configuration that requires more conductor L than L_{targ}. Moreover, to the cost function in Eq. 2.12, the parameters k and l are used to weight the three terms differently, according to the sensitiveness of the equation. For the problem of optimizing ESMA dipole with an insulated configuration, the parameters have been set to the values in Tab. 2.2. The optimization acted on the geometric terms of Eq. 2.11, thus varying the number, the thickness, and the positions of the cross sections of the coils before calculating the field and evaluating the cost function. An additional constraint on the coil displacement was to have an even number of coil per side, so that the connection could be performed as in classical double pancakes, and to favor a configuration with equal coils to ease the manufacturing process. The coils were allowed to be placed within the area above the aperture, since only flat racetrack in a Helmholtz like configuration were allowed. Moreover, in agreement with ASG Superconductors, a forbidden circular area of diameter d = 110 mm - including the rectangular aperture, had to be considered to provide sufficient space to have a free bore at room temperature. The cable cross section considered for the optimization of the insulated layout is represented in Fig.2.8, and, in addition to the two HTS tapes, considers an additional 0.1 mm thick of copper supplementary stabilizer and a 0.03 mm insulating layer. The current fed to the tapes has been fixed to 1 kA, which corresponds to a J_{eng} of $\sim$ 310 A/mm^2 on the area of the cross section pictured in Fig. 2.8, which is sketched to highlight the constituent materials and their thicknesses relative to the cable unit.

A solution problem was found consisting of four racetracks per side of the aperture, each consisting of 493 cable turns for a total width of about 128 mm. The coils are placed at 67 mm from the center at a height of 55 mm and separated by 5 mm between each other, to fit the mechanical support. This whole layout uses 14.36 km of tape and produces a central field of about 8.5 T, with a maximum field variation of $\tilde{1}$.5% with respect to the

$By_{0target}$	8.5 T
B_{res}	0.2 T
$B_{quality}$	0.01 T
L_{targ}	10 km
k	0.05
l	0.05

Table 2.2: Optimization parameters for insulated winding

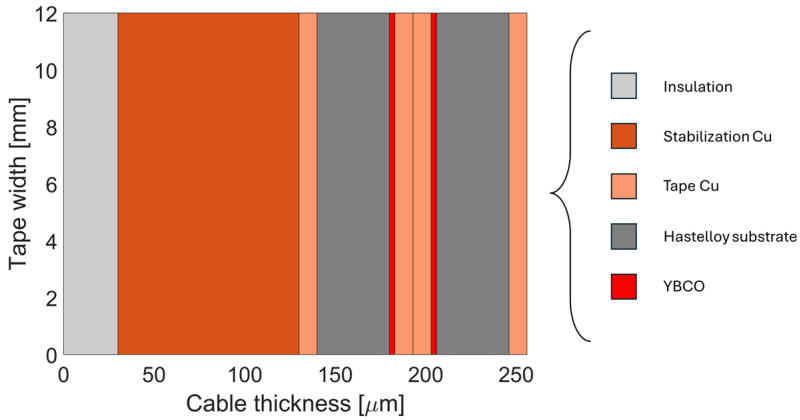


Figure 2.8: Visual representation of the insulated cable cross section.

central field. The addition of the iron poles and of the iron yoke would enhance the field to 10 T. With these parameters the current margin has been estimated on the 2D problem to be about 20% and the temperature margin more than 10 K on the most critical point of the layout. In principle this configuration could meet the specifications required for ESMA. However a preliminary estimation of the hot-spot temperature has been calculated using QLASA [62]. QLASA is a code developed at LASA laboratory to simulate a quench event in a classical LTS superconducting magnet by building an equivalent solenoid-shaped geometry. In addition to the normally required information as the materials involved and the corresponding properties, the code requires a voltage threshold above which a sudden discharge of the magnet is simulated. In order to adapt the code to simulate the quench in HTS tapes, the critical curve has been given considering the worst angle orientation of the magnetic field, since anisotropy of the superconducting material is not supported. Moreover, the normal zone propagation velocity has been artificially set to roughly 10 cm/s following literature data for HTS [63] magnet, given the high temperature margins of REBCO coated conductors. The cooling power has been set to the one of a real cryocooler, specifically AL325 from Bluefors [64]. Once the simulation premises are set, the protection parameters of a hypothetic detection and discharge have been set to: 100 mV as threshold, with 20 ms of validation time and 5 ms of switching time. The simulation results are graphed in Fig.2.9, where it can be observed a maximum hot-spot temperature of $\sim$ 300 K. A 300 K hot-spot value could be acceptable, however the large uncertainty driven by lack of accurate knowledge of critical parameters like quench velocity and properties of the coil composite, suggests that a larger amount of copper would be needed. This would make the coils even larger with a consequent impact on the amount of superconductor, on stored energy and on coil mechanical stability, beside delaying the quench detection. This result, combined with a high tape usage due to a diluted J_{eng}, resulted in the exclusion of insulated coils.

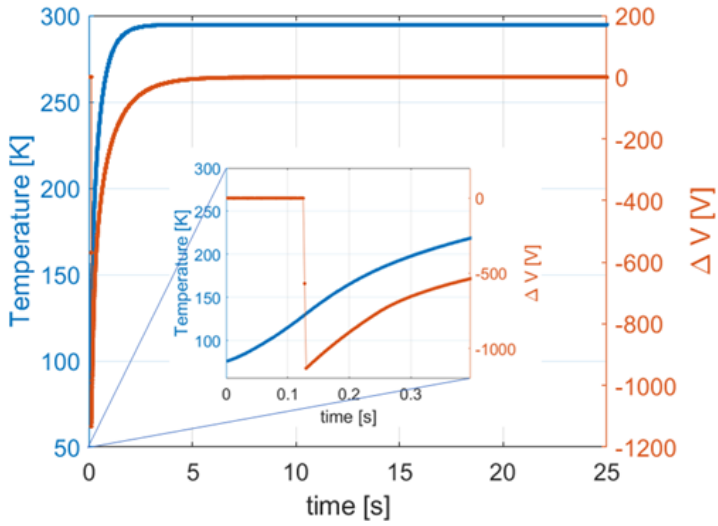


Figure 2.9: Detection and discharge simulation results performed with QLASA for the insulated configuration of the ESMA magnet following a quench event with a 100 mV detection threshold.

2.2.2 Non Insulation and Metal as Insulation

The baseline design on which ESMA was proposed within the IRIS project was inspired by the existing AMaSED-2 demonstrator coil [65], a no-insulation HTS coil developed for the ARCOS space spectrometer [66]. ARCOS was designed as a toroidal magnet composed of 12 racetrack double-pancake coils, operating cryogen-free at 20 K with a peak field of 12 T. One of these coils was successfully manufactured and tested in cryogenic helium gas at temperatures ranging from 10 K to 77 K [67]. Following this reference, a preliminary design of the ESMA magnet was carried out under the same constraints of length, aperture, GFR, and central field as mentioned before. The resulting dipole aimed at a slightly lower central field of 9 T at 20 K, consisting of two double-pancake racetrack coils per side of the aperture, each wound with a single 12 mm-wide REBCO tape in a no-insulation configuration. The first coil was positioned 27 mm from the midplane, separated by 6 mm from the coil above it, with an inner radius of 60 mm. Each upper double-pancake racetrack coil featured a cross section 77 mm wide. In addition, a set of smaller racetrack coils was positioned on the midplane and closed on the same side of the magnet. These coils had an inner diameter of 60 mm and a winding block width of 17 mm. They were arranged with 9 mm spacing between them and placed 60 mm away from the magnetic center, leaving 20 mm of margin between the coils and the aperture for the mechanical structure. With the overall magnet length designed to be about 1 m, the straight sections of the racetrack coils were estimated at 800 mm. When equipped with an iron yoke, this configuration was expected to achieve a central magnetic field of 9 T at 20 K, operating at an engineering current density J_{eng} = 400 A/mm^2, while maintaining a 20% load line margin. The total tape consumption was estimated

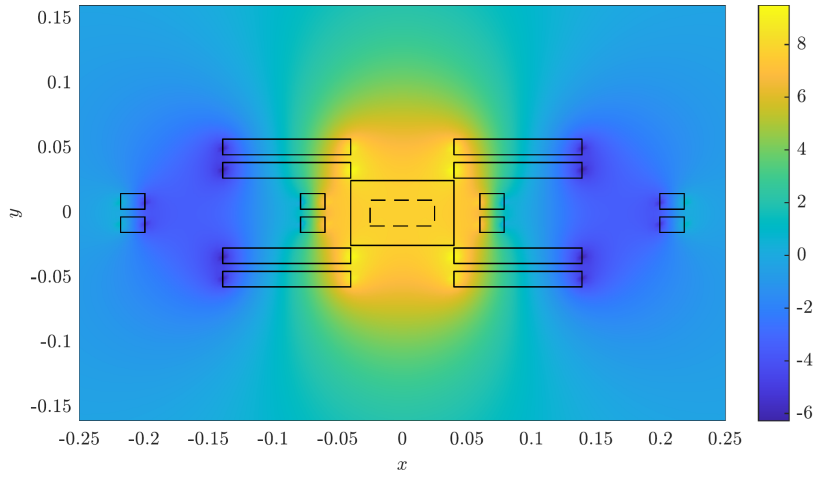


Figure 2.10: Magnetic field generated by the cross section of the preliminary configuration of the ESMA dipole powered with J_{eng} = 400 A/mm^2.

at approximately 7.5 km. The cross-section of the magnet and the corresponding field distribution without iron are shown in Fig.2.10. This preliminary study established the initial constraint on tape length, setting a maximum of 15 km for ESMA.

However, the study of a preliminary configuration with either a fully non-insulated winding or a partially insulated winding using the metal-as-insulation technique was largely based on the same analysis as for the insulated variant, since this design left little to no clearance for insulation around the aperture thus compromising the warm bore. It has also been shown that, in the case of flat coils, placing the conductor on the midplane is less efficient than positioning it above and below the aperture when the same amount of tape is used. In addition, such a layout would introduce a different coil geometry, thus complicating the manufacturing process. For these reasons, a new configuration had to be identified following the same design philosophy adopted for the insulated version, namely favoring a Helmholtz like layout with coil geometries that are as uniform as possible. The cable cross section used in this second optimization is sketched in Fig.2.11, and consists of two tapes facing each other on the superconducting side and, in the case of the metal-as-insulation option, of a 30 μm thick stainless steel tape. The optimization of this design was carried out using the same cost function defined in Eq.2.12, with identical parameters and a transport current of 1000 A. Due to its intrinsic compactness, the optimum configuration for the fully non-insulated option was found to be a stack of two racetracks above and two below the mid-plane, each consisting of 850 cable turns, for a total width of about 120 mm. The coils are positioned 70 mm from the magnetic center, at a height of 55 mm, and separated by 5 mm to accommodate the mechanical support. Assuming a straight section of 400 mm, this configuration requires 13.14 km of tape and generates a central field of approximately 8.3 T, with a maximum variation of about 1% relative to the central value.

However, since this design relies on a non-insulated winding, a finite charging time is expected during operation due to the presence of contact resistance. On the other

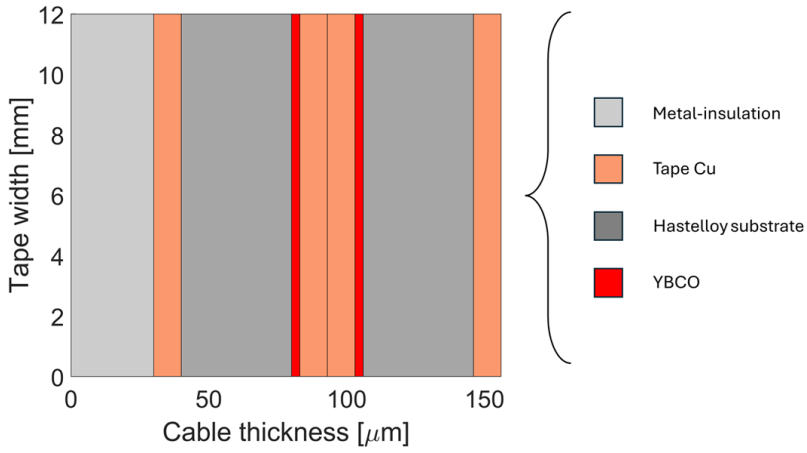


Figure 2.11: Non-insulated cable cross section.

hand, adopting the non-insulated technology facilitates quench protection, significantly reducing the hot-spot temperature compared to an insulated conductor. To estimate the charging time, a lumped element model was developed, consisting of a parallel circuit with an inductor and a resistor, representing the radial resistance. Each coil in the layout is modeled as one such parallel branch, with all branches inductively coupled. In addition, the thermal behavior was evaluated by solving the heat equation, with source terms including Joule heating from radial currents, heating of the resistive joints, the external thermal load, and the cooling power of the cryocooler. The electrical part of the model is governed by the following equation:

$$\frac{dI_\theta(t)}{dt} = L^{-1} R_r \cdot (I_{op}(t) - I_\theta(t)) \tag{2.13}$$

whereas for the thermal part:

$$\begin{aligned} \frac{dT(t)}{dt} = \frac{1}{m_{wd}\, c} \Bigg[& N_{\text{joints}} \left(\frac{I_\theta(t)}{2} \right)^2 R_{\text{joints}} + R_r I_r(t)^2 + Q_{\text{ext}} \\ & + (N_{\text{coils}} - 2) R_{\text{extJoints}} I_{op}(t)^2 - N_{\text{cryo}}\, Q_c(T) \Bigg] \end{aligned} \tag{2.14}$$

Where L is the inductance matrix, $R_r$is the radial resistance which has been calculated dividing the value of the specific contact resistance, taken equal to 37.9 $\mu\Omega{\cdot}\text{cm}^2$ following the AMaSED-2 experience [65] for the non-insulated case, by the total length of each coil, I_{op} is the current fed to the circuit which may be a function of time if the magnet is ramped up, I_θ is the current flowing azimuthally, I_r is the current flowing radially, m_{wd} is the mass of a single coil, c is the overall specific heat, N_{joints} is the number of internal joints per coil (a joint every 200 m of tape has been considered due to the availability of spools unit length due to production instabilities), R_{joints} is the resistance of each internal joint taken equal to 100 nΩ [68], which was considered an acceptable superior limit

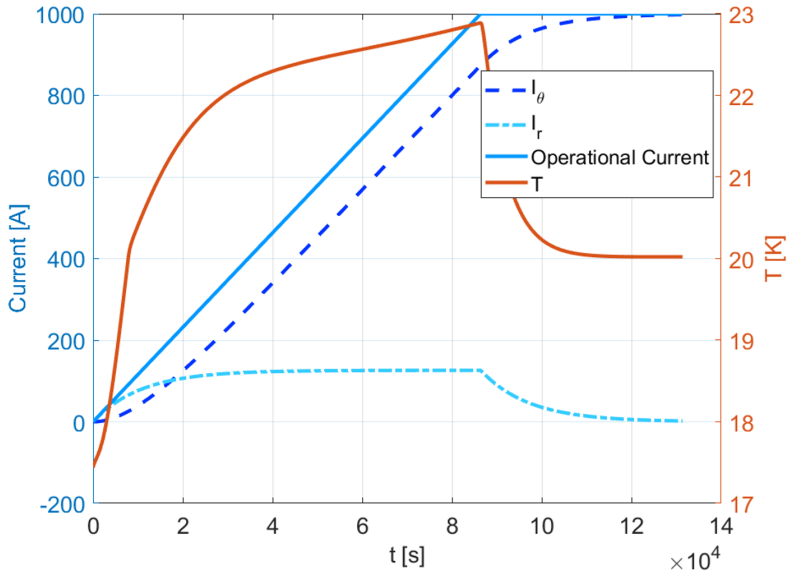


Figure 2.12: Simulation of the charging time of the non-insulated design. On the left axis are graphed the radial and azimuthal current together with the operational current fed to the circuit, while on the right axis there is the overall temperature.

coherently with the available thermal budget, Q_{ext} accounts for the external heat load taken equal to 3 W, Ncoils stands for the total number of coils considered, $R_{extJoints}$ is the resistance of the copper joints connecting different coils and it has been taken equal to 10 nΩ, and *Ncryo* indicates the number of cryocooler used, together with their heat extraction power Qc(T). For the simulations one cryocooler model AL325 from Bluefors [64] has been considered. One should notice the division by two in the first term of the thermal equation which accounts for the current sharing between the two tapes in proximity of an internal joint. Even though a non-insulated winding simplifies quench protection, the large inductance of the magnet, approximately 6 H, leads to a system time constant of about $\tau = L/R_r \sim 10^4$ s which is not compatible with the intended use of the magnet as a variable field test facility for superconducting cables. The results calculated with the lumped model are shown in Fig. 2.12, where it can be observed that nearly a full day would be required to reach the nominal operating current. Here only the slowest dynamic of the system has been represented. The current ramp also induces a temperature rise, mainly due to radial current flow, but this can be tolerated by the system since the resulting $\Delta T \sim 3$ K, with respect to the operating temperature of 20 K, remains below the estimated temperature margin of the magnet of about 10 K. Due to the too long charging time, a compromise between the feasibility of protection granted by a simple non-insulated design and the easiness of charging of the insulated option has been found into the increasing the contact resistance, thus leading to an additional preliminary design concerning the metal as insulation technique. Here the cross section has been optimized considering a cable as sketched in Fig. 2.11 comprising of a 30 µm thick tape of stainless steel tape in order to enhance the specific contact resistance by ap-

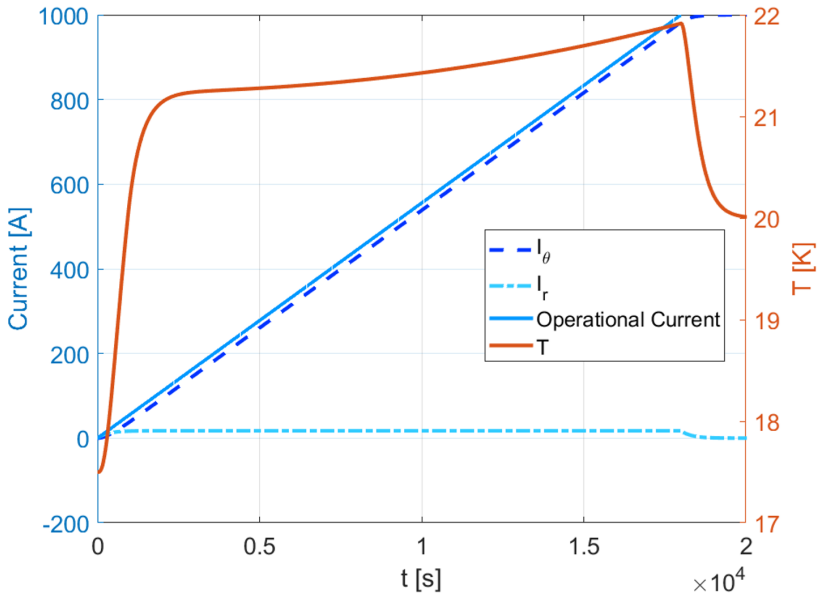


Figure 2.13: Simulation of the charging time of the metal-as-insulated design. On the left axis are graphed the radial and azimuthal current together with the operational current fed to the circuit, while on the right axis there is the overall temperature.

proximately a factor 30 [30]. The optimization ended up with a stack of four racetracks above the mid-plane and four below, with a vertical gap of 110 mm, each racetrack with a total horizontal width of about 80 mm requiring 14 km of tape. The operating current is 1 kA to reach 10 T of central field, with iron pole. Both the non-insulated and design with metal strip have a temperature margin of more than 10 K on the most critical points of the layouts, and in both cases an iron insert is foreseen to meet the 10 T assignment. Concerning the charging time, the results calculated with the same lumped model are reported in Fig. 2.13. Once again, as for the case of the NI design, only the slowest dynamic has been graphed. Although the physical time constant τ of the system was estimated to be around 310 s, the increase in radial resistance introduced by the resistive metallic band results in a significantly higher heat load due to radial current flow, assuming that the current ramp is linear. This poses the need of artificially limiting the charging time of the system to about two hours for a full charge. On the other hand, faster ramps may still be feasible for small current variations, bringing the design sufficiently close to our target of establishing ESMA as an operational test facility. Therefore, the solution with an inter-turn metallic strip has been selected, and further optimization will be carried out to improve each parameter. For every optimization the possibility of having different coils stacks instead of having them all the same has been considered, however this only improved the field quality by orders of fraction of percent. Since an accelerator like field quality which is not the focus of this dipole, for the sake of simplicity the coils have been chosen to be all equal one another. An extensive evaluation of the sensitivity of the central magnetic field to design parameters has been conducted employing FEM calcu-

lations (to account for the iron poles) around the baseline design presented above. This study resulted in the following summary of findings:

- Reducing the aperture clearance increases the central field by approximately +1 T per centimeter, though at the expense of useful space.
- Shortening the straight segment adds about +0.6 T per 10 cm of length reduction, but requires a careful optimization of coil and insert geometries to preserve field homogeneity.
- Adopting a full flux-return yoke provides an additional +0.75 T, though the larger thermal load significantly impacts cooling times.
- Implementing fully non-insulated coils yields a gain of +1 T due to more efficient conductor usage. However, the longer charging times make this solution poorly compatible with variable-field operation.
- Adding more tape increases the central field by about +0.4 T per kilometer. This effect is limited, since the 14 km per 10 T in the baseline design are already in the most efficient position to generate field, leaving additional conductor in non-optimal locations.

With these considerations in mind, the final choice for the metal-insulation (MI) design has been defined. A complete description of the final solution, including the role of the iron yoke and the steps leading to the final configuration, will be presented in the next section.

2.3 Final Electromagnetic Design

Based on the analysis of different winding technologies, and after carefully weighing the trade-offs between performance, protection, and operability, the adoption of a MI winding configuration was established as the baseline solution for ESMA. In the following sections, a detailed description of the design iterations that ultimately led to the final electromagnetic layout will be presented. The discussion begins with the studies on the role of the iron yoke, followed by the constraints imposed on field quality across the full operating range between 2 and 10 T within the GFR volume. Particular attention is then dedicated to the limitations imposed by the available conductor, both in terms of finite unit length, which necessitated the introduction of internal splices, and the requirement to reserve tape for test activities. Finally, the evaluation of operating margins is carried out based on the actual properties of the procured cable, and the section concludes with an outlook on future perspectives enabled by the experience gained throughout this work.

2.3.1 Preliminary Configuration

Starting from the optimized coil layout described in Sec.2.2.2, the role of the iron yoke has been addressed to achieve the ESMA target field of 10 T at 20 K, while also fulfilling the field quality constraints across the entire GFR in the 2 - 10 T operating range. The optimization of the iron yoke considered the adoption of an iron pole, excluding a full flux-return yoke to reduce overall inductance and ease the thermal design, since the cooling system relies on cryocoolers. To maximize the magnetic field provided by the iron, the yoke was designed with a pole extending up to the aperture. Because of the non-linear behavior of iron, the optimal pole geometry may vary between low and high fields. To address this, a dedicated optimization code was developed by coupling Matlab with the open-source FEM solver FEMM. The resulting 2D cross section of the design is shown in Fig. 2.15, along with the main dimensional parameters expressed in millimeters. This 2D model was then extrapolated to three dimensions. To perform the 3D optimization, an initial mesh of a parallelepiped shaped, unrefined pole was generated in MATLAB. Over this mesh, a Free-Form Deformation (FFD) lattice[69] was constructed to enable smooth and continuous geometric modifications of the pole. The FFD lattice acts as a control grid that deforms the underlying mesh by displacing its control points, allowing the creation of two distinct deformation profiles: one acting on the xy-plane (analogous to the 2D optimization case) and the other along the zy-plane, defining the longitudinal variation. The resulting deformed mesh was then imported into OPERA 3D, where a BH-curve was assigned to the material, and a full 3D magnetic field simulation was carried out. This setup allowed the MATLAB script to receive feedback from the 3D solver and perform an iterative optimization coherently. A schematic representation of the steps adopted to perform the iron pole optimization is showed in Fig. 2.14 . The first step illustrates the initial mesh, intentionally displayed as coarse for visualization purposes, followed by the red dots indicating the control points of the FFD lattice. The final step shows the resulting deformed pole geometry, which is then imported into OPERA

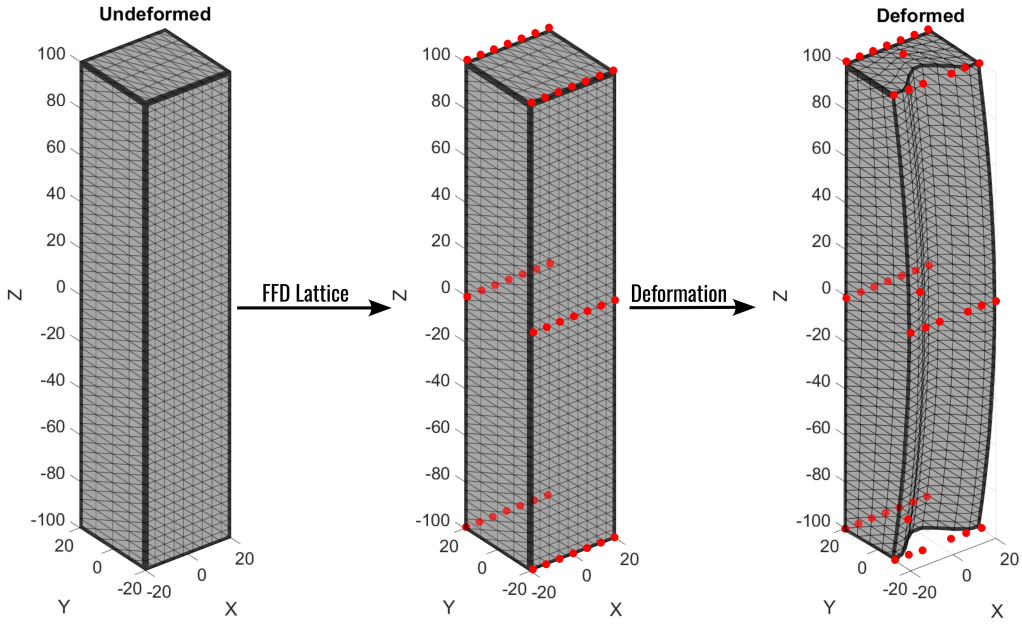


Figure 2.14: Visual representation of the steps adopted to carry out the iron pole optimization concept

3D to perform the non-linear magnetic simulation. The initial design guess used in this process featured a concave pole profile to provide additional field strength near the extremities of the rectangular aperture, thus acting to obtain a flattened field profile in the xy-plane. The same design philosophy was applied longitudinally, however, the concavity was inverted to compensate for the enhanced field generated by the coil heads. The preliminary optimized design is shown in Fig. 2.16 , guessed shape of the cryostat. The pole includes two holes and a mechanical groove on top, both to reduce the pole mass and to facilitate precise mechanical alignment. The overall radius of the circle enclosing the magnet, including the iron yoke, is 215 mm.

The criterion used to calculate the field homogeneity is the one of the relative difference $\Delta B/B_{ref}$ where the reference field is taken as the average of the y-component along the z-axis scanning the whole longitudinal length of the GFR, namely:

$$B_{ref} = \frac{1}{400} \cdot \int_{-200}^{200} By(0,0,z)dz \tag{2.15}$$

Despite the optimization of the pole geometry, the required field quality constraints of $\pm$ 1.5 % could not be satisfied across the entire GFR at all field levels, as shown in Fig. 2.17. On the other hand, these constraints were met in the preliminary iron-less optimization. However, without iron the target field of 10 T at 20 K could not be achieved within the specified aperture and under the constraint of a maximum conductor length of 15 km (including the clearance required to thermally insulate the warm bore from the

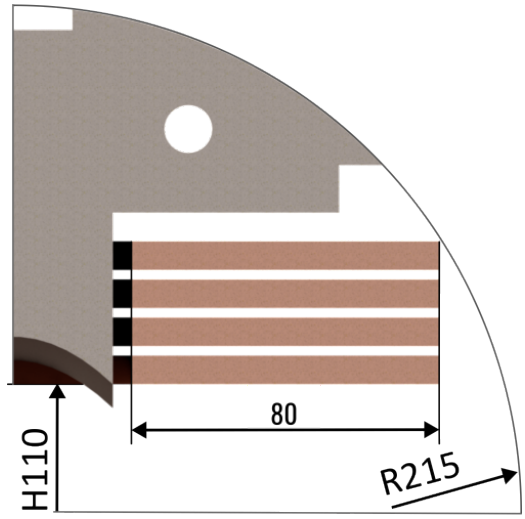


Figure 2.15: Visual representation of a quarter of the cross section of the preliminary design of ESMA, showing the four racetrack in orange and the iron pole in gray. Some key dimension are presented in millimeters as the distance between the two stack of coils, the coil width and the overall cold mass radius.

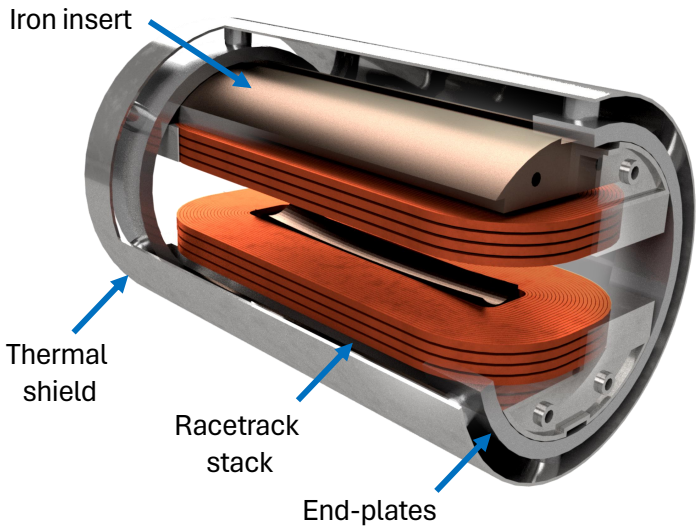


Figure 2.16: Rendered image of the preliminary design of ESMA with iron yoke

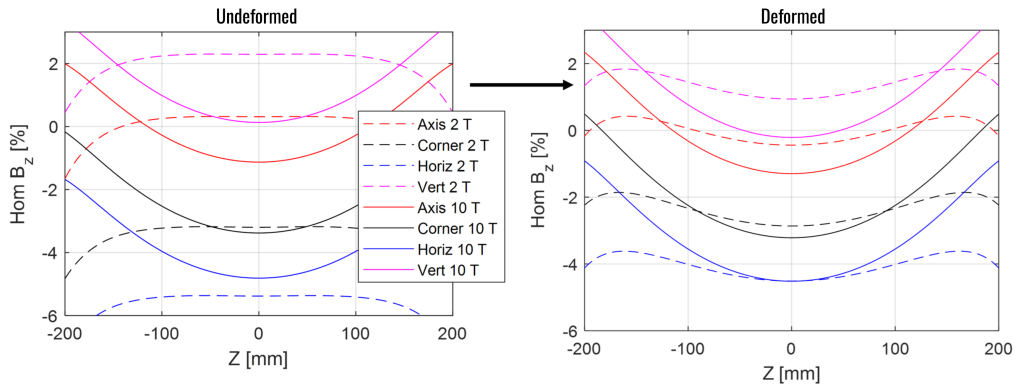


Figure 2.17: Field quality trend within the GFR at different magnetic fields

cold mass), unless performance is maximized by adopting a fully non-insulated winding. This option, however, was considered incompatible with the dual purpose of ESMA, namely functioning both as a technological demonstrator and as a variable-field test facility. To fulfill the field quality requirements while maintaining a layout based primarily on equal coils, the inclusion of iron could not be tolerated. Consequently, the design premises were revised to better address the issues identified during the project. As a result, the bore of the magnet was redefined and modified, leading to the current electromagnetic design of ESMA. In particular, the rectangular warm bore was replaced by a circular aperture with a diameter of 70 mm at the magnet operating temperature. This modification has been verified not to compromise the future operation of the magnet at the Genova testing facility, since the experiments will primarily be carried out within an anti-cryostat using liquid He. The study explained until now is resumed in [70]

2.3.2 Final electromagnetic optimization

Having redefined the ESMA bore, a final optimization of the electromagnetic layout was performed with the aim of fully exploiting the performance of the HTS conductor, to minimize the amount of tape needed and save some sparing for testing purposes. This approach went beyond the conservative minimum specification of 500 A at 15 T with the field parallel to the c-axis of the tape, adopting instead a more realistic performance estimation. This estimation would now consider the anisotropy of the tape, thus giving a performance estimation based on the magnetic field, its angle with respect to the c-axis and the working temperature. The reference critical surface, also suggested by the tape manufacturer, is based on measured values of the critical surface of REBCO tapes from Faraday Factory Japan, which are representative of the standard production, and is available at [71], [72]. These values were cross-checked against the producer's performance data at 77 K in self-field, obtained via Tapestar measurements on the actual 15 km procurement. To validate compliance with the minimum requirement of 500 A at 15 T parallel to the c-axis at 20 K, a lift factor was applied to the 77 K self-field measurements. This requirement was widely satisfied across the entire batch, with only a few localized

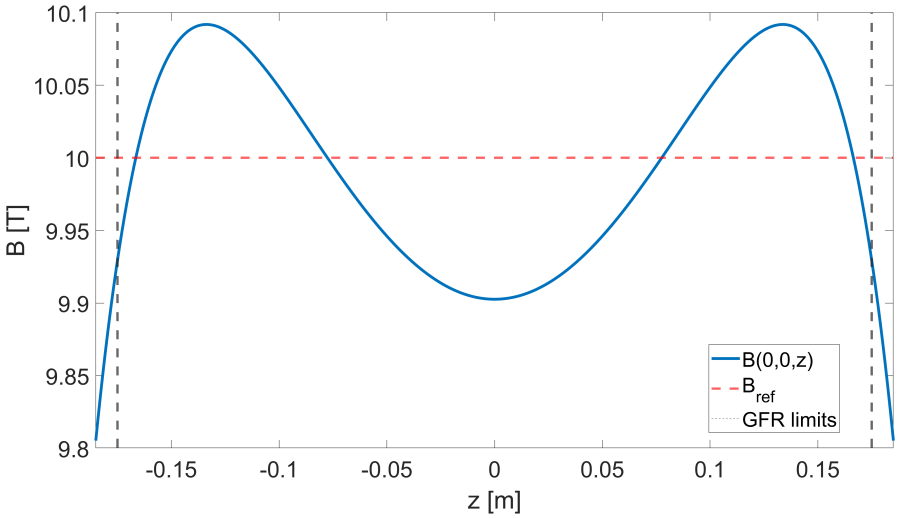


Figure 2.18: Magnetic field of ESMA at the central position along z-axis. The dashed red line highlights the reference field with respect to the field quality is evaluated, while the dashed gray lines set the GFR limits on the z-axis.

defects falling slightly above the threshold. The lift factor is an empirical scaling parameter, defined as the ratio of the critical current of a sample at a given temperature and magnetic field to its critical current at 77 K in self-field. A database of lift factors for FFJ tapes is available in the additional information of [73]. In this work, a value of 1.24 was adopted for the calculations, corresponding to the suggested average of 1.48 reduced by one standard deviation (0.24), to maintain a conservative margin.
Following this approach, the design optimization was carried out together with ASG Superconductors starting from the preliminary analysis of the MI configuration. The cable geometry was maintained, while the operating current was slightly increased to 1150 A. The target field was correspondingly raised to meet the 10 T requirement without relying on an iron yoke. The resulted layout consists of 12 racetrack coils and could be conceptually divided into two sectors, upper and lower, each comprising six windings. Within each sector, the nominal cold spacing between adjacent windings is 9 mm, with the exception of the sixth winding in each half of the magnet, which is separated by 12 mm. The nominal cold conductor-to-conductor spacing between the two sectors is 102 mm. The coils are positioned at a distance of 130 mm on the x-axis from the magnetic center, which also defines the curvature radius of the racetracks. The optimization, initially carried out in 2D, was then extended to the 3D case, with iterations performed on the length of the straight section. The objective was to minimize the overall conductor length while still meeting the field quality requirements in the good field region (GFR) along the longitudinal axis. The optimized straight-section length was determined to be 237.3 mm, a result that not only reduces conductor consumption, but also places the coil heads closer to the GFR, thereby contributing to an enhancement of the magnetic field at the longitu-

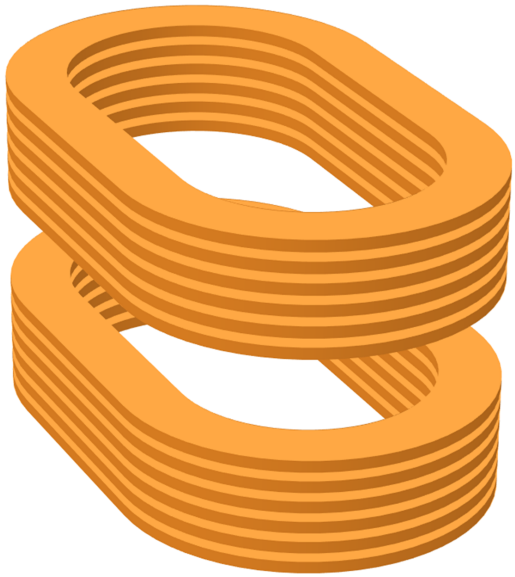


Figure 2.19: Representation of the ESMA final electromagnetic design consisting of a double stack of six racetrack coils

dinal extremities. This effect is clearly visible in the longitudinal magnetic field profile shown in Fig. 2.18. Each coil consists of 350 turns of cable, where the metallic tape serving as metal insulation was chosen to be a commercially available AISI 304 stainless steel tape with a thickness of 26 µm. Although harder materials, as Durnomag, have proven suitable for MI windings by effectively enhancing the turn-to-turn contact resistance R_{ct}, AISI 304 could be procured within the time constraints of the project. This choice was also accounted for during the optimization process, as it contributes to increasing the engineering current density J_{eng} up to 570 A/mm² at the specified maximum operating current of 1150 A. Each racetrack coil corresponds to approximately 516 m of cable, leading to a total estimated conductor length of 12.4 km for the complete winding. Electrical connections between racetracks are made using copper elements. The resulting geometrical peak-to-peak field homogeneity within the good field region is 2.4 %, and it is expected to remain within specification when accounting for magnetization effects as well as the mechanical tolerances associated with production and assembly. A possible variation in coil thickness due to tape thickness fluctuations was also considered and found to be negligible, as discussed in more detail in Sec. 4.3. This final configuration also reflects a compromise introduced during the 3D optimization, specifically regarding the overall tape consumption. To fully meet the field quality targets across the entire GFR, a total tape length close to 15 km would have been required, leaving no margin for contingencies or the fabrication of a spare coil. Such a spare could serve both as a prototype for preliminary tests and, if necessary, as a replacement within the magnet, thanks to the modular design approach adopted. To this purpose, the GFR length along the z-axis was reduced from 400 mm to 350 mm, thus lowering the conductor demand and

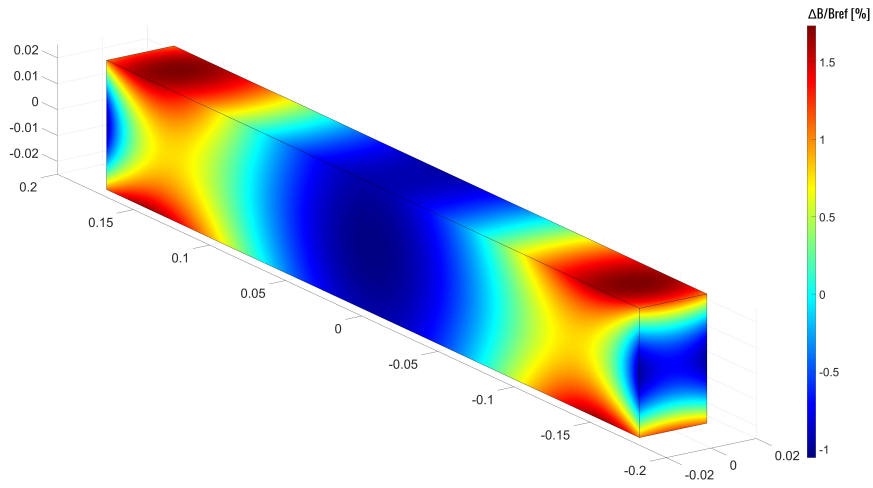


Figure 2.20: GFR volume of ESMA magnet where the relative differences with respect to the reference magnetic field B_{ref} expressed in percentage are reported.

leading to the proposed design while still remaining consistent with the design goals. The resulting and final electromagnetic configuration is represented in Fig. 2.19. Having established the final electromagnetic layout, the target field level was achieved while maintaining a maximum deviation of $\pm$ 1.5 % within the GFR boundaries. This result is confirmed by the calculations shown in Fig.2.20, which reports the relative deviation expressed as percentage with respect to the reference field value B_{ref} = 10.001 T, obtained from Eq. 2.15. The integral limits in the calculation were updated according to the new GFR length, and the field was evaluated at the operational current of 1150 A. As shown by the homogeneity plot, the maximum calculated deviation is approximately + 1.16 % and the minimum - 1.41 %. The resulting difference is 2.57 %, which is within the 3 % target.

The final electromagnetic design optimization considered the evaluation of operational margins and the peak field at the maximum central magnetic field, in order to exclude unfeasible layouts. The analysis was carried out assuming an operational temperature of 20 K and a powering current of 1150 A for the entire cable. The magnetic field was computed using the FEM software OPERA3D, in which the full three-dimensional electromagnetic model was implemented. The calculation incorporated the three critical parameters defining the superconducting critical surface, as well as the angle between the magnetic field and the c-axis of the tape, to account for its anisotropic behavior. This angular dependence was derived from the field components. Once the expected operating parameters of the magnet were fixed, the critical surface data cited at the beginning of this section were interpolated using a spline to calculate the operational margins of the configuration. The operational margin was estimated as the critical current fraction margin (Fig. 1.7). To this aim, 2D patches were created at the two most critical locations of the magnet: the middle of the straight section, where internal joints are most likely to

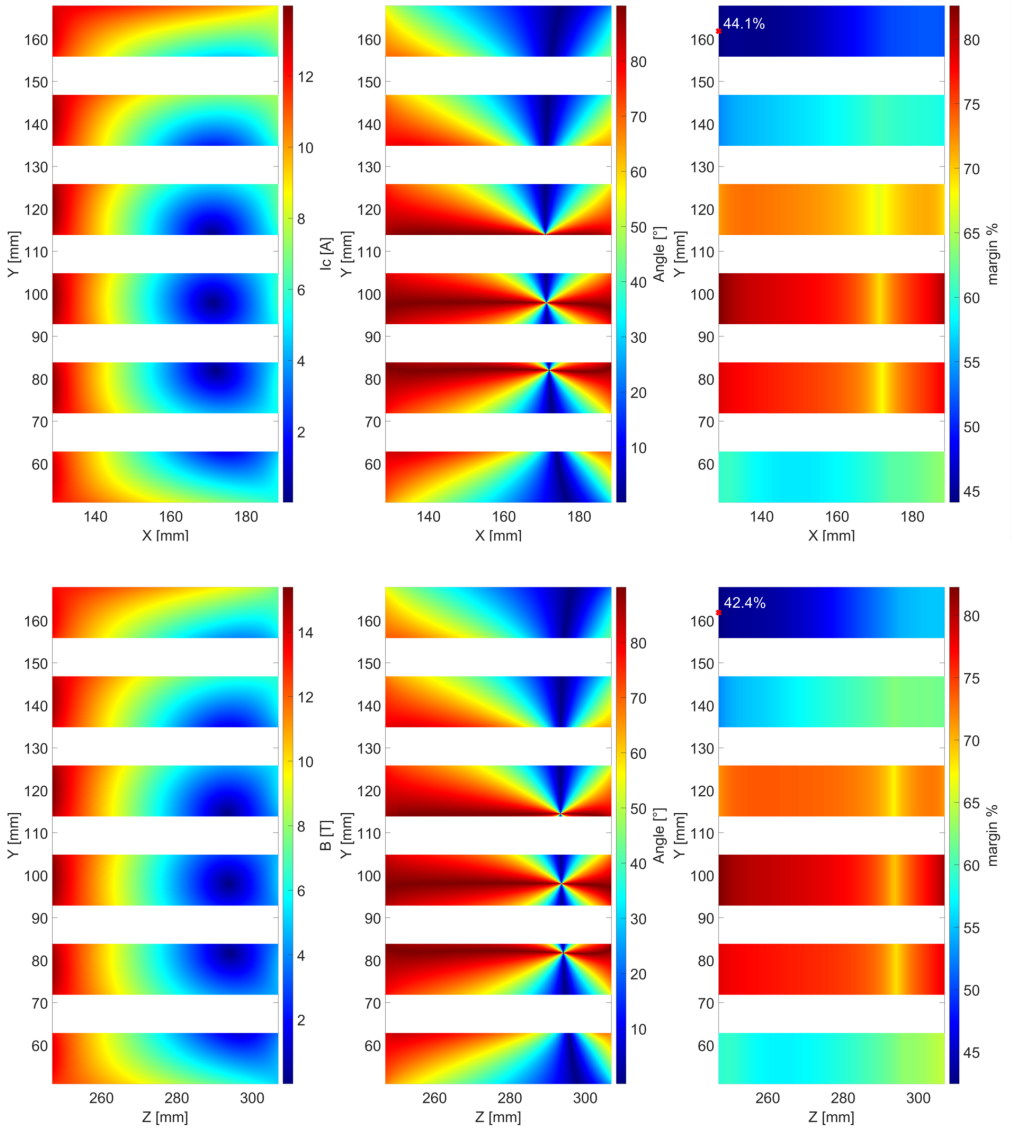


Figure 2.21: The image shows the magnetic field map (left), the angle the incidence angle of the magnetic field with respect to the c-axis of the tape (center) and the current margin (right) calculated on a patch at the center of the straight section (top) and at the center of the curved section (bottom) of one sector of the ESMA magnet consisting of six racetrack coils. The minimum margin value is written in white and the corresponding point is highlighted with a red cross.

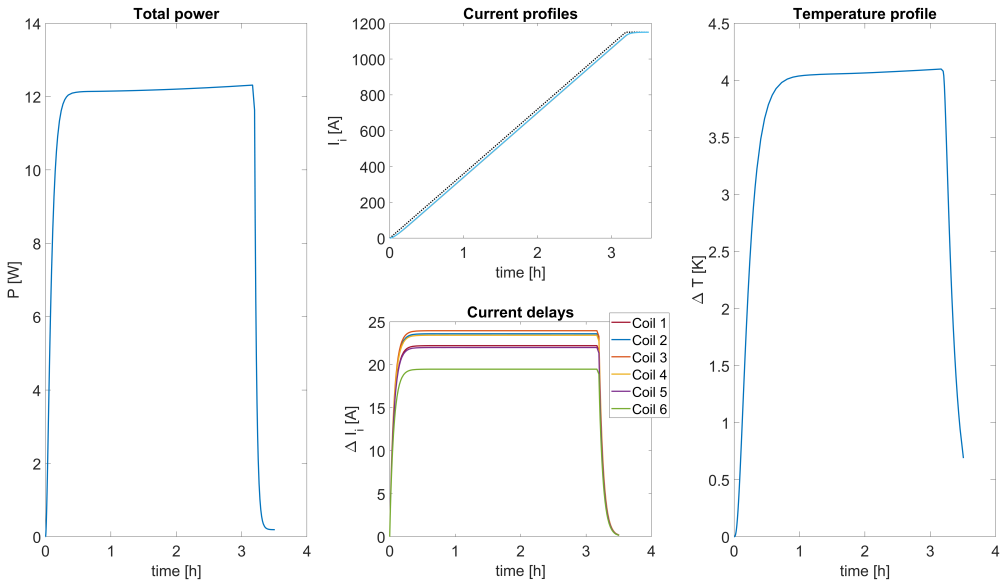


Figure 2.22: Summary of the charging behavior of the final layout of the ESMA magnet. The total power generated during a full ramp at 0.1 A/s is represented (left), together with the radial and azimuthal current profiles (middle). On the right is represented the temperature increase with respect to operational condition at 20 K.

occur, and the center of the racetrack heads, where the magnetic field reaches its maximum on the conductor. The collected values have then been averaged on the whole 12 mm width of the tape, corresponding to the coil height, since within each tape there is no interruption of the superconducting material. The corresponding results are shown in Fig. 2.21 top and bottom sections, respectively, without considering the presence of inner splices. These values correspond to a temperature margin in the most critical point of around 10 K.

One final major verification of this layout concerned its charging time behavior. For this purpose, the lumped element model previously used to evaluate the preliminary configuration was adopted. The value of the contact resistance was kept consistent with that assumed in the earlier MI design, as were the premises of the associated thermal model. The inductance matrix, was updated and now consists of a 12×12 matrix, accounting for each of the twelve racetrack coils in the layout, for a total inductance of 5.5 H. The results are graphed in Fig.2.22. In this figure, the current delays of the six coils forming one half of the ESMA magnet are graphed and referred to as Coil 1 to Coil 6 starting the numeration from the nearest coil with respect to the center and proceeding towards the most external one, namely Coil 6. In this new configuration the slowest dynamic corresponding to a time constant of about $\tau \sim 4$ minutes. However, due to the Joule heating generated by the radial current flow, ramping ESMA up to its maximum field must be artificially slowed down to keep the maximum ΔT below a safe threshold and

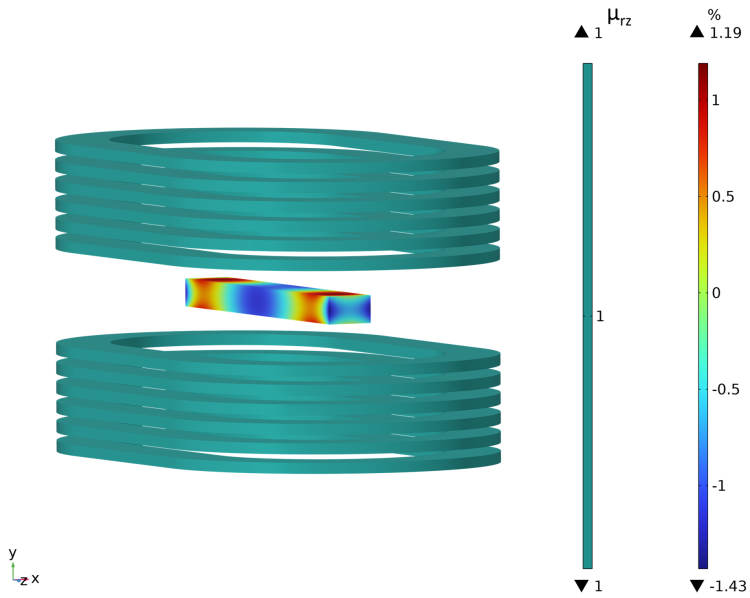


Figure 2.23: Analysis of the effect of the relative permeability of the AISI 304 stainless steel tape used as metal insulation. Here the relative permeability has been fixed to μ_r = 1. The box in the center of the magnet corresponds to the GFR volume and the values of $\Delta B/B_{ref}$ are reported in percentage.

prevent quenching. In the case shown, the ramp rate was limited to 0.1 A/s, resulting in a temperature rise of about 4 K. As previously noted, the magnet is designed using HTS tape conductors. The conductor size and morphology are equivalent to a single rectangular filament per tape, with dimensions of 12 mm $\times$ 3 μm. Due to superconducting properties of these tapes, the current density is not uniformly distributed throughout the winding volume. The analyses considered so far, referred to as nominal, did not account for dynamic effects. This remains an open issue for HTS magnets, requiring further effort both in modeling and in the development of mitigation strategies by manufacturers. Initial progress has already been made, for example through the first attempts at striating the tapes, as mentioned in the introduction of this thesis. In the case of ESMA, where an accelerator level field quality is not required, the impact of this effect was considered negligible. However, it should be carefully addressed in future studies aimed at magnets for particle accelerator applications.

2.3.3 Effect of residual permittivity

The metal-as-insulation winding technology adopted in the final layout of ESMA initially considered a 30 μm thick Durnomag tape, following the example of the high-field solenoid Nougat [29]. Since the increase in radial resistance is mainly governed by the contact resistance between cable components, with the bulk contribution being negligible, the metal band should ideally be as thin as possible, while still ensuring manufac-

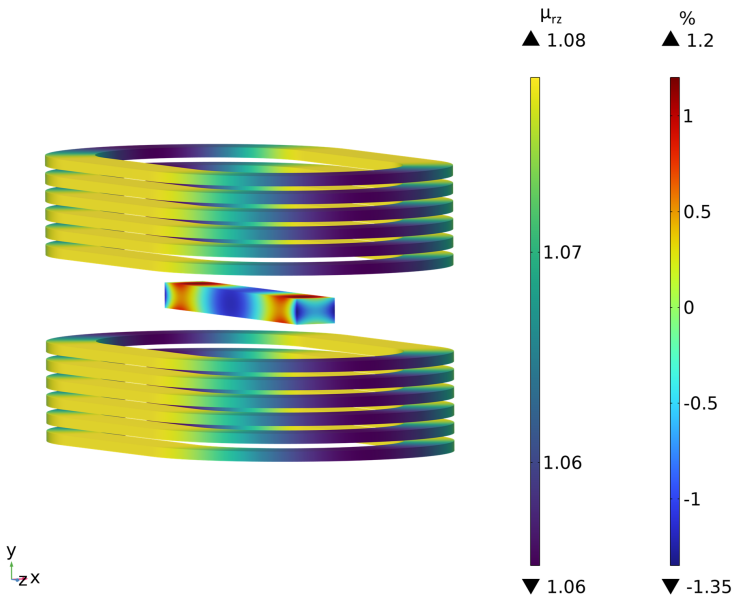


Figure 2.24: Analysis of the effect of the relative permeability of the AISI 304 stainless steel tape used as metal insulation. Here the relative permeability has been fixed to μ_r = 1.5. The box in the center of the magnet corresponds to the GFR volume and the values of $\Delta B/B_{ref}$ are reported in percentage.

turability and mechanical strength. Moreover, to further enhance the radial resistance, two thinner metal bands are more effective than a single tape of equivalent total thickness. An additional advantage of Durnomag lies in its non-magnetic properties. By contrast, standard AISI 304 stainless steel may develop slight magnetic behavior when laminated down to small thicknesses. For the ESMA conductor, Durnomag was initially considered, however, both the high cost and the long procurement time required for approximately 6 km of tape (corresponding to half of the conductor needed to wind the magnet, given the cable composition) motivated the search for an alternative. A suitable replacement was found in a commercially available AISI 304 stainless steel tape, 26 µm thick and 12 mm wide. The potential drawback of this choice lies in the residual magnetic properties of the material, which could affect the field homogeneity of ESMA. To assess this, a model of the magnet was developed in COMSOL, where the coils were assigned an overall linear, homogeneous, and anisotropic 3D permeability matrix. The relative permeability μ_r of the AISI 304 tape was varied from 1 up to an intentionally overestimated value of 50 and weighted by the volume fraction of steel relative to the REBCO tape within a coil. A local reference system was defined to follow the geometry of the racetrack coil. Specifically, two cylindrical coordinate systems were adopted at the racetrack heads, while two standard cartesian systems were used for the straight sections. The resulting framework is arranged so that one axis coincides with the coil winding direction, while the other two complete a right-handed orthogonal system: one

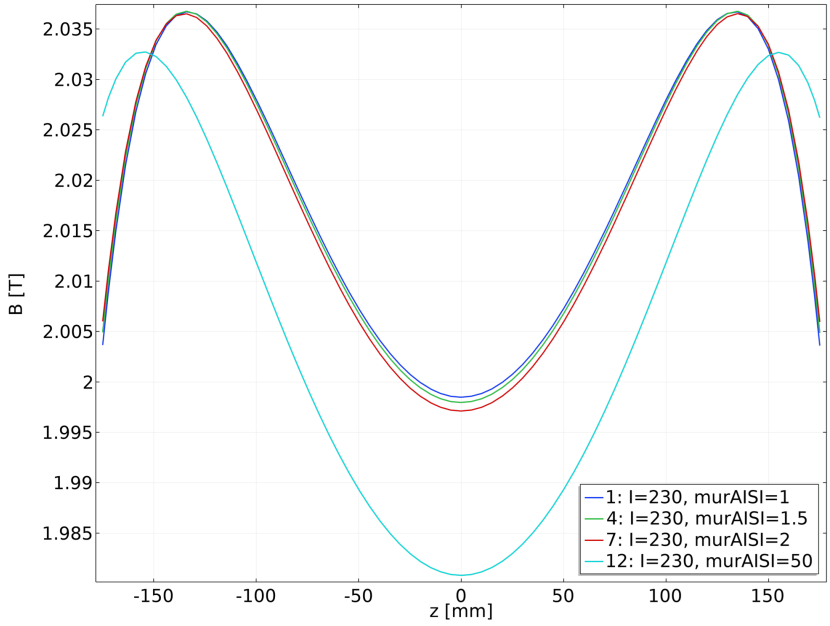


Figure 2.25: Magnetic field profile along the central line passing through the GFR at different relative magnetic permeability values of the stainless steel tape acting as metal insulation.

aligned with the c-axis of the tape and the other pointing vertically upward. The permeability matrix was then constructed as:

$$\boldsymbol{\mu_r} = \begin{bmatrix} \mu_{r11} & 0 & 0 \\ 0 & \mu_{r22} & 0 \\ 0 & 0 & \mu_{r33} \end{bmatrix}$$

where $\mu_{r11} = \mu_{r22} = \mu_{r33} = \mu_r$ refers to the values given as material property of the coil, expressed within the direction defined by the newly created local reference system. The simulation primarily focused on the GFR region to verify whether any of the tested values of relative permeability could introduce deviations from the field homogeneity target. The analysis was carried out for a current of I = 230 A, corresponding to the minimum central field of ESMA (2 T), which represents the worst-case condition where the relative influence of the magnetic properties of the material is expected to be most significant. As a reference, an initial simulation was performed with μ_r = 1, serving as the baseline case. The corresponding results are shown in Fig. 2.23. All remaining cases were also evaluated. As an example, Fig 2.24 reports the simulation results obtained by assigning a relative permeability of μ_r = 1.5 to the AISI 304 stainless steel tape. In this scenario, the GFR remains fully within the specified target boundaries, confirming the feasibility of employing this material in the ESMA winding. To complete the analysis, Fig. 2.25 and Fig. 2.26 show the magnetic field profiles along the center and the outermost corner of the GFR for all the assessed values of μ_r. The plots indicate that a relative permeability as high as 50 would be required to induce a field deviation on the order of

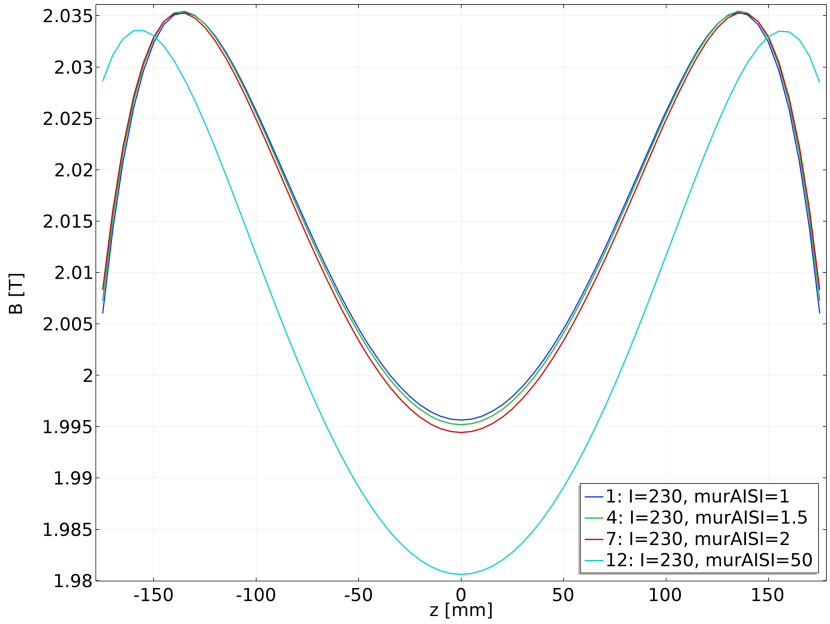


Figure 2.26: Magnetic field profile along the line passing through the outermost corner of the GFR at different relative magnetic permeability values of the stainless steel tape acting as metal insulation.

a percent within the GFR. Ultimately, the measured relative permeability of the stainless steel tape was found to be in the range $1.002 \sim 1.2$, thus further confirming the suitability of this material for use in the ESMA winding.

2.3.4 Fringe field

The fringe field constraints for ESMA were defined to ensure that the magnetic field remains below 0.5 mT at a distance of 7 m from the center of the magnet. This requirement is essential for safety reasons, as the magnet will ultimately be installed at INFN Genova. The proposed electromagnetic layout satisfies with this limit, however, additional analyses were carried out to verify that the ESMA fringe field would not interfere with nearby instrumentation or exceed safety thresholds in areas accessible to the public. A scaled picture of the INFN Genova laboratory is reported in Fig.2.27 With reference to the layout shown in the figure, the most critical aspects are the proximity of a laboratory wall located approximately 3.2 m from the center of ESMA, and the presence of the already existent high-field solenoid MA.RI.S.A. [74]. In contrast, the He buffer and liquefier are situated more than 7 m away from ESMA and are therefore exposed to a negligible magnetic field. In this configuration, ESMA will be positioned inside a pit, 0.6 m below the laboratory floor level. To assess the most suitable option for laboratory integration, the magnetic field of ESMA was evaluated at a reference height of 1.0 m above the floor, i.e., a representative level for human presence. The results are shown in Fig.2.28, where the outermost contour corresponds to the 0.5 mT threshold. Without any shielding, this

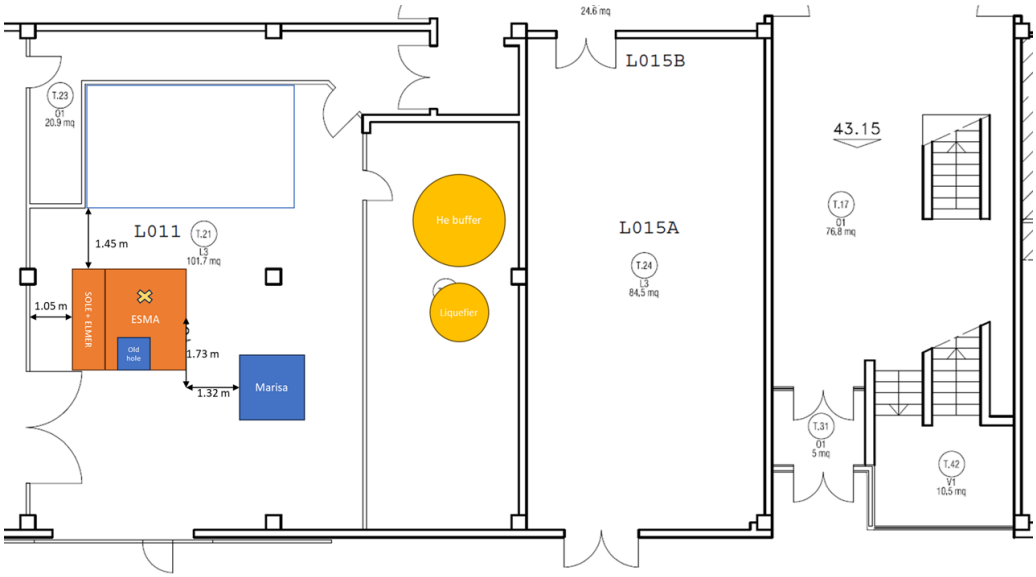


Figure 2.27: Map of INFN Genova laboratory. The central position referred to the location where ESMA is going to be placed is represented by the yellow cross.

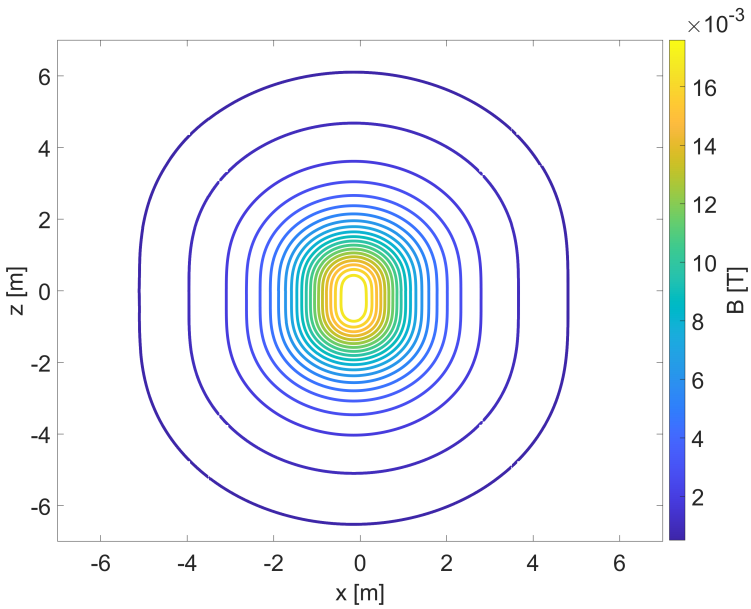


Figure 2.28: Contour plot representing the magnetic field magnitude levels for the ESMA magnet at 1.6 m from the magnetic center. The outermost countour line corresponds to 0.5 mT.

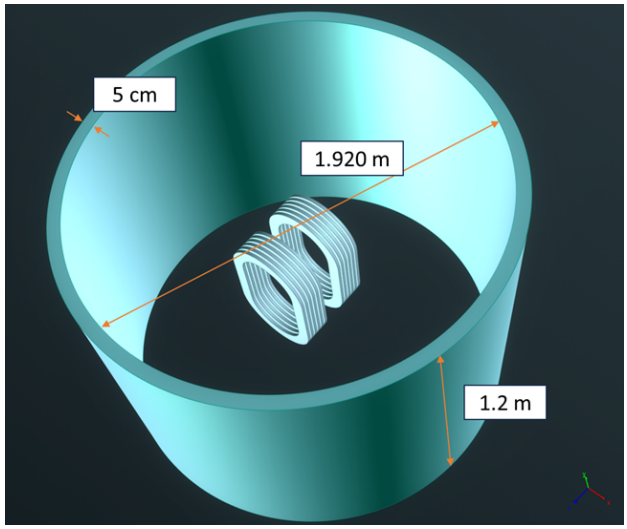


Figure 2.29: Visual representation of the ESMA magnet and a cylindrical iron shield of 5 cm of wall thickness modeled in RAT-GUI.

contour extends to approximately 5 m from the center of the magnet, i.e., about 1.8 m beyond the allocated laboratory area. MA.RI.S.A. falls within the fringe field region of ESMA, however, since the two magnets are not intended to operate simultaneously, this does not represent an issue. If the magnet were to operate under these conditions, access to the area outside the laboratory where the magnetic field exceeds the threshold would need to be restricted. This is considered a minor concern, since the affected area beyond the wall is relatively small and the field there is only slightly above the threshold limit. To further mitigate this issue, the use of an iron shield was investigated as a mean of reducing the fringe field volume. A preliminary design of a cylindrical iron shield was simulated around the ESMA magnet, with an internal diameter of 1.92 m (matching the ESMA pit), a thickness of 5 cm, and a height of 1.2 m. The shield is intended to be placed inside the pit together with the magnet. A visual representation of this configuration is shown in Fig. 2.29. To estimate the shielding effect, a 3D model was developed using the FEM software RAT-GUI, and the magnetostatic problem was solved at the maximum operating field of 10 T. The results show that the distance at which the magnetic field reaches 0.5 mT is reduced to approximately 4 m, thus still extending about 80 cm beyond the wall at a height of 1 m from the floor (neglecting wall thickness). The simulation was then repeated with increased shield thickness, and it was found that a thickness of 9 cm fully suppressed the fringe field beyond the wall. The results of this analysis, together with a cost estimate for the shield, are summarized in Tab.2.3. The evaluation of the cost of the iron shield has been estimated by a simple calculation of the mass of the cylindrical shield and considering a cost equal to 7 €/kg. This value has been provided by INFN Genova and is based on previous similar experiences of iron procurement. However, the placement of an iron shield could introduce challenges related to a possible misalignment of ESMA within the pit. To assess this risk, an order of

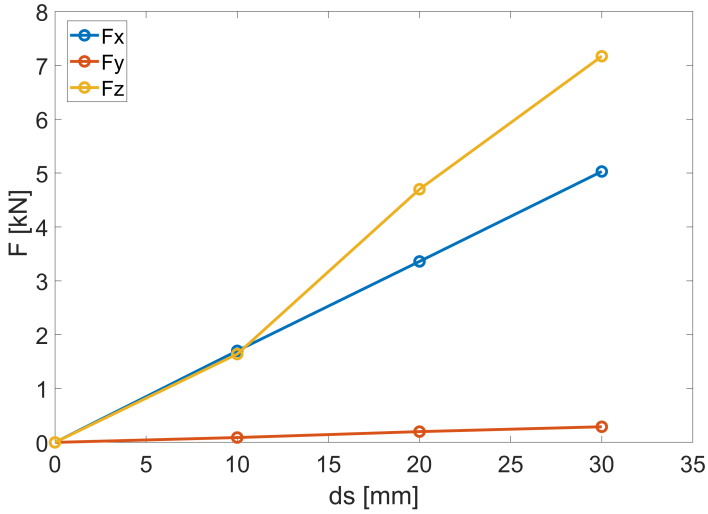


Figure 2.30: Misplacement forces analysis of ESMA within the iron shield given a misalignment error of up to 30 mm the x, y, and z directions

magnitude estimation of the forces generated by a non-symmetric positioning of ESMA inside the shield was performed considering a 5 cm thick iron shield, with results shown in Fig. 2.30. The analysis considered a displacement of up to 30 mm in each of the three spatial directions, denoted as ds in the figure. The results highlight the necessity of integrating a mechanical support structure within the pit in case an iron shield is adopted, capable of withstanding forces up to 8 kN and 5 kN for displacements in the plane parallel to the floor (the xz-plane). In contrast, significantly smaller forces are expected in the case of vertical misalignment (along the y-axis). If the shield were to be integrated, the potential impact of the iron on MA.RI.S.A. during operation would also need to be evaluated, since its placement could generate unbalanced forces. To address this, a model of the INFN Genova laboratory including MA.RI.S.A. was developed in RAT-GUI, as shown in Fig. 2.31, and the resulting forces induced by the iron were calculated with MA.RI.S.A. powered at its maximum field of 10 T. Results are summarized in Tab. 2.4, where it can be observed that only weak forces are produced. A dedicated control performed on the structure of MA.RI.S.A. confirmed the negligible impact of the presence of an iron shield. Based on these results, the final decision was to install ESMA without

	5 cm Fe	**7 cm Fe**	**8 cm Fe**	**9 cm Fe**	**0 cm Fe**
Cost [€]	20 467	28 945	33 246	37 589	0
Lab wall trespassing field @ 1 m [cm]	80	40	20	0	180

Table 2.3: Summary of the cost and effect different iron shield configurations. The last row reports in centimeters the area beyond the laboratory wall where the field exceeds the threshold limit of 0.5 mT at 1 m height from the floor level.

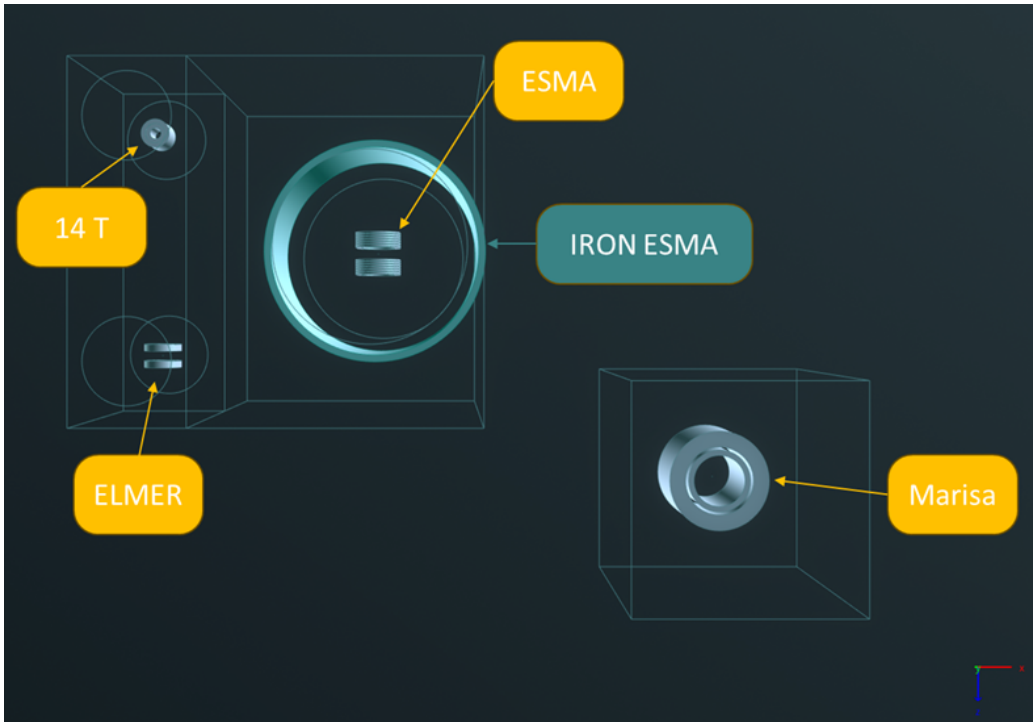


Figure 2.31: 3D RAT model of the magnets inside INFN Genova laboratory

	5 cm Fe	**9 cm Fe**
MA.RI.S.A. 10 T – Fx [N]	190	221
MA.RI.S.A. 10 T – Fy [N]	11	14
MA.RI.S.A. 10 T – Fz [N]	136	156

Table 2.4: Resulting forces on MA.RI.S.A. generated by the presence of an iron shield of two possible thicknesses around ESMA.

a magnetic shield. While this requires particular attention during magnet operation, it avoids the need to transport and assemble a large mass of iron inside the pit, to precisely align the magnet with respect to the shield center, and to design a mechanical structure capable of absorbing the forces resulting from a possible misalignment. In addition, the uneven current distribution that could arise during a quench, since the magnet is wound as a metal-as-insulated coil, would lead to asymmetric force distributions between the magnet and the shield, a phenomenon that has not yet been fully assessed. Developing accurate models of this dynamic remains an open challenge within the HTS magnet community. For these reasons, an iron-free solution was ultimately chosen.

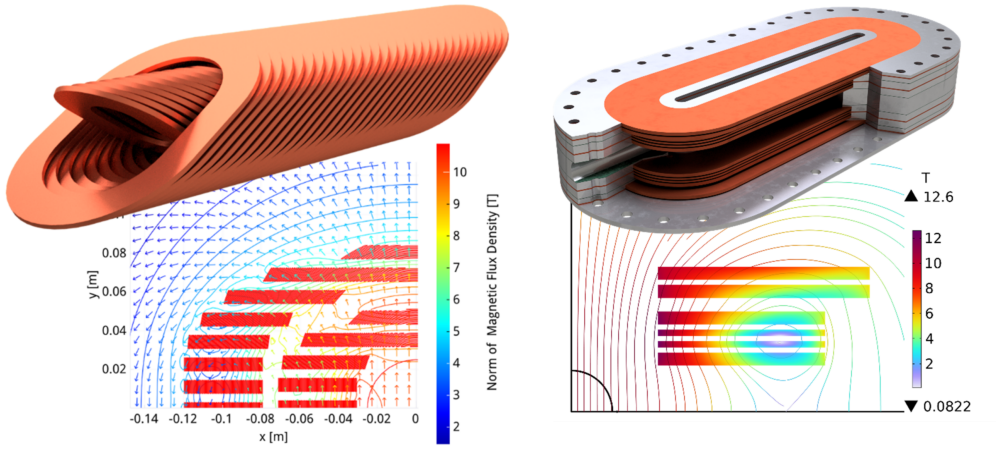


Figure 2.32: Visual representation of two possible HTS magnet designs based on racetrack coils for future particle accelerators, together with the field generated by a quarter of the cross section.

2.3.5 Towards an Accelerator Design

The purpose of ESMA as both a technological demonstrator and a test facility represents a first milestone toward the more ambitious goal of developing accelerator magnets based on HTS technology. Given the experience gained with flat-coil designs as for the ESMA layout, two preliminary studies are presented here as anticipatory steps toward the realization of a magnet with accelerator-level field quality, using flat racetrack coils. In these studies, the target central field has again been set to 10 T, with an aperture diameter of 50 mm and a straight section of at least 400 mm. Since these dipoles are conceived for use within an accelerator, achieving fast ramping and ensuring repeatable performance are mandatory requirements. For this reason, the designs have been developed with insulated cables, carefully dimensioning the copper fraction to relax protection constraints. Specifically, the copper fraction within the cable was set so that, under the assumption of a full current transfer to the stabilizer during a quench, the current density in the copper elements remains below 800 A/mm^2. The first configuration studied was a Helmholtz-like layout, inspired by the ESMA baseline. In this case, the optimization process was carried out using the built-in *patternsearch()* function of Matlab [75]. The constraints requiring identical coils were removed, and the possibility of using different tape widths for winding was introduced. The second configuration explored the feasibility of a modular Canted Cosine Theta (CCT) design, composed of identical racetrack coils tilted by an initial, non-optimized angle of 30° with respect to the horizontal plane. This study focused primarily on dimensioning the layout to meet the target field and margin requirements. In both designs, a minimum temperature margin of 10 K was imposed. The resulting configurations are shown in Fig.2.32, together with the corresponding field distributions within a quarter of their cross sections. A summary of the design results, including the required tape length, operational current, margins,

and field quality, is reported in Tab.2.5. For the sake of a coherent comparison, the tape length is expressed in terms of a 12 mm-wide equivalent, since the Helmholtz-like design considered the possibility of combining different tape widths. With respect to field quality, the values must approach a field quality level which shall be in this early stage, at least the order ~ 60 units. For this purpose, the magnetic field was computed on a circular region at a reference radius of 2/3 of the maximum aperture and decomposed into harmonics according to Eq.1.4. The two designs presented are yet to be optimized, but they are part of an ongoing effort to advance the application of HTS in the development of superconducting magnets.

Layout	**L [km] [12-mm]**	**I_{op} (A)**	**i = I/I_c (%)**	**ΔT (K)** ***margin***	**Loadline margin (%)**	**Field quality [10^{-4}]**
Racetrakcs	7.3	3330	67	10	22	< 20
Modular CCT	5.5	1440	69	10	23	100

Table 2.5: Summary of the design features achieved by the Helmholtz-like configuration and the modular CCT design studied for for future particle accelerators.

2.4 Summary and achievements

The research described in this chapter addresses the need to develop an electromagnetic design for the ESMA magnet capable of satisfying all the requirements necessary to serve both as a technological demonstrator and as a user magnet to be installed at INFN Genova. Specifically:

- A **Helmholtz-like layout** was demonstrated to be the most efficient configuration, given a rectangular aperture with an aspect ratio in which the base is larger than the height, as in the case of ESMA.
- Non-planar geometries as the **cloverleaf** proved to be more efficiently but the gain, approximately **15%**, was not enough to justify the construction complexity.
- Winding technology was identified as a **metal-insulated**, which combines compactness and mitigation of quench-induced damage. This approach reduces the charging time constant compared with a fully non-insulated design, thus meeting the requirements of a test facility.
- The metal-insulation was achieved by **co-winding AISI 304** which was verified not to affect the required field homogeneity over the good field region, despite its possible relative magnetic permeability $\boldsymbol{\mu_r \geq 1}$.
- The **final cable layout** was defined consisting of **two HTS tapes** and **one stainless steel tape**, for a total of three co-wound tapes per turn. This solution balances the need to reduce magnet inductance with the requirement to preserve the thermal budget by lowering the total operating current.
- The **final electromagnetic design** was carried out requiring $\sim$ **12 km of HTS tape,** meeting the required field quality over the entire good field region for all operating field levels between 2 T and 10 T, while maintaining sufficient operational margins to ensure robust operation.
- Despite the advantage of decreasing conductor usage, the inclusion of an **iron yoke** was found to be **unnecessary**, as the iron poles could not be optimized to meet the required field homogeneity of $\pm$ 1.5% for all target field values.
- The **magnetic fringe field** constraints within the INFN Genova laboratory were satisfied even in the absence of an iron yoke or an external iron shield.

CHAPTER 3

HTS tape electrical measurements

Having set the electromagnetic configuration of ESMA, and upon delivery of the procured tape, a first set of experimental measurements was initiated to validate the parameters adopted in the design. Regarding the electrical properties of the tapes, and to confirm the Tapestar data provided by the manufacturer, an initial verification was performed by measuring the critical current of small samples. The entire 15 km batch was then visually inspected, during which minor surface defects were detected. A dedicated study was therefore carried out to assess whether these inclusions could be detrimental to the magnet. Moreover, since ESMA requires nearly 1 km of tape per coil, corresponding to approximately 500 m of single tape, and given that the reels generally range between 200 and 300 m in length, at least one internal splice per coil is foreseen. To this aim, a dedicated experimental campaign was started with the objective of identifying the most effective procedure to achieve a low-resistance splice without damaging the tape.

3.1 Critical current measurements

The first set of measurements required to assess the quality of the tape is the determination of its critical current I_c. Given the property of HTS conductors to remain superconducting in liquid nitrogen, an experimental setup was developed to perform I_c measurements at 77 K, in self field conditions. The setup consists of:

- A cylindrical open dewar filled with liquid nitrogen, aperture 300 mm and 750 mm of inner height
- A Keithley-2182 nanovoltmeter to monitor the voltage drop across the superconducting sample
- A battery-powered power supply capable of providing currents up to 2500 A with a maximum output voltage of 4 V.
- A Direct Current Current Transformer (DCCT) for the measurement of the operating current



Figure 3.1: SnIn crucible with silicone brushes



Figure 3.2: Sample holder for I_c measurements of HTS tapes in LN_2

This configuration allows for a precise measurement of the transition to the normal conducting state under controlled conditions. For each measurement, a sample of HTS tape was cut from the spool and mounted on a dedicated sample holder. The sample holder was designed from a rectangular G10 support with copper bars fixed at its extremities, acting as current leads. The tape sample was brazed onto the copper leads using a SnIn alloy composed by 48 % tin and 52 % indium, with a melting temperature of 118 °C. To ensure proper adhesion, the tape surface was pre-tinned by applying Kiwa S-65 flux and submerging it in a crucible at a controlled bath temperature of 150 °C, forming a uniform SnIn layer. The deposition of the brazing alloy is controlled by a set of two silicone brushes mounted on the crucible structure. The set up structure is reported in Fig.3.1. The pre-tinned sample was then soldered on the copper leads with a temperature controlled welder, also operating at 150 °C. Finally, voltage taps are soldered on the surface of the tape at a distance of approximately 70 mm from each other, completing the preparation of the test sample. A completed sample holder with a mounted test sample is represented in Fig.3.2. Having established the setup and sample preparation procedure, a series of I_c measurements were performed. The raw V-I data were fitted with a power-law dependence (Eq. 1.9) in order to extract the critical current. For consistency the I_{c100} criterion was adopted, corresponding to the current at which the measured voltage

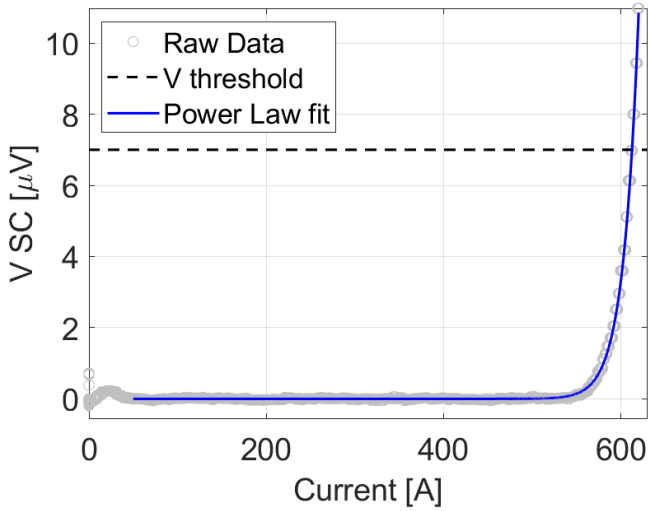


Figure 3.3: Voltage-Current graph of a measure performed on a sample of HTS tape from FFJ, 12 mm wide at 77 K self field.

reaches 7 µV in the described setup. A measurement example is reported in Fig. 3.3, for a sample taken from the ESMA procurement showing a transport critical current of 612 A and a n-value of 36. For comparison, the average value provided by the manufacturer and measured with Tapestar technology for the same spool amounts to 590 A. As shown in Fig.3.4, the probability distribution function of the Tapestar data can be fitted with a gaussian probability distribution function with an average value of 590 A and a standard deviation of 9 A. These values, when multiplied by the lift factor of 1.4 to match the expected performance at 20 K and 15 T in orthogonal field, confirm the conservative nature of the initial design assumption of a minimum required performance of 500 A at 20 K and 15 T, and also validate the critical surface values adopted during the development of the final electromagnetic layout. Indeed, for this particular spool dedicated to test measurements, more than 200 I_c values were collected. The average calculated from these tests was 594 A, with a standard deviation of 16 A. The measured dataset was then compared to the nominal Tapestar distribution shown in Fig. 3.4 using a z-test. The results indicated no significant deviation, with the null hypothesis being retained and a corresponding p-value of approximately 0.2. The results indicated no significant deviation, with the null hypothesis being retained and a corresponding p-value of approximately 0.2. This value can be explained by the fact that most of the measurements were performed on consecutive sections of the spool, thus sampling a localized region of the Tapestar rather than the entire population. Such sampling may lead to slight deviations in the average value and in the frequency distribution, without however compromising the overall statistical compatibility. The two probability distributions and their corresponding gaussian fits are shown in Fig.3.5, where a slight increase in the frequency of occurrences can be observed in the right-hand tail of the measured distribution, in the region where the Tapestar data have already decreased.

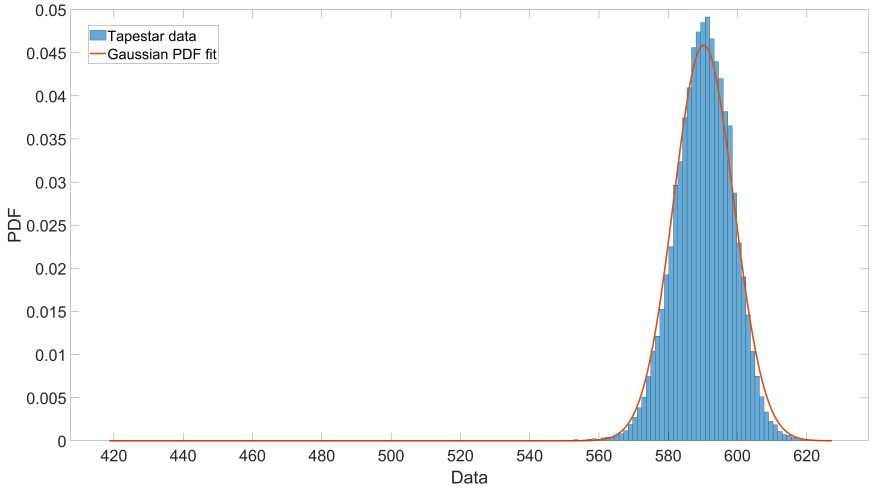


Figure 3.4: Probability distribution function of tapestar data for the specific spool used to perform electrical tests.

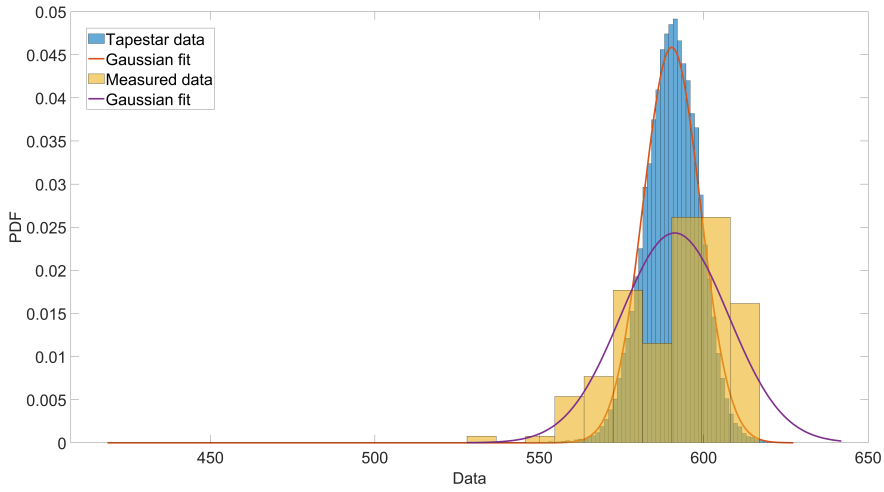


Figure 3.5: Probability distribution function of tapestar data and measured data for the specific spool used to perform electrical tests.

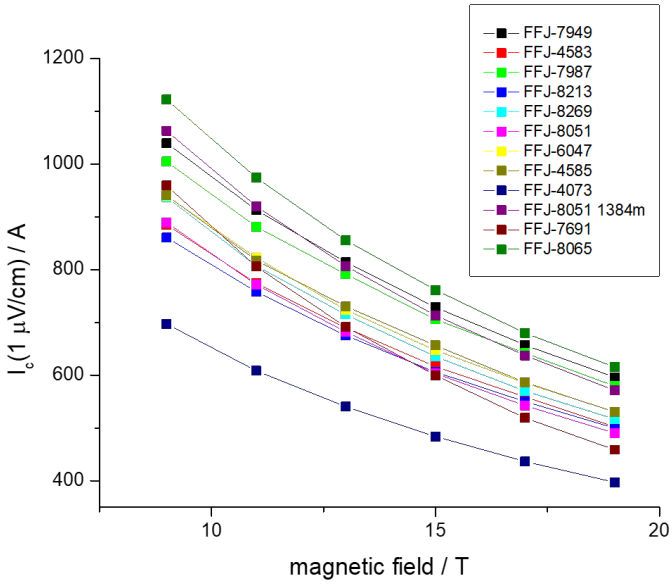


Figure 3.6: I_{c100} values measured at 20 K, magnetic field up to 20 T and parallel to the c-axis of the tape for 12 different HTS tape spools from FFJ.

3.1.1 Temperature, field and angle dependencies

To further validate the values adopted during the design phase and to achieve a more comprehensive characterization of the procured tape, a dedicated critical current measurement campaign was carried out at the University of Geneva. The measurements considered twelve 1 m long samples collected from twelve different spools of FFJ 12 mm HTS tape and two samples of 4 mm HTS tape from two different spool of the same producer. These measurements assessed the performance of the conductor under varying temperature, background magnetic field, and relative incident angle with respect to the c-axis. The tested samples were selected from different batches among the entire 15 km procurement, ensuring representative coverage of the supplied material. In particular, the adopted measurement procedure for the 12 mm samples consisted in mounting each sample on a sample holder, preliminarily testing it at 77 K in self-field to verify integrity, and then measured in field at 20 K with the magnetic field varied between 9 T and 19 T with the magnetic field being parallel to the c-axis of the tape. After the in-field measurements the sample was tested again at 77 K (self-field) to check for any degradation. If degradation was observed, the measurement sequence was repeated on a fresh sample from the same tape.

For 4 mm tapes the mounting and 77 K pre-test were performed as for the test of 12 mm samples, but in-field measurements were performed at both 4.2 K and 20 K: the applied field was stepped down from 19 T to the lowest value at which the sample could be measured without quench while remaining below the operational current limits, $\sim$ 2000 A at 4.2 K and $\sim$ 1000 A at 20 K. About the 4.2 K test with the field perpendicular to the c-axis

of the tape, I_c could be measured only at 19 T, due to the performances of the tape being higher of the maximum current of the power supply. Angular dependence measurements (4.2 K and 20 K) were carried out at four orientations: 90° (perpendicular to the tape ab-plane, parallel to the c-axis), 15°, 7.5° and 0° (parallel to the tape ab-plane, perpendicular to the c-axis) and each orientation required a separate holder and thus a fresh sample. Critical current was extracted according to two electric-field criteria (0.1 µV/cm and 1 µV/cm) on the longest voltage-tap span (20 mm), with additional analyses for the 10 mm span. Measurement results for 12 mm wide HTS tapes are represented in Fig. 3.6, where each sample was labeled as FFJ plus the serial number of the spool. As can be readily observed, the tape performances span a broad range, with a variation of approximately 300 A in the 15 - 19 T field region. Nevertheless, nearly all measured samples meet the specified minimum performance requirement of 500 A at 20 K in a background field of 15 T applied parallel to the c-axis of the tape. The only exception is the sample from the FFJ - 4073 spool, which exhibits an I_c value of 483 A under these conditions. However, considering that this corresponds to a relative deviation of less than 5 % from the acceptance threshold, and that the racetrack coils in the middle of the stack of ESMA yield a substantial operating margin, as showed in Fig. 2.21 , the tape from this spool could still be accepted.
An additional validation was performed to assess the expected lift factor for each spool. Specifically, the average I_c measured at 77 K, self-field, prior to the 20 K variable field tests was compared with the expected value provided by Tapestar data. Given the spatial resolution of approximately 2 mm for Tapestar measurements, a single expected critical current value was obtained by integrating the local electric fields along the 1 m tape length. Each 2 mm segment was assumed to carry the I_{c_i} value reported by the Tapestar, with the same applied current $I^\star$ along the entire sample. Under these assumptions, the total voltage developed during a hypothetical measurement can be expressed as

$$V = E_{th} \cdot l \cdot \sum_{i=1}^{N} \left(\frac{I^\star}{I_{c_i}} \right)^n \tag{3.1}$$

where E_{th} is the electrical field threshold given by the I_c measurement criterion adopted, l is the unit length that coincides with the spatial resolution of the Tapestar giving I_{c_i} for each piece, N is the total number of measurements available for each 1 m sample and V is the total voltage, which could also be written as $E_{th} \cdot 1 \cdot N$ when $I^\star$ coincides with the resulting critical current of the whole sample. The *n*-value was assumed to be the same throughout the sample. Given this the equation could be solved for $I^\star$, resulting in:

$$I^\star = \left(\frac{N}{\sum_{i=1}^{N} \left(\frac{1}{I_{c_i}} \right)^n} \right)^{(1/n)} \tag{3.2}$$

An example of a critical current equivalent value for one representative 1 m long sample Tapestar is represented in Fig. 3.7. The resulting values obtained for each of the twelve collected samples using Eq. 3.2 are graphed in Fig. 3.8 together with transport current measurements performed at University of Geneva before tests at 20 K and variable field

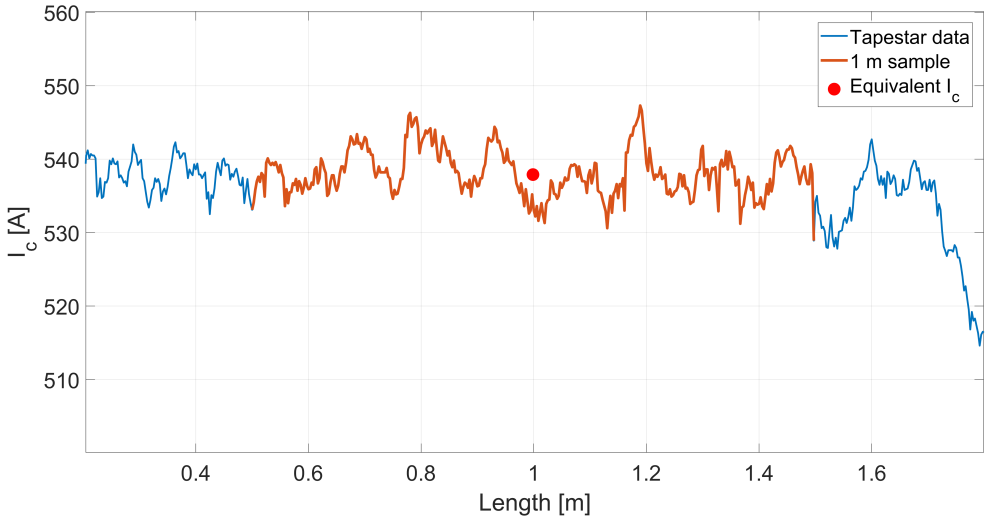


Figure 3.7: Equivalent estimated I_c value (red dot) of the 1 m long sample of FFJ 12 mm HTS tape collected from the spool FFJ-7987 and measured at the University of Geneva. Tapestar data are graphed in blue together with the highlighted section (orange) corresponding to the sample.

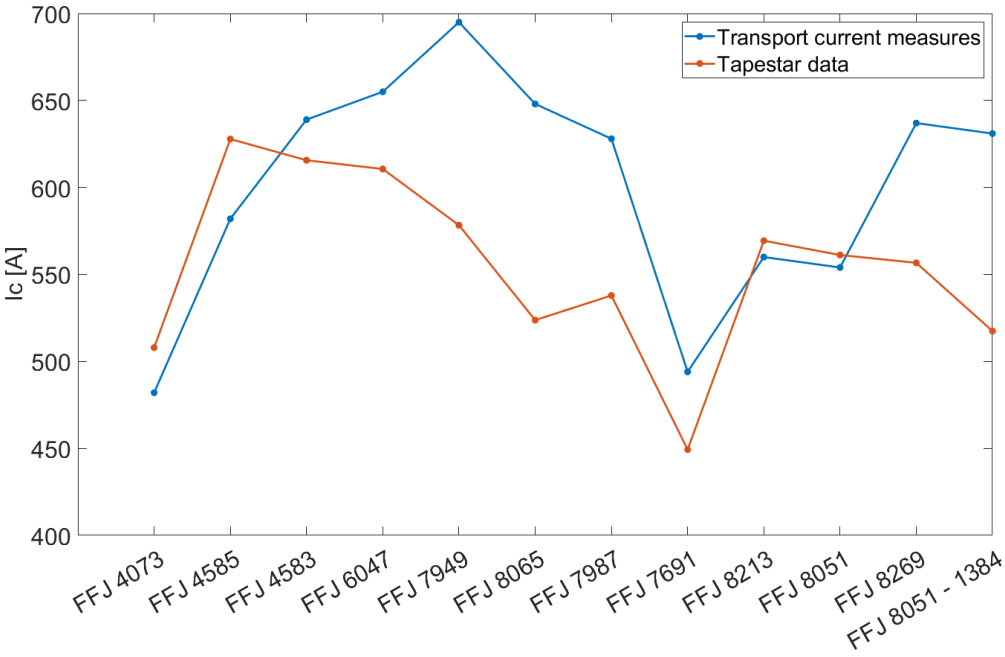


Figure 3.8: Transport current at 77 K self field (blue) and Tapestar (orange) measurement comparison for twelve samples collected from twelve different spools labeled on the x-axis.

Spool tag	Measured lift-factor	Tapestar estimated lift factor
FFJ 4073	1.00	0.95
FFJ 4585	1.06	0.98
FFJ 4583	1.03	1.07
FFJ 6047	0.99	1.06
FFJ 7949	1.05	1.26
FFJ 8065	1.18	1.45
FFJ 7987	1.12	1.31
FFJ 7691	1.21	1.34
FFJ 8213	1.08	1.06
FFJ 8051	1.09	1.07
FFJ 8269	1.00	1.14
FFJ 8051 - 1384	1.13	1.38
Average $\pm$ σ	**1.08 $\pm$ 0.07**	**1.17 $\pm$ 0.17**

Table 3.1: Lift factor from 77 K self field to 20 K, 15 T field parallel to c-axis

were carried out on the 12 mm samples. From these results, it can be observed that, although slight overestimations occasionally occur, the overall trend indicates that Tapestar data provide a conservative estimate of the expected performance of the HTS tapes. Given both data from measurements at 77 K self field and equivalent values estimated from tapestar data related to the 1 m samples collected, the lift factor could be estimated from measurements at 20 K, 15 T field parallel to c-axis reported in Fig. 3.6, resulting in values summarized in Tab. 3.1. With respect to the lift factor adopted during the electromagnetic design of ESMA, resulting from literature data described in [73] and equal to 1.25, both the average values obtained from transport current measurements and from Tapestar data yield slightly lower results. In particular, the lift factor derived from Tapestar data, for which this parameter is most commonly defined and applied, amounts to 1.17 ± 0.17, which lies within approximately one standard deviation of the design value. The lower lift factor obtained from transport current measurements can be attributed to the higher I_c values recorded at 77 K in self-field conditions using the transport method. This observation highlights that the method employed to determine the lift factor plays a crucial role in accurately predicting the expected performance of the tape under high-field, low-temperature operating conditions, and in avoiding both overestimation and underestimation of its capabilities. Angular-dependent measurements were performed on two samples of 4 mm-wide HTS tape from the FFJ batch, following the procedure described above. These measurements were conducted to expand the available dataset by providing critical current values at 4.2 K and 20 K for four different magnetic field orientations, with fields up to 19 T. Assuming that the critical current scales proportionally with tape width, these results will be integrated with data available in the literature to generate a more comprehensive dataset, thus supporting the design of superconducting magnets, including ESMA. The results obtained for the two samples are presented in Fig. 3.9 and Fig. 3.10. In each figure, the top-left and bottom-left panels display the measured critical current values, while the top-right and bottom-right panels show the

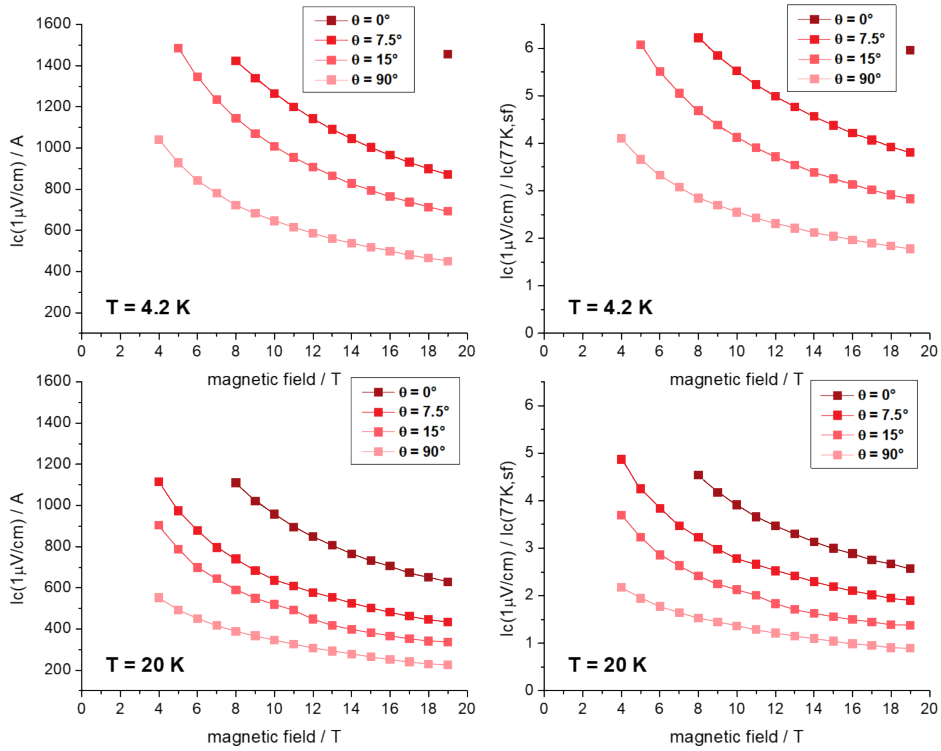


Figure 3.9: I_{c100} values measured at 4.2 K and 20 K, variable field at four different angles for a sample of 4 mm HTS tape from spool FFJ-3273. The vertical axis of the plots on the right side show the critical current normalized on transport current measurement performed at 77 K self field.

same data normalized to the critical current measured at 77 K in self-field conditions.

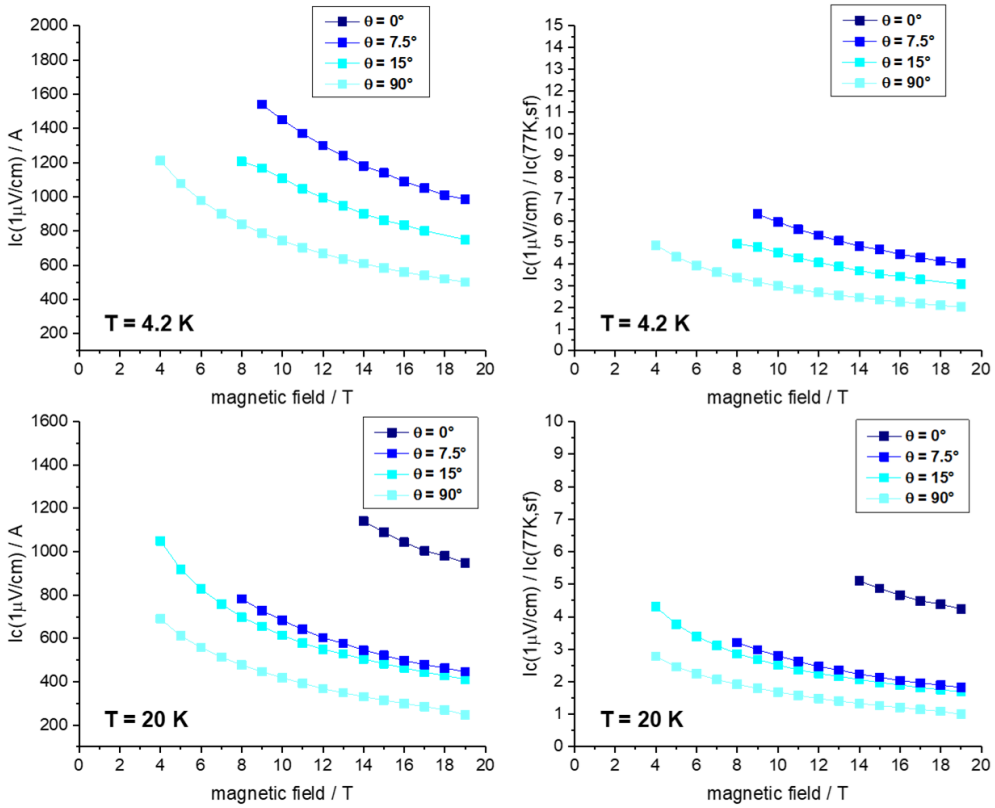


Figure 3.10: I_{c100} values measured at 4.2 K and 20 K, variable field at four different angles for a sample of 4 mm HTS tape from spool FFJ-3483. The vertical axis of the plots on the right side show the critical current normalized on transport current measurement performed at 77 K self field.

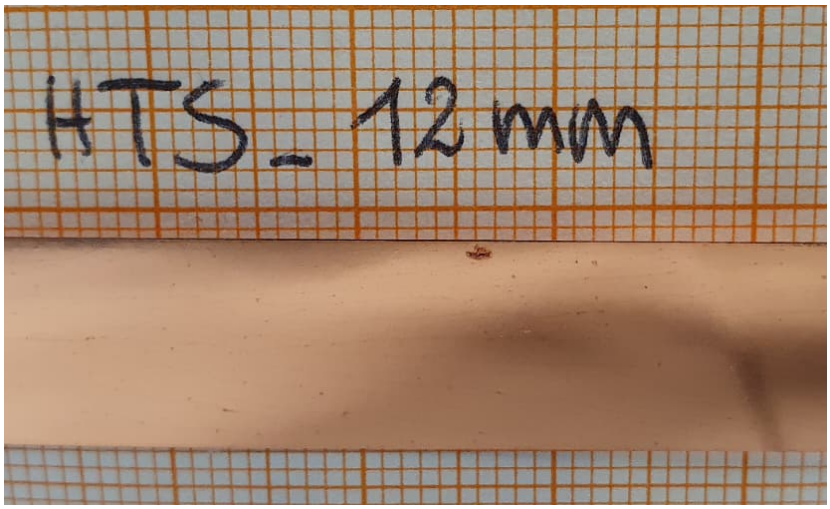


Figure 3.11: Example of a medium-large size inclusion found on FFJ 12 mm HTS tape

3.2 Superficial defects

Upon procurement of 15 km of HTS tape from FFJ, the quality assurance plan carried out at the LASA laboratory, started with I_c measurements at 77 K self-field and, in collaboration with the University of Geneva, at variable temperatures and background fields, also included a complete visual inspection of the entire procured tape length. To this purpose, each spool, containing one to four hundred meters of HTS tape, was fully unwound onto an empty spool of identical dimensions, and both sides of the tape were carefully visually inspected. This procedure led to the identification of superficial defects referred to as inclusions, appearing as small foreign bodies embedded on the tape surface and resulting in a localized increase in thickness. An example of such an inclusion is shown in Fig.3.11. Given this finding, an extensive experimental campaign was initiated to assess whether HTS tapes containing inclusions could still be used. The first step consisted in compiling a comprehensive collection of inclusions, which were then classified based on their overall thickness, measured using a micrometer with a sensitivity of 0.01 mm. Inclusions with a thickness below 30 µm were difficult to both detect and measure, as their superficial extension was significantly less pronounced than the other measured defects, and were therefore excluded from the statistical analysis. The resulting statistical distribution is shown in Fig.3.12, where the x-axis was shifted according to the smallest detectable defect size. To this end, a horizontal shift of 25 µm was introduced to ensure that all recorded inclusions, including those of 30 µm, were considered in the analysis while excluding potentially smaller defects that fall below the measurement sensitivity threshold. Due to the absence of experimental data no assumption could be made on the range of thicknesses between 0 and 20 µm. Consequently, the statistical analysis was conducted with reference to a threshold size of 25 µm, strictly above which a surface inclusion was effectively classified as a defect. The measurement

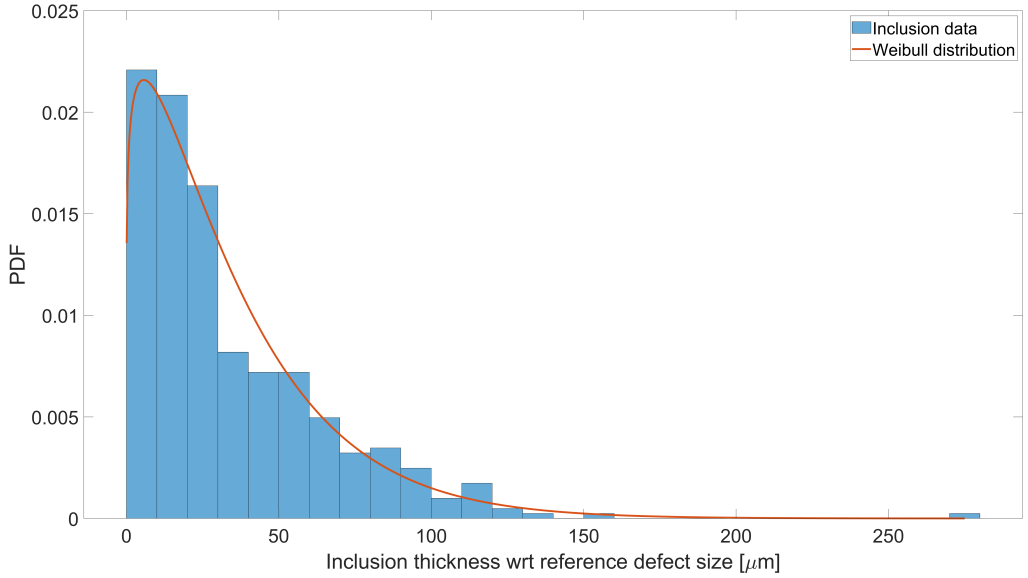


Figure 3.12: Probability distribution of the inclusion thicknesses on the HTS tape surface with a minimum inclusion size of 30 µm. In orange is graphed the fitted weibull probability distribution function.

campaign identified a total of 403 inclusions across 52 spools, out of the 64 inspected. Most inclusions were found on the superconducting side of the tape, typically near the edges, while only 20 were observed on the substrate side. The resulting statistics was fitted with a weibull probability distribution function, described by:

$$PDF(x) = \frac{k}{\lambda}\left(\frac{x}{\lambda}\right)^{(k-1)} \cdot e^{-(x/\lambda)^k} \quad for \quad x \geq 0 \tag{3.3}$$

where the scale parameter λ was found to be 36.13, indicating that 63.2 % of inclusions are expected to have a size below 61 μm. This value was obtained by adding the x-axis shift of 25 µm to the value of λ, the values resulting from the distribution should be interpreted as positive deviations with respect to the minimum established size of 25 µm. The shape parameter k was found to be 1.14. Since $k > 1$, the probability distribution suggests that the risk of encountering an inclusion whose size exceeds the reference one peaks around the mode and then decreases. This trend is consistent with expectations in tape production: many small inclusions and fewer large ones, since the tape manufacturing process is interrupted upon detecting large defects. The mode of the size deviation can be estimated as:

$$x_{mode} = \lambda\left(\frac{k-1}{k}\right)^{(1/k)} \tag{3.4}$$

which is equal to ~ 5.7 μm in the considered case, thus centering the peak on the recorded defects with the smallest thickness, i.e.: 30 µm. Instead the mean value of a weibull dis-

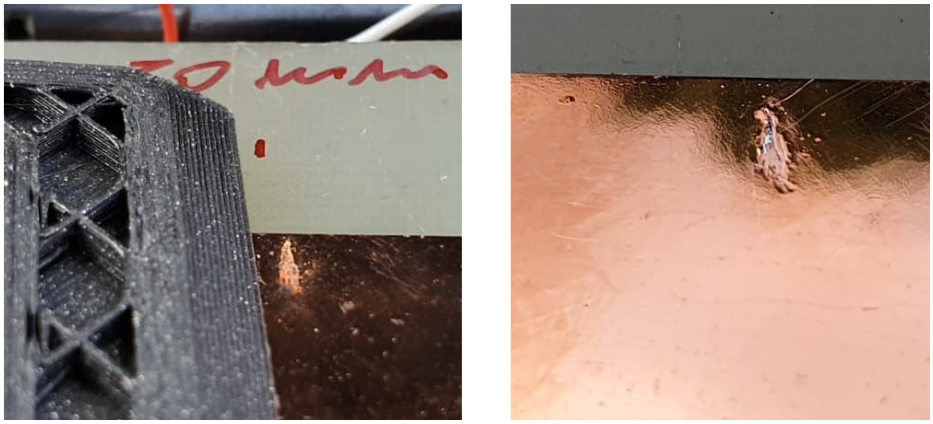


Figure 3.13: Removal process of the inclusion (left picture) and leftover imprint of the removed defect (right picture).

tribution may be evaluated as:

$$\mu = \lambda\Gamma\left(1 + \frac{1}{k}\right) \tag{3.5}$$

where Γ is referred to the gamma function evaluated for (1 + 1/k). In this case the mean size increment deviation amounts to $\sim$ 34.5 μm, mainly due to the long tail caused by the few large defect present.

Given the statistics on inclusion occurrences, and assuming that such defects are uniformly distributed across all batches of the procured tape, it is possible to estimate the probability of encountering a defect larger than the tape thickness itself in future procurements of comparable quality. The 64 spools examined correspond to a total tape length of approximately 21 km, resulting in an inclusion occurrence rate of one defect every 52 m, equivalent to an average of six inclusions per 300 m spool. Based on the reconstructed weibull distribution of surface inclusions classified as effective defects, the probability of finding an inclusion larger than the tape thickness (67 µm for the ESMA tape) was obtained by integrating the probability density function. The results indicate a 31% probability of encountering inclusions larger than 67 µm, decreasing to about 10% for inclusions exceeding 100 µm. This translates into an expected average of approximately two inclusions larger than 67 µm in a 300 m spool. Instead, for a procurement of 3 km of tape, the expected number of total defects rises to about 58, of which roughly 18 are expected to exceed 67 µm and 6 to exceed 100 µm.

Without an extensive study, the number of inclusions found would have implied rejecting the tape, which would result in discarding more than half of the entire procurement. In fact, if even a single inclusion was located near the middle of a spool, removing it by cutting the tape in two smaller batches would halve the usable length of that spool and could necessitate an additional internal splice. This would introduce another vulnerable spot and increase local heat generation during operation. However, cutting out the inclusion remains the most reliable solution in cases where the defect is located after few meters from the extremities of the spool. Regarding the nature of these inclusions, dis-



Figure 3.14: Inclusion leftover imprint showing REBCO layer (black spot).

cussions with the manufacturer (FFJ) led to the most widely accepted hypothesis that the defects originate from silver clumps sputtered during the deposition of the silver layer, and subsequently covered by the electroplated copper. This observation is consistent with the statistical distribution exhibiting a k-value greater than one, as sputtering failures tend to worsen over time, leading to an increasing number of small defects. When larger defects are eventually detected, the production process is typically interrupted. To further investigate the impact of inclusions on tape performance, two complementary approaches were adopted. The first focused on mechanically removing inclusions from the tape surface using a plastic spatula, while the second aimed at assessing the effect of inclusions when subjected to external pressure, as occurs in a magnet under operation or simply due to the radial stress induced by winding tension. In the first approach, inclusions were manually removed using a spatula 3D-printed in PLA, applying a gentle pressure directly onto the defect. This proved to be a direct method to completely remove the defect without leaving residuals. Any possible associated degradation, even in cases where the REBCO layer underneath the copper was exposed, will be discussed in the following paragraphs. A picture showing the removal process, together with the leftover imprint of the inclusion is reported in Fig. 3.13. As anticipated, upon removal, the resulting imprint of the inclusion sometimes revealed the underlying REBCO layer, as showed in 3.14. This effect may be due to a complete removal of the silver layer caused by the process itself, as well as by a delamination process induced by the removal of the defect. The purpose of this study was therefore to assess whether exposure of the tape to the atmosphere, in cases where superficial defects were removed, including instances where the REBCO layer was directly exposed, could lead to a reduction in the critical current of the samples. To this aim, five samples containing inclusions, together with a control sample without defects, were collected from a single spool and mounted on a dedicated sample holder, following the preparation procedure described in the previous section. The samples were labeled according to the convention SH24-*, with numbers from 1 to 6 identifying each sample. Within this scheme, SH24-6 corresponds to the control tape, i.e., the defect-free sample. In each case the samples

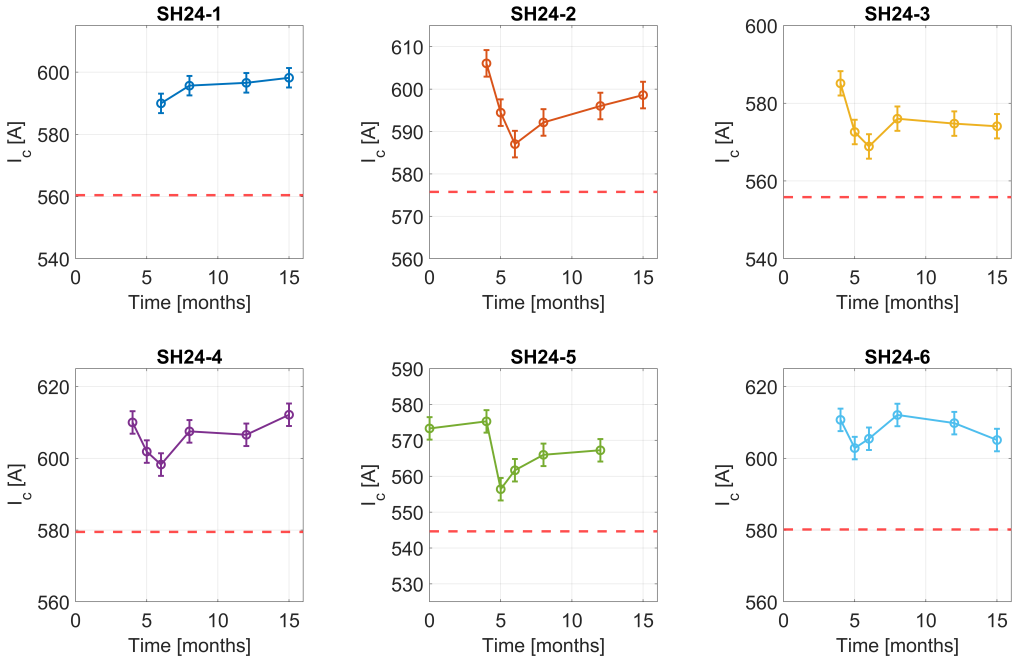


Figure 3.15: Critical current measurement results over time of the samples carrying a superficial defect. The defect was removed right after the first point for each case. The degradation threshold corresponding to the 95 % of the first measured I_c value is represented by the dashed red line.

were first tested to measure their I_c, after which the defect was removed. Upon removal, all samples were tested again to assess a possible degradation related to the removal process. The removal procedure caused the exposition of the REBCO layer in samples SH21-1 and SH24-2. Following each measurement, the samples were allowed to naturally warm up and were then stored in ambient atmosphere without humidity or temperature control. After the first I_c measurement, the data collected from the unperturbed sample containing a defect were subjected to a z-test against the nominal distribution shown in Fig.3.4, in order to verify whether the mere presence of the defect could affect the tape performance. The results confirmed that the dataset is statistically consistent with the reference distribution given a p value of $p \sim 0.15$, providing evidence that the defect alone does not degrade the conductor. About the p-value, the same consideration described in the previous section for the statistic concerning I_c measures applies. Measures have been repeated for over a year and results are reported in Fig. 3.15. The figure reports the critical current measurement results for each of the samples carrying a superficial defect, including the control sample SH24-6. For each case, the defect was removed immediately after the first measurement point. Samples were tested again soon after the removal processes, resulting into a measurement data superimposable with the first point represented, related with the sample still carrying the defect, thus stating that

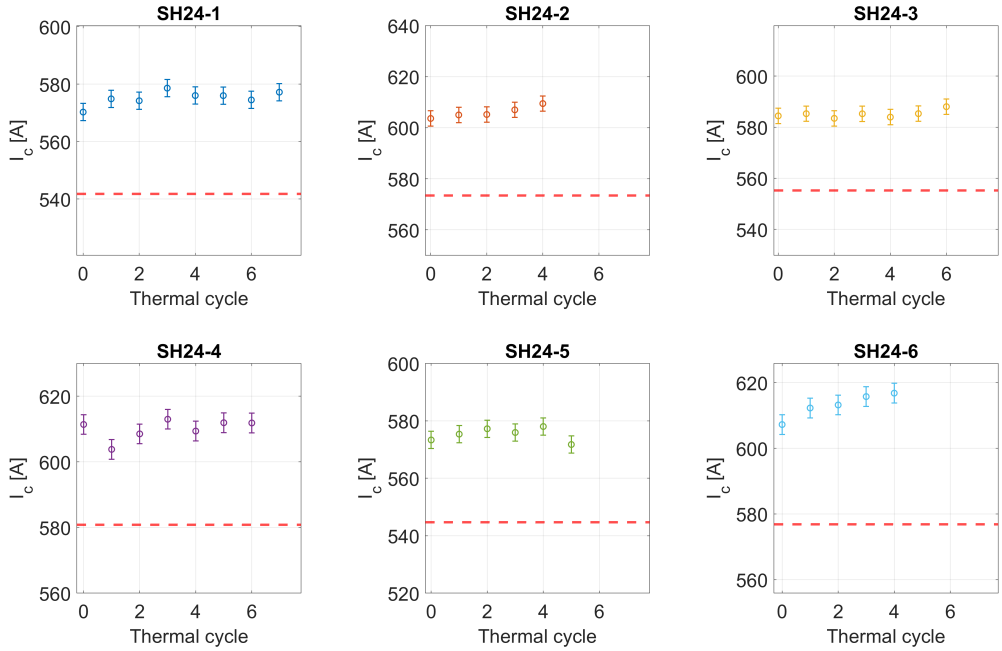


Figure 3.16: Critical current measurement results over multiple thermal cycles of the samples where the superficial defect was removed. The degradation threshold corresponding to the 95 % of the first measured I_c value is represented by the dashed red line.

the removal process itself does not introduce any variation. The degradation threshold, corresponding to 95 % of the initial I_c value, is indicated by the dashed red line. The error bars ± 3 A represent the statistical uncertainty derived from repeated measurements performed within the same day using the setup described in the previous section. In the plots, month zero corresponds to June 2024, when the defects were first identified. A slight but systematic drop in I_c between months 5 and 6 can be observed for all samples, followed by a gradual recovery in subsequent months. This behavior may be attributed either to variations in atmospheric conditions or to changes in the positioning of the measurement setup within the laboratory. Since the dynamic is also observed within the control sample it is to be excluded that is something related to the presence of defects. In addition, a thermal cycling test in LN_2 was carried out. The samples were repeatedly cooled down, measured, warmed to ambient temperature using a heat gun, and tested again. The results, shown in Fig.3.16, revealed no significant deviations. Overall, the measurements remain stable, consistently above the degradation threshold, and in agreement with the behavior of the defect-free control sample SH24-6. These results support the conclusion that I_c performance is not significantly affected when such defects are removed. The only remaining concern arises in scenarios requiring the application of a superficial coating on areas where the REBCO layer is exposed. In such cases, the impact of the coating and its possible reaction with the REBCO must be care-

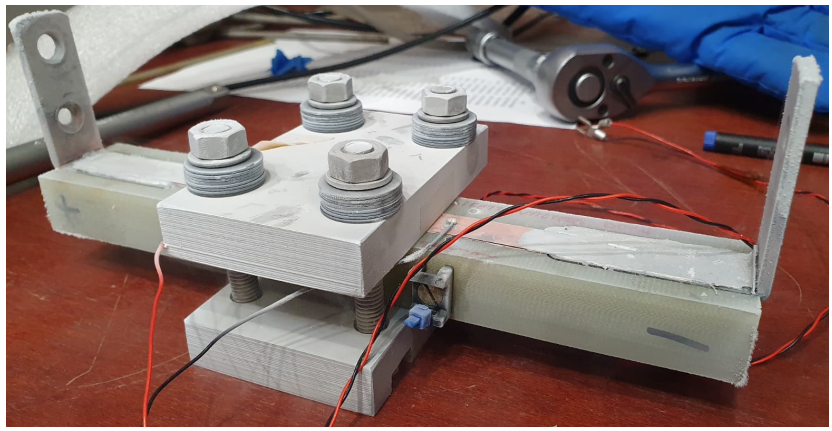


Figure 3.17: Measurement set up for testing defects under external pressure.

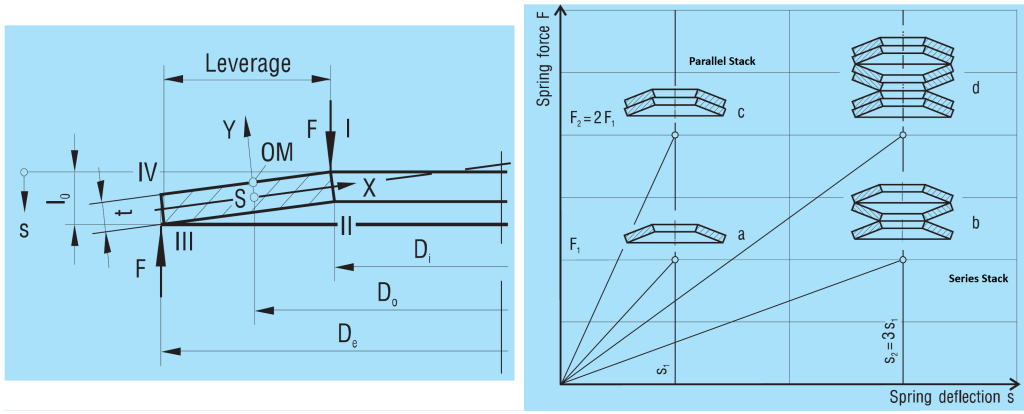


Figure 3.18: Scheme of the geometrical parameters referred to a disc spring (left) and possible arrangements for multiple disc springs (right). (adapted from [76]).

fully assessed. On the other hand another possibility consists in leaving the defects on the tape. As anticipated, a test under external pressure was performed considering two HTS tapes facing each other on the superconducting side and mounted on the sample holder following the above-described procedure. The external pressure has been provided by two 15 mm thick steel plates placed above and under the sample holder and connected with four M8 screws, as pictured in Fig.3.17. To avoid stress concentrations on the tape caused by the edges of the top steel plate, the edges were rounded using a belt sander. The compressive force has been given by tightening a specified set of bellevilles designed to provide a certain amount of force. The procured disc springs characteristics are summarized in Tab.3.5 and the force given by compressing a disc spring, neglecting friction, was calculated using the following equation [76]:

$$F = \frac{4E}{1-\mu^2}\frac{t^4}{K_1 D_e^2}\frac{s}{t}\left[\left(\frac{l_0-t}{t}-\frac{s}{t}\right)\left(\frac{l_0-t}{t}-\frac{s}{2t}\right)+1\right] \tag{3.6}$$

Disc springs properties		
Quantity	**unit**	**value**
D_e	mm	20
D_i	mm	8.2
l_0	mm	1.4
t	mm	0.8
E	GPa	206
μ	N/A	0.3

Table 3.2: Geometrical parameters and material properties of the adopted set of disc springs

where E is the Young's modulus of the belleville material and μ its Poisson ratio, which for the considered case were taken equal to 206 GPa and 0.3 respectively. All dimensional parameters expressed in the equation are labeled in Fig.3.18, together with a scheme representing a series and a parallel of such springs. The parameter s corresponds to the deformation of the spring. The parameter K_1 instead equals to:

$$K_1 = \frac{1}{\pi} \frac{\left(\frac{\delta-1}{\delta}\right)^2}{\frac{\delta+1}{\delta-1} - \frac{2}{ln(\delta)}} \tag{3.7}$$

and where δ corresponds to the ratio between the external and internal diameters. When combining multiple springs, as illustrated in Fig.3.18, both the resulting force and the overall deflection are affected. In particular, for a parallel stack of n springs, the maximum deflection remains the same as that of a single spring, while the force increases linearly with the number of springs:

$$F_{res} = n \cdot F \tag{3.8}$$

Instead for a series stack of i springs the force remains the same while the deflection will increase with the number of springs as:

$$s_{res} = i \cdot s \tag{3.9}$$

When performing a combined stack of n parallel and i series both the variation will apply.
In this study, a total of seven samples with defects and five defect-free samples were investigated. In both cases, the samples were mounted on the sample holder, compressed using the press equipped with disc springs, and submerged in LN_2 for critical current measurements. After each measurement, the setup was warmed back to room temperature, the spring configuration was adjusted to increase the applied pressure, and a new I_c measurement was performed. To ensure that the applied force could be quantified, the compression of the springs was calculated from the screw displacement, based on the pitch of the M8 screw thread (1.25 mm per full turn). All spring combinations and screw turns used in the campaign, together with the corresponding pressures applied to the tape contact area of 55×12 mm^2 with the steel plate, are summarized in Tab.3.3.

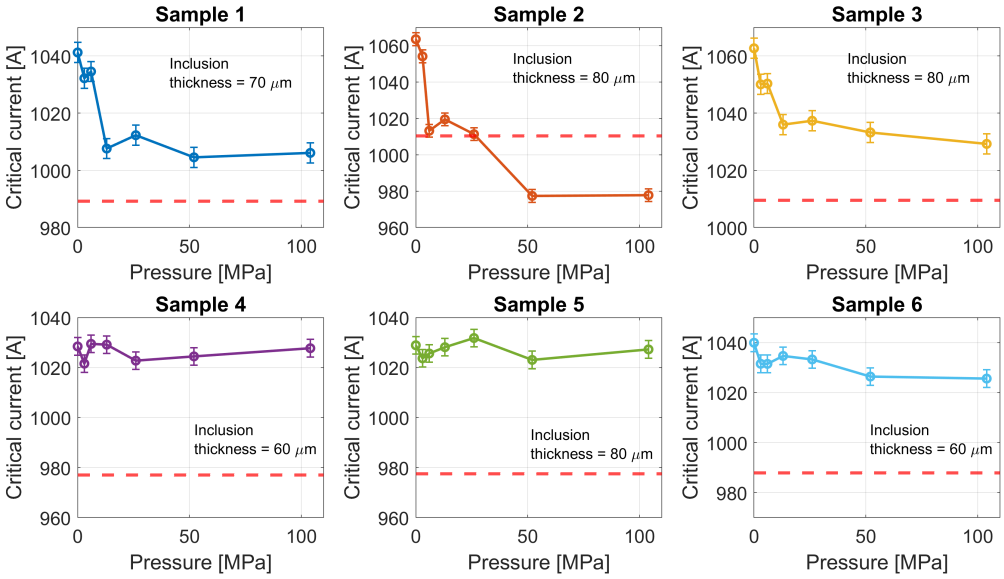


Figure 3.19: Critical current measurement results of the samples carrying a superficial defect while subjected to the external compressive load reported on the x-axis. The degradation threshold corresponding to the 95 % of the first measured I_c value is represented by the dashed red line.

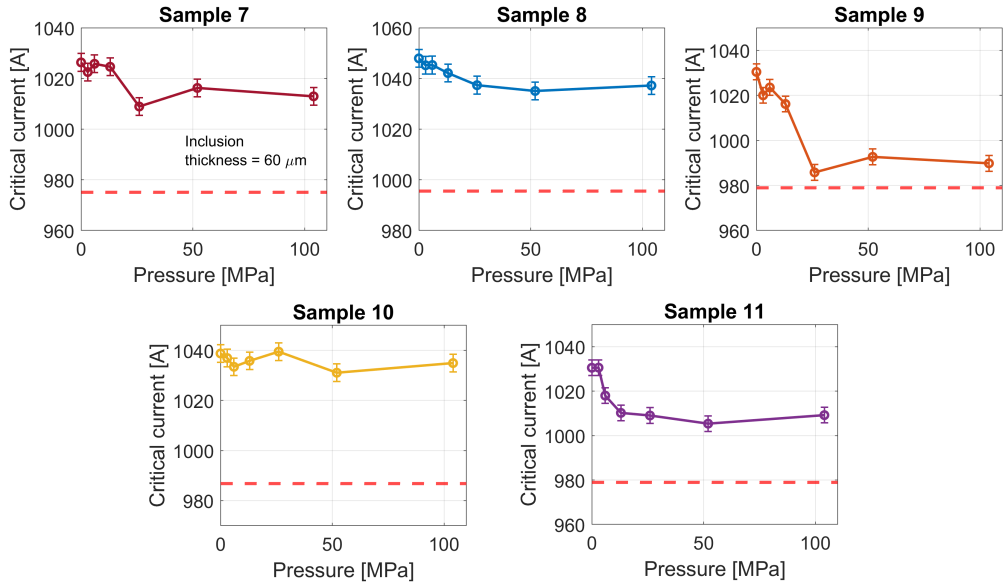


Figure 3.20: Critical current measurement results of a sample carrying a superficial defect and defect-free samples while subjected to the external compressive load reported on the x-axis. The degradation threshold corresponding to the 95 % of the first measured I_c value is represented by the dashed red line.

Spring in series	Sprigs in parallel	M8 screw turn fraction	Pressure [MPa]
2	1	1/2	3
2	2	1/2	6
2	4	1/2	13
1	8	1/4	26
1	16	1/4	52
1	32	1/4	104

Table 3.3: Summary of the adopted combinations of disc springs and the correspondent turn fraction given to all the screws together with the resulting estimated pressure.

Sample	Defect size [μm]	Defect size after test [μm]
1	70	30
2	80	50
3	80	40
4	60	30
5	80	50
6	60	40
7	60	40

Table 3.4: Summary of inclusion sizes on HTS tapes tested under external compressive load.

For each sample containing an inclusion, the defect thickness was measured in order to investigate a possible correlation with I_c degradation. The measured thicknesses values are summarized in Tab.3.4. Measurement results are graphed in Fig.3.19 and Fig. 3.20, where the defect thickness is labeled on the correspondent plot. Graphs without label are referred to tests performed on defect-free samples. From the measured results, it can be observed that nearly all samples carrying an inclusion tolerated the applied external pressure without significant degradation. Furthermore, the presence of such defects did not induce any measurable damage in the opposing tape facing the defect. Minor oscillations with a slight decreasing trend were observed in both types of measurements, suggesting that the manual setup, specifically the method of applying the external load by tightening screws, is limited by the screws themselves, which prevent a gradual and uniform application of pressure. This could explain the different behavior observed in both Sample 2 (containing a defect) and Sample 9 (defect-free), which exhibited a larger degradation in performance compared with the other tested samples. Overall, even under these test conditions, the tapes did not suffer major damage. It is also important to note the condition of the samples before and after testing, as shown in Fig. 3.21 and Fig.3.22, respectively. After measurement and application of the external load, the tape carrying the defect indented the opposing tape, as showed in Fig. 3.23, but without causing noticeable degradation in performance. This process also resulted in a partial flattening of the defect, whose effective thickness was reduced as reported in Tab.3.4. Moreover, an additional estimation was carried out using Fujifilm Prescale [77], a pressure-sensitive film, with the purpose of identifying the area effectively sub-



Figure 3.21: Superficial defect on HTS tape before applying the compressive load and measuring the critical current.



Figure 3.22: Superficial defect on HTS tape after applying the compressive load and measuring the critical current.

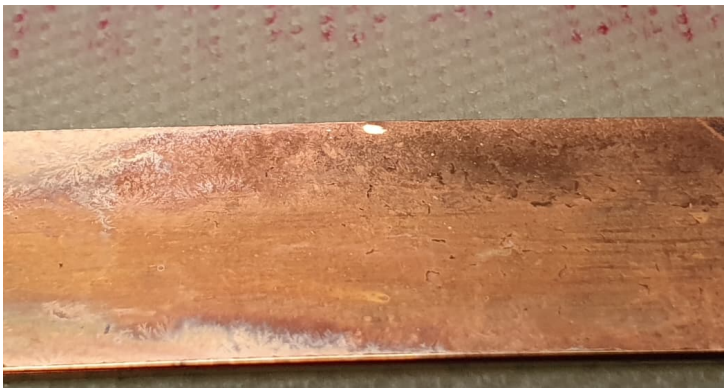


Figure 3.23: HTS tape pair mounted on sample holder after applying the compressive load and measuring the critical current. The indent caused on the defect-free sample by the defect itself can be observed.

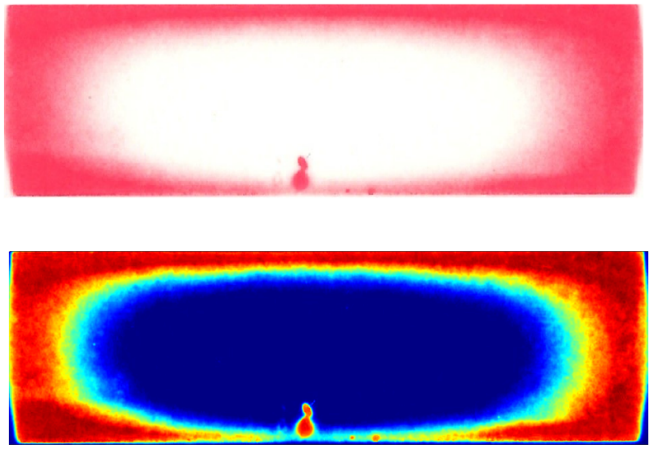


Figure 3.24: The top picture represents the Fujifilm Prescale paper after being impressed by the HTS tape subjected by a compressive load, whereas the bottom picture shows its digitalized version. In both images, the regions colored in magenta (top) and red (bottom) represent the areas where pressure was effectively applied and exceeded the threshold of the pressure-sensitive film, contrarily to the white (top) and blue (bottom) regions. The defect is clearly visible at the center of the lower half of the tape and is highlighted by the high pressure induced by its extra thickness.

jected to compressive load. The test was performed with Fujifilm Prescale MW film, which changes color under pressures ranging from 10 to 50 MPa. The film was placed above the pair of HTS tapes before applying a compressive load of 10 MPa and was then subsequently scanned and digitized to evaluate the effective contact area. A threshold criterion based on the mean signal intensity was adopted to discriminate whether a pixel should be considered as contact or not. Fig. 3.24 shows both the Fujifilm Prescale sheet

after testing and its digitized version. The resulting contact area was estimated to be 44 %, effectively doubling the applied pressure on the samples. From the imprint left on the Fujifilm sensitive sheet, another concern emerged: in addition to the mark of the defect, the edges of the tape were also found to be in contact with the steel plates, while the central region showed limited contact. This observation suggests that, despite continuous improvements in HTS tape manufacturing, a dog-bone effect is still present. This aspect will be further discussed in Sec. 4.2.2. The analysis of these defects indicates that leaving them on the tapes does not compromise conductor performance, even under nominal compressive stress levels of up to $\sim$ 100 MPa applied over the entire area, as evidenced by the agreement with experimental data from defect-free samples. Unlike the removal option, which risks exposing the underlying REBCO layer, keeping the inclusion avoids direct exposure. However, the extra thickness introduced by superficial defects may lead to unwanted consequences during magnet winding, for example, insulation breakdown in the case of insulated cables, or localized low-resistance contacts in NI or MI windings, potentially resulting in radial current concentration and magnet damage. Moreover, magnet operation and cycling could induce additional degradation associated with the presence of a localized defect. Therefore, unless the cable preparation involves a superficial coating or soldering process where the defect would be embedded (and where exposed REBCO could undergo contamination), defect removal remains the preferred option for conventional insulated cables or NI and MI dry-wound magnets.

3.3 Internal splices

As previously discussed and confirmed at procurement, REBCO tapes are delivered in continuous pieces typically reaching lengths of 200 - 300 m. This intrinsically limits the maximum tape length available for winding a coil without internal splicing. Splices are known to be the weakest points in a coil, as they introduce additional resistive heat generation, thus may leading to a reduction in current carrying capacity. Although small NI coils can naturally self-protect against splice-related risks through current bypassing, larger coils, especially conduction-cooled or partially insulated ones, exhibit a reduced self-protecting capability. Consequently, splice performance becomes a critical design factor. The challenge is further compounded in large-scale magnets, which often rely on a multi-tape cable and co-winding. For ESMA, the final electromagnetic design foresees 12 racetrack coils, each requiring 516 m of single tape. This makes at least one resistive splice unavoidable per coil. To address this, a dedicated study was conducted to investigate different joint layouts for double tape HTS cables, representative of the ESMA configuration, through dedicated electrical experiments. Resistive splices were fabricated using a copper press capable of applying controlled pressure and temperature. The press, sketched in Fig. 3.25, consists of two copper components: a bottom piece with a 12.5 mm wide, 3 mm deep groove, and a complementary top piece featuring a 4 mm protruding part. This thickness mismatch ensures that the flat surface of the top piece does not directly contact the bottom one, thus allowing for variable pressure distribution and compensating for misalignments when tapes are inserted. Pressure is applied over an active area of 12×50 mm^2 through four M6 screws combined with disc

Disc springs properties		
Quantity	**unit**	**value**
D_e	mm	12
D_i	mm	6.2
l_0	mm	0.95
t	mm	0.6
E	GPa	206
μ	N/A	0.3

Table 3.5: Geometrical parameters and material properties of the adopted set of disc springs

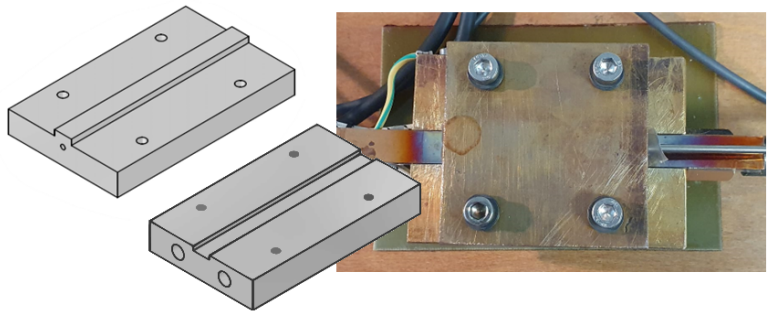


Figure 3.25: Temperature and pressure controlled tool to perform resistive splices on HTS tapes.

springs, covering a range between 17 kPa and 1.5 MPa. The equivalent applied force was calculated using Eq.3.6, based on spring properties summarized in Tab. 3.5, and cross-checked with load-cell measurements. The contact quality between the two copper pieces was further characterized using Fujifilm Prescale LLW sheets (sensitivity range: 0.6–1.5 MPa). The resulting imprints are shown in Fig. 3.26. The press was closed by tightening the screws in a cross pattern. However, as illustrated in the top image of Fig. 3.26, the manual procedure led to non-uniform pressure profiles. A more homogeneous distribution was achieved after compensating the tightening procedure by screwing for an additional quarter of turn the disc springs on the side where pressure was verified to be lower (bottom image of Fig. 3.26), though this remains a key source of uncertainty in the process. Temperature is provided by two 100 W resistive heaters controlled with a PID circuit connected to a thermometer inserted into a dedicated hole reaching the center of the bottom part of the tool. A temperature probe is placed on the top part to check that entire assembly is above the melting point of the brazing alloy. Different types of junctions were fabricated using the above-described manufacturing tool. The joints were carefully oriented to preserve the designed configuration, with the superconducting layers of the two HTS tapes always facing each other. This resulted in three junction geometries, illustrated in Fig. 3.27, starting from the top: a flat junction, a lap junction, and a bridge junction. In the sketch, the superconducting REBCO layer is shown in red, the tape in orange, and the brazing alloy in gray.
The flat junction is realized by placing the continuous tape beneath the interrupted one,

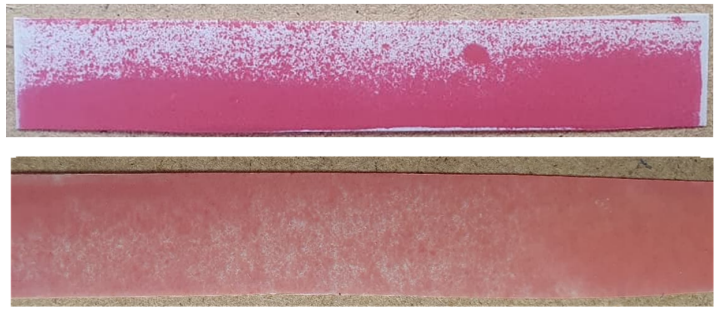


Figure 3.26: Fujifilm Prescale LLW sheet pressure profile of the splicing tool. The top image shows a non-uniform profile caused by uneven screw tightening. The bottom image displays the improved, more homogeneous pressure distribution achieved after compensating the tightening procedure.

Brazing Alloy	Set Point ($°C$)	Flux
SnIn (48% Sn 52% In)	140	Kiwa S-65
SnPb (40% Sn 60% Pb)	195	Self low-residual
SnAg (96% Sn 4% Ag)	230	Mob-39

Table 3.6: Tested brazing alloys, together with the temperature set on the manufacturing tool and the corresponding flux.

which acts as a support. This geometry ensures that there is no extra thickness in the joint region but reduces the effective critical current by 50 %, as only the bottom tape carries current across the junction. In contrast, the lap and bridge junctions, adapted from classical designs found in the literature, [78], [79], to suit the double-tape configuration, preserve the current continuity in both tapes, thus theoretically maintaining the tapes performances, at the cost of additional thickness in the splice region. In addition, it is important to notice that the lap joint was oriented such that the substrate side of one HTS tape is facing the superconducting side of the other to maintain the correct orientation of the superconducting faces of the cable, thus performing the splice on the interrupted tape on the side with the highest resistivity. This constraint does not apply to the bridge junction, where all superconducting faces can be aligned directly. Finally, to ensure a coherent comparison, the bottom tape used in the flat junction was also included in the lap and bridge junctions study. The resistive splices were initially realized by manually pre-tinning the surfaces of the HTS tapes. Several brazing alloys were investigated, each combined with a dedicated flux, and for each alloy a specific temperature set point was defined on the manufacturing tool. The details of the alloys and their processing parameters are summarized in Tab. 3.6. In particular, all bridge and flat junctions were fabricated using SnIn, whereas the lap junctions were manufactured with all three alloys reported in the table. Once manufactured, the joints were mounted on the G10 samples holders, with the tape extremities brazed to copper current leads, following the procedure used for I_c measurements. The assemblies were then tested in

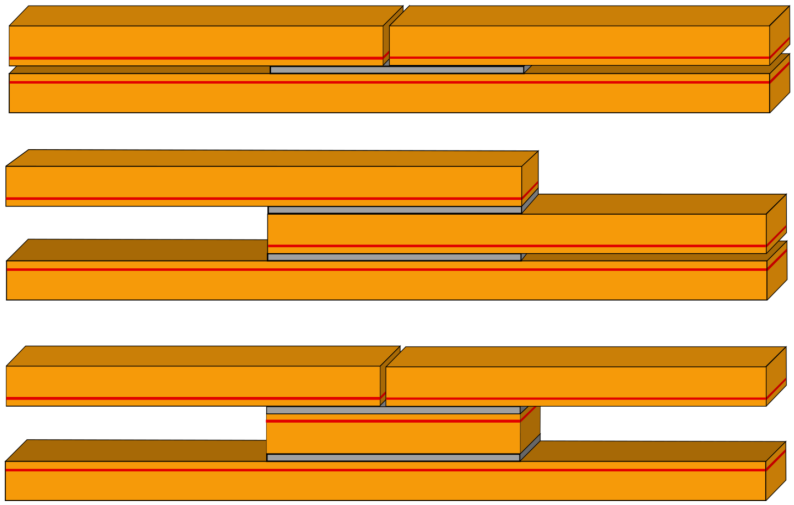


Figure 3.27: Schematic representation of the manufactured resistive joints, starting from the top the joints are referred to as: flat, lap and bridge. The orange block stands for the superconducting HTS tape, the red line represents the position of the REBCO layer and the gray part is the brazing alloy.

LN_2 under linear current ramps, and in selected cases, the samples were powered up to electrical breakdown. An example of a manufactured bridge joint is shown in Fig. 3.28. For inspection and visualization purposes, the joint was deliberately opened after testing to expose the internal region and verify the correct orientation of the tapes. The black layer, corresponding to the REBCO film, was used as a reference. Since the tape exhibits low resistance to peeling stress, delamination of the superconducting layer can easily occur in soldered samples when the brazing is properly executed. Alternatively, if an issue occurs during the brazing process, the joint tends to peel off instead of delaminating the HTS tape. A similar inspection was carried out on lap joints, as shown in Fig. 3.29, where both an intact joint and the corresponding deliberately opened joint are reported. Each junction was made with the same HTS tape from the supply for the ESMA magnet. Specifically, the tape used for the junctions was taken from the same reel as for the I_c measurement and inclusions inspection campaigns. A total of four flat junctions have been successfully tested. A sample is represented in the top picture of Fig.3.30, whereas a representative measurement is reported in Fig.3.31. For these measurements, the baseline was fitted with a straight line to derive the resistance from its slope. The baseline was then subtracted from the data to measure Ic using the Ic_{100} criterion. Following this procedure, an average value of (583 ± 34) A with an n-value of (31 ± 3) was found. These data are statistically compatible with the reference data probability density function showed in Fig.3.4, resulting in a positive z-test on the reference values with a p-value of ~ 0.15. The average values for the resistive baseline yielded the following result, $(0.101 \pm 0.046)\ \mu\Omega \cdot cm^2$. Another detail that emerged from breakdown measurements is that the breakdown position for the flat junctions always occurs in the



Figure 3.28: Manufactured bridge joint on a double tape HTS cable

middle of the tape, where the top tape is interrupted, as it can be observed in the bottom part of Fig. 3.30. Indeed, this is the only point where the entire current flows through the bottom tape, therefore making it the most vulnerable one. For these types of junctions, the average breakdown value was found to be (609 ± 47) A. The associated error results from the standard deviation across the different sample measurements. The same applies to the results that are yet to be described.

The experimental data from lap and bridge junctions exhibited a peculiar voltage - current behavior, as shown in Fig.3.32 and Fig.3.33. To capture this response, dedicated lumped-element electrical models were developed. The models are schematized in Fig.3.34: the top circuit corresponds to the lap joint, while the bottom represents the bridge joint. In both cases, R_{add} accounts for the resistance between the current adductors and the tape pair, as well as the inter-tape resistance within the junction. The parameter R_{sc} represents the non-linear superconductor resistance described by the power law (Eq. 1.9): specifically, R_{sc1} refers to the interrupted tape, R_{sc2} to the continuous tape, and in the bridge model R_{sc3} to the bridging tape. R_c models the contact resistance between the top and bottom tapes, since the joint area is fully soldered. Finally, R_j indicates the intrinsic resistance of the joint. The model parameters were defined as follows: R_{add} was experimentally determined from previous I_c measurements and set to 1.5 $\mu\Omega$, while R_c was extracted from the initial linear slope of the measurements prior to the elbow. This baseline corresponds to current redistribution from the top to the bottom tape while the latter remains superconducting, with current bypassing the resistive element R_j. When the I_c of the bottom tape is reached, the curve displays an elbow followed by a steeper slope, from which the I_c of the bottom tape can be extracted. R_{sc3} was assumed to reflect the mean performance of the spool, i.e. $I_c \sim 590$ A. Model fitting was then performed with the I_c of the interrupted tape, the n-value, and R_j as free parameters. The calculated voltages (orange curves in Fig. 3.32 and Fig.3.33) showed good agreement with the experimental data (blue curves). In total, sixteen lap joint samples were manufactured and tested, varying both applied pressure and brazing alloy. Nine were tested up to breakdown, yielding an average breakdown current of (1010 ± 70) A. Among these, five datasets were successfully fitted to the model, resulting in an average interrupted-tape



Figure 3.29: Manufactured lap joint on a double tape HTS cable. The top picture represents the intact joint, while the bottom picture reports the joint where the top tape was removed.

(260 ± 50) A together with a n-value of (20 ± 5) while the specific resistance of the joint Rj has been found to be (10 ± 5) $\mu\Omega \cdot cm^2$. For bridge joints, eight samples were tested, with four taken to breakdown. The average rupture current was (1060 ± 50) A. Out of these measurements, one sample could be reliably fitted to the model, giving a critical current of 370 A, a n-value of 28, and Rj of 0.912 $\mu\Omega \cdot cm^2$. In both lap and bridge cases, breakdown consistently occurred immediately before or after the joint, confirming the mechanical robustness of the brazed section, as it can be observed from Fig.3.35 showing the rupture point of a bridge joint. However, not all datasets could be described by the models, mainly due to the marked reduction of I_c in the interrupted tape. Unlike flat resistive joints, both lap and bridge geometries suffered significant degradation of the top tape during manufacturing. This behavior may be attributed to the extra tape thickness in these geometries, which likely introduces a higher mechanical stress. The issue is further emphasized by the large variability of the specific resistance values, which remain one order of magnitude higher than the 0.1 $\mu\Omega \cdot cm^2$ typically reported in the literature [80] for joints with where REBCO layers are faced to each other. To obtain a preliminary confirmation of the information deduced from the model, a classical single lap joint has been performed with the same manufacturing procedure resulting in a measured I_c of 327 A, with respect to an average expected performance at 77 K self field of 590 A, a n-value of 25 and a joint specific resistance of 6 $\mu\Omega \cdot cm^2$. This both supports the model results and on the other hand determines once again the necessity of revising the procedure due to the criticality of the extra-tape thickness which could cause the degradation of the tape performances. Finally, no systematic influence was observed from either the applied pressure or the choice of brazing alloy during joint manufacture. The results disclosed up to now, summarized in [81], led to the necessity

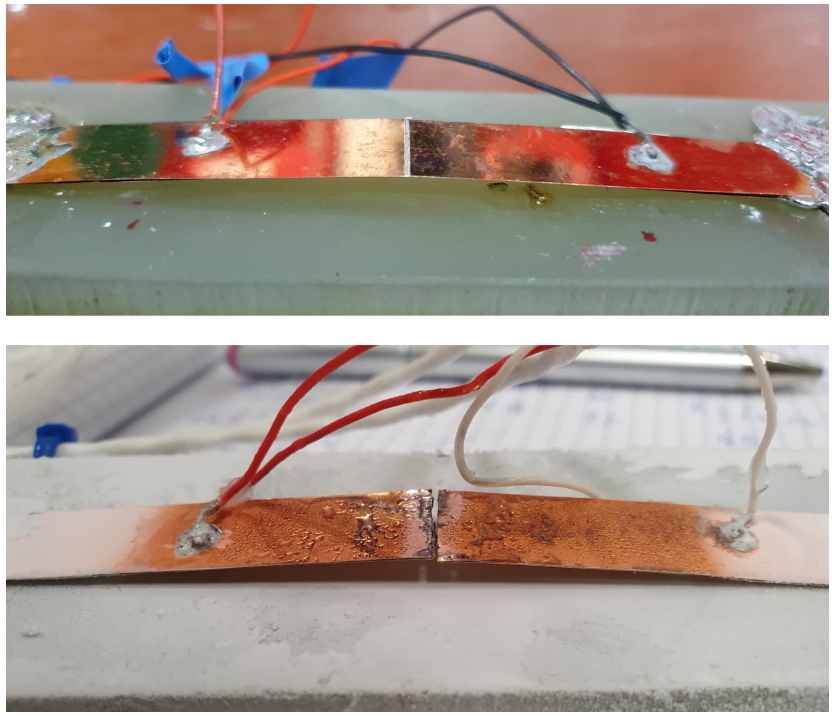


Figure 3.30: Manufactured flat joint on a double tape HTS cable. The top picture represents the intact joint, while the bottom picture reports the joint after a breakdown induced by overcurrent.

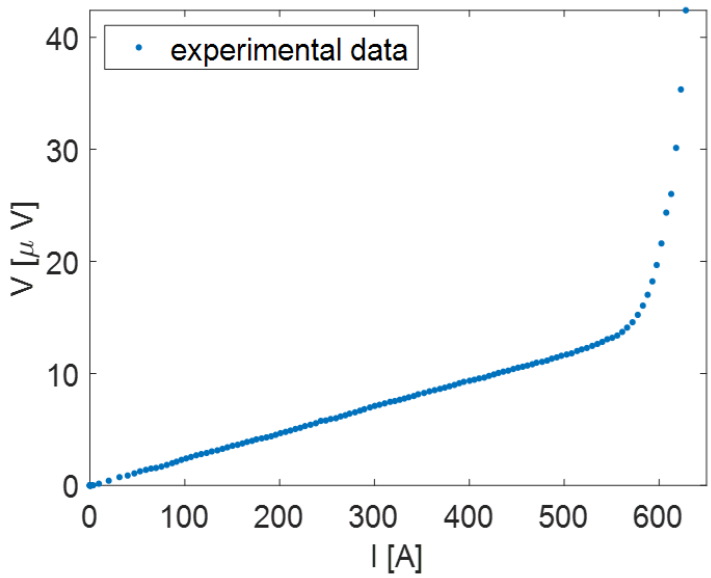


Figure 3.31: Experimental data of critical current measurement on a flat junction. On the y-axis the voltage across the junction is reported in μV while on the x-axis there is the current coming from the power supply in A

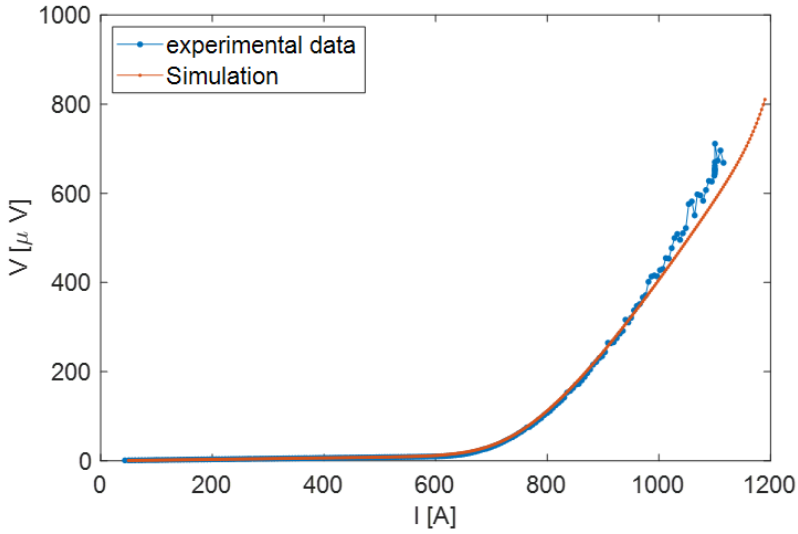


Figure 3.32: Experimental data (blue) and simulated data (orange) of critical current measurement on a lap junction. On the y-axis the voltage across the junction is reported in μV while on the x-axis there is the current coming from the power supply in A.

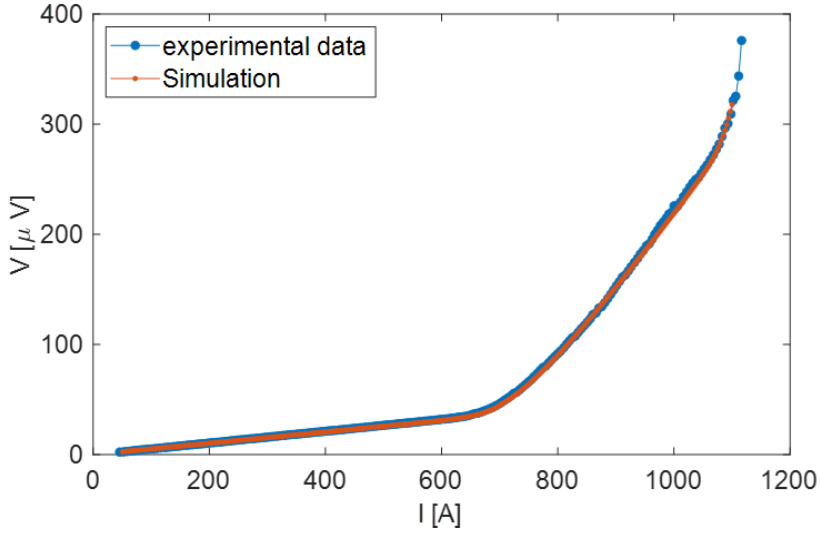


Figure 3.33: Experimental data (blue) and simulated data (orange) of critical current measurement on a bridge junction. On the y-axis the voltage across the junction is reported in μV while on the x-axis there is the current coming from the power supply in A.

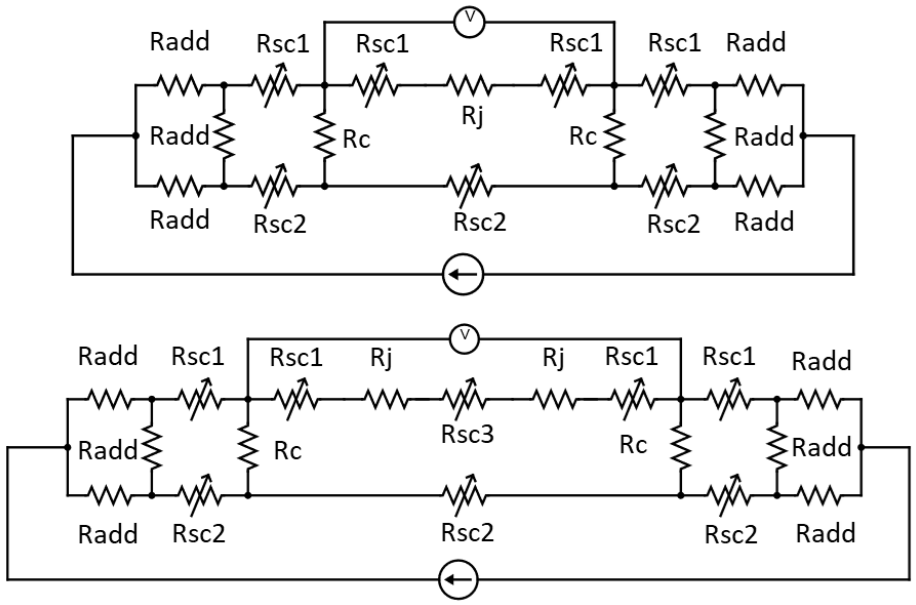


Figure 3.34: Lumped element electrical model of the lap (top figure) and bridge junction (bottom figure).

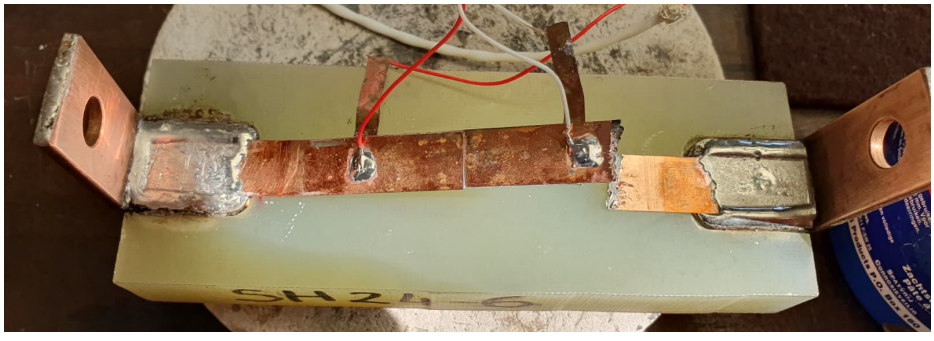


Figure 3.35: Bridge joint breakdown induced by overcurrent.

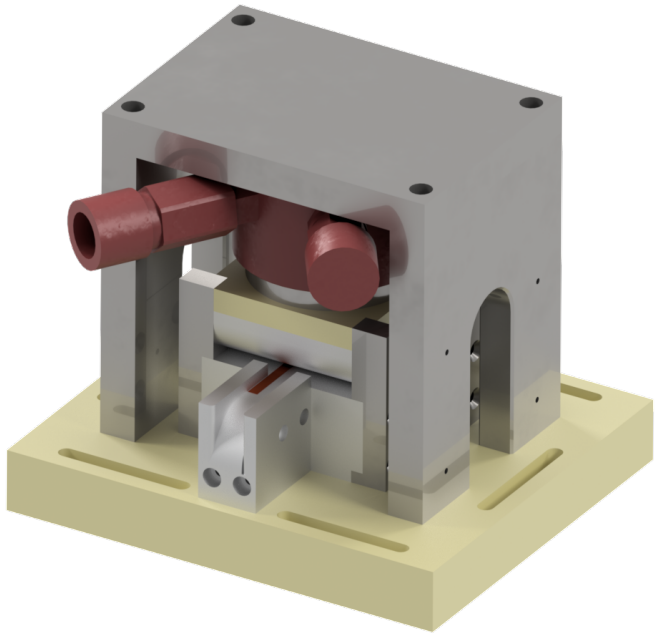


Figure 3.36: Visual representation of the conceptual design for the improved tool for joints manufacturing.

of completely revising the joint manufacturing tool with the aim of avoiding the HTS tape degradation and ultimately reaching a target specific resistance below $0.1\ \mu\Omega \cdot cm^2$. To this purpose the first step was to exclude a manual procedure for giving pressure, as tightening screws with bellevilles, and relying on a system which could give force directly from the center, to avoid unbalancing effect. For this reason a second version of the joint manufacturing tool was designed as shown in Fig. 3.36. The tool consists of an AISI 316 stainless steel case, containing a hydraulic piston to apply controlled pressure, and a thermally-controlled aluminum base to reach the desired temperature. The pressure is measured on top of the piston by a pressure gauge and the temperature is handled using system of the previous tool. The aluminum pressor was designed with a pronounced curvature radius of 15 mm connecting the base with the vertical faces to ensure a smooth transition from the edges of the pressor and to avoid stress concentrations. Mechanical tolerances of $\pm$ 0.05 mm were achieved on the planarity of both faces, and verified with a FARO arm [82], ensuring uniform contact with the tape surface. The pressor is guided by AISI 316 stainless steel rails to guarantee a strictly vertical descent. The base is made of Duratron U2300, selected for its mechanical robustness and thermal insulation properties, thus minimizing heat dispersion. Duratron U2300 was also used to insulate the piston from the pressor to prevent heating of the oil inside the piston. The

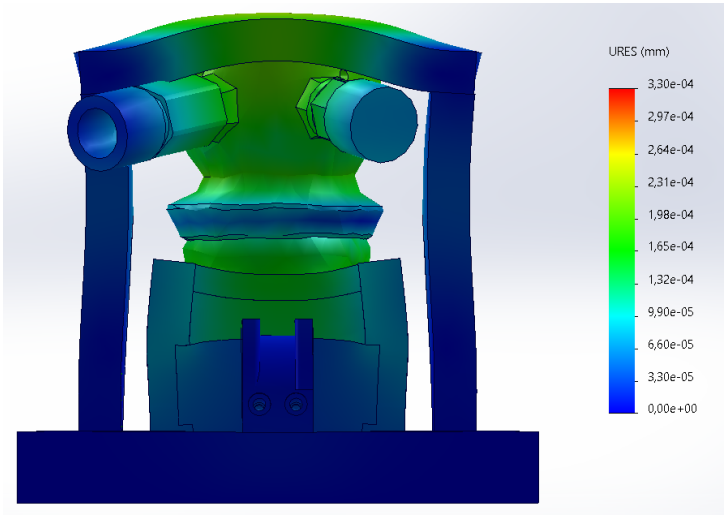


Figure 3.37: Mechanical simulation of the displacements for the resistive splices tool performed with a load of 4800 N. The representation adopts a visual scale 1:57

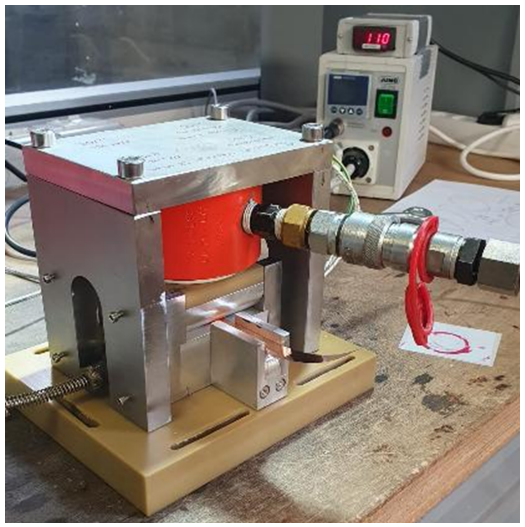


Figure 3.38: Improved resistive splice manufacturing tool

system was designed to accommodate both 4 mm and 12 mm wide tapes. A mechanical simulation was performed to assess the structural integrity of the design. A total force of 4800 N was assigned to the piston, corresponding to 10 MPa on a 12 mm tape, which represents the maximum target pressure for joint manufacturing. Fixed constraints were applied at the screwed points of the stainless steel box and along the supporting base. The results, shown in Fig. 3.37, include visually magnified displacements by a factor of 57. The average displacement was found to be ~ 0.002 mm, confirming that the setup is mechanically safe and stiff within this load range. Moreover, within the simulation, a 4

mm wide HTS tape was positioned asymmetrically against one shoulder of the external guide, thereby introducing a misaligned constraint relative to the center of mass of the pressor. Even under this condition, no unbalanced displacements were observed. To validate the setup, the real prototype shown in Fig.3.38 was used to manufacture and test four 12 mm lap joints with the HTS side of one tape facing the other. The same SnIn previously adopted was selected as the brazing alloy due to its low melting point, which ensures a safe working temperature for HTS conductors, while Kiwa-S65 was adopted as the flux. The brazing procedure consisted in pre-tinning the samples as described in Sec. 3.1, heating the system to 150 °C, then applying 5 MPa. Once the target pressure was reached, heaters were turned off, and the splice was cooled in air under constant pressure. The resulting joints showed an average specific resistivity of 80 nΩ·cm^2. This value is in agreement with values reported in the literature [80], confirming both the reliability of the setup and the suitability of the adopted procedure.

3.3.1 Enhanced flat joint

The new set up demonstrated that splice resistances can be kept within acceptable ranges. However, for ESMA, a novel splice design was developed to overcome the uncertainties introduced by the extra thickness, both during joint fabrication and in the winding process. The concept resembles the flat joint geometry, but with a key difference: the tape cut is performed at an oblique angle rather than perpendicular to the longitudinal axis, as illustrated in Fig. 3.39. This geometry allows for the current to progressively transfer across the triangular section of the oblique cut, starting from the tip and gradually passing through the joint as the bottom tape saturates, due to the current saturation. In contrast, the flat junction forces the entire current transfer to occur at a single point, temporarily concentrating the current of two tapes onto a single one within a reduced region comprising only of the junction region where the tape is interrupted. With the oblique splice, a progressive redistribution avoids a localized current concentration, effectively enhancing the critical current of the cable compared to that of a single tape. This splice concept is currently under patent consideration, as Italian patent application No. 102024000025341, submitted on November 11th, 2024, under the title "Superconducting tape junction". The application was jointly proposed by ASG Superconductors S.p.A., INFN, and the University of Milan. The listed inventors are E. Cavanna, A. Capelluto, R. Marabotto, S. Sorti, and M. Statera.
To confirm the expected behavior of this junction an electrical simulation was performed both in COMSOL and OPERA3D. The simulation set up consisted in modeling the tape using two materials: copper, to which a resistivity of $2.0 \cdot 10^{-9}\Omega$/m was assigned, and the YBCO itself, whose behavior was described by its power law Eq. 1.9, having set the voltage threshold to 100 µV/m, as in the I_{c100} criterion and interpolating the critical surface described in Sec. 2.3.2 to calculate the critical current value for each tape. The first simulation was run at the temperature of 20 K and addressed the current distribution between the two tapes during a linear current ramp in order to confirm the physical phenomenon behind this joint geometry. In particular the current from the power sup-

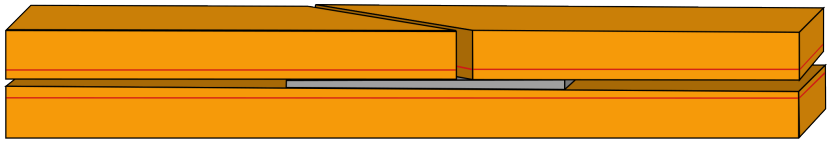


Figure 3.39: Schematic representation of the enhanced flat joint. The orange block stands for the superconducting HTS tape, the red line represents the position of the REBCO layer and the gray part is the brazing alloy

ply was linearly ramped from zero until the saturation the saturation of the two tapes critical current transport properties. Relevant results of the time evolution of the current redistribution are showed in Fig. 3.40. The figure illustrates the map of the current density ratio, J/J_c , at a given transport current I supplied by the power source. The red arrows indicate the current transfer between the upper, interrupted HTS tape and the lower, continuous one. In the top panel, corresponding to low transport current, the current flows almost entirely through the continuous superconducting tape, effectively bypassing the resistive junction. As the current increases, the continuous tape begins to approach its critical current density J_c , while the interrupted tape remains nearly equipotential. In this regime, the current starts to redistribute, flowing from the interrupted tape into the continuous one in roughly equal measure. The region where both tape currents overlap corresponds to the area of maximum J/J_c. When the lower tape approaches its critical current, a potential gradient develops across the interrupted tape as well. At this stage, current begins to flow along most of the interrupted tape, with current transfer becoming increasingly localized near the tips of the cut. This behavior allows current to avoid the central region of the continuous tape, which is already saturated. This current redistribution process continues as long as an unsaturated area remains within the joint region of the continuous tape and the interrupted tape can still carry current to the end of the discontinuity. The net effect is a smoother and delayed superconducting transition across the joint, enabling this oblique-cut junction to sustain a higher critical current than a conventional flat joint with a perpendicular (90°) cut relative to the longitudinal axis of the tape.

The effect of the oblique-cut depends on the inclination angle of such cut, as readily demonstrated by the first straightforward example of passing from a 90° angle to a different inclination. To further asses this point and individuate the optimum angle conciliating both the mechanical feasibility of the cut and the net performance gain of the joint, comparing to the single tape performance, a parametric study was conducted by modeling the joint with a cut approaching a progressively lower inclination angle. Results are showed in Fig. 3.41, where progressively lower angles starting from 90° up to 5° were studied. In the left panel are represented the simulated geometries corresponding to the operating condition specified in the graph on the right: the colored map represents the J/J_c ratio at a given transport current I, while in black and white the current density crossing the resistive junction between the above interrupted tape and the continuous one below. In the right panel a double-scale graph reports the J/J_c ratio within the junction for different I/I_c ratios referred to the performances of a single tape, as a function of

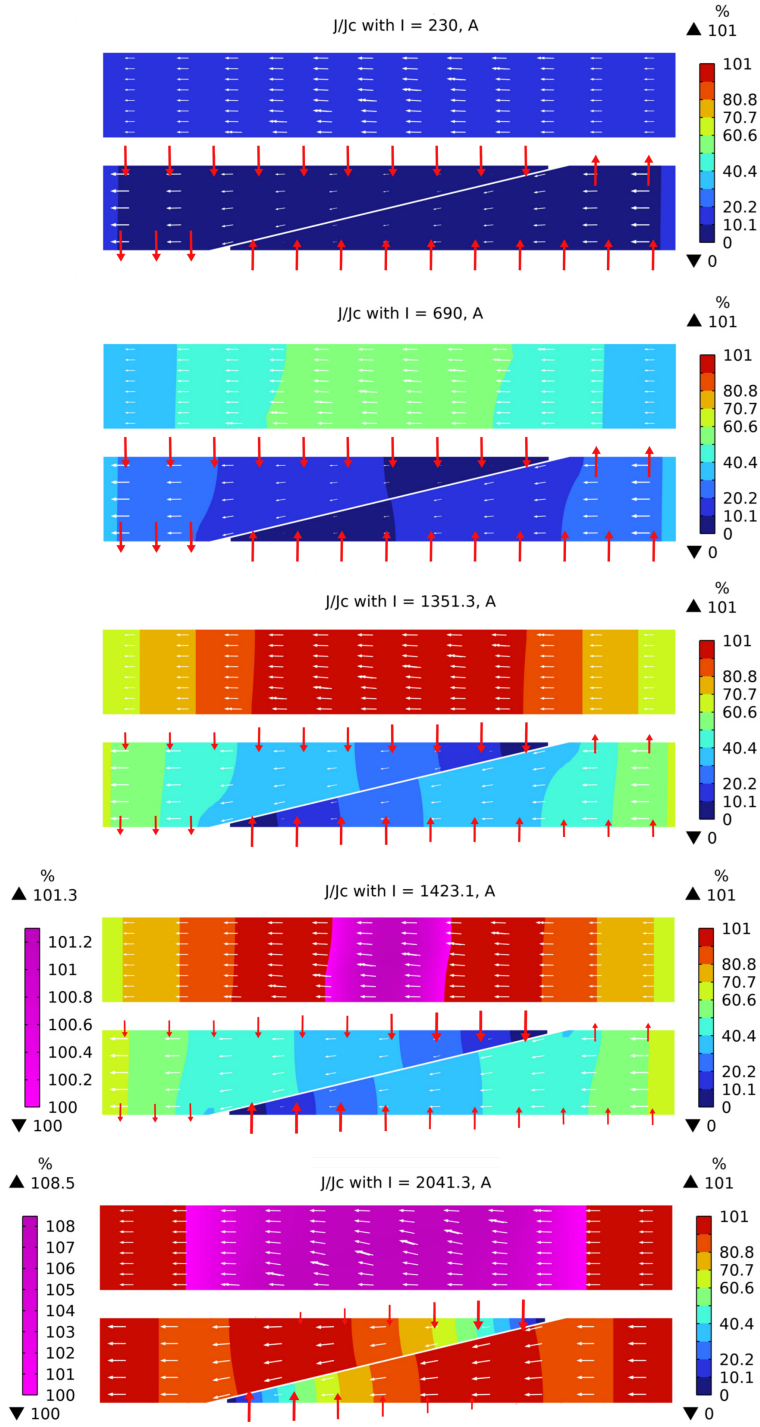


Figure 3.40: Current redistribution within the enhanced flat joint during a linear current ramp represented as the ratio J/J_c at the current I fed from the power supply. Red arrows represents the current flow between the above interrupted tape and the contentious one below.

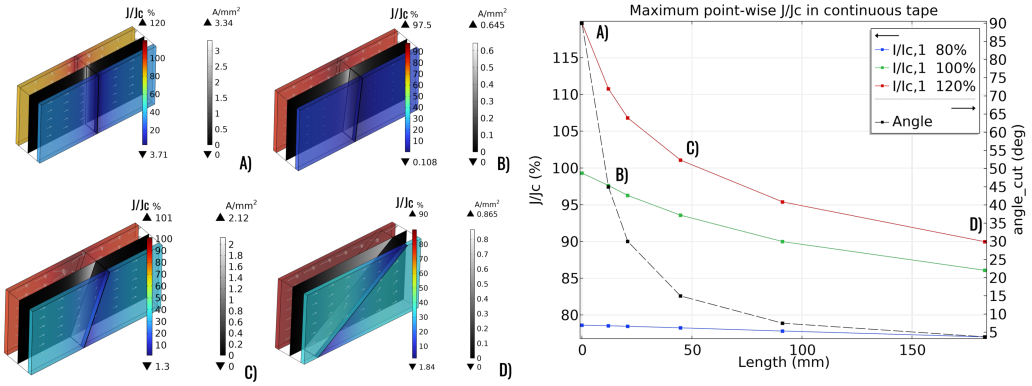


Figure 3.41: Parametric study on the cutting angle for the enhanced flat joint, the left picture represents the simulated geometries, which are sketched out of scale for visualization purposes. In particular the colored map reports the value of the J/J_c ratio for a given transport current, while in black and white is reported the current density flowing through the resistive joint. The double-scale plot on the right panel shows the trend of the J/J_c value within the joint for each of the simulated geometries, considering three different value of powering current with respect to the single tape I_c performances.

the joint length, which identifies the cutting angle of the junction. From the graph it can be observed, as expected, a increasing trend for the joint performances coherently with the increasing of the joint length and, consequently, the decreasing of the cutting angle. The manufacturing of such joints becomes more and more difficult as the cutting angle decreases, due to the low thickness of the tape which tends to lead to a curling effect of the tips after a low angle oblique cut is performed, as in the case of the 5° angle. To this purpose, the optimal geometry to conciliate both performances and manufacturing feasibility was found to be at $\sim 10°$, corresponding to a joint length of approximately 80 mm, which allows for a net gain of 20 % on the nominal single tape I_c performances, while still maintaining 5 % of critical current margin.
This physical phenomenon occurs for each non-orthogonal continuous cut with respect to the longitudinal axis of the tape since it is related to the increasing of the area where the current can transfer to the other extremity of the tape through the continuous one. Therefore, other geometries could be evaluated such as an L-shaped cut as the one pictured in the top left image of Fig.3.42, which will be referred to as tetris cut. In this second case the phenomenon is analogue to that of the slant geometry and performance gains varies with the distance between the orthogonal sections of the cut. To compare the relative gain of the two proposed geometries the same parametric study was performed and results are showed in Fig. 3.42. As it can be observed, the relative advantage introduced in both cases is very similar, thus leading to the conclusion that diluting current transfer from one tape to the other by producing a cut which is non-orthogonal to the longitudinal axis of the tape is rather independent on the geometry of the cut itself. Given this result the so-called tetris cut surely allows for longer joint manufacturing without introducing mechanical issues to the tape integrity, however such cut cannot be

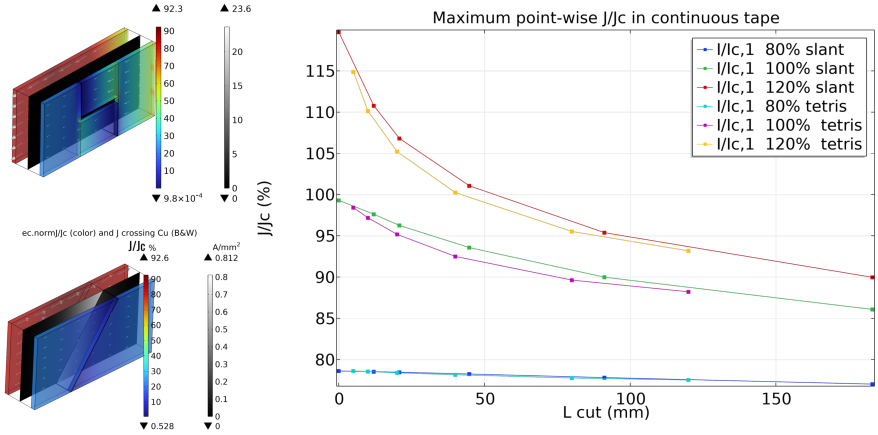


Figure 3.42: Parametric study two possible cutting geometries for the enhanced flat joint, the left picture represents the simulated geometries, which are sketched out of scale for visualization purposes. In particular the colored map reports the value of the J/J_c ratio for a given transport current, while in black and white is reported the current density flowing through the resistive joint. The right panel shows the trend of the J/J_c value within the joint for each of the simulated geometries, considering three different value of powering current with respect to the single tape I_c performances.

easily performed with a blade and necessitates of a dedicated tool. For this reason the splice geometry adopted in ESMA followed the oblique geometry.
A further simulation was performed to foresee the behavior of such splice in LN_2 in order to confront the results with experimental measures. To this purpose the considered splice geometry consisted into an oblique cut with an angle of $\sim 16°$ for an overall joint length of around 45 mm, coherently with the experimental results described below. Indeed, to start the experimental validation of the performance increasing of such joint, a cutting angle which could initially ease the joint manufacturing while still keeping a measurable improvement of the joint performance was chosen. The specific joint resistance was set to ~ 23 nΩ·cm^2 and the single tape I_c performances at 77 K self field where set to three different value representative of the whole HTS tape procurement for ESMA. Results are showed in Fig. 3.43. The figure represents the voltage-current simulated curves for the enhanced flat joint for three different values of the single tape I_c performance. The dashed lines are referred to the single tape behavior, thus resulting in the standard power-law transition, while solid lines are the transition curves resulting from the simulated enhanced flat geometry. The initial resistive baseline was subtracted to highlight the splice behavior. As it can be observed, the diluting of the current transfer region described before results into a slower transition which matches the electrical field threshold of the I_{c100} criterion at a higher current with respect to the single tape behavior described by the power law. The slope of the voltage-current curve of the enhanced flat joint is related to the resistivity of the junction itself, since as described in Fig. 3.40, the current transfer across the resistive joint becomes significant as the continuous tape below approaches its saturation. After both tapes saturate, the curve diverges with a

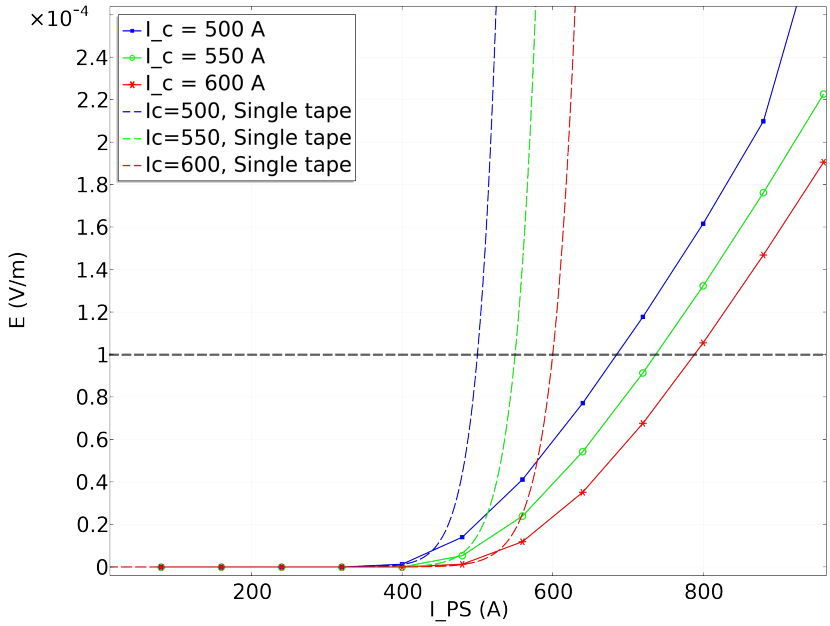


Figure 3.43: Voltage-current simulated curves for the enhanced flat joint for three different values of the single tape I_c performance. The dashed lines are referred to the single tape behavior, thus resulting in the standard power-law transition, while solid lines are the transition curves resulting from the simulated enhanced flat geometry.

similar behavior as for the single tape power law. From simulation in LN_2 such joint with a target specific resistance of $\sim$ 23 nΩcm^2 is expected to provide a $\sim$ 20 % higher critical current value with respect to the single tape performance. Based on the simulation results, an initial experimental campaign was started to validate this splice concept. The oblique cut was designed to extend over a junction length of 50 mm. The junctions were carried out using the initial copper press, as the upgraded version was not yet available. The fabricated sample was then mounted on a dedicated sample holder, as shown in Fig. 3.44, and tested in LN_2 to measure its critical current. An example of a measurement performed on such junction is shown in Fig.3.45, where a first linear baseline can be observed, similar to what occurs in the flat junction. However, in this case a second linear trend appears approximately at the transition current of a single tape, where the joint begins to progressively transfer current across the splice region. Based on these results, the I_c value was determined using the I_{c100} criterion, which in this case consisted into applying a 5 μV threshold after subtracting the contribution of the first linear baseline. A total of eleven enhanced flat joints were successfully manufactured and tested, yielding an average I_c of 654 A $\pm$ 26 A. Although the manufacturing procedure still requires optimization, this first experimental campaign demonstrated a $\sim$ 10 % increase compared to the nominal I_c of a single tape, with reference to the spool characteristics (Fig. 3.4). This improvement was confirmed with statistical significance through a z-test, which rejected the null hypothesis. The probability distribution functions of the

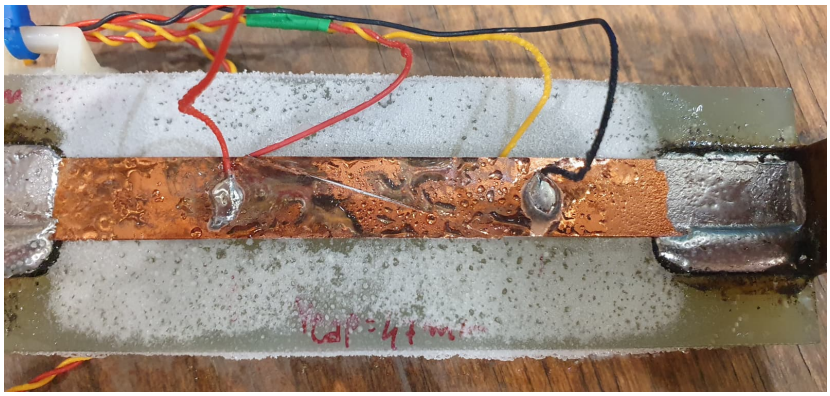


Figure 3.44: Manufactured enhanced flat joint on a double tape HTS cable mounted on the sample holder.

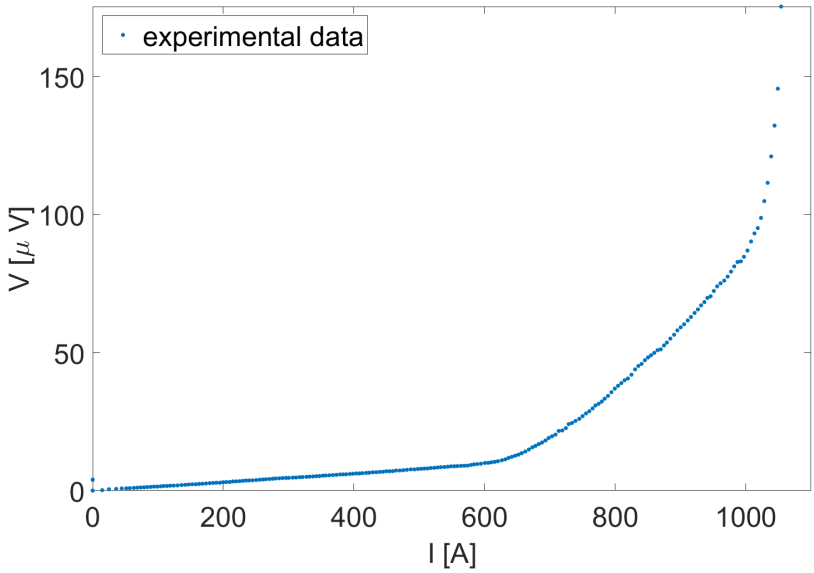


Figure 3.45: Experimental data of a critical current measurement on an enhanced flat junction. On the y-axis the voltage across the junction is reported in μV while on the x-axis there is the current coming from the power supply in A.

single-tape reference I_c values and of the enhanced flat junction are shown in Fig. 3.46. A significant improvement in breakdown current was also observed with respect to standard flat joints. The average breakdown current was measured to be 1031 A $\pm$ 39 A, approaching the values obtained for bridge and lap joints, where performances are consistent with those of a two-tape cable. The rupture point systematically occurred at the beginning of the joint, as shown in Fig. 3.47, which is consistent with the simulations results showed in Fig.3.40 that highlights a progressive saturation of the top discontinuous tap tape from the tip of the oblique cut to the beginning of the junction itself. To ensure compatibility with the ESMA design without exceeding the operational margin of the magnet (Fig. 2.21), the splice manufacturing procedure was developed by ASG Superconductors. The improvements achieved allow the splice region to retain approximately 130% of the performance of a single tape. Since splices are expected to be located in the second half of the coil cross section along the straight region, where the coil with the lowest margin yields a current margin approaching 60 %, and given a net gain of about 30 % over the nominal tape I_c, the coil configuration preserves a sufficient operational margin despite the presence of splices and without including elements carrying an extra thickness as would happen in the case of a bridge or lap joint choice.

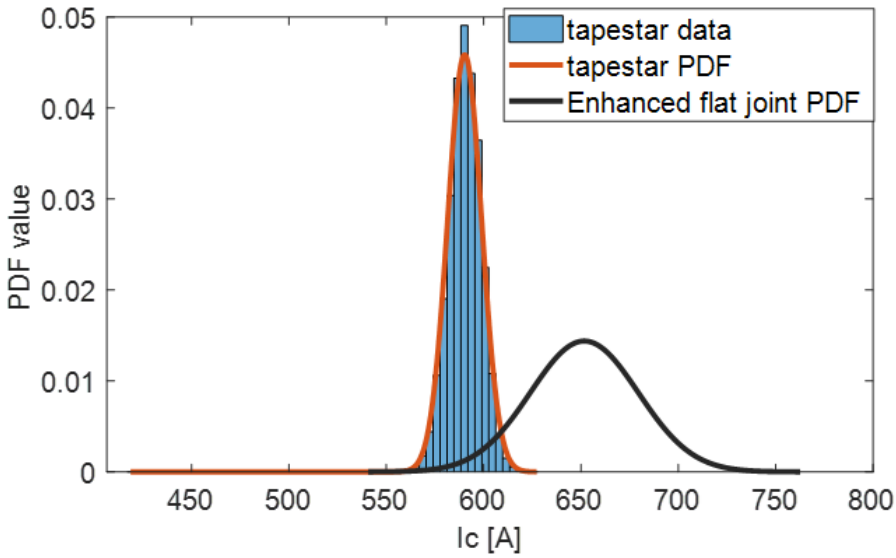


Figure 3.46: The picture shows in blue the histogram referred to the probability distribution function of the HTS tape reference data given from FFJ, in orange the fitted gaussian distribution and in black the probability distribution function associated to the enhanced flat junctions measurements.

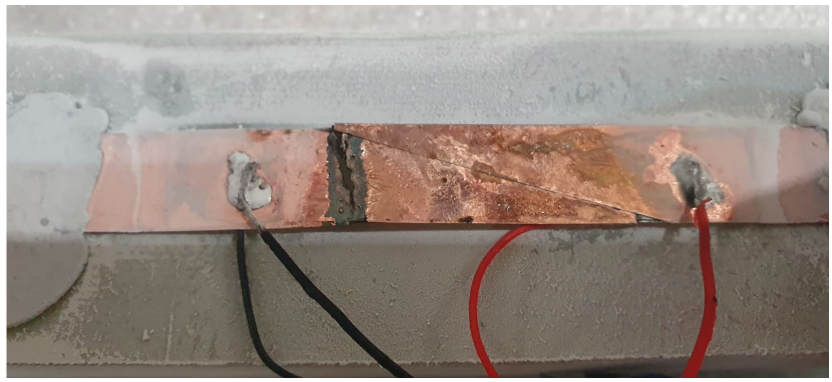


Figure 3.47: Enhanced flat joint breakdown induced by overcurrent.

3.4 Summary and achievements

The research described in this chapter focuses on validating the design choices presented in the previous chapter by characterizing the procured conductor. To this purpose:

- A preliminary **critical current measurement** campaign was carried out in **liquid nitrogen, self-field**. This campaign successfully **validated** the **experimental setup, sample holders, and procedures**, as well as **Tapestar data** provided by the manufacturer, describing the tape performance on a millimeter-scale.
- **Critical current measurements** were conducted in collaboration with the University of Geneva to investigate the **temperature** and **angular dependence** of the critical current. These measurements were performed on **4 mm** tapes at **4.2 K** and at the operational temperature of **20 K**, under variable magnetic field and **angular orientation** with respect to the tape *c*-axis. Additional measurements were carried out at **20 K** under variable magnetic field applied **parallel to the *c*-axis** for the **12 mm** wide tape procured for the ESMA magnet.
- The measurement results were compared with both liquid-nitrogen transport current measurements and the corresponding Tapestar data in order to **validate the lift factors** used in the electromagnetic design of ESMA.
- **Unexpected superficial inclusions** were identified and subsequently characterized in terms of size and potential impact on tape performance. This last point concerned both the effect of **defect removal** and **test under known applied external loads**. The results indicate that such inclusions, by themselves, **do not compromise tape performance**.
- Due to the unit length available of REBCO tapes, **internal joints** are needed in each coil of ESMA. To this end, conventional joint geometries, such as **lap, bridge, and flat joints**, were investigated leading to a joint manufacturing procedure targeting specific resistances $\leq$ **80 μΩ·cm**^{2}.
- A **novel flat joint geometry was developed**. This solution preserves a flat profile, avoiding extra thickness within the cable, while simultaneously preventing the full transport current from flowing through a single tape. As a result, a **performance increase** of approximately **30%** with respect to a single tape was achieved.

CHAPTER 4

Thermo-Mechanical design of ESMA

The ESMA magnet represents a particularly demanding case study in the design of superconducting devices, since nearly every subsystem needs to solve non-trivial challenges. The combination of large Lorentz forces, high magnetic fields, and high current densities imposes stringent requirements on the mechanical support structure, while the aim to operate the system cryogen-free further complicates the thermal management strategy. This chapter presents the principles of the thermal and mechanical design of ESMA, carried out primarily by ASG Superconductors and supported by complementary analyses and measurements performed within this work. The magnet is entirely conduction-cooled through three cryocoolers, a choice that necessitates optimization of thermal bridges, current leads, and coil geometry in order to balance performance with a limited cooling budget. Special attention is given to the MI winding layout, which aids protection and stability, but on the other hand introduces additional heat generation during charging cycles due to the inter-turn contact resistance. In parallel, the chapter explores the structural aspects of the design. Each coil is enclosed within a dedicated support module designed to withstand the electromagnetic stresses encountered during cool-down and operation.

4.1 Thermal design

The thermal design mainly addresses two macro-regions, also corresponding to the two main parts of the adopted two-stages cryocoolers: the first stage, including current leads, and the second stage, leading to the cold mass. The overall scheme of the thermal design at which the upcoming description will refer is showed in Fig. 4.1. Concerning the first stage, thermal bridges linking the coils to the cold heads combine BSCCO current leads, commercially available and chosen for their high T_c, and brass/copper components. Each current lead is composed of two sections: the first in brass and the second in copper, mechanically clamped together with an indium foil layer between the two interfaces. The length and cross section of these two materials was optimized to enhance both thermal and electrical conductivity in the space available. A copper heat exchanger is then applied to the copper section, and through dedicated copper braids it serves to drain the heat generated by both joule effect and temperature gradient. At the lower end of the copper section, a copper block is placed, onto which the superconducting

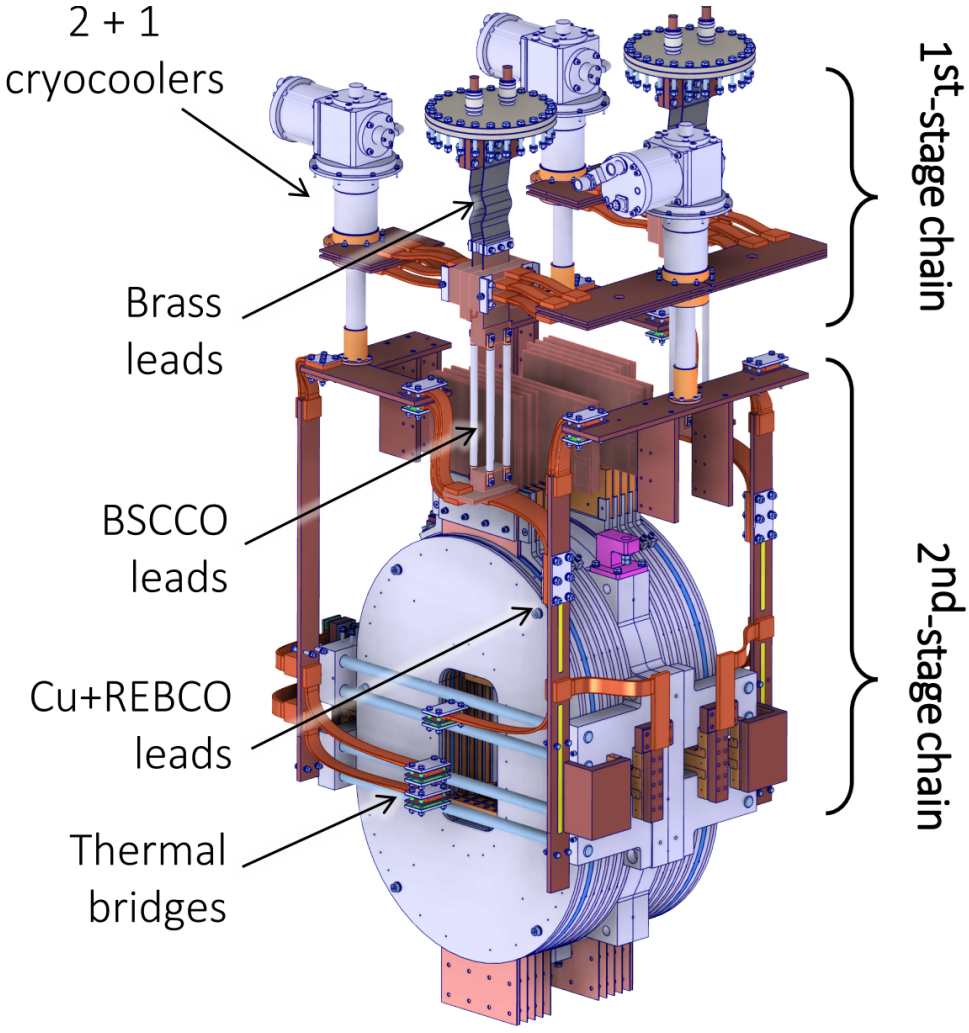


Figure 4.1: Overview of the cooling system for ESMA, highlighting the principal electrical and thermal elements.

BSCCO components of the current lead are mechanically fixed. Around the system, a thermal shield is inserted, consisting of an aluminum cylinder wrapped with 30 layers of MLI (Multi-Layer Insulator). In this way, the radiation from the cryostat walls is reduced, and the system only experiences radiation corresponding to the temperature of the shield. The estimated thermal power arriving at the first stage is due to:

- Heat generated by the thermal gradient, from room temperature at 300 K down to the temperature at which the HTS is assumed to be connected.
- Joule heating generated by the current flowing inside the brass and copper sections of the current leads, calculated, where the current per lead is I = 1150 A.
- Contribution from radiation incident on the thermal shield, which intercepts and suppresses the radiation that would otherwise impact the magnet and the first stage of the leads.

The contributions originating from the current leads were optimized, yielding 57.7 W per lead, for a total of 115.4 W. In addition the 30 MLI layers wrapped around an aluminum cylinder, suppress the radiation contribute to about 2 W/m^2. Considering a shield surface of ~ 10 m^2, this corresponds to a radiation heat load of ~ 20 W. Thermal power is also conducted through two Ti-6Al-4V tie rods which connect the cold mass to the top cover of the thermal shield, providing an additional 0.33 W. A thermostatic simulation performed by ASG Superconductors confirmed that the temperature at the end of the lead remains below 64 K with the estimated operational power of P = 135.73 W. Moreover, the cryocoolers operate at two different temperatures due to the configuration of the shield connections, which are linked to only two cryocoolers out of three. As a result, the working temperatures are 44.8 K for two cryocoolers and 38.6 K for the remaining one. The power map for the cryocoolers in Fig. 4.2, together with the operating points, shows in orange the point corresponding to the one cryocooler operating at 38.6 K, removing 37 W, while the green points correspond to the two cryocoolers operating at 44.8 K, each removing 49.5 W. In total, the system extracts 136 W, such that the cooling system designed for the current leads allows the BSCCO interface end to be maintained at 56 K, i.e. with a temperature margin of 6 K below the threshold of 64 K, required for safe current-lead operation. Meanwhile, the thermal shield reaches 58.3 K at the lower cover and 56 K at the upper cover, thus cooling the tie rods to minimize the heat transferred by thermal gradient while also reducing the radiation load on both the first and second stages.

The cold mass is cooled through a copper structure, including the coils current adductors, that extends from the second stage of the cryocooler to the magnet base and is enclosed within the thermal shield. The structure, shown in Fig. 4.1 and extrapolated alone on the right picture of Fig.4.3, consists of the second stage heads of the cryocoolers fixed to a copper shelf, equipped with a vertical rack that accommodates all copper braids extracting heat from the machine. These copper braids connect the rack to the upper heat exchanger, which is itself connected to the lower exchanger extending from the steel container of the coils. In this section, the heat produced by the magnet is removed, making it essential to guarantee efficient thermal contacts. For this reason, all elements

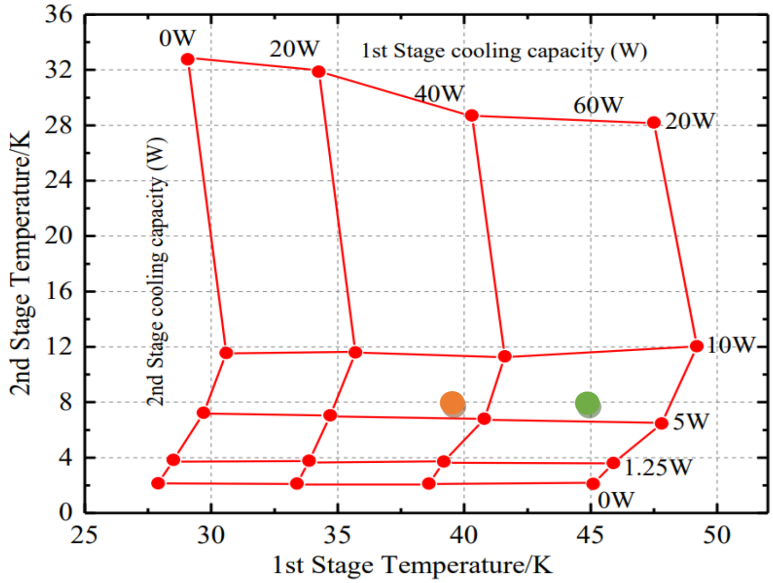


Figure 4.2: Power map of the cryocoolers of ESMA: the orange dot indicates the working point of one out of three cryocoolers, while the green dot represents the remaining two.

connected to the copper plates at the base of the cryocooler are joined using mechanical clamping with an indium foil between interfaces to maximize conductivity. The thermal power of the second stage, neglecting convection effects due to the operating vacuum pressure, has multiple contributions:

- Heat generated by magnet charging (AC losses), P $\sim$ 15.31 W;
- Heat generated by the inner current leads due to Joule heating, with I = 1150 A per lead, yielding P $\sim$ 1.575 W;
- Heat generated by the outer current leads, P $\sim$ 2.25 W;
- Heat generated by the four pairs of BSSCO current leads, P $\sim$ 0.54 W;
- Radiation from the thermal shield at 60 K estimated to be $P_{rad} \sim 0.3$ W.

In addition, heat is conducted through two Ti-6Al-4V tie rods , which connect the cold mass to the upper cover of the thermal shield, giving P = 0.011 W for both tie rods, leading to a total power of $\sim$ 20 W. The main challenge for the operation in cryogen-free mode, i.e. the limited cooling power, is worsened in this magnet by the non-insulted winding. In fact, during charging/discharging, the finite contact resistance in between turns results in a radial component of the current generating additional heat. Electrical measurements performed by ASG on a stack of tapes resembling a portion of the ESMA coil, i.e. built with a ratio 2:1 of HTS tapes and AISI 304 stainless steel, and pressed to simulate the winding tension and stresses during operation such as the contact would be similar as in the real magnet, resulted into a specific contact resistance of about 0.2 -

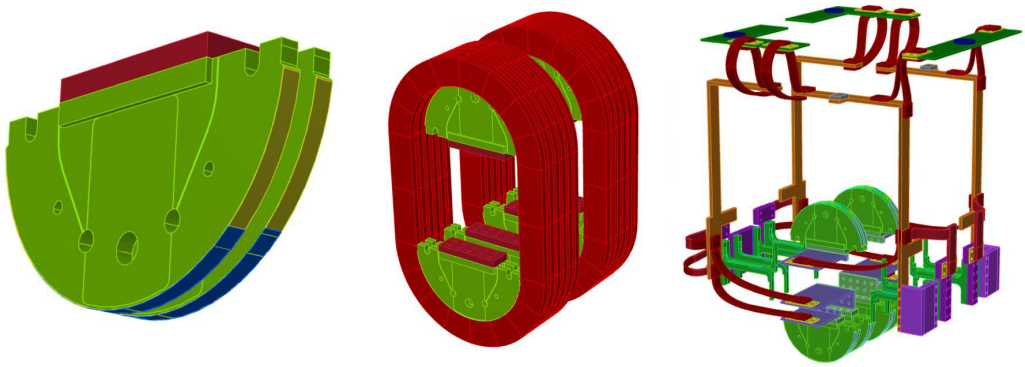


Figure 4.3: From left to right: internal adductors of ESMA coils together with the region where the tape is going to be brazed to start the winding. Assembly of the internal adductors and ESMA coil. Thermal and electrical assembly of the ESMA magnet in the second stage.

0.3 mΩ·cm^2. With this parameter, the charging of the magnet could be simulated again to update the previous estimation performed in Sec. 2.3.2, and used to address the problem of the power generated during the ramp. In particular, for a specific resistance of 0.3 mΩ·cm^2, corresponding to a total resistance of 5.5 mΩ, the charging time constant is $\tau \sim$ 16 minutes. With a ramp rate of 50 mA/s, the reference cycle, targeting 15 W of power, as previously reported together with all contributions, brings the magnet from zero to 10 T in about 6 hours. This has been evaluated with full time-domain 3D models of the magnet from Little Beast Engineering [83]. The model includes the current redistribution within superconductors. It is important to highlight once again that the τ of the system is much shorter than the 6 hours ramping time. The bottleneck for charging speed is thus not the electromagnetic transient, but the generated heat. Coil charging losses are by far the largest contribution to the cold mass heat load. The peak coil temperature approaches the design target during ramping but drops significantly once steady state is reached, confirming that ramp-up is the dominant heat source. With the maximum coil temperature fixed at 20 K, simulations indicate a peak value of 17.6 K during ramping which later stabilizes to 12 K in steady state. To mitigate the impact of unforeseen local dissipation, as additional AC and radial losses that could affect magnet stability, as well as potential local joint degradation leading to increased electrical resistance and dissipation, the magnet will be operated by targeting a fixed power dissipation rather than a fixed ramping time. To this end, the magnet will be supported by a dedicated system for monitoring the dissipated power, which can adjust the ramp rate as needed to maintain the dissipation below 20 W. The simulation validated that with $P_{tot} \sim$ 20 W, the maximum coil temperature is 17.6 K, with one cryocooler at 8.6 K and the other two at 8.8 K. As graphed in the load map in Fig. 4.2, the orange point corresponds to the cryocooler operating at T = 8.8 K, removing 37 W, while the green points correspond to the pair of cryocoolers at T = 8.6 K, each removing 49.5 W, for a total of 136 W.
Copper connectors link adjacent superconducting coils and connect them to the current leads as well as to cryocoolers. These components serve both electrical and thermal

functions, transferring current between coils while acting as thermal bridges to extract dissipated heat to the second stage of the cryocoolers The cold mass, which includes all components between the second stage and the coil base within the thermal shield, relies on copper braids connected to the copper adducors of the coils via mechanically tightened joints with indium foils to maximize thermal conductivity, extracting roughly 80 % of the total heat load of the magnet. The external adductors, visible in the right picture of Fig.4.3, are T-shaped and soldered to the superconducting tape side. Current is transported through copper blocks while copper braids link these blocks to heat exchangers and cryocoolers. Similarly, internal adductors, showed in the left and central pictures of Fig.4.3, have a semi-circumference shape and are attached at the coil inner winding start as the tape is soldered on the highlighted part in blue for a 45 degree angle, with reference to the picture. Copper bars at the magnet corners distribute current, connect to braids, serve as current leads for first/last coil copper adductors, and act as thermal anchors, while heat exchangers are screwed to the current adductors blocks to direct braids over reinforcement bars. The total dissipated power was included in the previous estimation of the total 20 W for the cold mass.

4.1.1 Thermal conductivity measurements

In order to complete the optimization of the current adductors and ensure efficient extraction of heat generated during magnet operation, thermal conductivity measurements are required, particularly because the tapes composing the cable of ESMA are dry-wound, which significantly reduces thermal contact compared to impregnated options. As already noted in Sec. 2.3.5, where ESMA design expertise is being applied to study configurations for particle accelerators, insulated cables are generally preferred, since NI or MI winding options would result in a finite charging transient. To this purpose, a thermal conductivity measurement campaign of HTS stacks emulating real magnet windings was initiated, with sample preparation performed at the LASA laboratory and testing conducted at the CERN Cryolab. The thermal analysis of windings is particularly challenging due to their complex structure and the variety of materials involved: the normal component of thermal conductivity depends on the intrinsic properties of the HTS material, the type of insulation employed (e.g., fiberglass or metal), the conductivity of fillers, the thermal contact resistance between layers, and the mechanical stress applied during winding. Accurate determination of this parameter requires low-temperature measurements across the possible material configurations, which is why both insulated and dry samples were produced for thermal conductivity characterization.
The sample design was driven by the experimental set up geometry, described later on. For the insulated version, the sample consists of ten 12 mm $\times$ 45 mm REBCO tapes, belonging to the same procurement as for ESMA magnet, each alternated by one fiberglass tape 15 mm×45 mm (nine layers). The stack was impregnated with paraffin wax to maintain all layers in position and mimic wax impregnation conditions. Four small fiberglass inserts were placed, two at the edges of the lower HTS tape and two at the edges of the upper HTS tape to improve compactness. The other sample composition was prepared with the aim of recreating the composition of the ESMA magnet, thus con-

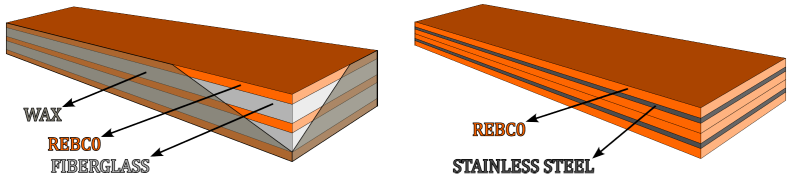


Figure 4.4: Visual representation of the two types of stack considered in the thermal conductivity measurement campaign: on the left the wax-impregnated stack, and on the right the dry stack alternating two HTS tapes and one stainless steel tape.

sisting in a stack of four stages of HTS - Stainless Steel (SS) - HTS. A scheme of the two types of stack is represented in Fig . 4.4.

While the dry stack was simply cut and assemble in the experimental set up, the wax-impregnated sample manufacturing required a dedicated mold for both the dry stack assembly and its impregnation. The mold, 3D printed in PLA with a 100 % set filling, was shaped as a pool with four removable pins and an upper block, as illustrated in Fig. 4.5. Two stainless steel blocks applied the desired pressure through disc springs, using the same procedure as for the inclusion study described in Sec. 3.2. A considerable number of test samples were produced to optimize the procedure. To prevent wax adhesion, the inner surface of the mold was covered with Kapton. The stack was assembled by alternating layers of HTS and fiberglass, after which the mold was closed and placed in an oven at 55 °C. The stainless steel blocks, prepared with the appropriate disc spring configuration, were also inserted into the oven. In parallel, the wax was placed in a vacuum chamber, heated to 90 °C, and degassed by reducing the chamber pressure to 2.5 mBar. Once both the mold and blocks were removed from the oven, the molten wax was deposited into the mold and pressed, as shown in Fig. 4.6. The system was then left to cool for two hours, after which it was extracted and measured. The nominal thickness of the dry samples was 2.050 mm, since the HTS thickness is 70 μm and that of the fiberglass is 150 μm. Samples were produced in sets subjected to different pressures of 30, 10, 5.5, 1, and 0 MPa, with pressed samples showing a thickness reduction of 0.2 up to 0.4 mm compared to the nominal value. One of the key parameters for the wax-impregnated sample manufacturing is the applied pressure, which must reflect the stress experienced by the tapes in the winding. A higher stress implies a higher thermal conductivity both in the winding and in the sample. However, estimating this stress is not trivial, since an HTS magnet cannot be fully modeled as a thick cylinder. To address this, several models were explored to provide an analytical estimation of the radial stress induced by winding tension. As analytical solutions are only available for circular geometries, the results in the case of the racetrack windings of ESMA are strictly valid only at the center of the circular sections of the coils. Radial stresses are expected to be lower in the remaining parts of the coil, although they may ultimately be homogenized by applying external compression during manufacturing. To carry out the analytical estimation, two main approaches were considered:

- Lamé thick-wall approximation, where the winding is treated as a thick cylin-



Figure 4.5: PLA mold for thermal conduction measurements sample preparation. From left to right: alignment pins, impregnation pool, and upper pressor.

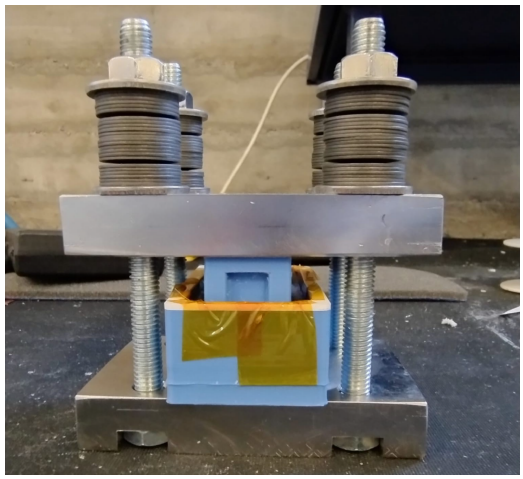


Figure 4.6: PLA mold under external applied pressure.

der, thus solving the Lamè system of equations for thick-walled pressure vessels. Boundary conditions are imposed at the outer radius, with radial stress set to 10 MPa and hoop stress equal to the winding tension. Solutions may be find in literature, as [84] and [85].

- Winding layer superposition. Here the stress is calculated by considering the contribution of each layer as it is wound. The same boundary conditions as the previous case are applied. Examples of this method are described for solenoids or circular HTS windings [86][87][88].

A comparison of the five different models presented in the above-cited literature was performed using the design parameters of the ESMA magnet summarized in Tab. 4.1. From the data reported in Tab. 4.1 , a significant difference can be observed between the radial and azimuthal Young's modulus of the tape. The azimuthal Young's modulus

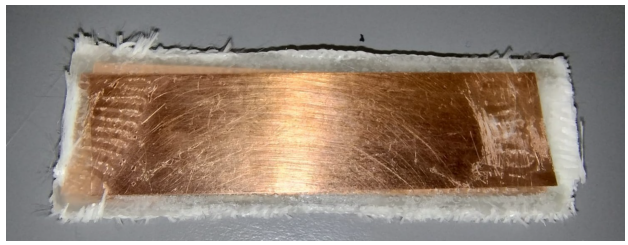


Figure 4.7: Wax-impregnated sample for thermal conductivity measurements

was derived by considering the contributions of the materials forming the layers of the HTS tape and was set equal to the value adopted by ASG for consistency. In contrast, the radial Young's modulus was directly measured by ASG through tests performed under external pressure using a hydraulic press. The results yielded a surprisingly low value compared to the expected properties of the individual tape layers, as for the value obtained from the azimuthal Young's modulus. Results are reported in Fig. 4.8, where a

Parameter	Unit	Value
$E_{r,tape}$	GPa	12
$E_{r,mandrel}$	GPa	200
$E_{\theta,tape}$	GPa	157
$E_{\theta,mandrel}$	GPa	200
ν_{tape}	N/A	0.2
$\nu_{mandrel}$	N/A	0.3
Winding tension	N	100
Tape thickness	mm	0.167
$R_{in,winding}$	mm	35
$R_{in,mandrel}$	mm	130
Turns	N/A	350

Table 4.1: Design parameters and material properties of ESMA adopted in the analytical estimation of the radial stress induced by the winding tension.

pre-compression of 10 MPa is given to the ESMA coil at the end of the winding and was therefore used as boundary condition at the outer radius. The graph presents the analytical evaluation of the radial stress induced by the winding tension performed with five different models labeled in the legend and where possible included the mandrel with its correspondent material properties. A sixth reference line is reported in light blue, corresponding to a 3D FEM analysis performed by ASG on the coils of ESMA, in the same point assessed from the analytical estimation. The target pressures selected was therefore of 30 MPa, roughly corresponding to the expected peak radial stress estimated with the analytical model described in [87] which better approaches the results found by ASG. Additional reference values of 10 MPa, 1 MPa, and 0 MPa were also considered, to represent the outer pressure imposed to ESMA coils and other cases or applications where radial stress is expected to be lower.

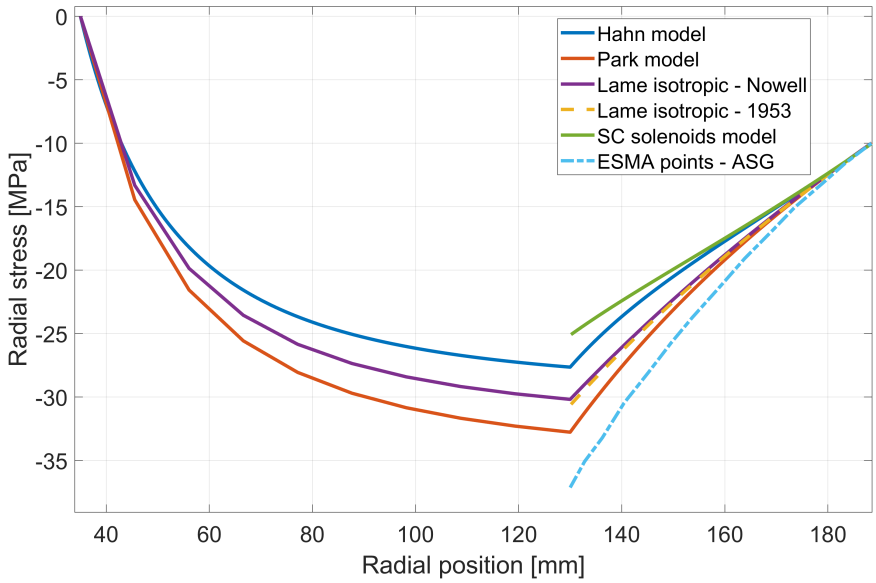


Figure 4.8: Analytical evaluation of the radial stress induced by the winding tension at the center of the coil circular section in the ESMA dipole. The estimation assessed five different models labeled in the legend and where possible included the mandrel with its correspondent material properties.

The low-temperature thermal conductivity measurements were carried out at the Cryolab at CERN. The experimental setup, showed in of Fig. 4.9, consists of a cryocooler, a sample holder, temperature sensors, a heater, and the data acquisition system [89]. The cooling of the system is hadled by a two stages cryocooler (Model SRP-082, Sumitomo Heavy Industries, Ltd.). The sample holder, shown the right picture of Fig.4.9, is made of oxygen-free high-conductivity (OFHC) copper to ensure optimal thermal conduction. It consists of a platform that connects to the cryocooler base and four copper blocks: two outer, longer blocks serve as the cold side of the sample, while the two inner, shorter blocks are heated, thus providing a uniform hot side. The symmetric geometry of the structure ensures that the entire heat flow passes exclusively through the samples, eliminating any alternative thermal paths. The measurement setup includes six sensors: two CERNOX sensors mounted on one sample, two PT100 sensors on the other, and two Carbon Ceramic Sensors (CCS, also known by their Russian name TVO [90]) placed on the sample holder base to monitor the reference temperature T_{Ref}. All sensors are Resistance Temperature Detectors (RTD), each with a dedicated calibration curve relating resistance to temperature. To measure electrical resistance, the four-wire method was used. A precision current source (LakeShore 120) provided a stable current of 10 μA, while a Keithley 2182A nanovoltmeter measured the corresponding voltage drop across the sensors. The sensors were fixed to the sample surfaces using cryogenic GE Varnish. To establish a temperature gradient across the thin samples, one side was

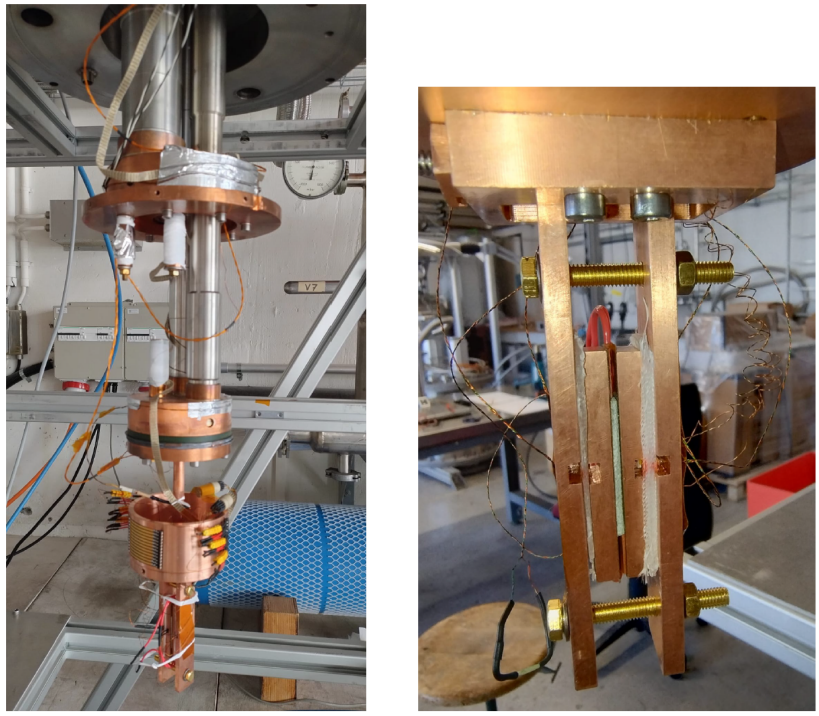


Figure 4.9: Thermal conductivity measurements experimental set-up (left figure) and a close up of the sample holder (right figure).

heated using four 5 W ARCOL FCR5 resistors in series. Thermal conductivity measurements were performed under steady-state conditions: the heater was powered on, heat flowed through the samples, and sensor readings were monitored until equilibrium was reached. Subsequently, the heater was switched off, and the system was monitored until cooled back to T_{Ref}. For each sample, two temperature differences were determined:

- ΔT_{on}: the temperature gradient during steady-state heating,
- ΔT_{off} : the offset between the two sensors when the heater was off.

The temperature gradient across the sample is therefore obtained as:

$$\Delta T_{sample} = \Delta T_{on} - \Delta T_{off} \tag{4.1}$$

To perform the measure at a different temperature a heater integrated into the cryocooler second stage can be turned on. By increasing T_{Ref}, it becomes possible to measure thermal conductivity at different temperatures without adjusting the input power to the sample holder heater. The normal thermal conductivity for all acquired ΔT_{sample} can be estimated as:

$$k = \frac{Qd}{A\Delta T_{sample}} \tag{4.2}$$

where Q is the heater power, A is the sample area and d the sample thickness. For the uncertainty estimation, the root sum square method [91] was used to determine the

overall uncertainty of the measured data. Accordingly, the overall uncertainty is given by:

$$\sigma_k = \left[\left(\frac{Q}{A\Delta T_{sample}} \right)^2 \cdot \sigma_d^2 + \left(\frac{d}{A\Delta T_{sample}} \right)^2 \cdot \sigma_Q^2 + \left(-\frac{Qd}{A^2 \Delta T_{sample}} \right)^2 \cdot \sigma_A^2 + \left(-\frac{Qd}{A\Delta T_{sample}^2} \right)^2 \cdot \sigma_{\Delta T_{sample}}^2 \right]^{1/2} \tag{4.3}$$

where the uncertainty on the heat load Q applied to the sample, is resulting from the voltage and current measurements:

$$\sigma_Q = \left(V^2 \cdot \sigma_I^2 + I^2 \cdot \sigma_V^2 \right)^{1/2} \tag{4.4}$$

Here, σ_I and σ_V corresponds to the accuracy of the current source and the nanovoltmeter, respectively, as specified by the manufacturer for the relevant measurement range and valid over a two-year calibration period. These values are $\pm$ 0.1 % on the supplied current for the current source [92], whereas it can be calculated as $\pm$ (ppm of the reading + ppm of the range) for the nanovoltmeter [93].
The sample cross section is rectangular, and its uncertainty can be easily found as:

$$\sigma_A = \left(a^2 \cdot \sigma_b^2 + b^2 \cdot \sigma_a^2 \right)^{1/2} \tag{4.5}$$

Where $\sigma_a = \sigma_b = 5 \cdot 10^{-5}$ m, with a and b being the dimensions of the rectangle. The same value of was considered for the stack thickness: $\sigma_d = 5 \cdot 10^{-5}$ m . The uncertainty was estimated after repeated measures on the samples using a caliber, and results higher than the 10^{-5} m sensitivity of the instrument due to the irregular shape of the sample. For what concerns the uncertainty over the measure of the temperature gradient through the stack, since the temperature was derived from the temperature calibration curve, the uncertainty is related to the measure of the resistance R of the sensor, thus holding the same value of σ_V as for the measure of the heat and $\pm$ 0.05 % on the 10 μA supplied by the current source [92], but propagated using the Ohm's law:

$$\sigma_R = \left[\left(\frac{1}{I} \right)^2 \cdot \sigma_V^2 + \left(-\frac{V}{I^2} \right)^2 \cdot \sigma_I^2 \right]^{1/2} \tag{4.6}$$

With the calibration curve, this uncertainty in resistance can be translated into a temperature uncertainty for ith- sensor independently as:

$$\sigma_{T_i} = max(|T_i(R) - T(R + \sigma_R)|, |T_i(r) - T(R - \sigma_R)|) \tag{4.7}$$

The resulting values could then be combined to calculate the uncertainty on ΔT as:

$$\sigma_{\Delta T} = \left(\sigma_{\Delta T_1}^2 + \sigma_{\Delta T_2}^2 \right) \tag{4.8}$$

The measurements were conducted at an internal pressure below 10^{-6}mbar, under the assumption that the heat flowed equally through the two samples. In addition, the total

thermal gradient was assumed to be distributed entirely across the sample thickness. The temperature sensors were powered with a fixed current, and their voltage drop was recorded, making it possible to calculate the resistance R. This resistance was then converted into temperature using the appropriate calibration curve for each sensor. A typical measurement run consisted in stabilizing the base temperature of the sample at a series of pre-defined setpoints. Once a setpoint was reached, the heater was activated, and the temperature variation over a defined time window was monitored for each sensor. The difference between the maximum and minimum temperatures within that interval was compared to a predefined stability threshold. When all sensors exhibited temperature fluctuations below this threshold, the heater was switched off. Subsequently, the power supplied to the second-stage heater was increased, and a new steady-state condition was established following the same stabilization criteria as in the heating phase. This procedure was repeated for all the required steps, power inputs are summarized in Tab. 4.2. As mentioned before, the other sample which was measured was a dry stack of tapes resembling the ESMA cable configuration, i.e.: composed by alternating two HTS tapes and one 26 μm AISI 304 stainless steel tape. The stack was composed directly in the sample holder and measured following the same procedure as for the wax impregnated sample. Once assembled, the sample holder was tightened using screws combined with disc springs in order to give a effective compression of 1 MPa on the stack. In this condition, the overall thickness of the sample was measured to be 0.688 mm. Data from multiple runs of the same sample were combined to reconstruct the final thermal conductivity profile of the sample stack. However, of the above-mentioned wax-impregnated samples prepared at different pressures, only the ones subjected to a 30 MPa load were measured during the campaign. This limitation was due to instrumentation problems that slowed down data acquisition. Results were calculated via Eq.4.2 and are presented as the thermal conductivity k as a function of the average temperature measured by the sensors (CERNOX and PT100). Results for the wax-impregnated sample pressed at 30 MPa are reported in Fig.4.10, error bars not visible are smaller than the marker used. The PT100 sensors disagree with the CERNOX data for temperatures below 40 K. Below 40 K, the PT100 are far from their working range, so the readings deviate significantly from the CERNOX data, which instead display a nearly linear dependence of thermal conductivity on temperature. Based on the CERNOX results, it can be deduced that the thermal conductivity of this sample in this temperature range appears to exhibit a lin-

Sample type	**Power [W]**
Wax-Impregnated	0.001
Wax-Impregnated	0.022
Wax-Impregnated	0.035
HTS-SS-HTS	0.024
HTS-SS-HTS	0.050
HTS-SS-HTS	0.097

Table 4.2: Heat power input for the two types of prepared samples

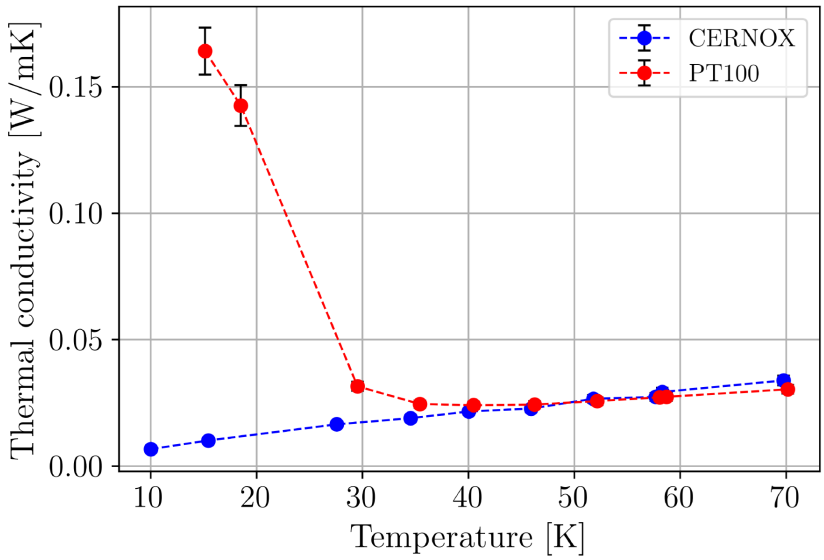


Figure 4.10: Themal conductivity measuremet results of the wax impregnated sample prepared with an external load of 30 MPa

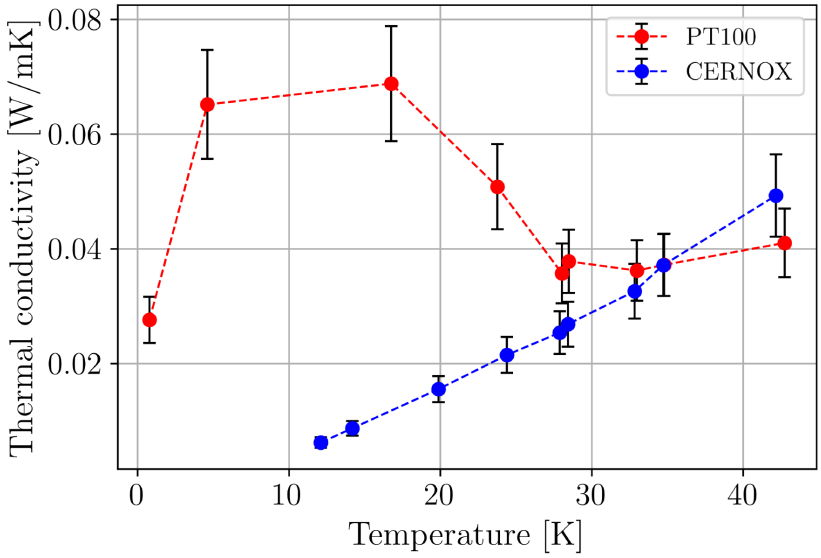


Figure 4.11: Themal conductivity measuremet results of the dry sample composed alternating two layers of HTS tape and a stainless steel tape, as in the cable of ESMA.

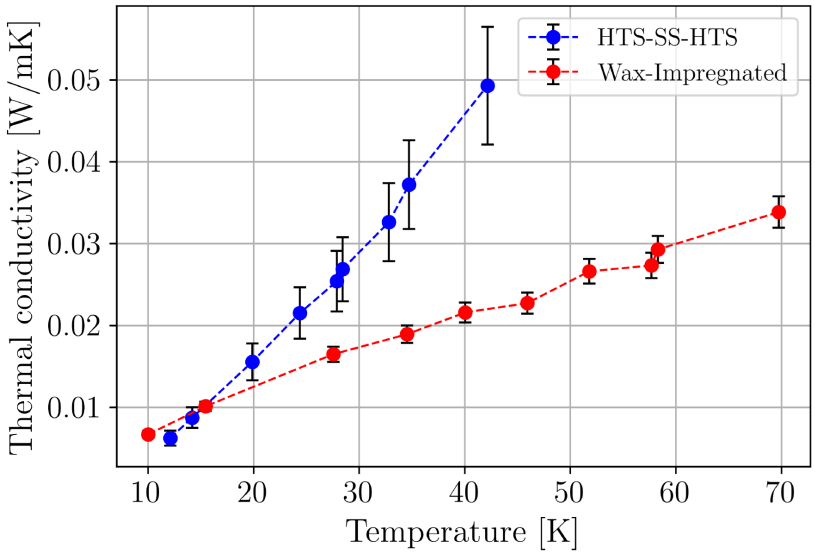


Figure 4.12: Thermal conductivity measuremet results of the dry (blue) and wax impregnated (red) samples measured via CERNOX sensors.

ear dependence with respect to the surrounding temperature. At higher temperatures, the measurements require longer acquisition times due to the increased heat capacity of the sample and the larger temperature fluctuations, which slow the achievement of steady-state conditions. The main factors influencing the thermal conductivity of the sample are: the multilayer structure of the tape stack, including the REBCO layer and the thermal contact resistance between adjacent layers, and the pressure applied to the sample during manufacturing. In the dry stack, the thermal contact resistance is the dominant factor reducing the effective bulk thermal conductivity of copper and steel, and it is strongly dependent on the externally applied pressure. The applied pressure of 1 MPa is not representative of the actual conditions in the ESMA magnet but provides a lower bound for the thermal conductivity of the stack. Higher pressures, which would better approximate operating conditions, could not be applied due to the limited mechanical robustness of the sample holder. Measurement results, both acquired with a PT100 and CERNOX sensors, are showed in Fig. 4.11. In this case, no agreement is observed between the PT100 and CERNOX measurements, with the first extending to temperature values beyond the accessible range of the cryocooler and thus resulting in unreliable data. In contrast, the CERNOX data consistently exhibit a linear dependence of thermal conductivity on temperature, with values approximately twice those measured for the wax-impregnated insulated sample. This behavior agrees with expectations, since the absence of insulating material between layers reduces thermal contact resistance. Results of thermal conductivity measured using CERNOX sensors for both samples are represented together in Fig.4.12. The wax-impregnated sample reflects the presence of wax and fiberglass as insulating materials, resulting in lower absolute values and a lower slope.

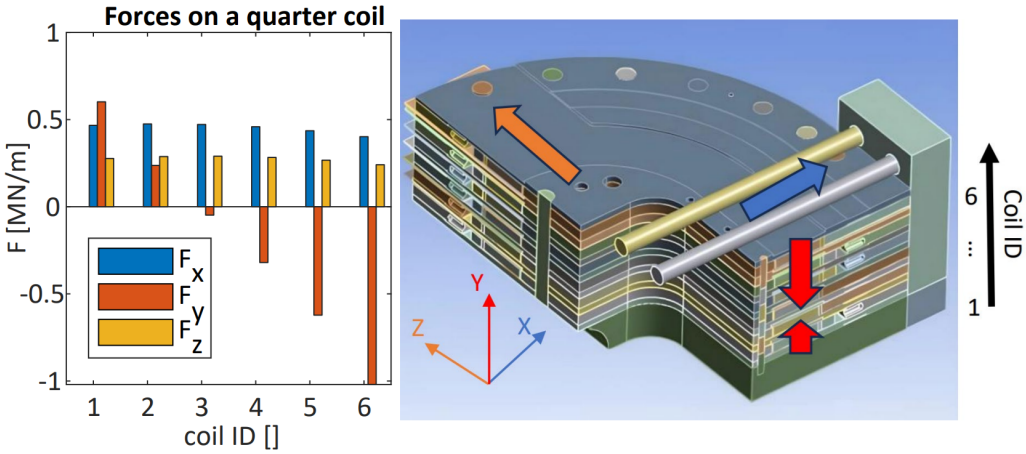


Figure 4.13: Overview of the integrated Lorentz forces on a quarter magnet

4.2 Mechanical design

The mechanical structure of the magnet follows the modular approach of the electromagnetic design and is built to support the twelve racetrack coils that form ESMA. It is divided into two identical halves, each comprising a supporting base for the respective six coils. Each coil is mounted on a tray holding the winding mandrel and equipped with an external pressing system designed to withstand the Lorentz forces that tend to make the coils expand radially and compress axially toward the magnet center. Each coil is encased within a support structure made primarily of AISI 316LN stainless steel, chosen for its high strength under stress, while threaded spacers are made of Inconel 718 to handle the most demanding load conditions. The insulation is realized with G10, and the heat-exchanger plates are made of copper. This structure, as shown in the left panel of Fig. 4.14, pushes presser structures against the coil, providing most of the radial support during cool-down and operation. Axial forces are instead counteracts by the full stack structure, as showed in the right panel of Fig. 4.14. Detailed structural analyses were performed using 3D finite element models in ANSYS. A summary of the forces analysis is reported in Fig.4.13, where Lorentz forces were calculated at maximum operating current of 1150 A. Despite the extensive use of high-strength materials, some components (labeled in bold in Fig. 4.14) exhibit a safety factor of peak equivalent (von Mises) stress against Ultimate Tensile Strength in between 1.5 and 2. The lowest-safety area is a localized spot on the coil plate, at the edge of the connection with the stacking rods. However, even assuming that this spot plasticizes, the surrounding material has been evaluated to be more than enough to accommodate the additional load due to stress redistribution.

The coils themselves were modeled as solids with anisotropic properties derived from experimental measurements, with a radial Young's modulus of 6.6 GPa in the radial winding direction and about 160 GPa longitudinally and vertically. Due to the surpris-

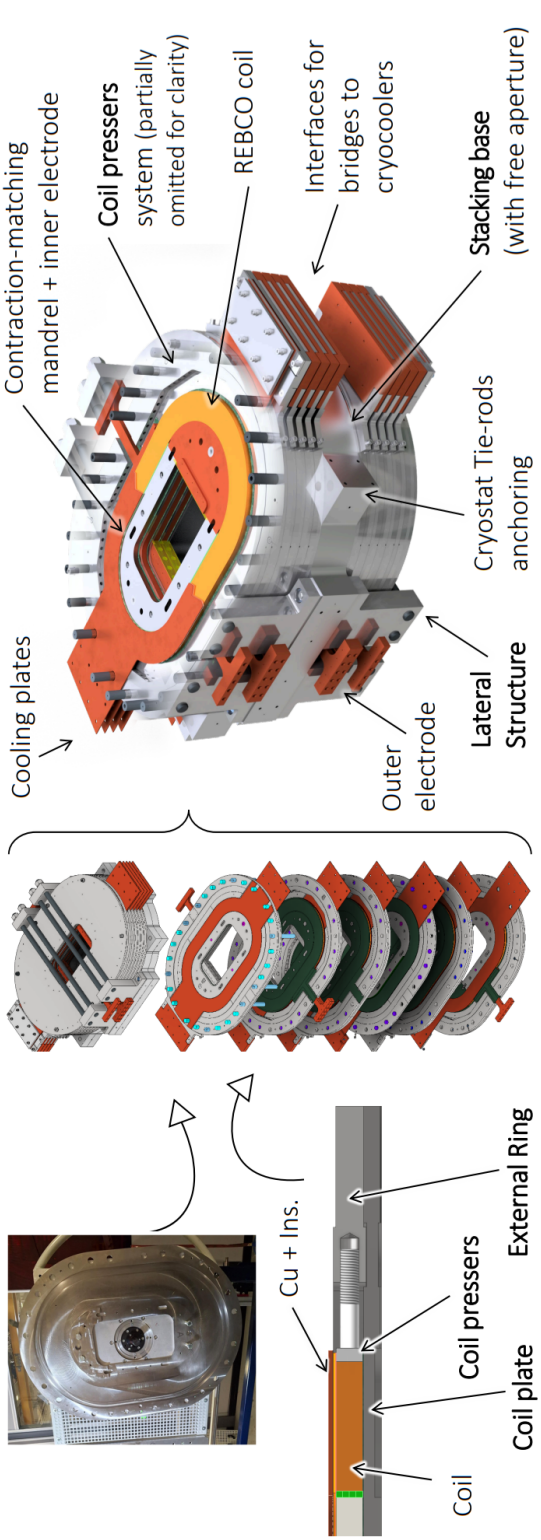


Figure 4.14: Overview of the structural design of ESMA. From left to right: the electromagnetic forces containment system for a single coil, the stacking of the modules, and the main components in the final assembly

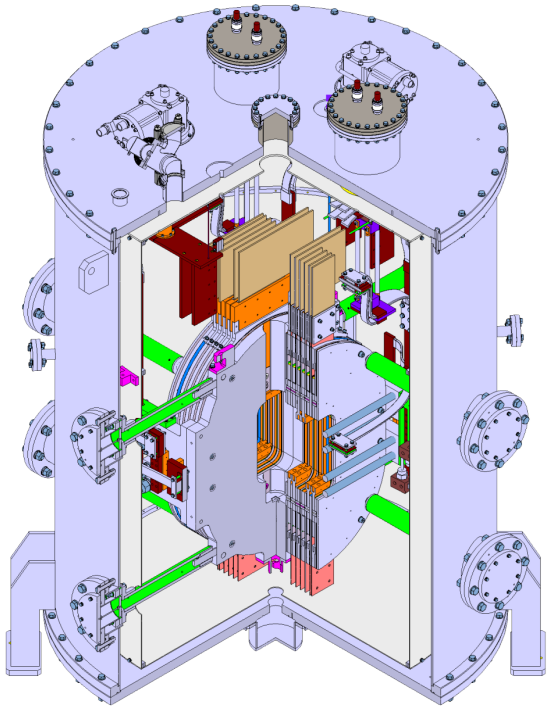


Figure 4.15: A section of the ESMA magnet inside its cryostat, in the final configuration for operations.

ingly low measured radial modulus, detailed calculations for the straight sections of the coil indicate stresses as high as 520 MPa, close to the degradation limit of 600 MPa (corresponding to a 0.4 % strain), with displacements up to 0.2 mm along the z-direction and a maximum vertical compression of 0.37 mm. A displacement of 0.2 mm may be critical mostly in correspondence of the inner current adductor, where the tape is rigidly bounded by the brazing. To this purpose a dedicated experimental set up was developed to investigate the degradation induced by the peeling stress caused by such displacement, as a consequence of the low radial Young's modulus of the tape. The set up, together with experimental results are described in Sec. 4.2.3. In parallel, the lower-than-expected effective mechanical modulus of the winding pack, of a few GPa [94], is expected to be mitigated by pre-production winding tests. The winding mandrel is composed of four elements, made of copper, stainless steel, and titanium, connected through pins and keys to allow differential thermal contraction relative to the tray. This material combination was chosen to match the thermal contraction of REBCO tapes, experimentally measured to be 2.4 mm/m between 300 K and 77 K, as described in Sec. 4.2.1. The copper element, as already mentioned, also serves as the electrical adductor of the coil, with the first turn soldered onto on a 45° arc centered in the middle of the circular section. During winding, a tension of $\sim$ 100 N per turn is applied to the cable, inducing axial compression on the mandrel and radial pressure on the curved sections. The tension is distributed as follow: 40 N per HTS tape and 20 N to the stainless steel tape. After

winding, a pressurization of 10 MPa is applied to the coil pack, adding further stress to the mandrel. The final design of the magnet, comprising of both thermal and mechanical parts is represented in Fig.4.15

4.2.1 Thermal contraction measurements

The design of the inner mechanical structure of the ESMA racetrack coils, which also serves as the winding mandrel, is strongly based to the thermal contraction behavior of the HTS tape. The mandrel was specifically engineered using a combination of materials chosen to match the thermal contraction of the winding, thus preventing additional stresses to arise during magnet cooldown or, alternatively, avoiding tension losses that could result if the mandrel contracts more than the tape. Since the winding is performed without impregnation, both scenarios would be critical: stresses from differential contraction or tension loss from excessive mandrel shrinkage would alter the electrical properties of the coils by affecting the contact resistance between tapes. Such changes would lead to unpredictable and potentially unsafe dynamics. A higher contact resistance could accelerate charging but compromise the MI property to mitigate quench damage, while a lower resistance would slow down charging and limit the magnet operation at INFN Genova facility.
To this purpose an experimental set up was designed and realized, to measure the integral thermal contraction of the HTS tape from room temperature to 77 K. Due to the set up limitations a complete measure up to 20 K could not be performed, however as for the majority of materials, the residual contraction below 77 K is much less than that from room temperature to 77 K and it was consequently neglected. The set up is sketched in Fig.4.16 and mainly consists in a glass cryostat, which allows for a visual inspection from outside. The sample consisted of a $\sim$ 1 m long HTS tape, mechanically fastened with screws through punched holes on both its top and bottom extremities. At the bottom, a brass weight machined with a cone shaped end was attached to keep the sample straight. This conical termination was designed to make an electrical contact with an aluminum base placed at the bottom of the cryostat, which served as the reference target for thermal contraction measurements. The top end of the sample was fastened to a G10 rod passing through the top flange via a quick coupling, enabling sample movement from outside the cryostat. The motion of the sample was monitored by measuring the relative displacement of the G10 rod using a mechanical indicator. The experimental procedure was first performed at room temperature and later repeated at 77 K. The measurement consisted in moving the rod until the brass weight made contact with the aluminum base. The two metallic components were connected to a multimeter through copper wires, and the device was set to signal electrical contact. At the moment of contact, the position of the indicator was recorded. After the room temperature measurement, the cryostat thermal shield, and consequentially the innermost chamber, were filled with liquid nitrogen and cooled down to 77 K, and the procedure was repeated under the same conditions. Three additional samples of copper, anticorodal aluminum, and a AISI 316 stainless steel tape were prepared and measured to assess the characteristic uncertainty of the set up by comparing its measurements with known results. Calibration measurement results,

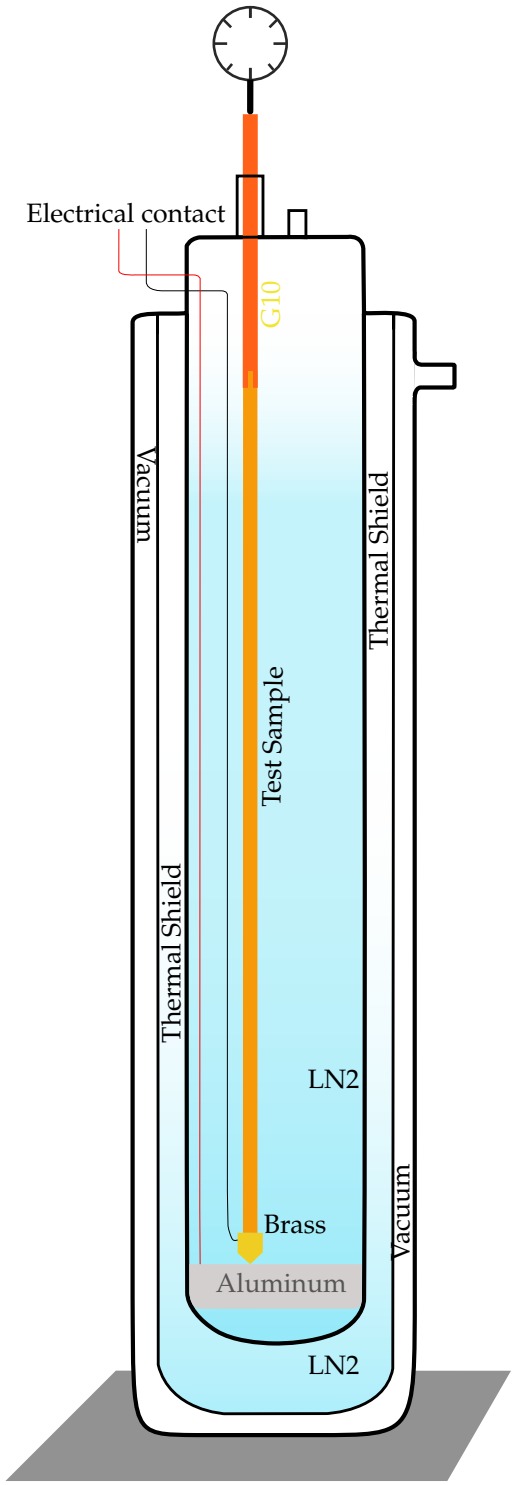


Figure 4.16: Experimental set up for thermal contraction measurements.

compared with the expected integral thermal contraction from the measured room temperature to 77 K are reported in Tab. 4.3. The error on the final measure was calculated combining the standard deviation of repeated measures and the instrumental uncertainty of the indicator, namely 0.01 mm by performing the square root sum of the two contributes. The results yielded an average calibration correction value of (-0.17 $\pm$ 0.03) m to be summed to future measurements. Here the error was calculated as the mean half spread between the smallest and largest correction values resulting from each reference material. Based on this calibration, the same measurement procedure was applied to estimate the thermal contraction of an HTS tape, with results corrected accordingly using the obtained set up calibration value. In addition to the HTS tape, other materials were also tested with the same experimental setup, namely 3D-printed PLA and 3D-printed PolyPropylene reinforced with Glass Fibers (PPGF). These tests were performed to characterize their thermal contraction properties and to assess their potential suitability for rapid prototyping applications. The results are summarized in Tab. 4.4, where the uncertainties were calculated as for the case of the reference materials, but this time including the uncertainty over the calibration value. Moreover, for each relative thermal contraction result, the uncertainty in the sample length was propagated along with all other contributing error sources to determine the overall uncertainty on the final result.

Material	**Sample length [mm]**	**T$_{room}$ [K]**	**Expected value [mm]**	**Raw measured value [mm]**	**Measured relative value - corrected [mm/m]**
AISI 316	805 $\pm$ 1	296	2.29	2.44 $\pm$ 0.02	2.84 $\pm$ 0.05
Copper	810 $\pm$ 1	295	2.49	2.70 $\pm$ 0.04	3.07 $\pm$ 0.06
Aluminum	832 $\pm$ 1	293	3.23	3.37 $\pm$ 0.04	3.88 $\pm$ 0.06

Table 4.3: Thermal contraction results of reference materials used for calibration of the experimental setup.

Material	**Sample length [mm]**	**T$_{room}$ [K]**	**Raw measured value [mm]**	**Relative contraction - corrected [mm/m]**
HTS tape	815 $\pm$ 1	300	2.27 $\pm$ 0.02	2.58 $\pm$ 0.05
3D printed PLA	825 $\pm$ 1	299	12.01$\pm$ 0.02	14.35 $\pm$ 0.05
3D printed PPGF	830 $\pm$ 1	298	5.18 $\pm$ 0.04	6.04 $\pm$ 0.06

Table 4.4: Thermal contraction results of reference materials used for calibration of the experimental setup.

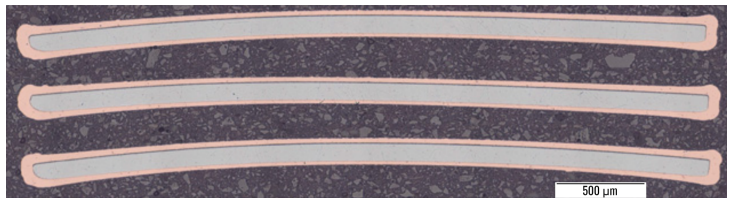


Figure 4.17: Cross section of HTS tapes showing dog-bone effect. (Reprinted from [95].)

4.2.2 Uniaxial compressive load test

REBCO tapes suffers from the so-called "dog-bone" effect, showed in Fig.4.17, caused by the higher electric field generating at the edges of the tape itself when the copper layer is electroplated. Although this issue has been mitigated with the improvement of HTS manufacturing [96], it is still important to achieve a controlled winding to quantify and eventually account for this effect [97]. To this purpose, a preliminary measurement campaign was performed to get an order of magnitude of the "dog-bone" effect of the procured conductor for ESMA coils manufacturing. The test involved 12 short samples from 12 different spools of 12 mm tape where tape thickness were probed using a micrometer, sensitivity ($\pm$ 1 µm), at three points: the leftmost, rightmost, and central point within the tape width. The measurements highlighted an average thickness measured at the center of 67 µm $\pm$ 1 µm with an average difference in thickness of 6 µm $\pm$ 1 µm of the leftmost side with respect to the center and of 4 µm $\pm$ 1 µm for the rightmost side. Whereas the maximum excursion between the two extremities has been of $\sim$ 10 µm. The same verification has been performed on 4 mm tape, however the small width of the tape has represented a major obstacle since the ratio between the instrument sensitive part and the tape width was much more higher in this case. Moreover, the thickness variation resulted to be smaller, contributing to increase the measurement uncertainty. The thickness variation concerting 4 mm tape has been estimated to be around 3 µm on a single spool. Moreover, it is important to state that the 4 mm wide tape are covered with only a 5 µm layer of copper, in contrast to the 10 µm thick layer in the case of the 12 mm wide tape, thus indicating that thicker copper layers lead to a more non-homogeneous cross section, which might be caused from issues in the electroplating process or since the electroplated copper may amplify pre-existent thickness differences. The conclusion of this preliminary campaign is that the effect is not negligible, and therefore additional measurements are required which were carried out using a universal testing machine. In particular, the variations observed in the 12 mm tape revealed a non-symmetric profile, leading to a trapezoidal cross section. Such asymmetry could accumulate during winding and potentially cause the coil to slip or pop out of the mandrel in case this uneven coherently thickness builds up.

Both 4 mm wide and 12 mm wide tapes were stacked and tested under uniaxial compression in order to evaluate both the contact area between adjacent turns and to assess potential degradation mechanisms due to stress concentration at the edges that could lead to mechanical failure within a coil. The set up used to transfer a compressive load onto the sample is sketched in the left part of Fig.4.18 and in Fig. 4.19 where the stack

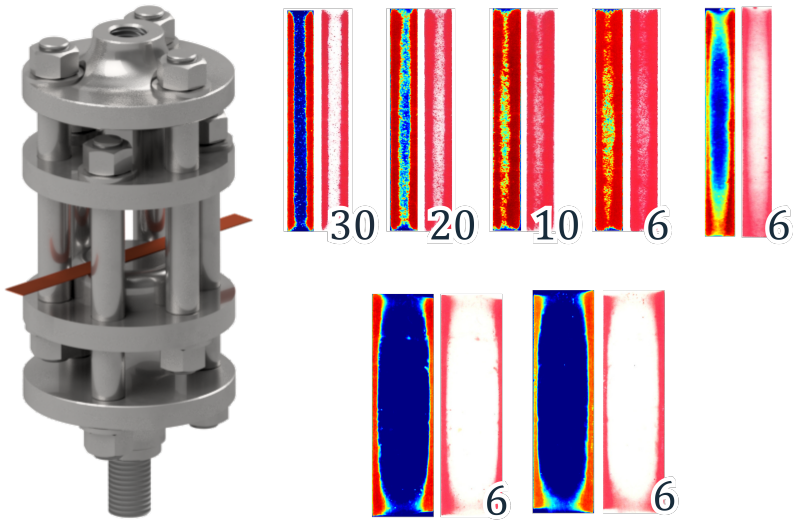


Figure 4.18: Stainless steel insert to convert uniaxial tensile stress into a compressive load (left). Digitalized and original Fujifilm Prescale paper impressed with the afterimage of the tape stack (right). The number represent the number of tapes composing the stack itself.

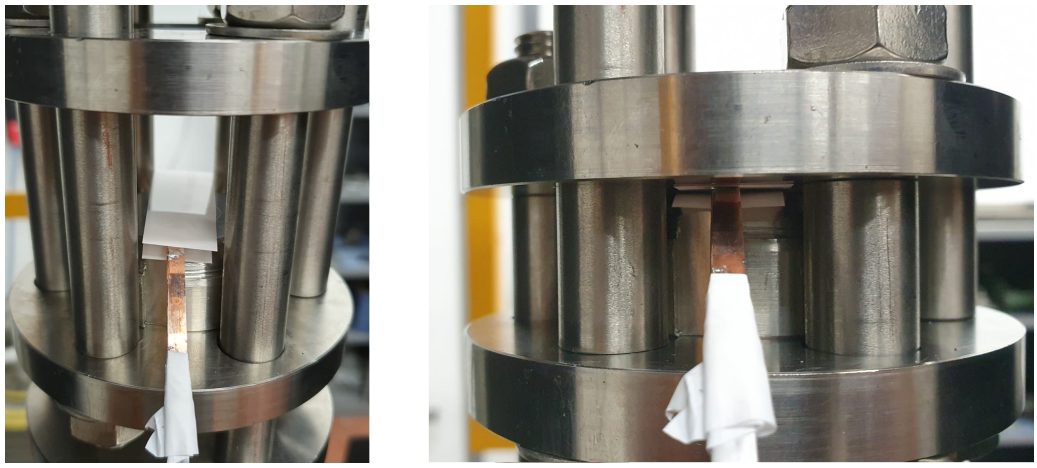


Figure 4.19: Example of uniaxial compressive stress test on 4 mm tapes inside the stainless steel insert for the universal test machine.

before and after compression is represented inside the compression set up together with Fujifil Prescale pressure sensitive paper. Indeed, to evaluate the contact area, an increasing number of 4 mm tape has been piled up to form a stack so that the progressive build up of the extra thickness at the edges could be observed through the imprint left on the pressure sensitive film. The stack underwent uniaxial compressive load, given through the universal test machine adapted with the ad hoc stainless steel insert. The compressive load was set to apply 10 MPa to the nominal tape area (i.e. calculated assuming a perfectly flat tape), which was taken as a representative value as, for instance, is equal to ESMA pre-compression stress value. Fujifilm Prescale MS film was used for this pressure value. To evaluate the contact area, the pressure-sensitive paper was scanned, and the contact area was quantified pixel by pixel using the image average intensity as a threshold, as previously described in the previous chapter. The results are shown on the top right part of Fig. 4.18 and the corresponding value of the contact area are in the first half of Tab. 4.5. The process has been iterated with up to 30 tapes in the stack, when the contact area would not decrease anymore. As shown in Fig. 4.18 and reported in Tab. 4.5, increasing the number of stacked turns may be related to cumulative effect caused by the dog-bone shape of the tape, ultimately leading to a reduced turn-to-turn contact area. This also leads to a localized increase in effective pressure, as the mechanical load becomes concentrated along the tape edges, which means roughly a factor 2 increase in the expected stress for 4 mm tapes.
To evaluate a possible damage introduced by a reduction of the effective contact area, the process was repeated considering also 12 mm wide tape, with a compressive load up to 100 MPa. This value approaches the overall compressive stresses inside a racetrack coil of ESMA. In this second case a total number of six tapes, both 4 mm and 12 mm, were first tested in LN_2, before composing the stack, to measure their critical current. After the stacking and the 100 MPa load, the six tapes were tested again in LN_2 to evaluate a possible degradation of the critical current. The afterimages of the 12 mm tape are shown in the bottom right part of Fig.4.18 and the contact area result are summarized in the second half of Tab. 4.5. From the resulting contact area, the effective stress on the 4 mm and 12 mm stacks, resulted to be 200 MPa and 350 MPa respectively. To asses a possible cumulative effect also on 12 mm wide tape, although the images obtained with only six tapes show a contact area reduction already the order of $\sim$ 70 %, a stack of 20

Tape width[mm]	P[MPa]	Stacked tapes	Contact area[%]
4	10	6	72
	10	10	71
	10	20	61
	10	30	52
	100	6	50
12	100	6	29
	100	6	27

Table 4.5: Compressive stress test samples



Figure 4.20: Imprint left on Fujifilm Prescale MS film by a stack of 20, 12 mm wide, HTS tapes under a compressive load of 30 MPa, resulting into an effective contact area of 22.7 %.



Figure 4.21: Imprint left on Fujifilm Prescale HS film by a stack of 20, 12 mm wide, HTS tapes under a compressive load of 30 MPa, resulting into an effective contact area of 14.1 %.

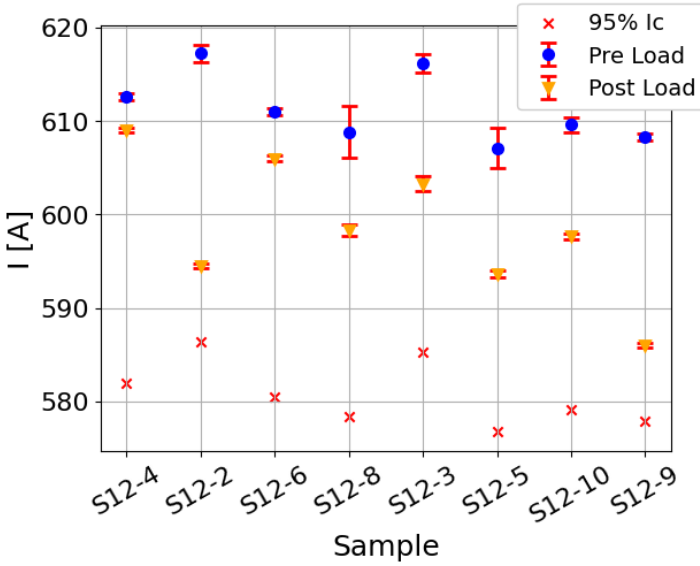


Figure 4.22: Compression test results for 12 mm tape: for each sample, the I_c value before the test, the margin of 95% calculated on this measure and the value after compression are reported.

tapes was created and pressed following the same procedure at 30 MPa. Two different Fujifilm Prescale sensitive films were used to impress different ranges of pressure: MS (10-50 MPa) and HS (50-130 MPa). The leftover imprints are showed in Fig. 4.20 and 4.21 respectively, where an effective contact of 22.7 % and 14.1 % was estimated, thus indicating that a slight build up could still be observed even though it saturates quickly with only few tapes due to the higher thickness difference. Moreover, the image taken using the HS film, confirmed that although the effective contact may be higher than the 20 %, the area were stresses are concentrated the most is further reduced to the very edges of the tape.

For what concerns the degradation, in the case of the 4 mm tapes, 4 out of 6 samples exhibits a degradation under the 5% threshold, while the remaining two samples show a degradation of 14.3% and 10.8% (Fig. 4.23). Further measurements, to increase the sample size, are needed to draw conclusions. In particular, handling damages during samples preparation cannot be excluded, especially with 4 mm tapes which are mechanically more fragile than the 12 mm ones. Instead, every 12 mm sample exhibits a Ic degradation under the 5% threshold, meaning no significant degradation can be observed, as in Fig. 4.22. In the figure, two pre-campaign measurements are included, being the tapes used to validate the process, which shown no degradation, too. In both cases the error-bar results from the standard deviation of multiple I_c measures performed consequentially on the same sample. A more comprehensive experimental campaign is under development to include measurements of the stack Young's modulus and to increase the sample size for I_c measurements following the application of a known compressive load. Moreover, the effects of load cycling will be investigated to exclude the possibility

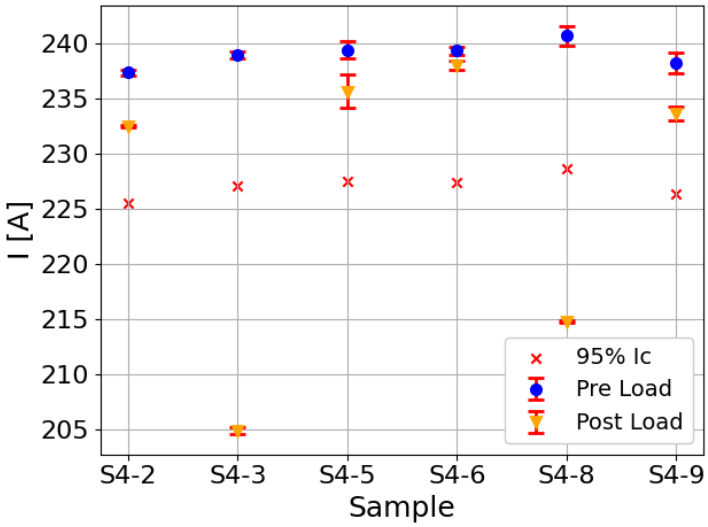


Figure 4.23: Compression test results for 4 mm tape: for each sample the Ic value before the test, the margin of 95% calculated on this measure and the value after compression are reported.

of crack initiation and further propagation during repeated magnet cycling.
The effective area reduction value could be used to estimate the real value of the contact resistance inside a MI or NI magnet which is fundamental to build a full 3D model discretizing the geometry over the tape width. The same consideration applies to thermal conductivity, as the performed measurements yield only an effective value, which may appear lower than expected, given the absence of an insulator. The intrinsic thermal conductivity of the material can instead be obtained by applying the appropriate area reduction correction to Eq. 4.2, thus resulting into a higher value which contributes to explain the results obtained while performing the measurement on the dry HTS MI stack.

4.2.3 Peeling

The measurements results observed by ASG Superconductors during the compressive stress test campaign on HTS tape stacks resembling the ESMA cable, highlighted a surprisingly low Young's modulus. This property for dry winding is known to be significantly lower than the bulk materials equivalent [98] and could lead to significant displacements within the coil when powering the magnet. As described in Sec. 4.2, a displacement of 0.2 mm is expected as a response to Lorentz forces acting to expand the coil in the xy-plane. This displacement is particularly critical near the inner junction, represented in blue in the left panel of Fig.4.3, since a shift applied to a fixed part, such as the brazed arc over the current adductor, may induce a peeling stress on the tape, potentially causing its delamination. To investigate this possibility, which could result in permanent damage inside the winding, a dedicated measurement setup was developed. The experimental set up, shown in Fig.4.24, consists into applying a controlled displace-

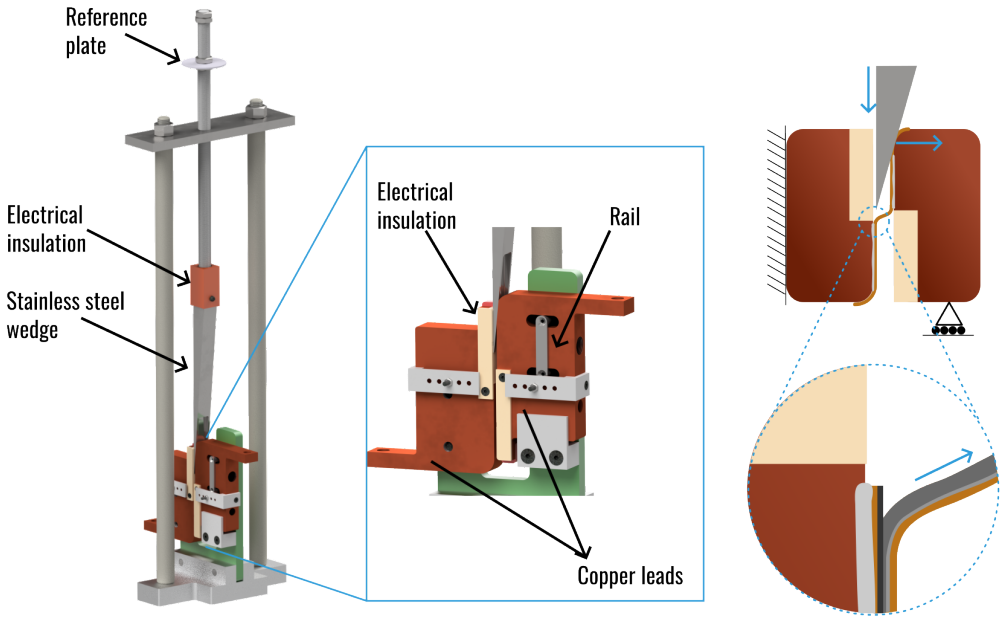


Figure 4.24: Visual representation of peeling test set up

ment between two copper leads using a precision wedge. One copper lead is fixed, while the other is mounted on a rail, allowing movement. A sketch of this working principle is showed in the right panel of Fig. 4.24. Both leads feature an uncovered copper section where the HTS tape is brazed and an insulated section to continue the tape connection onto the opposite lead. The brazing process involves pre-tinning both the HTS tape and the copper leads with SnIn, followed by heating to 150 °C using two 100 W heaters controlled by a PID temperature system. Displacement is applied by rotating a threaded rod that drives the wedge, designed with a 1:10 ratio: a full turn of the rod, with a thread pitch of 1 mm, corresponds to a 0.1 mm displacement, enhancing measurement sensitivity. The relative position of the threaded rod is monitored with a mechanical indicator (0.01 mm sensitivity) pointing to a reference plate, ensuring accurate displacement measurement. The zero point is defined by mechanically flushing the copper leads, from which the wedge begins to separate the movable section. Therefore, once the HTS sample is mounted on the copper leads, critical current measurements could be performed for different displacement values of the wedge, which could be directly translated in terms of displacement of the HTS tape with respect to the adductors themselves. This allows to create a critical current curve as a function of the mechanical displacement with respect to the current adductor, thus allowing to state a mechanical limit above which the tape delamination irreversibly compromise the tape performances. At the time of writing this thesis, the experimental setup is under manufacture, and the results will be disclosed in future publications.

4.3 Design of the magnetic measurement system

Upon realizing the full magnet, the Factory Acceptance Test (FAT) requires that the target field values between 2 T and 10 T with a minimum acceptance value of 8 T are reached and that field quality constraints within the GFR are satisfied. To this purpose, a dedicated magnetic measurement system was designed and set up in collaboration with ASG Superconductors. The magnetic measurement system for ESMA consists in a PEEC support hosting an array of seven calibrated Hall probe sensors. This system is represented in Fig. 4.25 placed within the bore of ESMA and the nominal position of the sensors with respect to the magnetic center is reported in Tab. 4.6 and graphed along the magnetic field profile in Fig. 4.26, where three sensors are aligned along the x-axis at the location corresponding to the central orange dot, as highlighted by the slots in the visual representation of the setup. To asses the robustness of the ESMA design as well as of the designed measurement system, a sensitivity analysis of ESMA was carried out using a Monte-Carlo like method where a full 3D model of the magnet was build in OPERA 3D and both the mechanical tolerances of the magnet and the uncertainties related to the placement of the measurement system were considered. A magnetic simulation was then performed and the field within the bore at the position of the sensors calculated to simulate the measure. In particular, a first step consisted into randomly changing the nominal position of the Hall probes in the measurement system. The considered displacement are represented in the left panel of Fig 4.25, where each probe is allowed to move by a certain amount Δx, Δy, and Δz with respect to their central position. Moreover, each slot is given a planarity uncertainty that may impact the final orientation of the probe with respect to the nominal field. The amount of these shift was randomly extracted using a uniform probability distribution to resemble the uncertainty of mechanical manufacturing. The system itself is then allowed to rotate around its axis up to a maximum amount δ, since its positioning will occur by coupling the squared piece on the bottom extremity to an analogue squared shaped slot on the bottom of the bore. The tolerances related to this joint could allow a rotation of the system. Another allowed rotation related to the positioning of the system, which is carried out by machining an edge on the bottom of the ESMA bore, is the possibility of the system of leaning towards this edge, thus resulting in a maximum estimated rotation angle α, as showed

Sensor	**x-position [mm]**	**y-position [mm]**	**z-position [mm]**
Sensor 1	0	0	- 134.8
Sensor 2	0	0	-76.1
Sensor 3 - Central	0	0	0
Sensor 3 - Left	-20	0	0
Sensor 3 - Right	20	0	0
Sensor 4	0	0	76.1
Sensor 5	0	0	134.8

Table 4.6: Nominal Hall probe positions within the ESMA magnetic measurement system

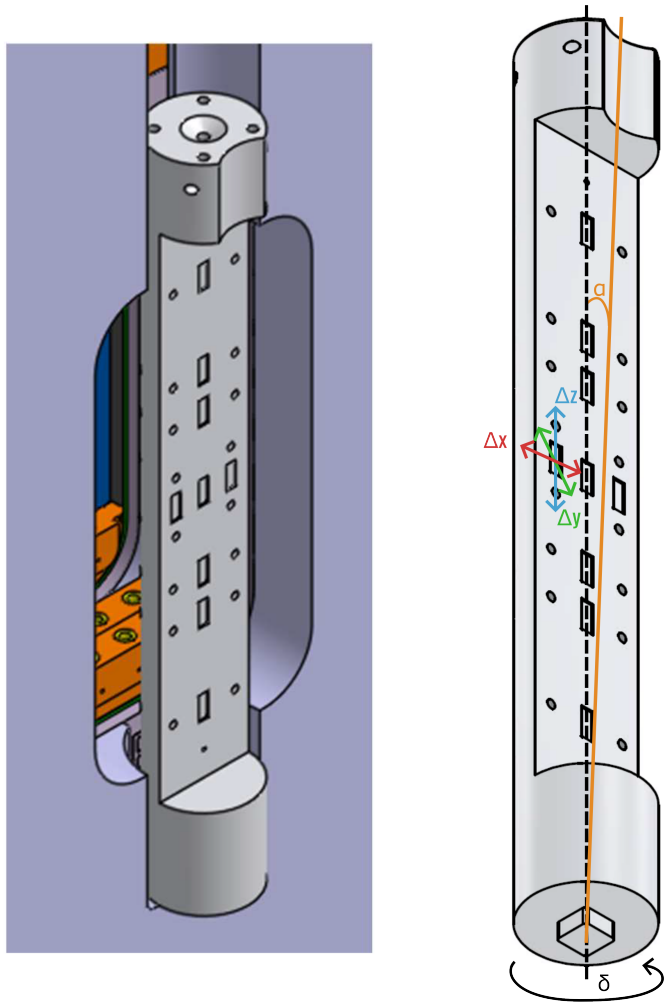


Figure 4.25: The left panel shows the magnetic measurement system for ESMA, placed within the bore of the magnet. The right panel shows the set up together with all the possible uncertainties on the Hall probe position caused by the manufacturing process and the positioning within the bore.

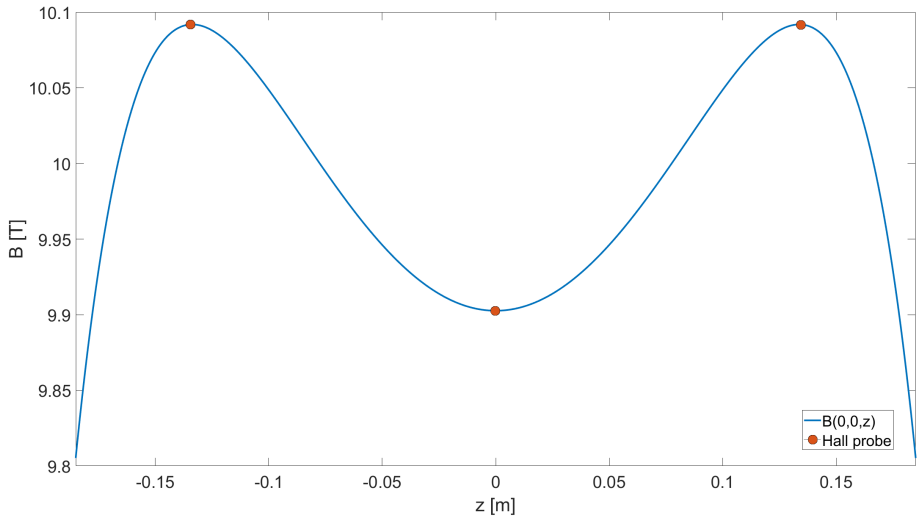


Figure 4.26: Magnetic field profile at the center of the magnet as a function of the longitudinal position. The orange dots represent the nominal position of

Parameter	Unit	Uncertainty
Δx	mm	$\pm$ 2
Δy	mm	$\pm$ 2
Δz	mm	$\pm$ 3
Flatness	deg	$0 \sim 0.5$
α	deg	$0 \sim 1$
γ	deg	$0 \sim 2$

Table 4.7: Summary of the uncertainties ranges related to the Hall probe sensor positioning in the magnetic measurement system for ESMA

in the left panel of Fig. 4.25. Also these quantities where included in the model and applied randomly by probing a uniform probability distribution. The range of values considered in this analysis regarding the tolerances on manufacturing and positioning of the measurement system is resumed in Tab. 4.7. The same procedure was applied to estimate the uncertainties expected in coil manufacturing and their mechanical structure. Data provided by ASG Superconductors, describing the possible deviations from the nominal coil positions, are summarized inTab. 4.8. Here,Δx, Δy, and Δz represent the positioning uncertainties of a single racetrack coil module with respect to its nominal center. In contrast, Δx_{ext}, Δy_{ext}, and Δz_{ext} denote the same type of positioning errors but for the two outermost coils, which are spaced 12 mm along the y-axis from the rest of the coil stack instead of 9 mm as for all other racetrack coils. Ultimately, the uncertainty on the coil width results from an estimation of the cumulative effect of the uncertainties on the thickness of a single tape, which is given likewise from the cumulative effect of uncertainties on each layer composing the HTS tape. The two sources

Parameter	Unit	Uncertainty
Δx	mm	$\pm$ 0.5
Δy	mm	$\pm$ 0.5
Δz	mm	$\pm$ 0.5
Δx_{ext}	mm	$\pm$ 0.5
Δy_{ext}	mm	$\pm$ 0.8
Δz_{ext}	mm	$\pm$ 0.5
Flatness	deg	$0 \sim 0.03$
Width	mm	$\pm$ 1

Table 4.8: Summary of the uncertainties ranges related to coil positioning and shape of ESMA.

of uncertainties were considered and a number of 10^5 magnetic simulations were performed. In each simulation the reference field was calculated using Eq. 2.15 and using data provided by the three sensors along the longitudinal axis, then the corresponding relative difference was calculated to retrieve the value of the field homogeneity. However, since the reference value was calculated on a integral over the longitudinal section passing from the center, the possibility of performing an average of these values to calculate the reference field was also investigate, although the difference in the calculated field homogeneity was negligible. Therefore, the data collected using this method used to calculate the corresponding probability distribution function which is represented for each sensor in Fig.4.27 The picture represents the probability distribution functions of the expected measurement results performed by the magnetic measurement system of ESMA. Each graph is referred to a single Hall probe sensor, numbered starting from the top one, with the three central plot referred to the three sensors in the center of the system. In each plot is reported the probability distribution function of the combined effect of all uncertainties (blue), together with the distribution caused by isolating the effect of the tolerances affecting the measurement system (green), and the ESMA magnet structure and windings (yellow). In particular it can be observed that the dominant effect on the overall distribution varies depending on the considered sensor: in case of the outermost sensors (sensors 1 and sensor 6), the standard deviation of the distribution is dominated by the uncertainties on the magnet assembly and winding, as the yellow and blue histograms are almost perfectly superimposed, whereas the opposite applies for the two sensors approaching the central ones where the error is dominated by the tolerances on the measurement system manufacturing and placement. For the set of three central sensors, the two sources of error are contributing almost equally to the final distribution. The probability distribution function are all centered on their x-axis on the homogeneity measure performed in the ideal case of each component in its nominal position. In each case the performed measure oscillates within a range which does not exceed the boundaries of the field quality requested for the ESMA magnet, i.e.: $\pm$ 1.5 %, thus stating the expected robustness of the system.

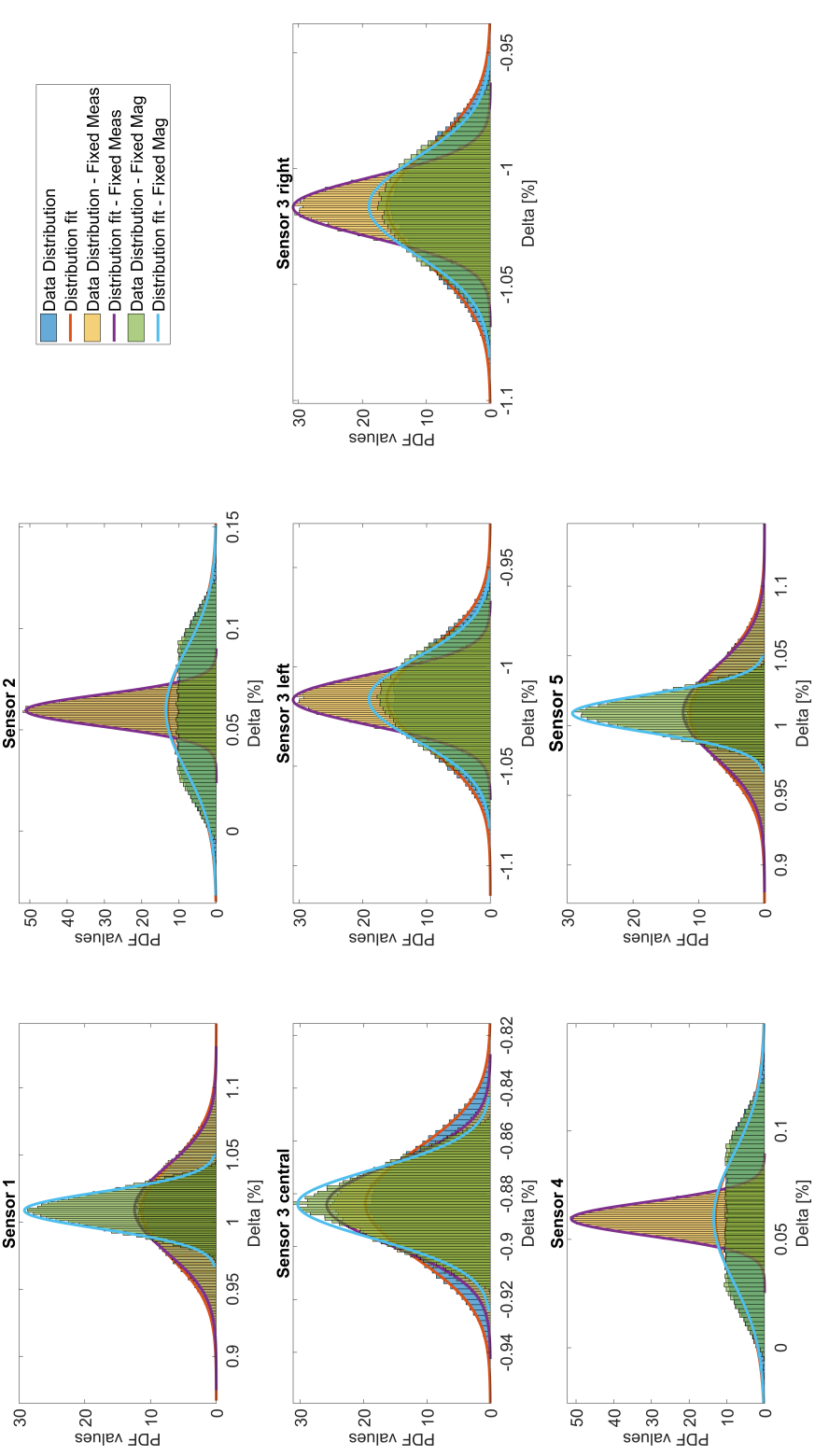


Figure 4.27: Probability distribution functions of the expected measurement results performed by the magnetic measurement system of ESMA. Each graph is referred to a single Hall probe sensor, numbered starting from the top one, with the three central plot referred to the three sensors in the center of the system. In each plot is reported the probability distribution function of the combined effect of all uncertainties (blue), together with the distribution caused by isolating the effect of the tolerances affecting the measurement system (green), and the ESMA magnet structure and windings (yellow).

4.4 Summary and achievements

This chapter describes the principles of the thermal and mechanical design of ESMA, together with synergic analyses, experimental measures and calculations which are subject of this thesis and listed below:

- To accurately predict the cool-down behavior of the magnet, as well as to aid further calculation on heat propagation in case of quenches, the thermal properties of the winding were characterized through **thermal conductivity measurements** performed on **tape stacks** representative of the metal-insulated ESMA cable.
- A major limitation was identified in the sample holder of the measurement setup, which could not sustain compressive stresses comparable to those expected in the ESMA coil, i.e., on the order of 100 MPa. As a result, **only a lower bound** for the **thermal conductivity** of a **dry-wound, metal-insulated coil** could be established, equal to approximately **0.015 W/m·K at 20 K** under a compressive stress of about **1 MPa**.
- Additional measurements were carried out on **wax-impregnated stacks** prepared under a defined pre-compressive load, in order to simulate the effects of winding tension and operational stresses for a potential insulated configuration aimed at ramped accelerator magnets.
- A dedicated experimental setup was then developed to support the mechanical design by measuring the **integral thermal contraction** of the HTS tape, found to be approximately **2.6 mm/m**. This value was used to design the winding mandrel so as to match the contraction of the winding itself, thereby avoiding losses in winding tension during cool-down.
- **Tape stacks** were tested under **uniaxial compressive load** to evaluate potential degradation at stress levels expected at the maximum operating field of 10 T within the ESMA magnet. **No degradation** was observed under these conditions. On the other hand, these tests highlighted two major mechanical characteristics of HTS tapes: a **lower than expected Young's modulus** and a **dog-bone** shaped profile.
- The **low Young's modulus** may lead to significant displacements within the coil, emphasizing the importance of proper winding pre-compression. Such displacements may also cause **tape delamination** in the region next to the inner splice. To investigate this effect, a **dedicated setup** was designed to measure performance degradation as a function of **displacement induced peeling**.
- A **magnetic measurement system** was developed to characterize the field homogeneity of ESMA. **A sensitivity analysis** was performed to assess whether the tolerance chain, accounting for both mechanical assembly and winding accuracy, could lead to a final measured field homogeneity above the accepted range within the good field region. However, the results confirmed that the design is robust and is expected to meet the required specifications.

CHAPTER 5

ESMA operation

With the final design of the ESMA magnet now established, comprising its complete electromagnetic, mechanical, and thermal architecture, the focus shifts to its operational aspects. Since the winding technology is based on a MI stack of twelve racetrack coils, specific challenges arise for both steady-state performance and transient behavior. In particular, the flow of radial currents during ramping results in significant heat generation, which must be carefully managed to ensure that the magnet remains within acceptable thermal limits while maintaining the reliable operation of a user facility. Beyond thermal considerations, the quench dynamics of the system must also be investigated in order to define an intervention strategy, also for scenarios where a quench is anticipated in the short term. To address these issues, this chapter first presents an operational methodology aimed at optimizing the charging process of ESMA within a prescribed temperature rise limit. It then proceeds to examine the expected quench dynamics of the magnet, with particular emphasis on the implications of sudden discharges, as employed in conventional detection and discharge protection strategy.

5.1 Charging time optimization

Although ESMA is designed using the MI winding technique to benefit both reduced charging times and enhanced operational stability, the challenge of prolonged charging remains. Charging times may increase not only due to the intrinsic charging behavior of the magnet being MI, but also because the flow of radial currents introduces an additional heat load. If the ramping rate is too fast, this heat load may exceed the available thermal budget, even though the electrical time constant would allow for faster charging. To mitigate this, the introduction of nonlinear ramping strategies offers the potential to shorten charging times while maintaining coil temperatures within safe limits. To address this issue, advanced methods from nonlinear optimal control theory [99] were employed. Specifically, an algorithm was developed to optimize input current profiles using a lumped-parameter model of the HTS system. Nonlinear optimal control provides a versatile mathematical framework capable of optimizing virtually any dynamic system by defining cost functions that incorporate state variables, inputs, and outputs over time. Among the control strategies proposed in the literature, Proportional-Integral-Derivative (PID) control has demonstrated the ability to reduce charging time

[100]. However, this approach inevitably produces additional heating. While this may not be an issue in helium bath, it is critical for cryogen-free magnets as ESMA where thermal budget is limited. PID control acts only on current, specifically on a current target, but control over the heating of the magnet is still an open point. PID control directly regulates current, specifically targeting current profiles, but does not explicitly address magnet heating, leaving control over the heating of the magnet still an open point. To overcome these limitations, nonlinear optimal control was adopted with the dual purpose of reducing charging time and actively managing coil heating. Nonlinear optimal control relies on mathematical principles to optimize system responses while accounting for constraints and objectives, and while maintaining scientific rigor, allows for relatively simple implementations, still widely capable of improving magnet performances. Despite the motivation lies in the specific need for the operation of ESMA, the proposed techniques are valid for virtually any non-chaotic or ill-posed system and could therefore be employed for any magnet.

5.1.1 Nonlinear Optimal Control

Nonlinear Optimal Control is a tool to compute the input for a dynamical system, over a period of time, such that an objective function is optimized and constraints are respected. The approach proposed is the Pontryagin Minimum (or Maximum) Principle, which is a necessary condition for optimally. This is also a sufficient condition for very simple problems (for instance, for linear systems under quadratic cost functions), however, for general systems, the sufficient condition is to satisfy the so-called Hamilton-Jacobi-Bellman (HJB) equation. Due to the practical difficulties to solve it even for moderately-sized systems, it is often acceptable to respect only the necessary conditions and evaluate the goodness of the solution with other means. Solving HJB equations, even for not-so-large systems, is still a field of study [101] [102]. To further discuss the theory, consider a dynamic system written as:

$$\dot{x}(t) = f(x(t), u(t)) \tag{5.1}$$

where t is time, x is the state-variables vector, u is the input vector and f is the system equation describing the time-derivative of x. For a magnet-like system, u is the current/voltage from power supply, while x is the set of current, temperatures, etc. inside the magnet.
The technique is meant to provide the feedforward, offline optimal input to minimize the following cost function:

$$J = \int_{t_0}^{t_f} L(x(t), u(t), t)dt + \Phi(x(t_f)) \tag{5.2}$$

where L is the instantaneous cost (it may be power consumption), while Φ accounts for the cost at final time, depending on a target value for the state. In particular, Φ penalizes any solution not reaching, at the final instant t_f, the desired values for current and temperature.
The main element of the Nonlinear Optimal Control based on Pontryagin principle is

the Hamiltonian. The Hamiltonian expresses how the system evolves in time and how good the objective is fulfilled. In this respect, the sensitivity of the system to the different outputs is expressed by the Adjoint Vector λ. These are additional variables (in the fashion of Lagrange Multipliers for classical optimization) to be solved in time. The Hamiltonian could be written as:

$$H(x(t), u(t), l(t), t) = L(x(t), u(t), t) + \lambda(t)^T f(x(t), u(t)), \tag{5.3}$$

and the equation that adjoint vector must fulfill as:

$$\dot{\lambda}(t) = -\frac{\partial H}{\partial x}(x(t), u(t), l(t), t) \tag{5.4}$$

A peculiarity of optimal control is that the boundary condition of adjoint vector is defined at the final time, so that backward time-integration is needed. This is because this condition is meant to guarantee that the optimality of final cost $\Phi(x(t_f))$ is guaranteed. It writes:

$$\lambda(t_f) = \frac{\partial \Phi}{\partial x}(x(t_f)) \tag{5.5}$$

The last element to be defined is the expression for the Pontryagin Minimum Principle, which is the condition to discern, among all the state trajectories fulfilling the equations above, the ones respecting the necessary condition for optimality:

$$u^*(t) = \text{argmin}_u H(x(t), u(t), l(t), t). \tag{5.6}$$

This writing of the principle is exploited later on in the algorithm construction. The theory presented up to this point is not explicitly accommodating constraints. The need for hard limitations of state x and/or input u is unsurprisingly common in real-life problems. One of the typical example is the input saturation, which means that the values of u must be limited in a certain range. For instance, any power supply is rated for a minimum and maximum current, voltage and power.
Constraints, in principle, should be respected with the same severity as the system equations. This means to introduce an additional adjoint vector $\boldsymbol{\mu}(t)$ to guarantee that constraint conditions are respected, again in a similar fashion to Lagrange Multipliers. For instance, to limit input u to be in the interval $(-u_{\text{lim}}, u_{\text{lim}})$, we add $\boldsymbol{\mu}(t)(|u| < u_{\text{lim}})$ in Eq. 5.3 and Eq. 5.4. In practice, this approach, the hard constraint approach, is avoided, by adding penalty terms in $L(x(t), u(t), t)$ (soft constraint approach). This can be done with piecewise-functions or barrier functions. An example of the former may be:

$$S(t) = \begin{cases} 0 & \text{if } |u| \leq u_{\text{lim}} \\ (u - u_{\text{lim}})^2 & \text{if } |u| > u_{\text{lim}} \end{cases} \tag{5.7}$$

The optimization process is conducted using a gradient-based method implemented in MATLAB. The method main characteristics include:

- The gradient of the Hamiltonian $\frac{dH}{du}$ as a key component for the approach, mutated from Eq. 5.6. Control inputs are updated iteratively based on the computed $\frac{dH}{du}$, with the incorporation of a relaxation factor to aid convergence.

- Being a gradient-based method, the optimization is executed iteratively, stopped by a specified number of iterations or convergence criterion.
- All ODEs (Ordinary Differential Equation) are solved numerically in time using MATLAB built-in functions.

While this implementation offers flexibility and generality, it is worth noting that due to its numerical nature and the complexity of the problems it may address, a substantial number of iterations, typically in the range of 10^2 to 10^3, may be necessary to achieve convergence. A pseudo-code is reported here, following the cost function defined in Eq. 5.2. Consider that function `i1()` is the contraction for the built-in function `interp1()`, while `f()`, `Adjoint()`, `Compute_dH()`, and `Compute_J()` are user-written functions:

```
% Initialization
N_iter_max = ...; % Max. number of iterations
t0 = ...; % Initial time
tf = ...; % Final time
X_t0 = ...;  % State at t_0 (Initial condition)
X_tf = ...;  % State at t_f (Terminal condition)
Q = ...; % Weight matrix Q (Cost function)
R = ...; % Weight matrix R (Cost function)
P = ...; % Weight matrix P (Cost function)
epsilon = ...; % Convergence threshold
weight = ...;    % Step-size for control update
for ii = 1:N_iter_max
    % Forward Integration
    [Tx, X] = ode45(f(t, X, i1(T, u, t)), [t0, tf], X_t0);
    % Update Terminal Adjoint Condition
    lambda_f = P * (X(end) - X_ref);
    % Backward Integration for Adjoint Vector (stiff!)
    [T_lambda, lambda] = ode15s(Adjoint(t, lambda, i1(T, u, t),i1(T_x, X, t), Q, R), [tf, t0
        ], lambda_f);
    % Align Vectors and Times
    X = i1(Tx, X, T);
    lambda = i1(T_lambda, lambda, T);
    % Calculate Delta H
    dHdu = Compute_dH(T, lambda, u, X, Q, R);
    H_norm = norm(dHdu, inf);
    % Calculate Cost Components
    J = Compute_J(T, lambda, u, X, Q, R, P, X_tf);
    % Check Convergence and Update Control
    if H_norm < epsilon
        break;
    else
        u_corr = weight * dHdu;
        u = u - u_corr;
    end
end
```

5.1.2 ESMA case study

The simple lumped-element model described in Sec. 1.2.4 is used to describe the behavior of ESMA while charging, considering both the electrical and thermal behavior. The model is not accounting for the superconducting behavior of the coil because the problem of charging NI coils typically regards currents below the critical current. If needed, an additional nonlinear resistance can be added in series with the inductance, without affecting the optimization procedure.

The cost function can address a wide spectrum of performance targets, reflecting various aspects of a superconducting magnet behavior. In the context of ESMA, which incorporates cryocoolers for cooling, two primary objectives are emphasized:

- Heat generation control: given the utilization of cryocoolers, it is imperative to limit the heat generation during the magnet charging process. It is possible to introduce a cost term in $L(t)$ regarding the heat generation, but, considering that the practical interest regards the rise in temperature, a (soft) constraint over temperature rise was chosen.
- Charging time optimization: while heat control is crucial, it is equally vital to achieve a charging time of the magnet that is practical for users. To strike a balance, the cost function includes terms to minimize the charging time. This task is performed by a cost term which penalizes azimuthal currents far from the target value $\boldsymbol{I}_{\mathrm{ref}}$.

For the costs, quadratic functions are employed. Quadratic functions allow for the formulation of optimization problems that can be efficiently solved numerically. Regarding constraints, instead, exponential functions are utilized to represent soft constraints, offering a flexible means of accommodating tolerance levels for constraint violations. The cost function is therefore expressed as:

$$\Phi = \left(\boldsymbol{X}\left(t_f\right) - \boldsymbol{X}_{\mathrm{ref}}\left(t_f\right)\right)^{\mathrm{T}}\left[P\right]\left(\boldsymbol{X}\left(t_f\right) - \boldsymbol{X}_{\mathrm{ref}}\left(t_f\right)\right), \tag{5.8}$$

$$\begin{aligned} L(t) &= \left(\boldsymbol{X} - \boldsymbol{X}_{\mathrm{ref}}\right)^{\mathrm{T}}\left[Q\right]\left(\boldsymbol{X} - \boldsymbol{X}_{\mathrm{ref}}\right) + \\ &+ V\exp\left(W\frac{\boldsymbol{X} - \boldsymbol{X}_{\max}}{\boldsymbol{X}_{\max}}\right) + Y\exp\left(Z\frac{U - U_{\max}}{U_{\max}}\right). \end{aligned} \tag{5.9}$$

The main terms of the cost function are: the target values for state variables in time $\boldsymbol{X}_{\mathrm{ref}}$ (containing $\boldsymbol{I}_{\mathrm{ref}}$), the maximum limits for state and input $\boldsymbol{X}_{\max}$ and $U_{\max}$, the weighting matrices for final and time-wise quadratic costs $[P]$ and $[Q]$, and the parameters to tune the exponential (soft constraints) V, W, Y, Z. This last aspect, i.e. exponential tuning, may be needed for the sake of the numerical stability of the gradient-based method, avoiding too steep gradients. The parameters adopted to apply the nonlinear optima control to the ESMA magnet are summarized in Tab.5.1. Since $[Q]$ is assumed to be a diagonal matrix only the values for currents and temperature are reported. Units for $[P]$ are mixed and thus omitted in the table, while the others make for a dimensionless cost function J. The choice of parameters for the cost function is determined empirically. This may appear incompatible with the concept of optimality, because each set of parameters returns a different solution and so to a different optimum. However, once arbitrarily fixed $[Q_I]$, in this case simply equal to one, only V, W must be tuned, to correct the soft-constraints-induced error and settle on the desired temperature. In this respect, the ratio between V and $[Q_I]$ influences the behavior: a larger V will result in a temperature closer to the target value, at the expense of slowing down azimuthal current. Experience has shown that values for V about one order of magnitude lower than $[Q_I]$ yields an acceptable temperature error ($< 1\ K$) for the analyzed magnet. Vice-versa, W is set as high as possible, to better approximate a hard-constraint, with the limiting factor being

the stability of the numerical method. Fig. 5.1 collects a set of solutions for the ESMA optimization problem. All the solutions share the same set of parameters (Tab. 5.1), except the ones for the constraint on temperature. In fact, notice the discrepancy between the stated target in the legend and the actual value, due to the already discussed soft constraints approach. Results are consistent with the expected behavior of an optimized system: temperature remains constant at a limit level, up to the point where transient from ramp to steady-state occurs and so heat generation is reduced. A small overshoot of I_{op} is automatically included to make this transition faster. Notice that the physical model of the power supply is not provided to the algorithm (Eq. 2.13 and Eq. 2.14), so that the time-history I_{op} is only due to the optimization algorithm (e.g. I_{op} is suddenly risen to about 60 A at the beginning). In the proposed example, this simplification is acceptable, because current is flowing radially (with negligible inductance) through eight 2.5 mΩ resistances, demanding for approximately 1.5 V. Once the optimal current input is computed offline, it is provided as a reference for the power supply. Nevertheless, no numerical model is without uncertainty and the chances are that the real system behavior deviates from the simulated one. In this respect, an useful derivation of optimal control theory is the Linear Quadratic Regulation (LQR) [103], which is a feedback-loop based control architecture. LQR provides a correction of the input, to be superimposed to the optimal trajectory computed offline; this correction is produced in real-time by a feedback loop similar to classical PID control, i.e. by scaling the errors between measures and references with gains. In LQR, however, the gains are in a $N \times M$ matrix, with N being the number of state variables and M the size of controllable inputs. The other difference with respect to PID is that gains are not constant, but changing in time according to LQR theory. LQR needing all the state variables to work is critical for systems where some state variables cannot be measured. If a subset of state variables is measured, however, state-estimation techniques are available to fully reconstruct the variables needed for LQR. The most common one is certainly Kalman Filter [104]. In this context, filtering is the problem of determining the state of a system from a noisy and incomplete set of observations, this is done by estimating not only the missing state variables, but also the variance of all the states. Indeed, both LQR and Kalman Filtering could be considered to improve the operation of NI and NI magnets.

Magnet Model		Optimization	
Parameter	Value	Parameter	Value
Radial R per coil (8 coils)	2.5 mΩ	P	[0]
Total inductance	6 H	Q_I	1 $\text{A}^{-2}s^{-1}$
Cryocooler slope	3 W/K	Q_T	0 $\text{K}^{-2}s^{-1}$
Heat Capacity	1600 J/K	V, W	0.2 s^{-1}, 10
Joint Resistances	100 nΩ	Y, Z	0 s^{-1}, 0

Table 5.1: ESMA Model parameters and optimization weights

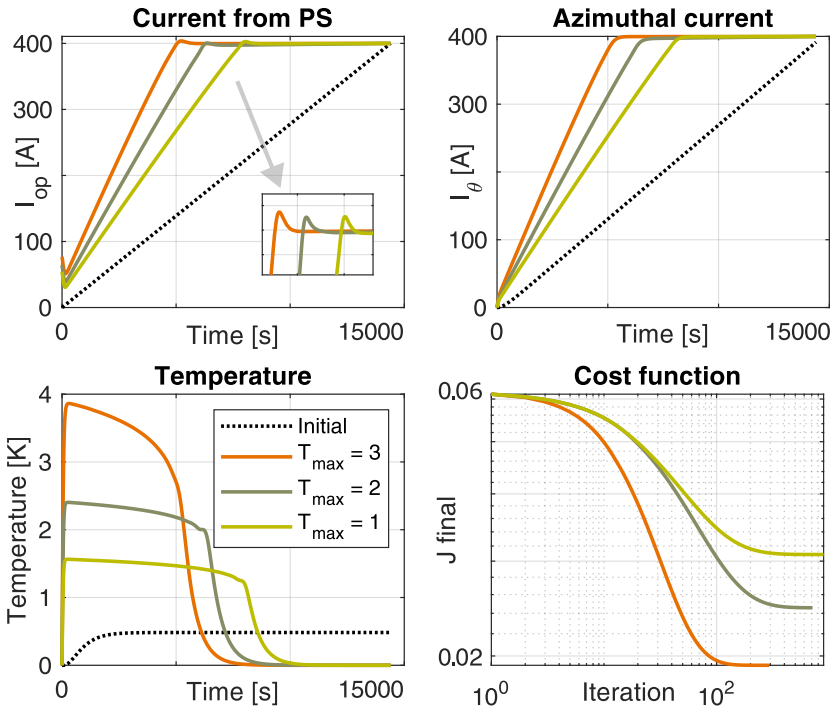


Figure 5.1: Three cases of optimal control for ESMA magnet. Time histories of the main quantities are shown, together with the evolution of the integral cost J as function of the solver iterations.

5.2 Quench analysis of ESMA

The design of ESMA is based on two HTS tapes wound in parallel, separated by a metal-insulation layer between each turn. The use of two parallel tapes mitigates the risk of localized defects within individual HTS conductors, while the MI configuration reduces the charging time and potentially preserves the self-protecting behavior characteristic of partially insulated HTS coils. However, the intrinsic self-protection capability of such coils decreases as the coil size increases. In NI coils the normal zone following a quench event propagates very rapidly in the radial direction but only slowly along the length of the conductor, as will be discussed in the simulations presented later. When the hot spot extends across the entire thickness of the winding pack, it obstructs current flow and causes local dissipation of the stored magnetic energy, resulting in elevated hot-spot temperatures. Additionally, a so-called shock-wave effect may occur: the electrical current is inductively transferred from quenched turns to still-superconducting ones, which may subsequently quench due to over-current. This cascade of high current density propagates through the coil, inducing large localized Lorentz forces. The shock-wave effect is considered a likely cause of mechanical damage in large HTS magnets. A detailed quench simulation, combined with a mechanical stress analysis based on the resulting current density distribution, is therefore necessary to evaluate whether the coil can withstand such events.

Parameter	Unit	Value
V_{Cu}	%	33
V_{Hast}	%	49
V_{304}	%	18
ρ_{Cu}	kg/m^3	8960
ρ_{Hast}	kg/m^3	8890
ρ_{304}	kg/m^3	7800
E_{mag}	MJ	3.6

Table 5.2: Material properties adopted in the preliminary quench analysis for ESMA

5.2.1 Preliminary quench considerations

As a first approximation to assess the self-protective behavior of the coil, the temperature rise by assuming that the entire stored magnetic energy of the system is dissipated uniformly within the coil volume can be estimated as:

$$\int_{T_0}^{T_{max}} c_p(T) \cdot V_{mag} \cdot \rho dT = E_{mag} = \frac{1}{2} L I^2 \tag{5.10}$$

In the case of ESMA this expression can be re-elaborated as:

$$\int_{T_0}^{T_{max}} \left(c_{pCu}(T) \cdot V_{Cu} \cdot \rho_{Cu} + c_{pHast}(T) \cdot V_{Hast} \cdot \rho_{Hast} + c_{p304}(T) \cdot V_{304} \cdot \rho_{304}\right) dT = E_{mag} \tag{5.11}$$

Where c_p, V_p, and ρ refer respectively to the specific heat, the volume fraction and the density of the material specified in the subscript. In particular the MI coils of ESMA were modeled as entirely built by copper and Hastelloy C-276 for what concerns the HTS tape, and AISI 304 for the MI layer. The volume fraction was calculated such that the sum of each contribute equals the volume of the 12 racetrack coils of ESMA. These values are reported together with the values of the density and magnetic energy in Tab. 5.2. The curves of the specific heat for stainless steel and copper were taken from MATPRO [105], whereas Hastelloy properties, including the deposited buffer layers, were taken from [106]. As a first approximation of the peak temperature following a quench, three scenarios were analyzed using Eq.5.11. In the first case, all the stored magnetic energy is assumed to be uniformly absorbed by the entire coil volume. In the second scenario, the normal zone extends longitudinally over 200 mm of winding, and the full magnetic energy is dissipated within that volume. In the third case, the normal zone spreads only 100 mm along the conductor. In all scenarios, the coil operates at its maximum magnetic field of 10 T, corresponding to a stored energy of 3.6 MJ. The total active coil volume (including the HTS tapes and MI layers) was calculated to be 0.0126 m^3, which reduces to 0.00084 m^3 and 0.00168 m^3 for the reduced cases. From Eq.5.11, it was determined that in case the entire stored magnetic energy was distributed overall the full coil volume, the

coil temperature would rise to approximately 185 K. When the energy is deposited over a 200 mm normal zone, the resulting peak temperature increases to around 827 K, and for a 100 mm zone it reaches approximately 1500 K. These results indicate that the coil must quench sufficiently fast to prevent excessive hot-spot temperatures. To promote heat diffusion and limit local overheating, one possible approach is to open the circuit breaker immediately after quench detection. This action interrupts the current supplied by the power source, forcing the current to flow radially through the coil and effectively heating the entire winding pack. If the radial resistance is sufficiently high, the coil can heat uniformly before the normal zone propagates further. The initial temperature increase following breaker opening can be estimated by dividing the power dissipated by the radial current, RI^2, by the volumetric heat capacity and the corresponding coil volume, as described by the following equation:

$$\frac{dT}{dt} = \frac{P}{C_p\rho \cdot V_{mag}} \tag{5.12}$$

Which again in the considered case can be expressed as:

$$\frac{dT}{dt} = \frac{P}{(c_{pCu}(T) \cdot V_{Cu} \cdot \rho_{Cu} + c_{pHast}(T) \cdot V_{Hast} \cdot \rho_{Hast} + c_{p304}(T) \cdot V_{304} \cdot \rho_{304})} \tag{5.13}$$

Based on the expected contact resistance of ESMA, measured on a dry stack representative of the MI cable and subjected to nominal compression at the maximum field of 10 T, a value of 240 $\mu\Omega\cdot cm^2$ was obtained. From this value, the total resistance of the twelve racetrack coils can be estimated to be approximately 0.5 mΩ per coil, corresponding to about 6 mΩ for the entire magnet. After opening the circuit breaker at the maximum operating current, the instantaneous power dissipated in the coil can be estimated as $P = RI^2 \simeq 8$ kW. The heat capacity of the materials constituting the magnet at the operational temperature of 20 K, together with their respective volume fractions, was determined using the same parameters adopted in the previous analysis. Same total magnet volume of 0.0126 m^3 was adopted. This yields an average temperature rise rate of approximately 11 K per second. In some regions of the coil, the temperature margin may reach values of around 40 K, implying that more than one second would be required for those areas to quench. This indicates that the quench protection strategy for this magnet requires further investigation, as its effectiveness strongly depends on the temporal evolution of the quench propagation. If the normal zone does not extend throughout the entire coil and no external protection mechanism is implemented, the local temperature rise in the hot-spot region would become excessively high, inevitably leading to coil damage during a quench event.

5.2.2 Single coil quench analysis

To further investigate the dynamic of ESMA during a quench event, a first quench analysis was performed on a single coil submerged in a background field of 10.55 T by Little Beast Engineering [83]. The primary objective of this analysis was to determine the physical behavior of a coil during a quench event, in order to state its self-protective



Figure 5.2: Position of the heater on one racetrack coil of ESMA for the quench analysis of a single coil in a background field of 10.55 T.

characteristics or to help elaborating a protection strategy. For the magnet to be self-protecting, it must be able to withstand the release of its stored magnetic energy without sustaining damage. Such damage could arise from excessive hot-spot temperatures, mechanical stresses induced by large thermal gradients, or from a shockwave effect caused by a rapid and violent discharge. To assess this behavior, a three-dimensional quench analysis was carried out using a 3D thermal-electromagnetic network solver capable of simulating time-dependent thermal, electrical, and magnetic interactions in superconducting systems.

To initiate a quench, a virtual 180 W heater was applied to one of the racetrack turns from 0.1 s to 1.16 s in terms of simulation time, after which the heat diffusion and current redistribution were simulated under adiabatic conditions. The position of the heater with respect to the racetrack coil is represented in Fig. 5.2. The analysis started with a simulation of a quench event without any protective intervention, in order to analyze the intrinsic physical behavior of the coil during a quench event and to assess whether quench detection and protection strategies could be realistically implemented. Consequently, the quench protection delay was investigated. The detection delay is defined as the time interval between quench detection and the activation of the protection system. It was soon observed that the time window during which any quench protection could effectively mitigate damage was extremely limited. Moreover, as it may occur during practical operation, there may be circumstances in which an operator needs to discharge the coil rapidly even in the absence of a quench. To explore these conditions, additional simulations were performed where no quench occurred but different discharge procedures were applied. These included opening the circuit breaker, ramping down the power supply at controlled rates of 2 A/s and 1 A/s, and performing a discharge through an external dump resistor. Simulation were performed assuming the expected value of the contact resistance in ESMA coils to be 240 $\mu\Omega{\cdot}mm^2$. The materials used to model the racetrack coil were, as for the preliminary analytical analysis, copper, Hastelloy C-276 and AISI 304, while the critical surface of the HTS tape was described using the measurements documented in the Robinson Research Institute data [71] as prelimi-

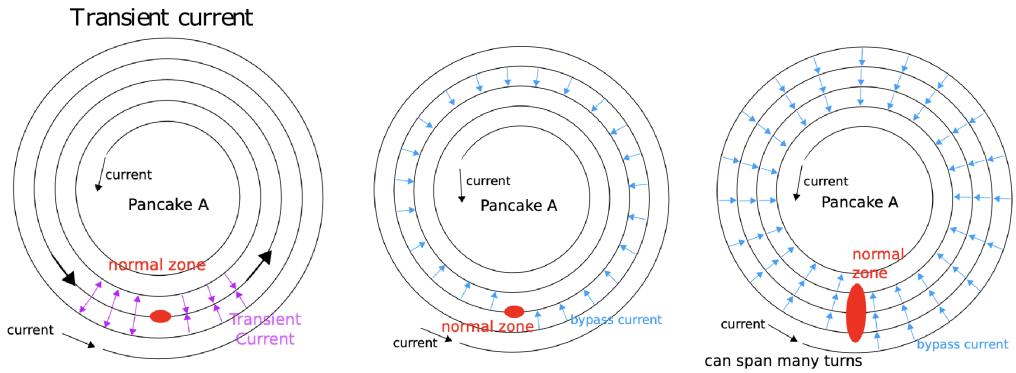


Figure 5.3: The current redistribution around a hot-spot or defect.

nary values. Moreover, the connection plate made of AISI 316 stainless steel, the cooling plate and two current leads both realized in copper were also included in each of the simulations.
The thermal conductivity of the MI winding was derived from its electrical resistivity, according to the Wiedemann–Franz law:

$$k = LT\sigma \tag{5.14}$$

where σ is the electrical conductivity, L is a constant value, defined as Lorentz number, equal to $2.44{\cdot}10^{-8}\mathrm{V}^2/\mathrm{K}^2$ and T is the temperature. It is important to note that this description is based on an assumption, as the Wiedemann–Franz law strictly applies to bulk materials. This highlights the necessity of performing dedicated thermal conductivity measurements on dry windings, where contact resistance and anisotropy can significantly affect heat transfer properties. Experimental measurements on the MI material, described by Fig. 4.12 in Sec. 4.1.1, however, indicates a thermal conductivity strongly lower than the theoretical value calculated using Eq. 5.14, consistent with the expected reduced heat transfer through dry-wound steel tape layers. Nevertheless, since the measurements could not reproduce the compressive stress conditions experienced by a single coil under winding tension, thus leading to an underestimation of the actual contact quality, the Wiedemann–Franz law was adopted in this first calculation as an approximation. Clearly, the actual value of the thermal conductivity is expected to lie between these two limits, as it strongly depends on the pressure applied between the tapes.

In order to interpret the results of the MI coil simulations, it is essential to understand the different paths that the current may follow within a NI or MI type of winding. As described in Sec. 1.2.4, a non insulated coil can be approximated by an equivalent electrical circuit consisting of an inductor and a resistor connected in parallel. The inductive branch represents the superconducting spiral path followed by the HTS tapes, while the resistive branch corresponds to the radial current path between adjacent turns, where the MI layer provides a finite contact resistance. When the current in varies, the resulting transient current in a non-insulated coil initially flows through the resistive radial path,

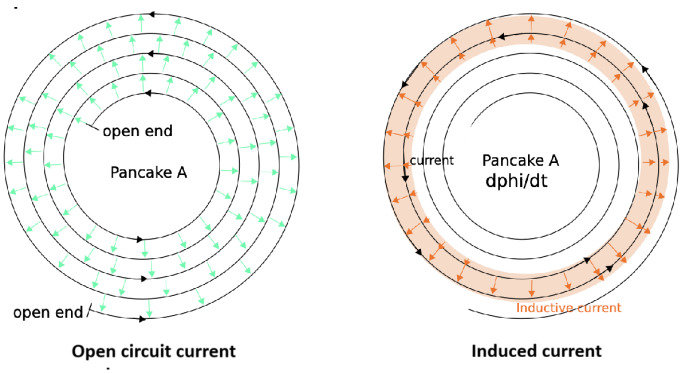


Figure 5.4: Current paths in the two analyzed cases of opening the coil circuit (left figure) or discharging the coil on a bypass diode (right figure).

in the case of ESMA, through the stainless steel layers of the MI. After a time consisting in roughly ~ 5 charging time constants τ, defined as $\tau = L/R_{rad}$, the current gradually settles into the superconducting spiral path. If a local hot spot develops in one of the turns of the MI coil, the transient current can bypass the affected region as showed in the first panel of Fig. 5.3, allowing neighboring turns to act as additional stabilizing elements. This mechanism significantly enhances the overall stability of the coil. In case the hot spot persists, the current eventually bypasses one or more turns entirely, as illustrated in the next panels of Fig. 5.3. Another important feature of MI windings is that the resistive radial path acts as a shunt between the coil terminals. When the power supply is disconnected, the current loop closes through this radial resistive path, allowing the coil to self-discharge without arcing, as shown in the first picture of Fig. 5.4. In this case, the stored magnetic energy is dissipated internally within the coil, partially converted into heat by joule effect through the radial resistive path. As the coil discharges, the changing magnetic field induces additional circulating currents within the winding, illustrated in the right picture of Fig 5.4. All these current pathways may operate simultaneously, which makes distinguishing their respective effects particularly complex when overlapping in time.

The first simulated scenario consisted in a quench event which was induced by a 180 W heater fired in the time window between 0.1 s and 1.16 s. Different heater settings were simulated, however it was found that the adopted heater setting was needed to start a quench in a single ESMA coil in a 10.55 T background field that would last, propagate, and continue to exist after the heater was switched off. For less powerful heater settings the quench would disappear. The heater caused a local normal zone voltage near the heater position. This normal zone voltage is shown in Fig. 5.5 together with the heater power during the first 5 s of the simulation. The evolution of the HTS temperature at the quench location, along with the average HTS temperature across the coil, is shown in the top panel of Fig. 5.6. As the heater is fired, the temperature rises due to the locally deposited heat which cannot diffuse from the nearby region as quickly as it is generated. Once the heater is switched off, the temperature begins to decrease momentarily. However, since the HTS cable has already transitioned to the normal state and

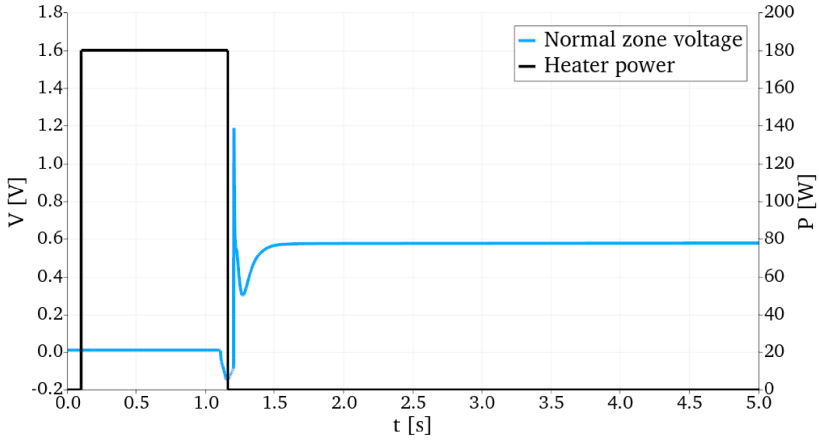


Figure 5.5: Normal zone voltage and the heater power as a function of time.

the power supply remains active, the resistive zone heats up due to joule heating, which contributes in further expanding the normal region. Consequently, the peak temperature in the HTS increase again, producing a second temperature rise, visible as a secondary bump in Fig. 5.6 around 1.3 s. The average and maximum temperatures of the coil, connection plate, cooling plates, and current leads as functions of time for the first 5 s of the simulation, are reported in the bottom panel of Fig. 5.6. After approximately 1.35 s, the maximum temperature in the HTS decreases once again. This occurs because the transport current diverts from the quenched region and redistributes through the metallic insulation into adjacent turns that remain superconducting. This local modification of the current path, and the associated change in magnetic field, induces an electromagnetic transient, observed as a current wave propagating through the HTS. The evolution of this phenomenon is reported in the top picture of Fig. 5.7, where the maximum and minimum longitudinal current densities in the HTS are graphed. As the current wave develops, both the maximum and minimum longitudinal current density increase in magnitude. The current wavefront progressively builds up current as additional turns quench and transfer their current into the propagating front. As a result, the average longitudinal current density decreases, while the magnitude of the minimum longitudinal current density grows exponentially. This behavior is already observed before the heater is switched off at 1.16 s. The average current densities in the HTS coil, connection plate, cooling plate, and current leads are shown in the bottom panel of Fig. 5.7. When the average current in the coil decreases, the variation in magnetic flux induces circulating currents in the closed-loop metallic structures of the connection and cooling plates. This induction effect explains the peaks observed in the average current curves of these components, as illustrated in the bottom graph of Fig. 5.7.

During the phase where the average current density decreases, the peak HTS temperature also drops, as the current is effectively diverted away from the quenched zone to the adjacent superconducting turns. Once no current flows through the normal zone, the heat generation ceases, and thermal diffusion causes the temperature around the

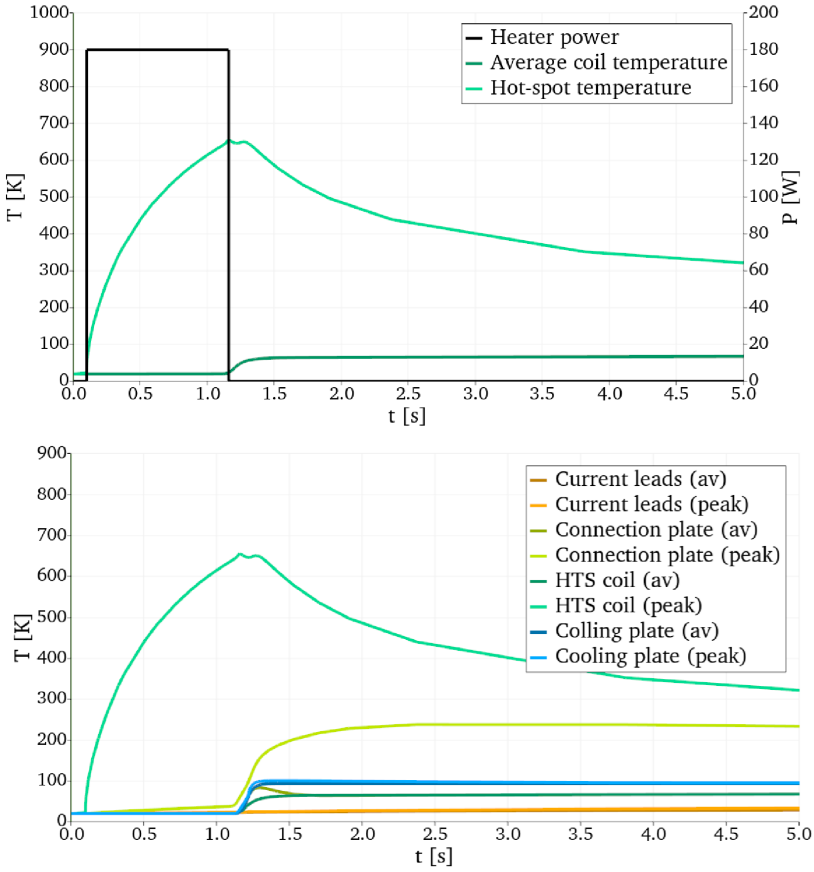


Figure 5.6: The temperature of the hot-spot and the average coil temperature are showed together with the heater power as a function of time in the top picture. The temperature in the HTS coil, connection plate, cooling plate, and current leads during as a function of time in case of no intervention during a quench event are graphed in the bottom figure.

quenched region to gradually decrease. Simulation results concerning the 3D temperature and longitudinal current density distributions in the quenched region of the single ESMA pancake at various times during the simulation are reported consequentially in Fig.5.8 and Fig. 5.9. In the early stage, the initial hot spot appears as a thin bright band on the inner side of the coil. The corresponding current density map shows that the quenched turns already carry no current, i.e.: 0 A/mm^2. As time evolves, the hot spot expands while a current wave propagates radially outward. The magnitude of the current density in this wave increases as it moves, whereas the current density in the inner turns drops to zero. The inner turns, being the first to quench, remain the hottest relative to the outer turns across the current wavefront. As the simulation progresses, the current wave continues to move radially outward until current remains only in the outer and inner turns and the current leads. This condition is shown in Fig. 5.9 at 2.4 s. At this point, the average current density in the HTS is approximately 1 A/mm^2, meaning

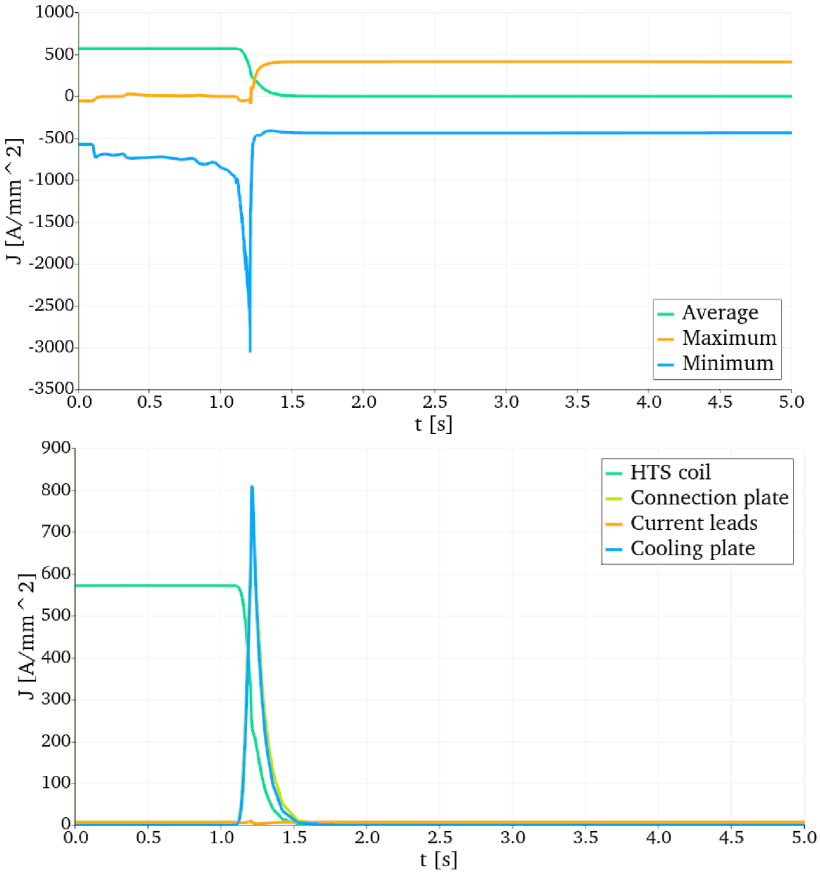


Figure 5.7: The maximum, the minimum, and the average longitudinal current density in the HTS coil during the first 5 s of the simulation are represented in the top picture. The average current density in the HTS coil, connection plate, cooling plate, and current leads in the same time range are graphed on the bottom.

that the majority of the coil was effectively discharged. Nevertheless, the power supply still delivers 1150 A to the magnet. The current thus follows a complex path: entering through the positive current lead, flowing around the HTS in the inner four turns, then moving radially through the HTS to the outer turns, circulating around approximately five turns before exiting through the outer current lead. Due to the finite radial resistance between turns, the coil continues to heat up as long as current is supplied. This effect is illustrated in Figure 5.10, which shows the evolution of both the maximum and average temperatures in the different components of the model over the full duration of the simulation, namely 1750 s. The corresponding longitudinal current density in the HTS and the voltage evolution across the various sections of the system are presented in Fig. 5.11 and Fig. 5.12, respectively.

From the obtained results, several key observations can be drawn. First, it was iteratively found that in order to initiate a quench capable of propagating throughout the

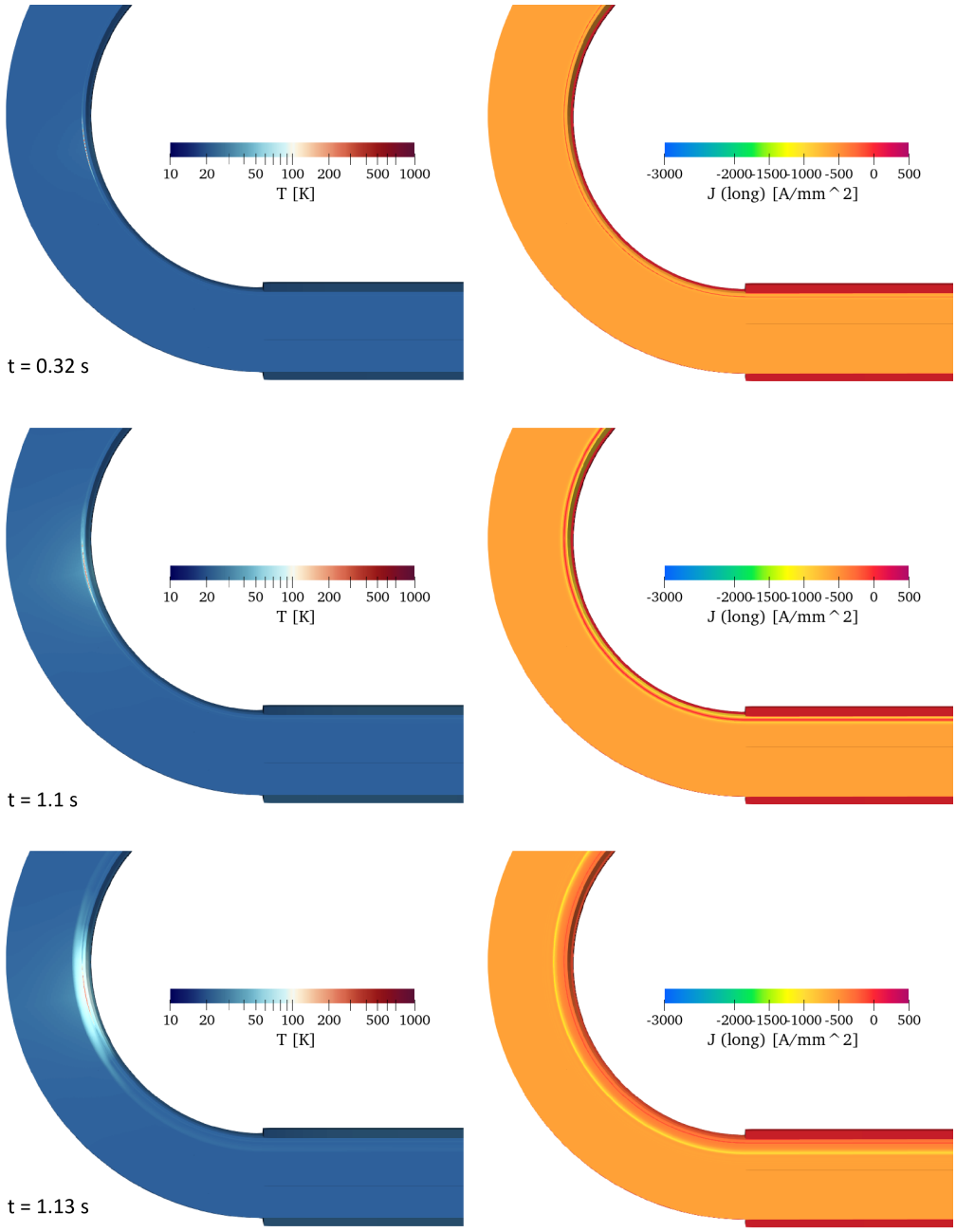


Figure 5.8: Temperature (left) and longitudinal current density (right) evolution for a single ESMA pancake in a background field of 10.55 T during a quench event represented at different times, from 0.32 s up to 1.13 s with respect to a quench initiating time of 0.1 s.

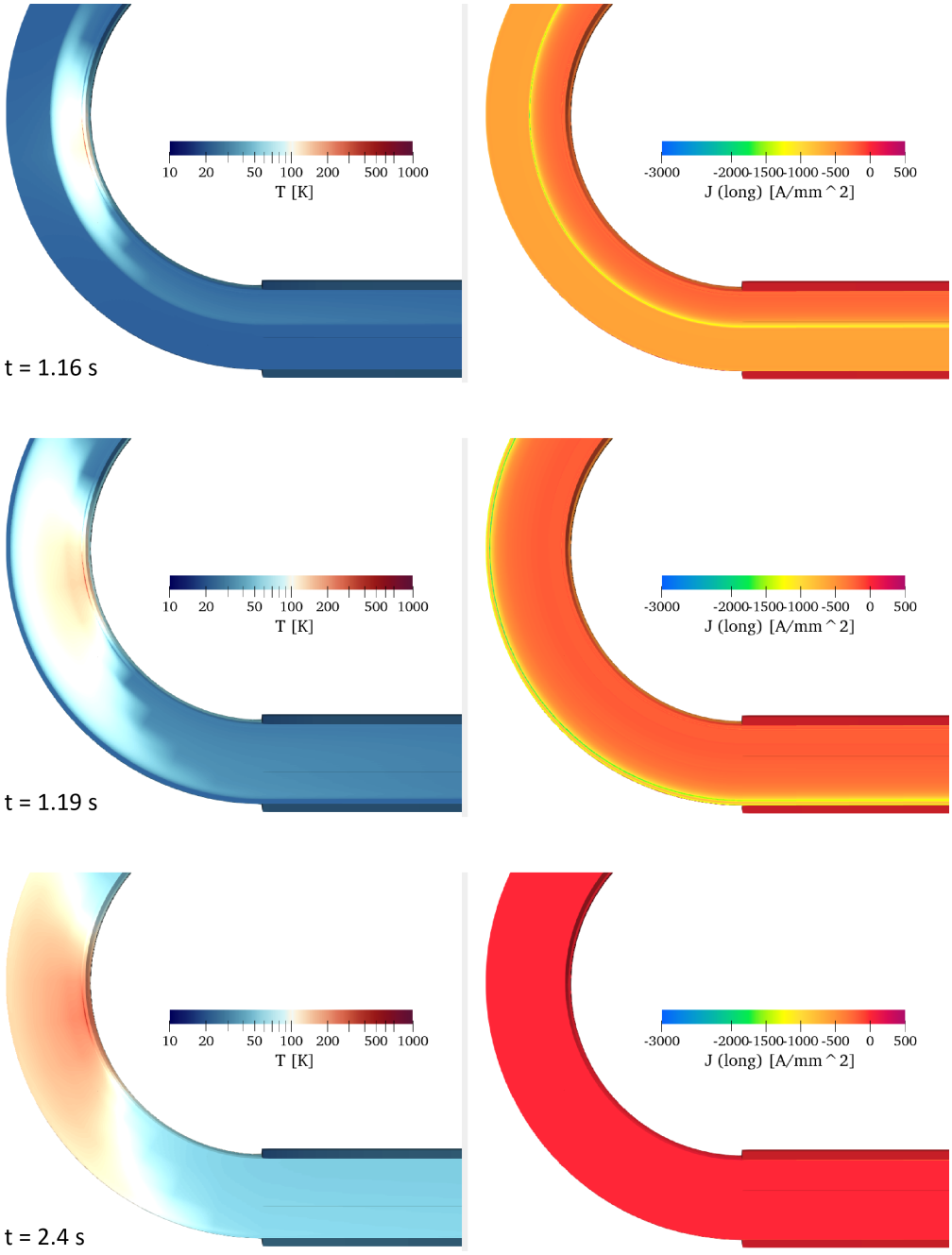


Figure 5.9: Temperature (left) and longitudinal current density (right) evolution for a single ESMA pancake in a background field of 10.55 T during a quench event represented at different times, from 0.32 s up to 1.16 s with respect to a quench initiating time of 2.4 s.

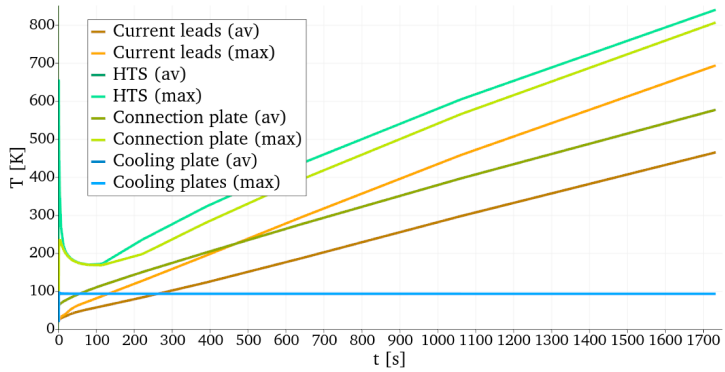


Figure 5.10: Temperature profiles of the coil, connection plate, cooling plate, and current leads as function of time during the quench simulation without intervention.

coil, a heating power of approximately 180 W must be applied for at least 1.1 seconds. This corresponds to an injected energy of about 200 J, deposited locally in a single point of the winding in the present simulation. Such an amount of energy is several orders of magnitude higher than what is typically required to trigger a quench in conventional LTS coils. It is therefore difficult to imagine a realistic scenario in which such localized energy deposition would occur accidentally, thus indicating that accidental quenches in ESMA are unlikely to occur. The most critical aspect identified during the simulation is the development of the current shock-wave. Examination of the coil temperature reveals that only the initial hot spot reaches temperatures exceeding 250 K, largely due to the artificially applied heater power. At 2.5 s, the average temperature of the coil peaks at around 65 K, while the main hot spot reaches approximately 220 K, with a very localized region rising to about 650 K. The current wave intensity, however, peaks earlier, around 1.3 s, and the associated Lorentz forces could potentially induce delamination of the HTS tapes or other forms of mechanical damage. This hypothesis should be further investigated through dedicated mechanical simulations. Ideally, the coil current should be extracted before 1.15 s to prevent the full development of this current wave. These findings highlight the extremely short time window available between quench onset and the formation of the current wave. Detecting such an event through voltage monitoring alone is therefore challenging, since once a turn quenches, the current rapidly redistributes away from that location, reducing the measurable normal-zone voltage. For this reason, quench detection strategies should consider combining voltage and temperature sensing, as temperature sensors may detect the quench earlier than voltage-based methods. A potential method to extract the current from the coil rapidly enough involves opening the circuit breaker of the power supply, thus completely disconnecting the coil from the current source. In this configuration, the current is forced to flow from the outermost turn back to the innermost one through the radial resistive path across the coil pack. The radial current flow would generate heat due to the finite radial resistance, ultimately driving the coil into a full quench and allowing the stored magnetic energy to be dissipated within the coil volume as quickly as possible. For these simulations, the

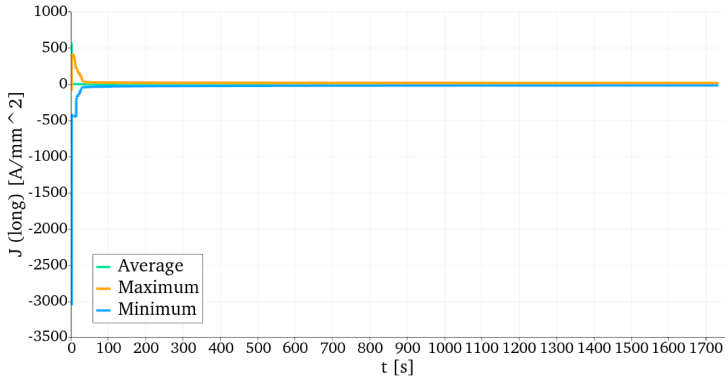


Figure 5.11: Maximum and minimum current density profiles of the coil during the quench simulation without intervention.

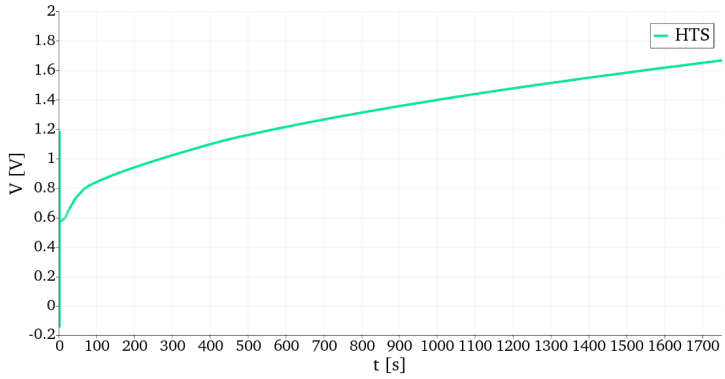


Figure 5.12: Voltage drop over the whole coil during the quench simulation without intervention.

quench detection threshold was set to 0.5 V, while the time delay between quench detection and the opening of the circuit breaker was varied. The time elapsed after the quench detection voltage had been reached, was set to the following values: [0.1, 0.2, 0.5, 1, 2, 5, 10, 30] s and a separate simulation was performed for each of these delay times. In each case, a single ESMA pancake coil, placed in a background magnetic field of 10.55 T, was initialized in a fully charged state, i.e.: powered with 1150 A. As in the previous case, a 180 W heater was activated for 1.16 s to trigger the quench. Once the voltage across the normal zone reached 0.5 V, the delay timer started, and after the specified delay, the protection system was activated by opening the circuit breaker. For all these simulations, the evolution of the normal-zone voltage, the maximum temperature in the HTS, and the difference between the maximum and minimum longitudinal current density in the HTS are shown in Fig. 5.13 Fig. 5.14. As observed in these results, the coil discharges significantly before the circuit breaker is opened in each simulation, coherently with the quench dynamic observed in the previous simulation where no intervention system was introduced. It is worth observing that for all cases summarized, the quench initiation phase, i.e.: up to approximately 1.16 s, is identical to that shown in Fig. 5.8, correspond-

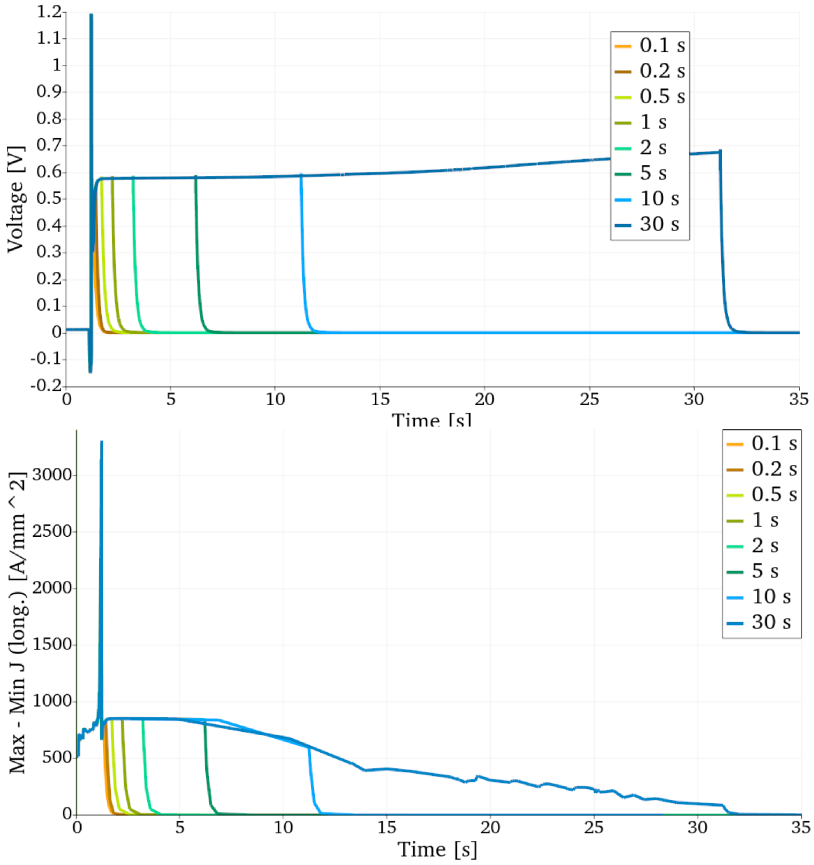


Figure 5.13: Normal zone voltage (top) and difference between the maximum and minimum longitudinal current density (bottom) a single coil of ESMA during a quench event for different delay times after which the circuit breaker is opened to extract the current.

ing to the period before the protection circuit is triggered.
However, an intervention system should ideally occur before the current shock-wave begins to grow exponentially in current density. To investigate this, a simulation was carried out in which the quench was initiated using the same procedure as in previous cases, but the circuit breaker was opened at t = 1.16 s, namely at the instant where the heater was switched off. In this scenario, quench detection corresponds to a voltage threshold on the order of 100 mV and a switching delay of approximately 40 ms. Considering an even faster protection trigger would result in too demanding detection and discharge criteria if relying only on conventional voltage-based methods.
The results of this simulation are presented in Fig. 5.15, which shows, starting from the top picture, the evolution of the normal-zone voltage, heater power, temperatures, and longitudinal current densities throughout the transient. From these results, it can be assessed that opening the circuit breaker at t = 1.16 s is not sufficient to prevent the formation of the current wave. In the last graph it is showed that the minimum longi-

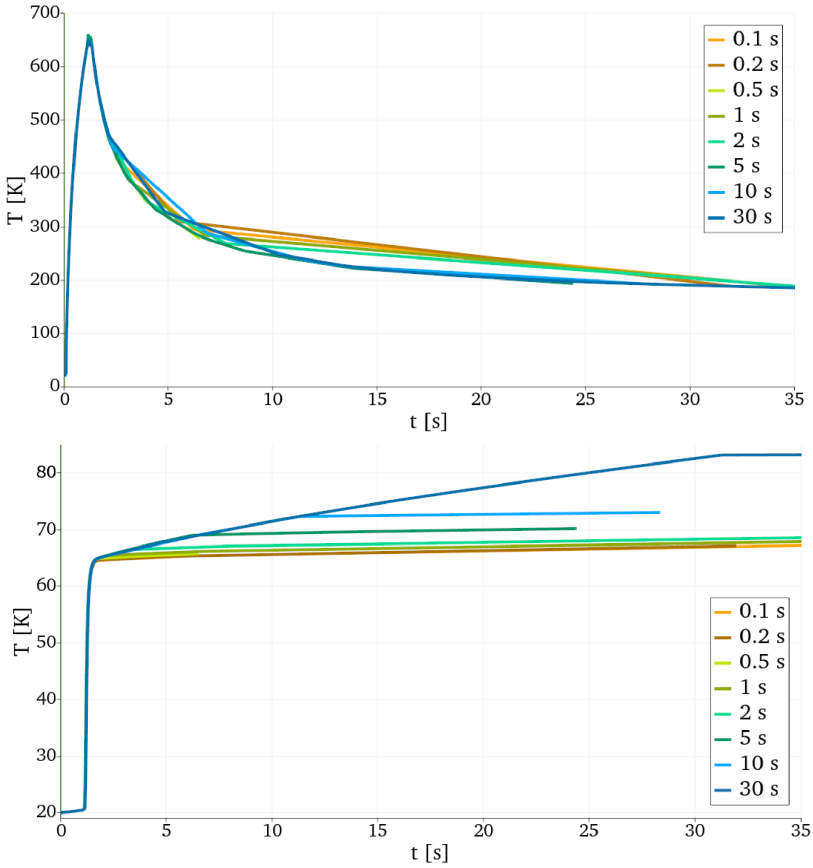


Figure 5.14: Normal zone hot-spot temperature (top) and coil average temperature (bottom) of a single ESMA coil during a quench event for different delay times after which the circuit breaker is opened to extract the current.

tudinal current density reaches its peak at t = 1.2 s, indicating that a 40 ms switching delay is inadequate to extract the current before the current wave attains its maximum amplitude. As in all quench simulations described, the hot-spot temperature appears artificially elevated, primarily due to the high heater power necessary to trigger a quench under the simulated conditions. The difficulty in initiating a quench is also reflected in the evolution of the normal-zone voltage. A detectable voltage, typically above 50 mV, does not appear if the heater is energized for too short a duration. Two main factors contribute to this behavior: primarily, the high thermal margin of the single pancake coil under a 10.55 T background field lies between 6.8 K and 17.2 K, making it inherently difficult to drive the coil normal by thermal excitation alone. Then, the current can redistribute away from the quenched region, allowing the affected turns to cool down. Once their temperature falls below the critical surface, these turns recover superconductivity and begin carrying current again.

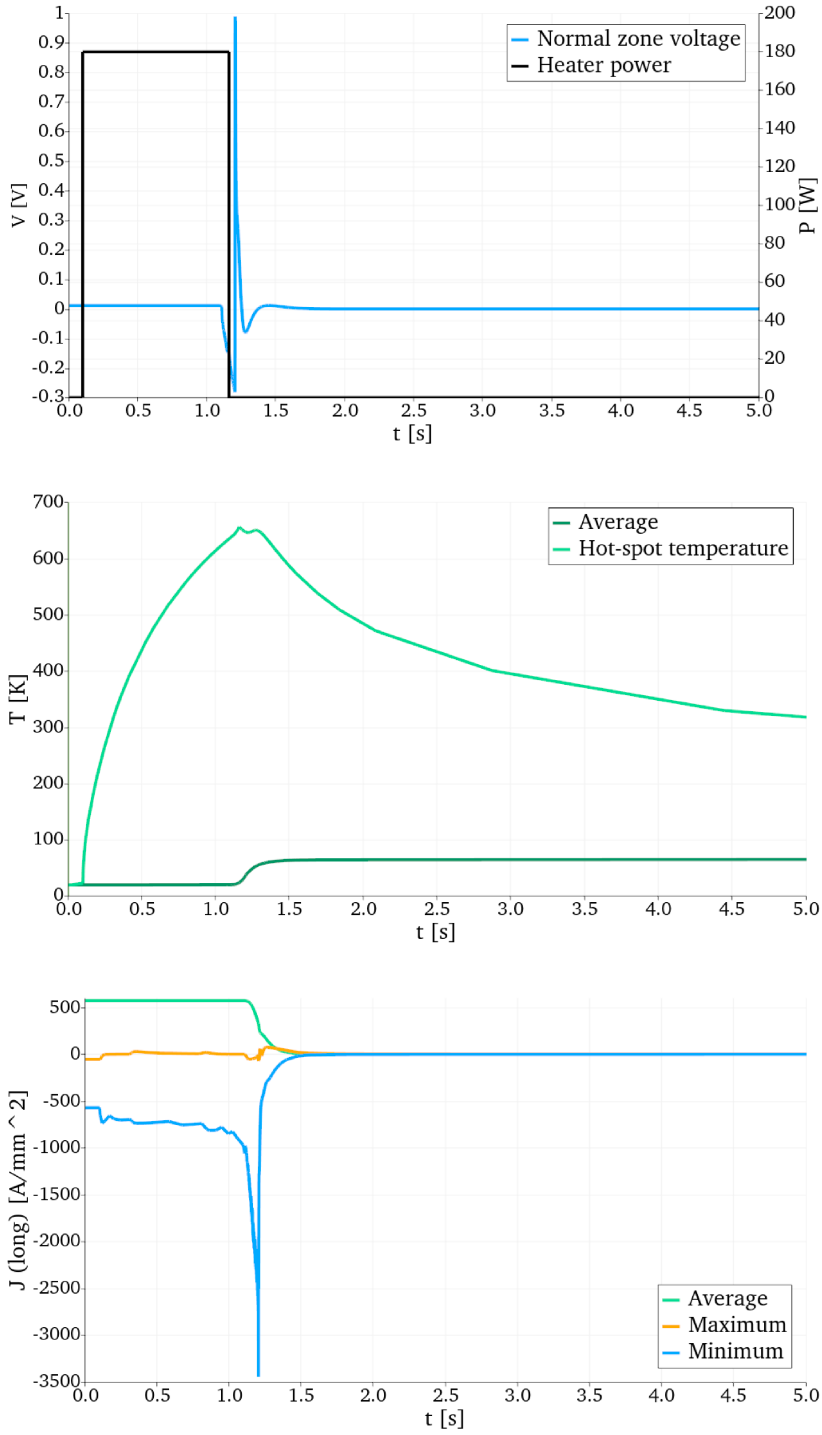


Figure 5.15: Normal zone voltage and heater power (top), hot-spot temperature and average coil temperature (center), and average longitudinal current density, maximum longitudinal current density, and minimum longitudinal current density (bottom) in a single ESMA coil for a quench simulation where the circuit breaker is opened at 1.16 s.

5.2.3 ESMA single coil discharge

In practical operation, there may be events that may require operators to discharge the magnet as rapidly as possible, even in the absence of an ongoing quench. To investigate this case, a fast-discharge scenario was modeled in which a single ESMA racetrack coil was charged to 1150 A, after which the circuit breaker was opened within 0.1 s. In particular, the breaker began to open at t = 0.2 s and was fully open at t = 0.3 s. The simulation assessed the full discharging time to analyze the transient electromagnetic and thermal behavior of the coil under these conditions. Results are summarized in Fig. 5.16, where the top picture shows the coil voltage, with the moment of circuit breaker opening indicated by a black line. Immediately after the circuit is opened, a voltage is induced across the coil due to the sudden change in current. Since the current can no longer circulate through the power supply, it is forced within the coil. Consequently, a radial current begins to flow between the first and last turns through the metal insulation. The associated joule heating resulting from the resistive radial current flow eventually causes some turns of the coil to quench, producing an additional voltage rise associated with the expanding normal zone around t = 3.2 s. As the quenched turns lose current, an inductive current wave develops and begins to propagate radially through the winding. This phenomenon is evident the bottom graph of Fig. 5.16, where the minimum longitudinal current density decreases rapidly as the current wave accumulates the current accumulated by previously quenched turns. A corresponding hot spot forms in the region with the lowest thermal margin, where most turns have transitioned to the normal state. A three-dimensional simulation at this stage, showing both temperature and longitudinal current density distributions, is presented in the top image of Fig. 5.17. The quench drives the radial current wave outward until the coil becomes fully discharged, transferring the stored magnetic energy into the coil and surrounding structures as heat. By t = 3.6 s, the discharge is complete, as illustrated in the bottom picture of Fig. 5.17. In this simulation, opening the circuit breaker, thus forcing the current to traverse radially through the coil, results in a complete quench within approximately 3.5 s. By t = 3.7 s, the energy is fully dissipated, and the maximum coil temperature reaches approximately 220 K. On the other hand, the radial current wave reaches a peak current density value of $\sim$ 1450 A/mm^2 before the coil is fully discharged, therefore originating non-negligible localized stresses which could severely damage the tape.

Since the simulation of a sudden discharge of the coil ultimately resulted in a potentially destructive quench event, a controlled slower discharge of the magnet is now investigated. Indeed, even in non-urgent situations, it may be necessary to completely discharge the magnet. To analyze this case, a slow discharge scenario was modeled, in which the current was forced to ramp down over 600 s. The resulting voltage, temperature, and current density evolutions are presented in Fig. 5.18. When the current source was ramped down at $\sim$ 2 A/s, the longitudinal current density in the coil decreased at an average rate of about 0.3 A/s. This discrepancy indicates that a fraction of the current was diverted through the radial resistive path provided by the MI layer and the associated joule heating gradually increased the local temperature within the coil. Since the current remained close to 90 % of the nominal operating value for a significant portion of

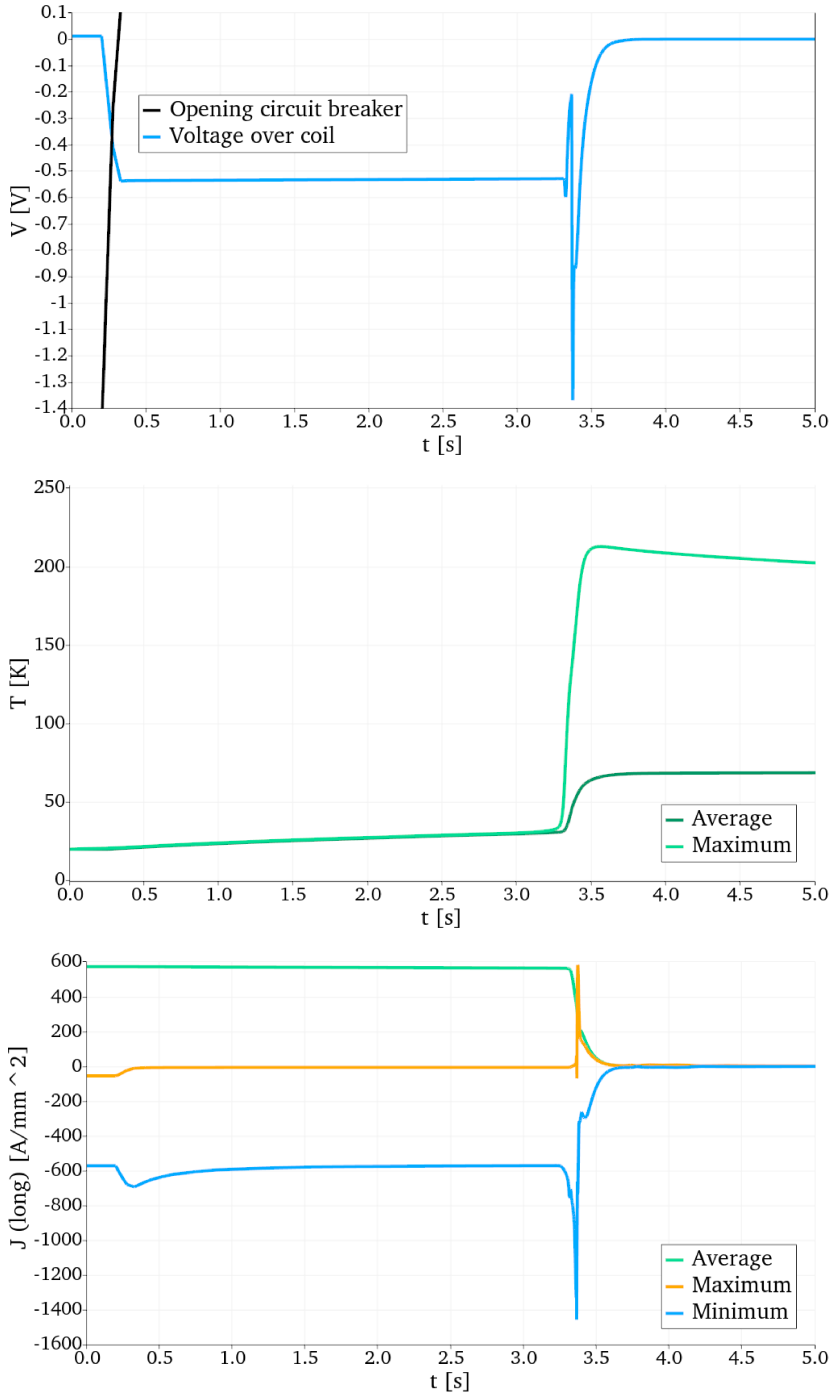


Figure 5.16: Voltage over the coil and the switching time (top), average and maximum coil temperature (center), and average longitudinal current density, maximum longitudinal current density, and minimum longitudinal current density (bottom) for a single ESMA coil in background field that is discharged by opening the circuit breaker.

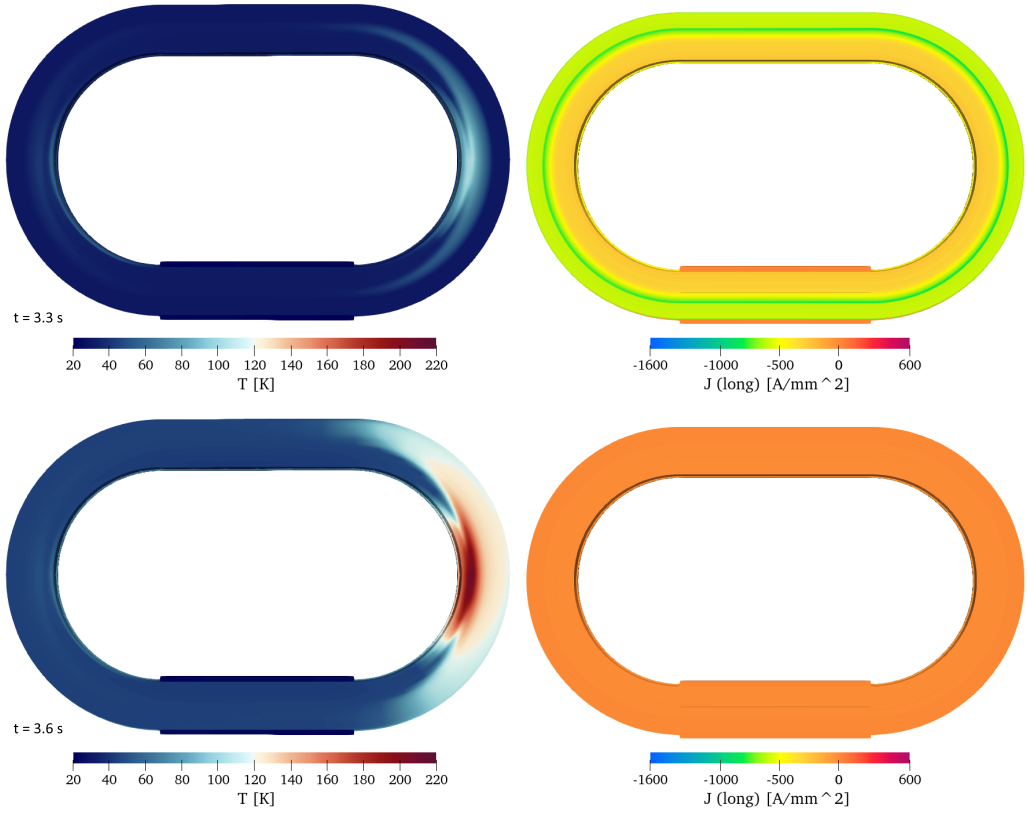


Figure 5.17: Temperature (left) and longitudinal current density (right) in a single ESMA pancake at 3.3 s (top) and 3.6 s (bottom) during a fast discharge.

the discharge, the coil eventually quenched. The quench developed in a similar manner to the previously discussed scenarios, giving rise to a radially propagating current wave that accelerated the discharge process. Although the power supply continued providing current until 600 s, the average current density after the passage of the current wave was reduced to ~ 1 A/mm^2. In this case, the quench initiated between turns 100 and 150, roughly at one-third of the coil width, as showed in the first panel of Fig. 5.19. From this location, the current redistribution occurred symmetrically toward both the inner and outer turns, giving rise to two waves propagating in opposite directions. The inner wavefront reached the first turn before the outer front reached the last, as illustrated further in Fig. 5.19. Ultimately, the current wave propagating outward reached the coil boundary, leaving only small current densities the order of ~ 1 A/mm^2 in the outermost and innermost turns while the power supply continued to provide current until the full discharge was completed at 600 s. To further investigate the influence of ramp rate, a second slow discharge simulation was carried out with a slower current ramp of 1 A/s, corresponding to a complete discharge in 1150 s. However results are qualitatively similar to those of the 2 A/s case, except for the quench starting time which is delayed by approximately a factor of two, consistent with the halved ramp rate. The reduced ramp

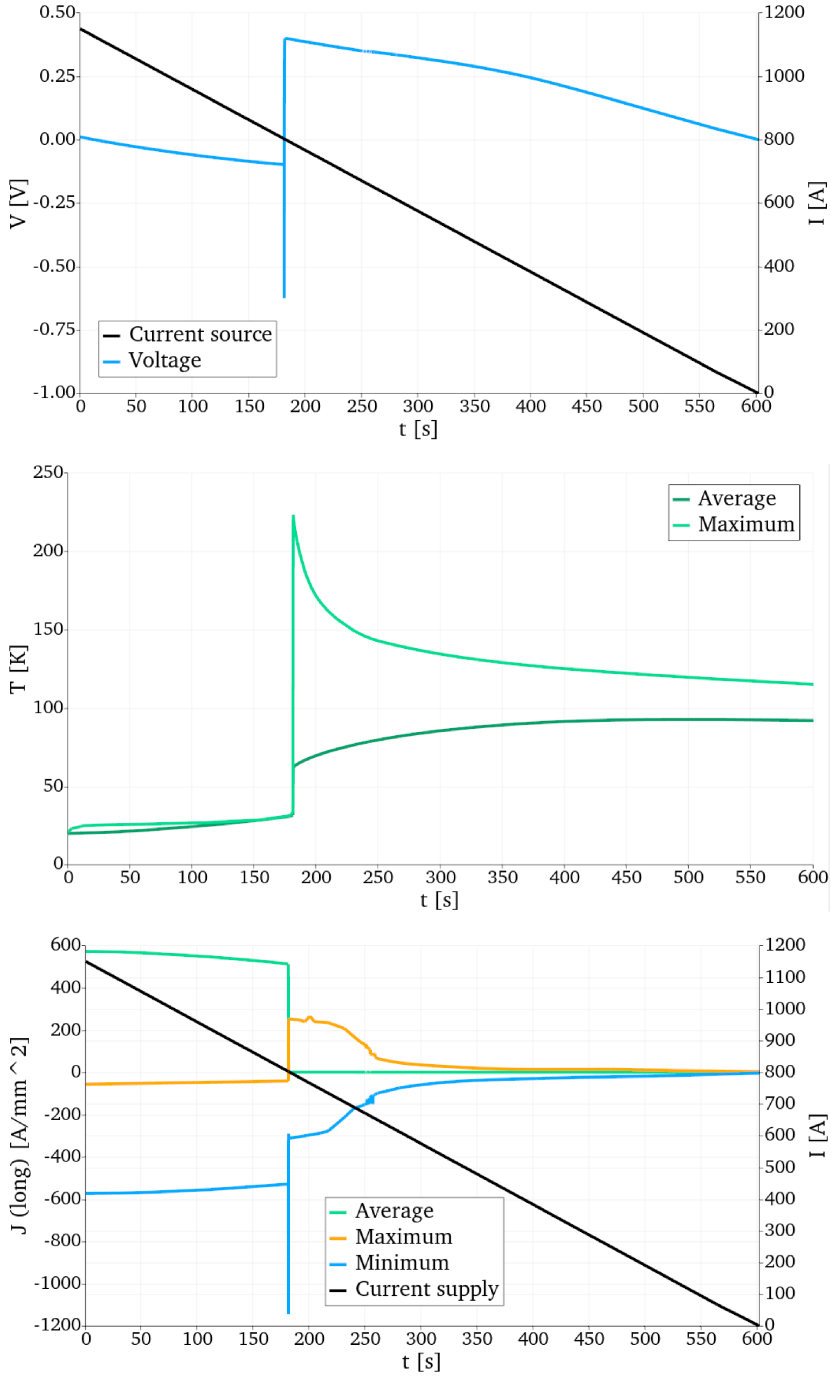


Figure 5.18: Voltage over the coil (top), average and maximum coil temperature (center), and average longitudinal current density, maximum longitudinal current density, and minimum longitudinal current density (bottom) for a single ESMA coil in background field that is discharged over 600 s from the nominal maximum operational current of 1150 A. In both top and botom figures the current from the power supply is included.

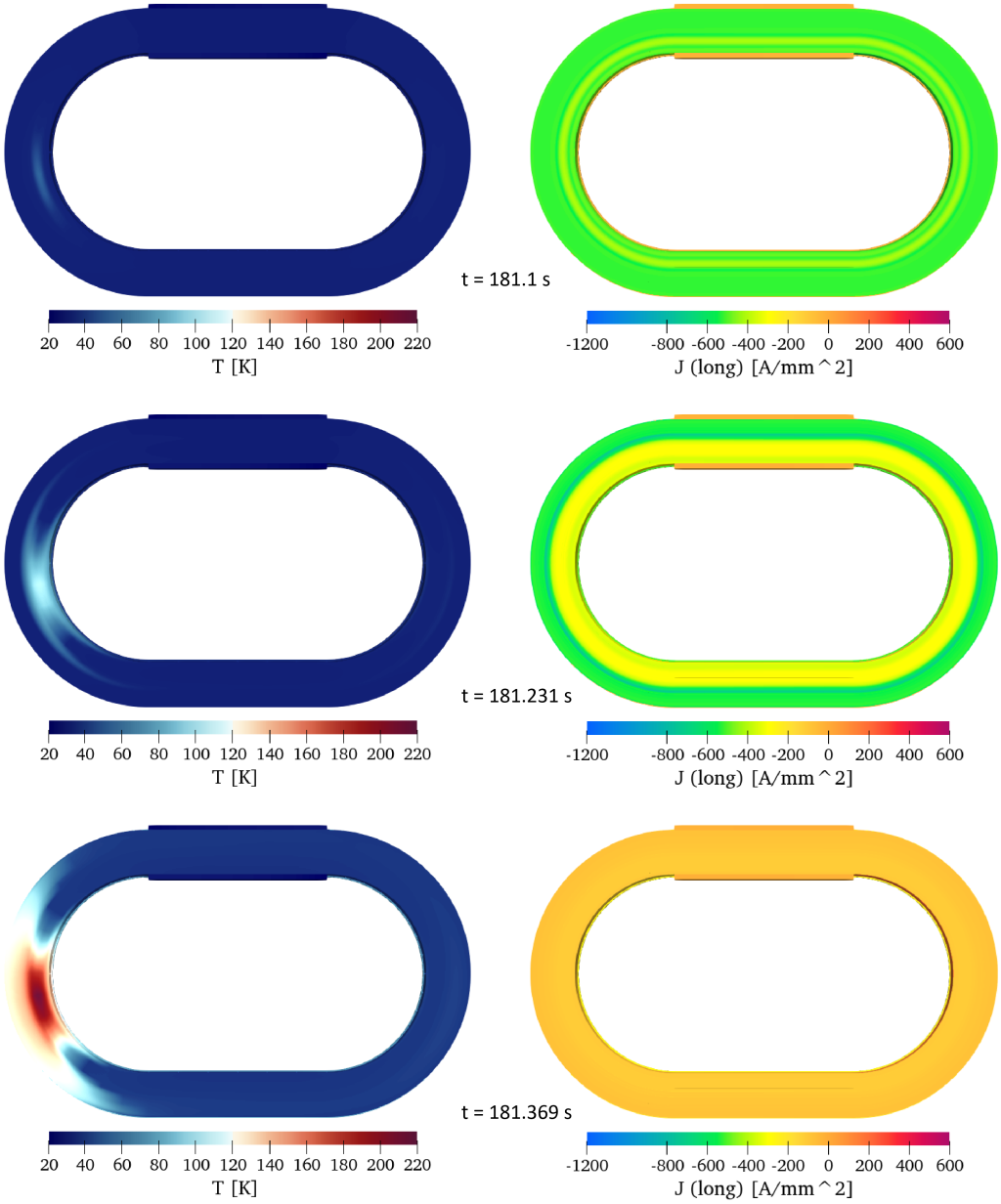


Figure 5.19: Temperature (left) and longitudinal current density (right) in a single ESMA pancake at different instants during a slow discharge at 2 A/s.

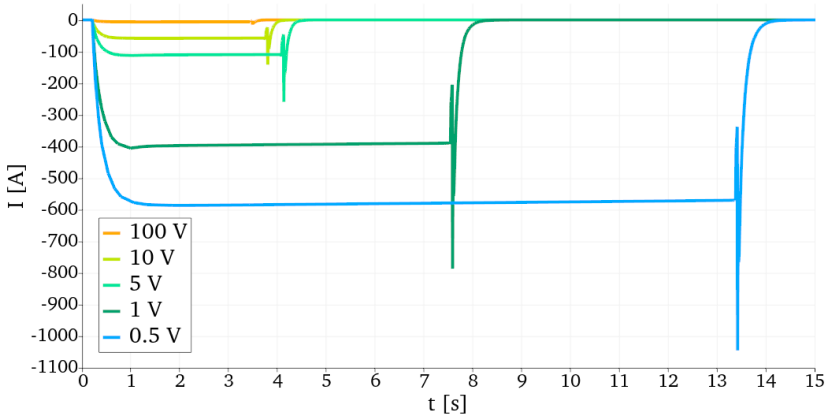


Figure 5.20: Current in the different dump resistors as function of time during simulations of a single ESMA coil in a background field of 10 T.

rate limits the radial current at each time step, thus reducing resistive heating. Nevertheless, due to the high time constant of the MI coil, the current in the winding does not immediately follow the imposed ramp, causing the current density be still about 86% of the operating current at the moment the coil quenches, demonstrating that even the 1 A/s discharge rate is insufficient to prevent quenching when cooling power is not included in the model.

Another method for rapidly extracting current from a superconducting coil following quench detection, or during a controlled discharge, involves connecting a dump resistor in series with the magnet while switching off the power supply. In such a configuration, the current decays through the resistor, dissipating the stored magnetic energy externally rather than within the coil windings. This approach is most effective for fully insulated coils, where the current is strictly constrained to the longitudinal direction and cannot bypass the dump resistor. In the case of ESMA, however, the effectiveness of a dump resistor is strongly dependent on the HTS - MI layer interface resistance. A dump resistor can aid current extraction only if its resistance is comparable or smaller than the effective radial resistance per turn. Although, if the dump resistance is too low, it will draw current without significantly accelerating the discharge, whereas if it is too high, the current will preferentially flow radially through the MI, leading to internal heating and potentially inducing a quench. To this purpose, a set of simulations was carried out always by Little Beast Engineering on a single ESMA coil in background field, using the same model as in the previous studies. In these simulations, no external heater was employed to artificially trigger a quench. The coil was initialized at 1150 A, and at t = 0.2 s the dump resistor was switched in series with the magnet while the power supply was simultaneously switched off. The circuit remained electrically closed through by-pass diodes in the power supply, allowing the current to continue circulating via the power supply circuit rather than being interrupted, as in the circuit-breaker scenario. This configuration was set to isolate the effect of the dump resistor itself. Five simulations were performed with different dump resistances, which were defined in terms of the voltage

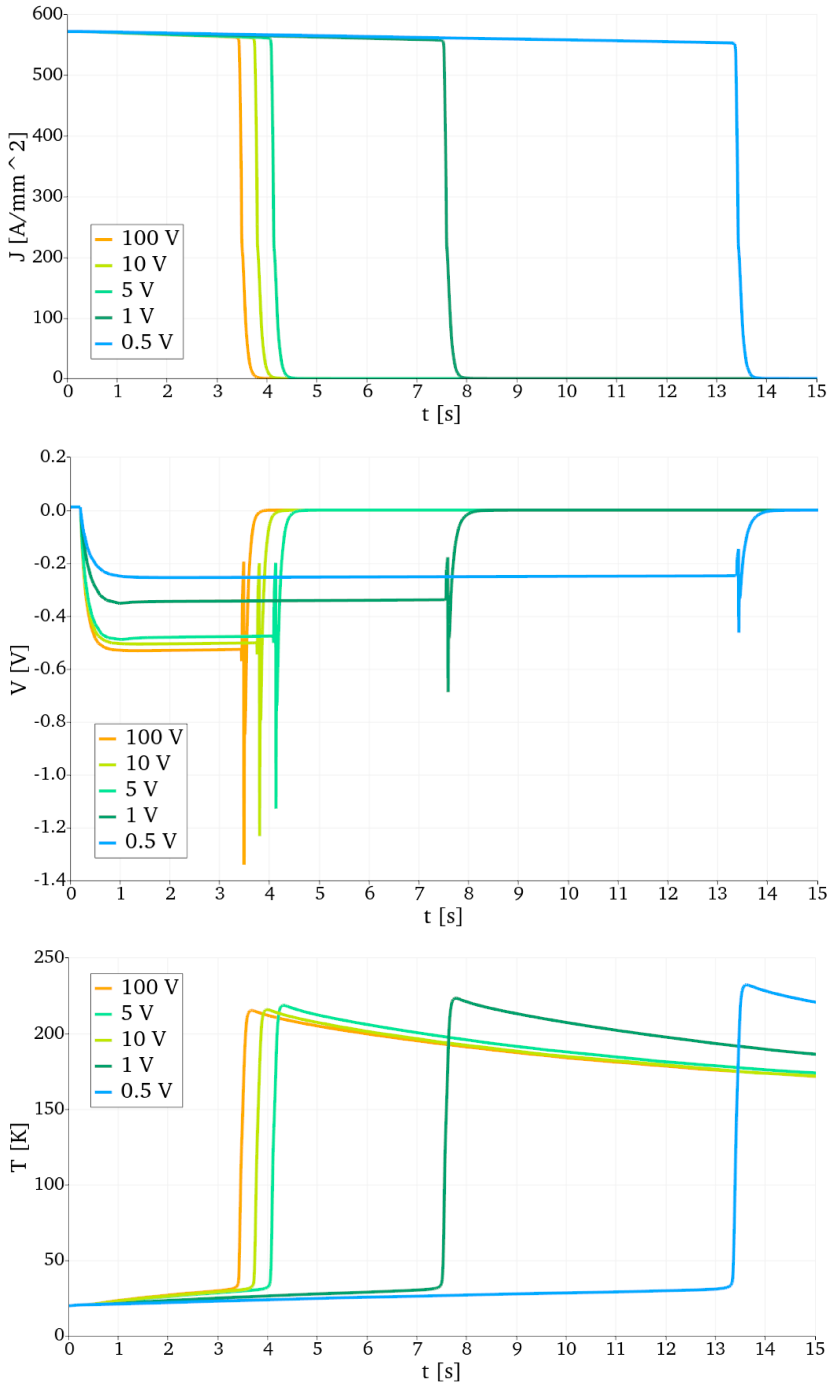


Figure 5.21: Average current density (top), voltage profiles over the coil (center), and maximum temperature (bottom) in a single ESMA coil in background field during a discharge simulation with different dump resistors.

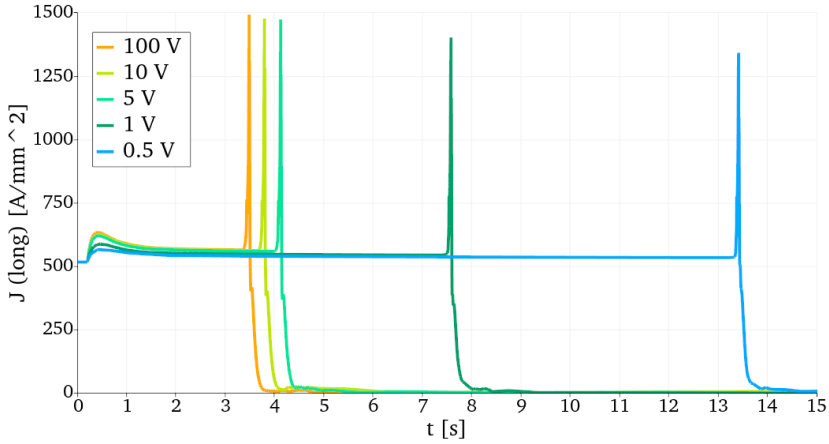


Figure 5.22: Difference between the maximum and minimum longitudinal current density in the single ESMA coil in background field during the simulations with different dump resistors.

drop at nominal current, namely V = R·I. The simulated voltage settings were 100 V, 10 V, 5 V, 1 V, and 0.5 V. Results representing the current flow through the dump resistor as a function of time is presented in Fig. 5.20. As expected, the higher-voltage, corresponding to a higher-resistance, cases resulted in lower initial current flow through the resistor. In all cases, a pronounced current peak appeared few seconds into the simulation, coinciding with the beginning of the quench and the development of the current wave, which produced a rapid discharge of the coil. This behavior can be confirmed by results showed in Fig. 5.21, particularly for what concerns the average current density in the HTS coil as function of the simulated time. The sudden current drop matches the resistor-current peaks in Fig. 5.20. Before the fast discharge, the current decayed only gradually, and even for the lowest-voltage case, over 90 % of the initial current remained in the HTS until a quench occurred, thus clearly demonstrating that the dump resistor does not significantly accelerate current extraction in the case of ESMA coil. The voltage across the coil during these simulations is reported in the central picture of Fig. 5.21. Since no heater was applied, no initial normal-zone voltage was present. At t = 0.2 s, when the dump resistor was connected and the power supply switched off, the voltage followed the expected RL transient behavior determined by the resistor value and the coil inductance. However, as the current was not removed quickly enough, a normal zone developed within the coil, producing a sharp voltage peak and consequently a full discharge within 0.5 s, which represents a behavior consistent with previous results. The formation of the current wave is further illustrated in Fig. 5.22, showing the evolution of the difference between the maximum and minimum longitudinal current densities. A small transient appears immediately after the dump resistor is connected, followed by a pronounced peak corresponding to the wave propagation. For what concerns the evolution of the maximum HTS temperature, results are reported in the last graph of Fig. 5.21, where the transient heating associated with the quench is represented. It is worth highlighting that the bypass diodes within the power supply possess a finite opening volt-

age, acting as resistors below this threshold. Consequently, the diode voltage defines the lower operational limit of the dump resistor voltage, since both components are electrically in series.

5.2.4 Full quench analysis

Upon resolving various cases concerning a single ESMA coil in a background field, a more demanding simulation of the entire ESMA magnet was performed by Little Beast Engineering, using the same expected value of turn-to-turn contact resistance of 240 $\mu\Omega \cdot mm^2$. Even in this case the simulation model included the copper plates responsible for both cooling and current supply. A virtual heater was located on the lowest coil of the bottom stack at a z-position of 164 mm, corresponding with the center of the curved section, and was used to start the quench. The heater was activated for 0.05 s with a power of 750 W, which successfully triggered a quench event. The quench detection voltage threshold was set to 0.05 V, and a detection delay of 0.06 s was applied. This delay also served as the switching delay, meaning that 0.06 s after the quench was detected, the circuit breaker was opened. For clarity in the discussion that follows, the coils are labeled starting from the one nearest to the center up to the outermost one with the Cn notation, with n ranging from 0 to 5 both for the top and bottom stacks. During this simulation, the heater was activated between 0.1 s and 0.15 s, initiating a quench that was detected at 0.475 s, when the normal-zone voltage reached the threshold of 0.05 V. This behavior is showed in the top picture of Fig. 5.23, where the green curve represents the heater power and the orange line corresponds to the normal-zone voltage. The circuit breaker was subsequently opened at 0.535 s, resulting in the sudden change in voltage observed at that instant. The temperature evolution of the normal zone induced by the heater is presented in the bottom part of Fig. 5.23. The plot includes the maximum coil temperature, the average coil temperature, and the heater power for reference. The maximum temperature reached in the dipole during this simulation was 580 K, while the first hot spot, directly induced by the heater, peaked at approximately 510 K. The current discharge occurred at 1.5 s and is illustrated in the first graph of Fig. 5.24, which shows the average longitudinal current density in the coils (yellow), the maximum and minimum longitudinal current densities (orange and blue, respectively), and the magnetic flux density at the dipole center (green). The wide variation between the maximum and minimum current density during ramp down is attributed to current shock waves induced by the redistribution of current from quenched turns. In this MI coil, when a turn quenches, the current can leave the superconducting path through the resistive metal insulation, causing rapid local magnetic field variations that induce transient currents in neighboring turns, as described in detail for the simulations concerning the single coil submerged in the background field of ESMA of $\sim$ 10 T The overall voltage evolution is reported in the central picture of Fig. 5.24: at the beginning of the discharge, the voltage is dominated by the formation of normal zones at various coil locations, leading to fast voltage fluctuations. As the discharge progresses and the magnetic field variation becomes predominant, the induced voltage assumes an inductive behavior, characterized by a polarity opposite to that of the normal-zone voltage. For a NI coil such as ESMA,

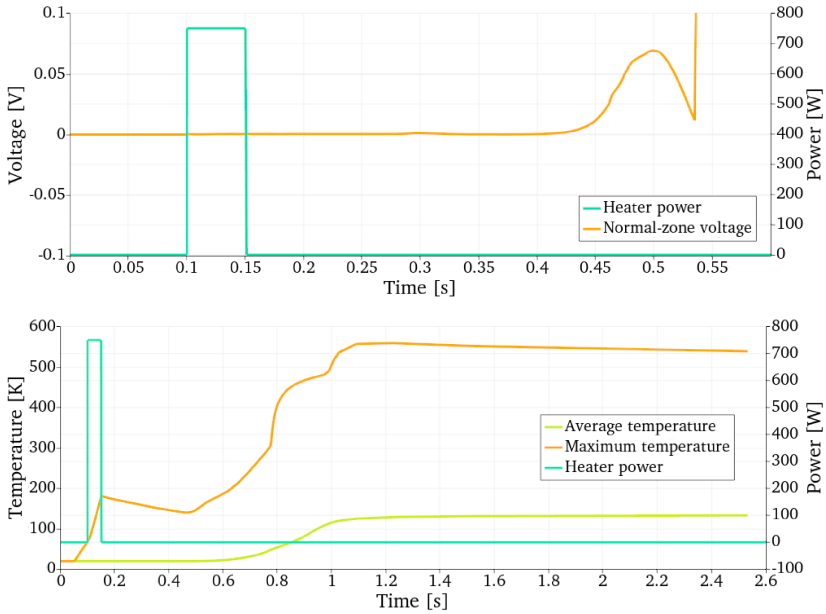


Figure 5.23: Normal zone voltage (top), and temperature of the first hot-spot in the bottom C5 coil, maximum temperature in the ESMA dipole and the average dipole temperature (bottom) as a function of time. In both graphs the heater power is reported.

two main aspects determine whether a quench could cause damage: the local temperature rise, which can induce thermal stresses, and the redistribution of current following a quench, which can generate current shock waves. To analyze these effects, Fig. 5.25 reports a three-dimensional map of the coil temperature and longitudinal current density on the dipole surface at t = 0.601 s. Additional time frames of this evolution are provided in Fig. 5.27, Fig. 5.28, and Fig. 5.29. From the three-dimensional analysis, it can be observed that each time a new quench arises, which can be visualized as a hot spot in the temperature map, a current wave generates near the quenched area and propagates radially outward across the pancake. Except for the initial quench induced by firing the heater, subsequent quenches mostly occur at the first turn of each pancake, corresponding to the current entry and exit points of the coil. In reality, copper current leads are attached at these locations, but they were not included in this specific simulation. Previous simulations that incorporated copper blocks to represent the current leads showed a reduction in the peak temperature around the joints, confirming the heat sinking effect of the copper interfaces. Once a section of the coil becomes resistive, ohmic losses arise, most of which are converted into heat dissipated in the coil under the adiabatic assumption of the model. Consequently, during discharge, the stored magnetic energy of the dipole, which amounts to 3.5 MJ, is progressively converted into thermal energy, as shown in the last graph of Fig. 5.24. The distribution of resistive power losses across the dipole is detailed in Fig. 5.26, where each plot contains six curves, each representing the sum of the corresponding top and bottom coil pancakes, for instance the C1 line in the first panel of Fig. 5.26, shows the combined losses of the upper and lower C1 racetrack

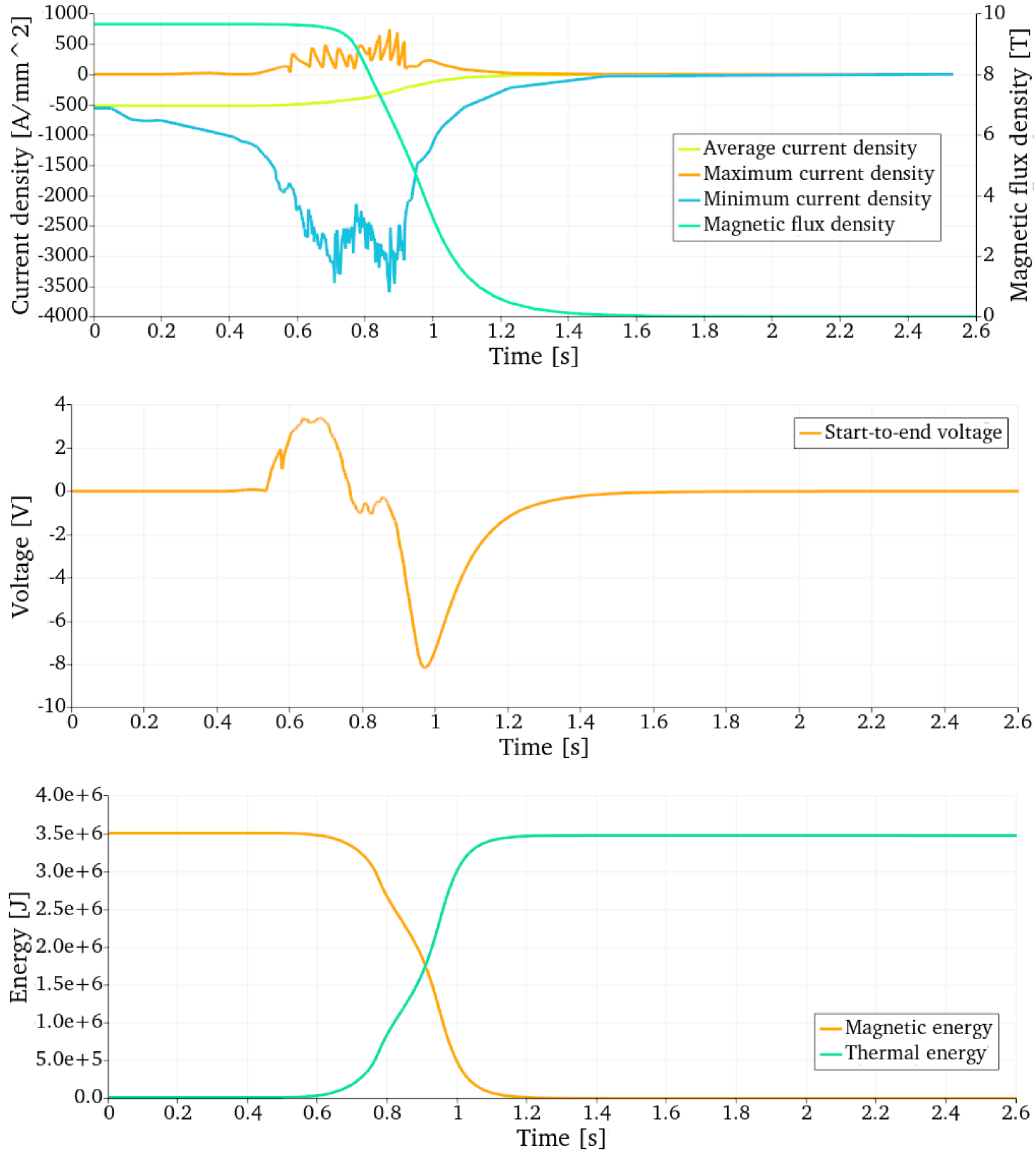


Figure 5.24: Average current density in the ESMA dipole and the magnetic flux density in the center of the dipole (top), the start-to-end voltage over the ESMA dipole (center), and energy conversion in the ESMA dipole during the full magnet quench simulation as functions of time.

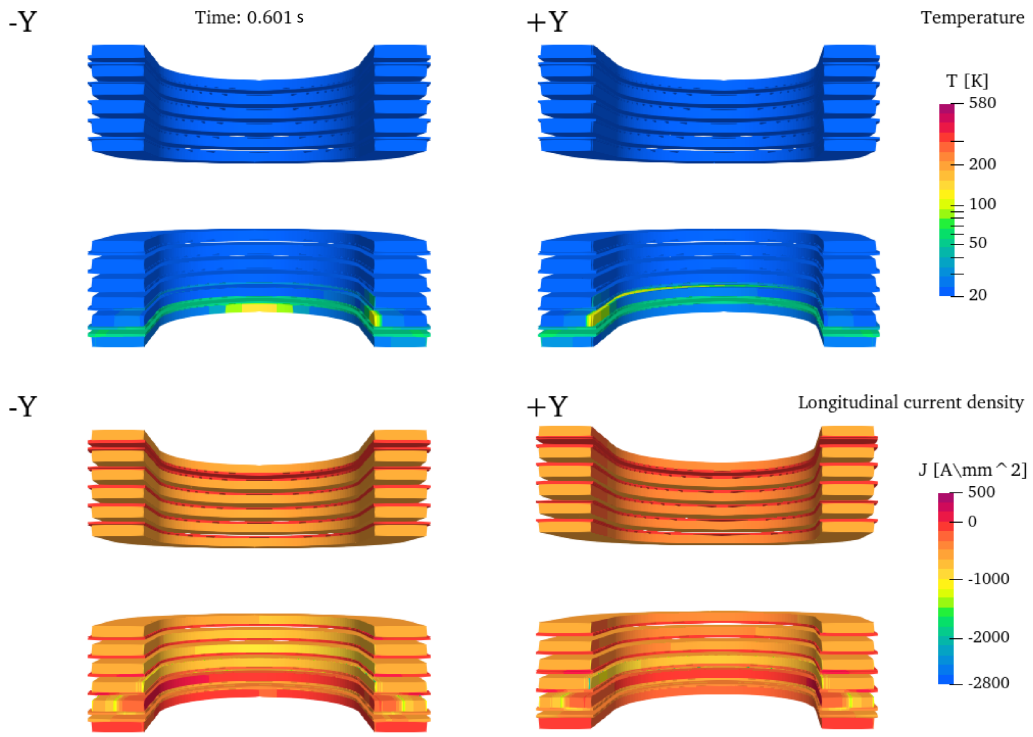
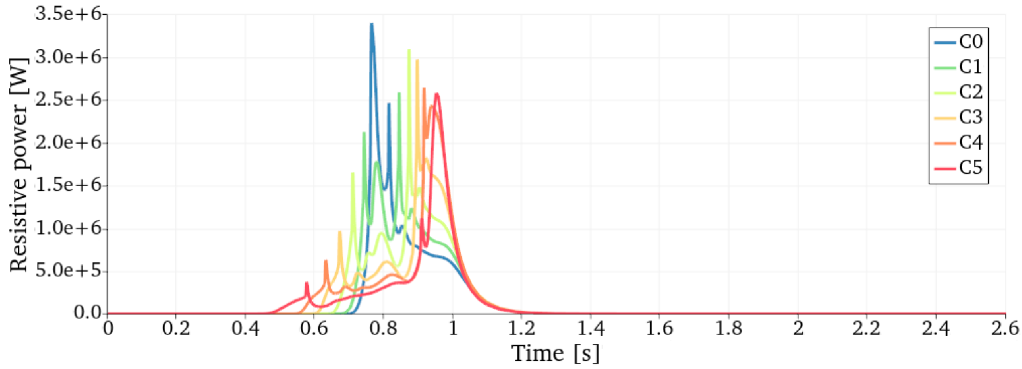
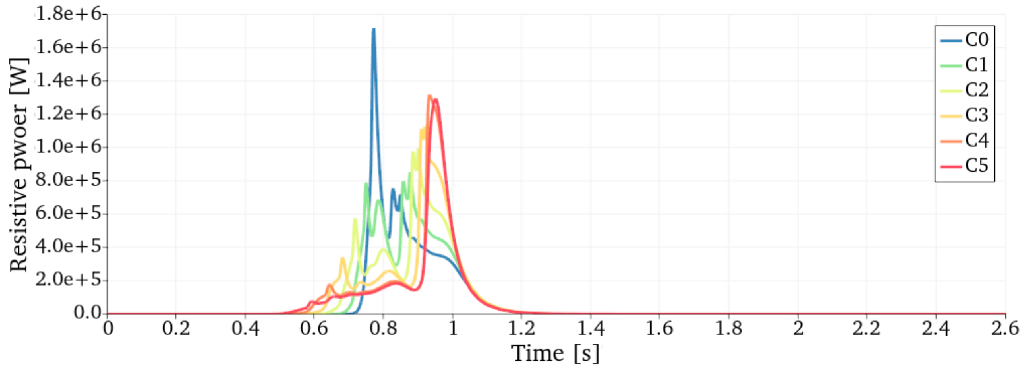


Figure 5.25: Temperature and the longitudinal current density map at t = 0.601 s for a quench simulation of the ESMA magnet.

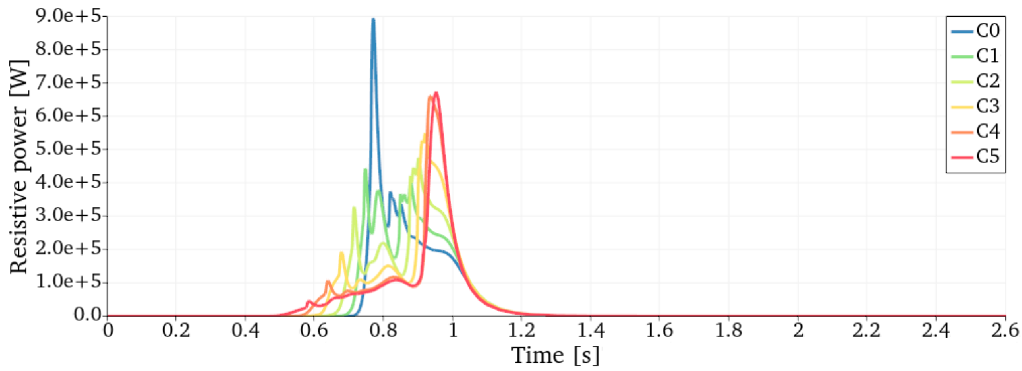
coils. An additional simulation was performed to assess a more demanding quench detection and discharge protection scenario. In this case, the quench was initiated in the top coil by activating a 200 W heater for 0.1 s, as shown in the top-left corner of Fig. 5.30. The detection threshold was set to 0.01 V with a validation time of 0.02 s, after which the circuit breaker was opened and the coil was subsequently discharged. A comprehensive visualization of the temperature evolution and current density distribution is presented in Fig. 5.30 and Fig.5.31, respectively. Each figure illustrates the twelve racetrack coils that constitute the two main stacks of the ESMA magnet. For every coil, the temperature and current density maps are represented as a function of time, starting from the beginning of the quench up to the complete discharge of the magnet. From these results, it can be observed that once the quench is triggered in the outermost racetrack coil, a localized temperature hot spot develops, corresponding to the generation of a current wave that ultimately leads to a full discharge of the coil. The propagation of the hot spot occurs mainly in the radial direction, causing a complete transition of the HTS tape to the normal conducting state and interrupting the azimuthal flow of superconducting current. The affected region reaches a peak temperature of approximately 400 K. Due to the inductive coupling between the coils, the current wave generated in the first coil induces a secondary wave in the adjacent one, leading to a cascade effect that propa-



(a) HTS coils.



(b) Cooling plates.



(c) Connection plates.

Figure 5.26: Resistive power as a function of time in different parts of the ESMA dipole, given the expected contact resistivity value of 0.024 $\Omega \cdot mm^2$. Each line represents two racetracks, so in the HTS plot the graph for C1 is the sum of both the top C1 coil resistive power and the bottom C1 coil resistive power.

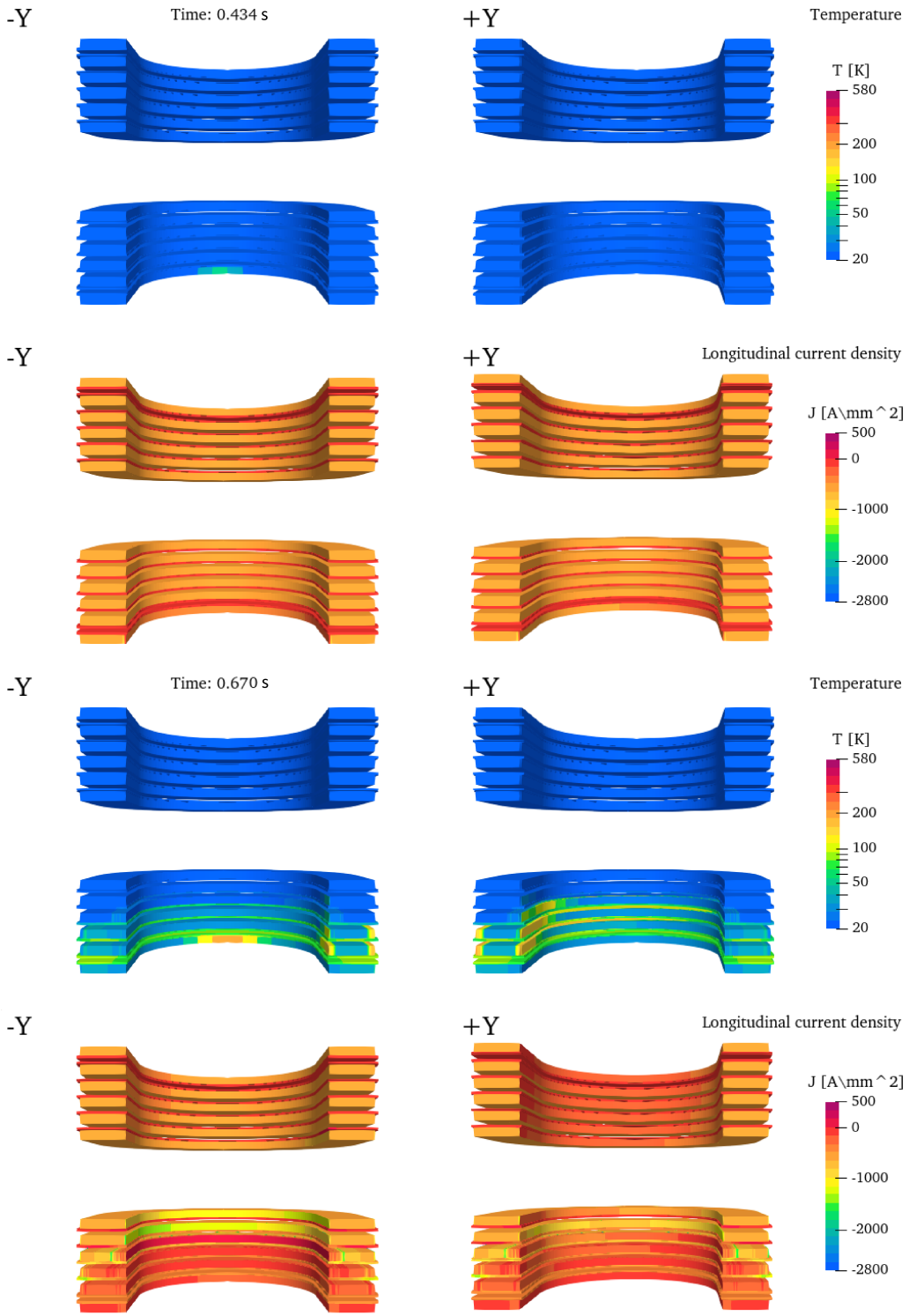


Figure 5.27: Temperature and the longitudinal current density map at t = 0.434 s and t = 0.670 s for a quench simulation of the ESMA magnet.

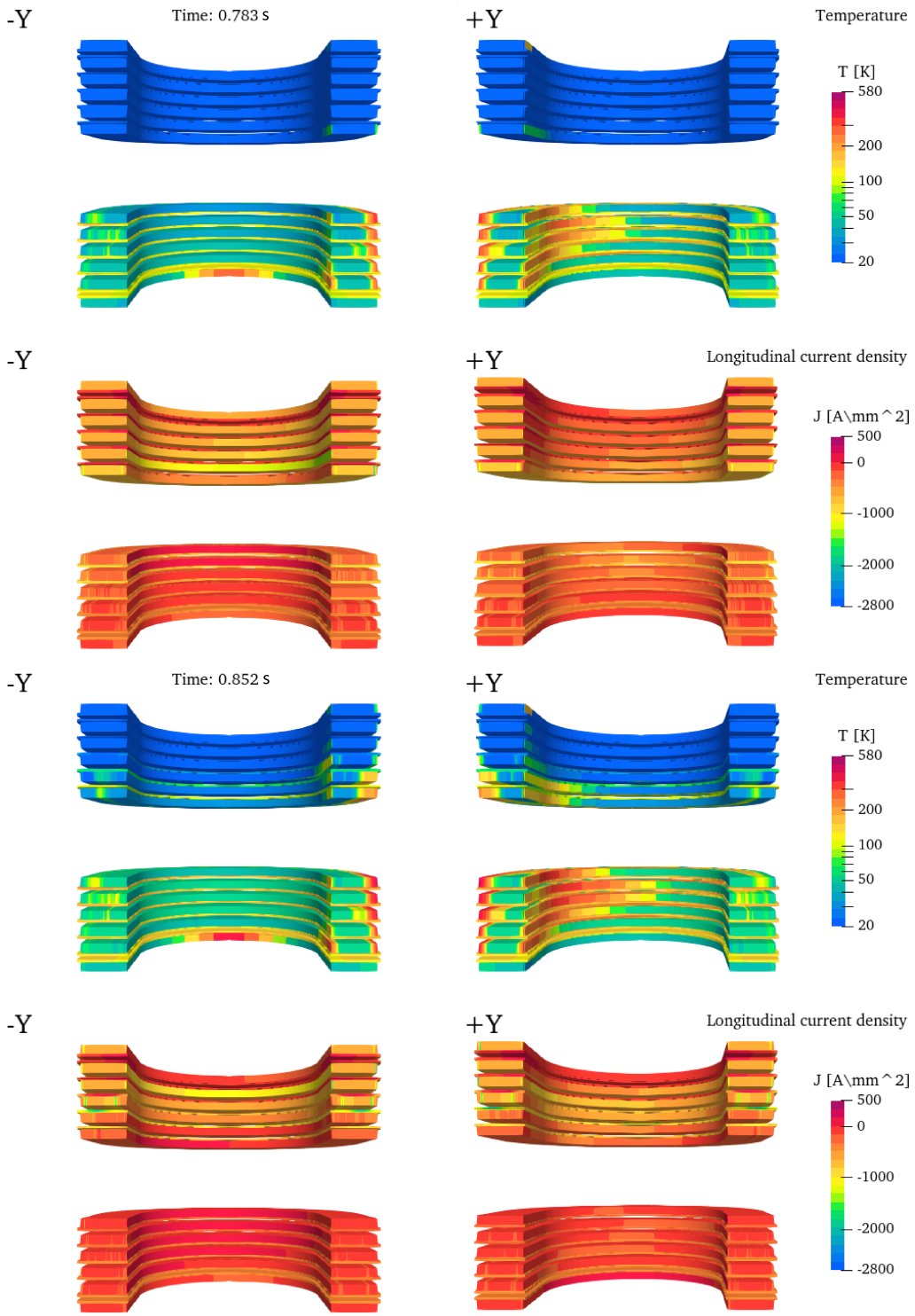


Figure 5.28: Temperature and the longitudinal current density map at t = 0.783 s and t = 0.852 s for a quench simulation of the ESMA magnet.

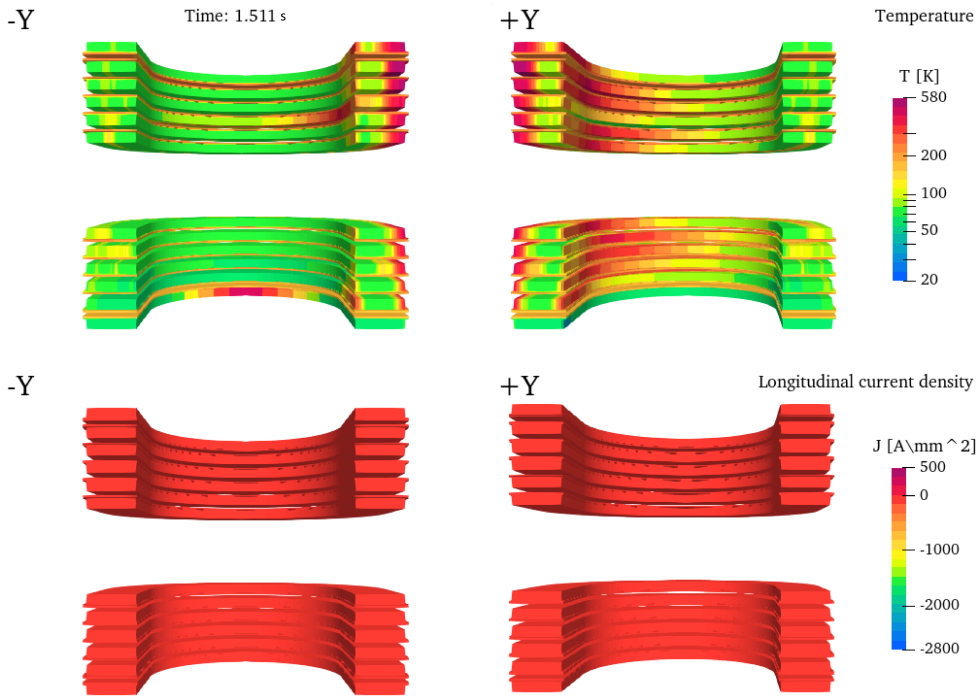


Figure 5.29: Temperature and the longitudinal current density map at t = 1.511 s for a quench simulation of the ESMA magnet.

gates throughout the magnet. This results in a complete discharge within less than one second, characterized by peak current densities of ~ 1200 A/mm^2. The combination of high current density and elevated temperature would likely cause irreversible damage to the HTS tape, both from mechanical and thermal stress.
Several quench scenarios were simulated, assessing both a single coil submerged in the background field of ESMA and a complete 3D analysis, considering different quench detection parameters as well as both a slow and fast discharge, with and without an external dump resistor. In all cases, a current shock wave was observed. This phenomenon arises from the inductive coupling between turns and the existence of a radial current path, resulting in significant mechanical stress due to high local current densities and radially spreading hot spots that obstruct the azimuthal flow of current. These findings may suggest a paradigm shift in the approach to quench protection for HTS magnets. Unlike conventional LTS magnets, where small energy disturbances can easily trigger a quench and protection systems focus on mitigating its consequences, HTS magnets, given their much higher temperature margins, require substantially more energy to initiate a quench. This indicates that quench events could, in principle, be avoided. Consequently, future HTS magnet designs may follow a protection strategy that aim primarily at preventing the generation of a quench, rather than trying protecting the system once it occurs, given the challenges posed by the current wave generation.

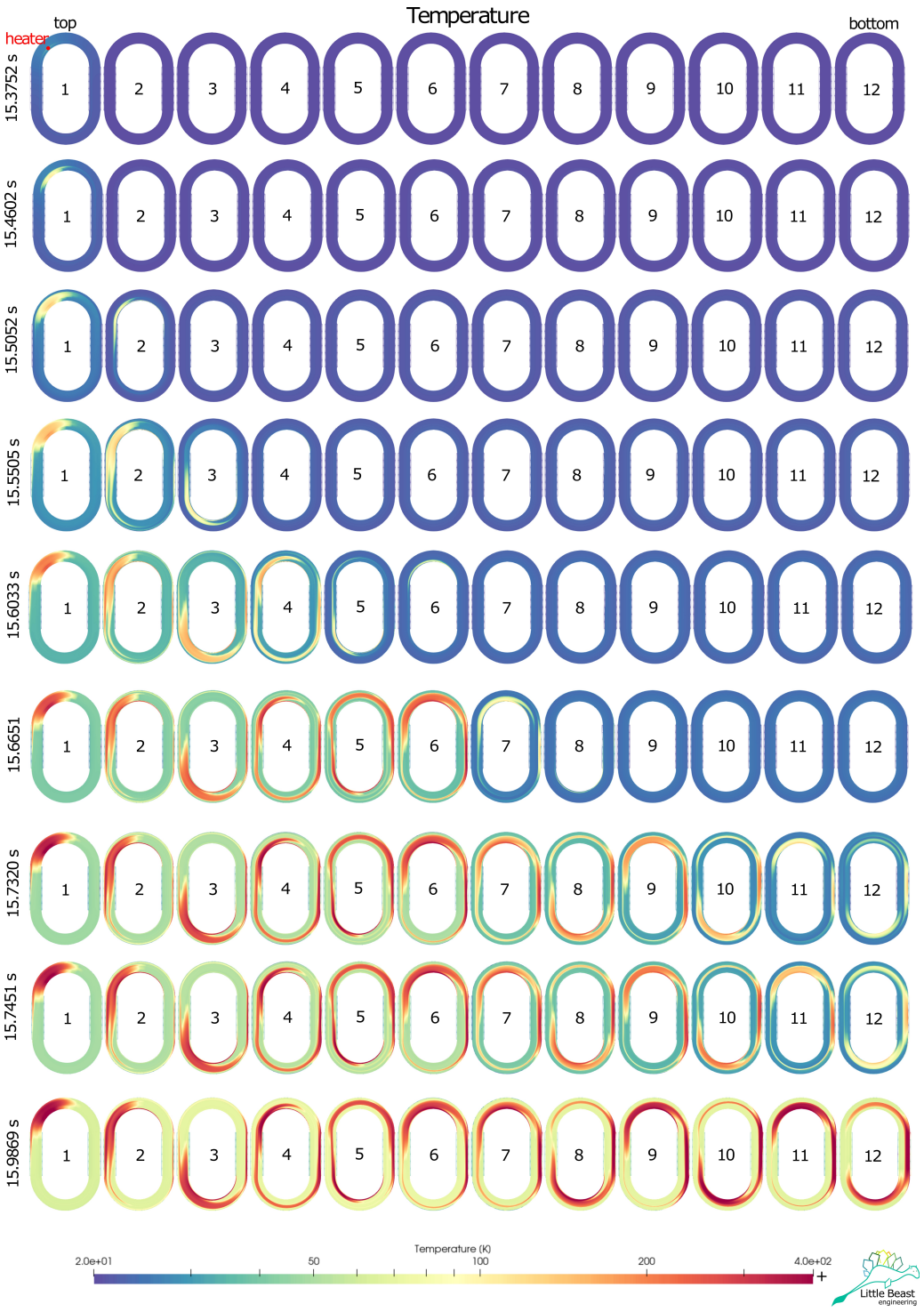


Figure 5.30: Temperature map as a function of time for each of the 12 racetrack coils of ESMA during a simulated quench event.

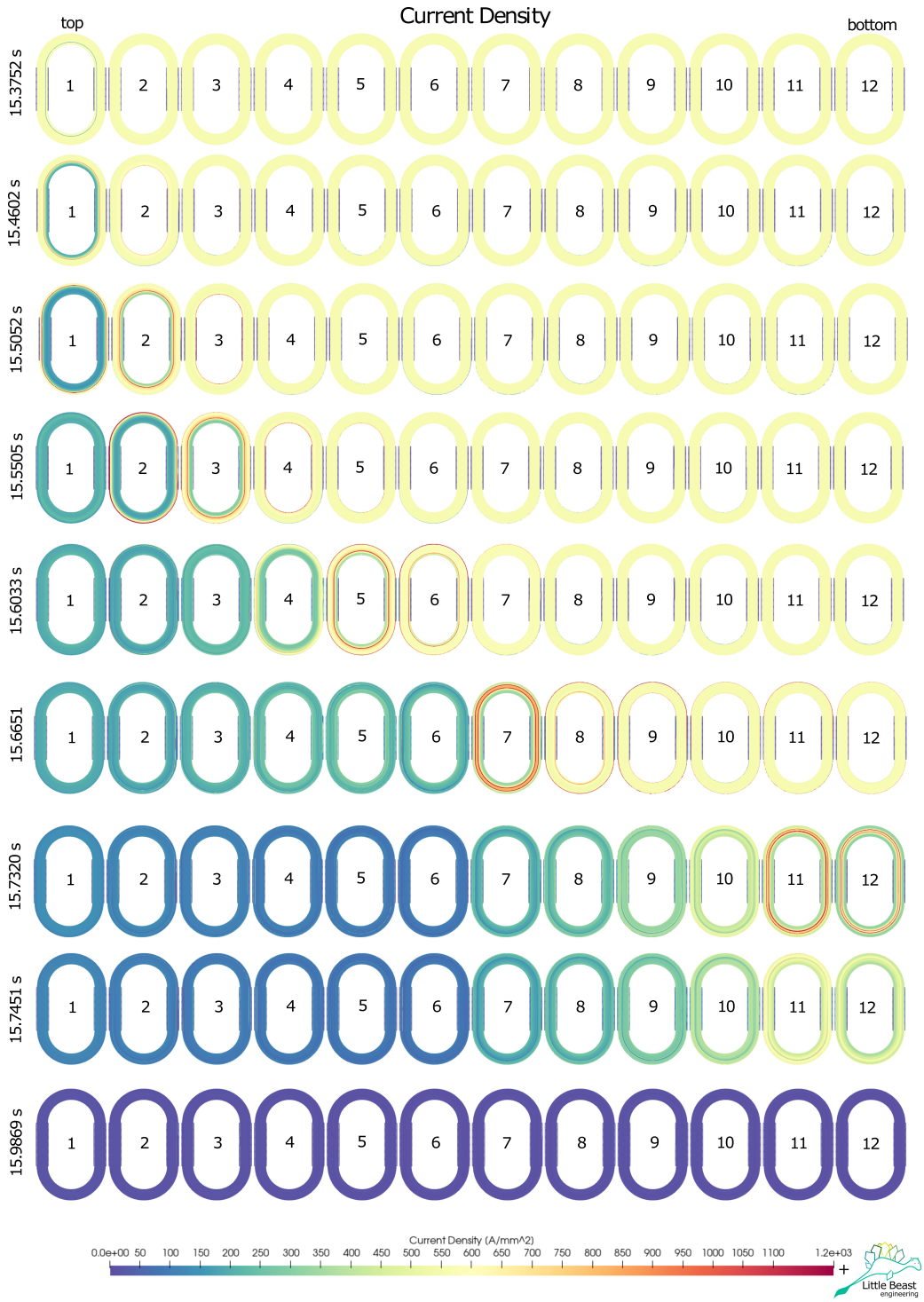
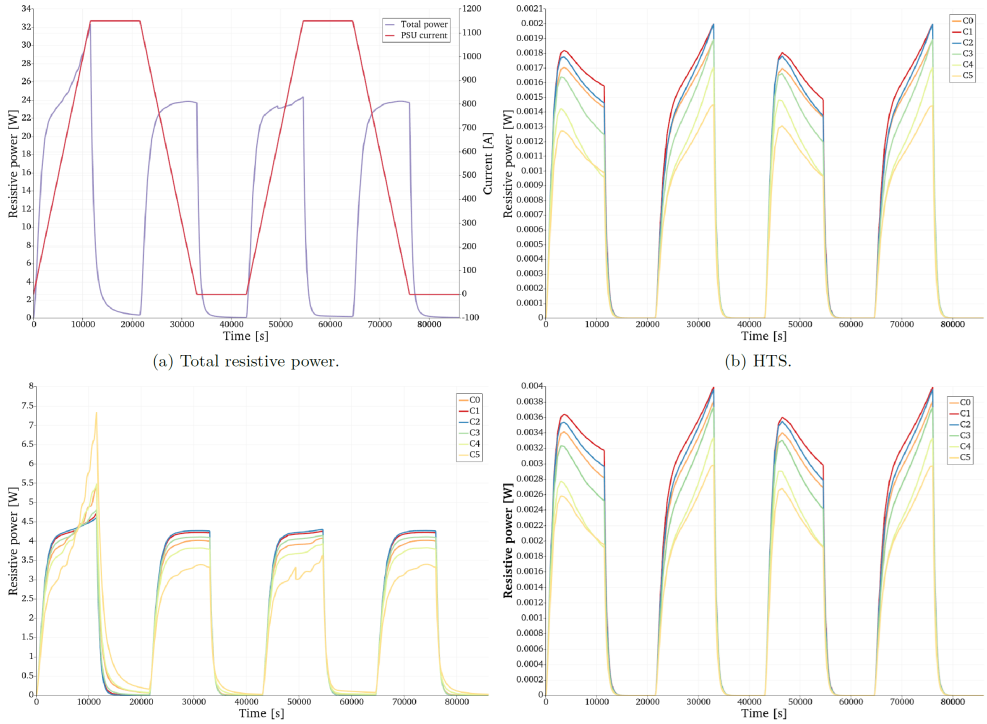


Figure 5.31: Current density map as a function of time for each of the 12 racetrack coils of ESMA during a simulated quench event.



(a) Total resistive power.

(b) HTS.

(c) Connection plates.

(d) Cooling plates.

Figure 5.32: The total resistive power (top, left) and the total resistive power (bottom, left) as a function of time for the top half of the ESMA dipole with a contact resistivity of 0.024 $\Omega \cdot mm^2$. On the right section, the resistive power in the 1 mm thin copper connection plates (top, right), and the resistive power as a function of time in the 2 mm thick copper cooling plates (bottom, right), in both cases for the top half of the ESMA dipole.

5.3 AC losses

An additional estimation which was commissioned to Little Beast Engineering concerned an overview of the AC-losses of the ESMA magnet, with particular focus on resistive power losses. The simulations included the copper plates used for cooling and current supply and considered two full charge-discharge cycles, during which the power losses in each coil and copper plate were calculated as a function of time. Mirror symmetry was applied along the mid-plane between the two coil stacks of the dipole to account for the field and mutual inductance of the lower six coils. Consequently, all loss values shown in the following figures must be doubled to obtain the total losses for the complete ESMA magnet. The HTS coils underwent two identical current cycles. From 0 s to $1{,}15 \cdot 10^4$ s, the coils were ramped up to 1150 A with a constant dI/dt of 0.1 A/s. The current was then held constant at 1150 A for 10^4 s. At t = $2.15 \cdot 10^4$ s, the current was ramped down at the same rate, followed by another 10^4 s at zero current. This full cycle was then repeated. The same power cycle was simulated for three different values of turn-to-turn contact resistivity: a low value of 240 $\mu\Omega \cdot mm^2$, an intermediate value of 920 $\mu\Omega \cdot mm^2$, and a

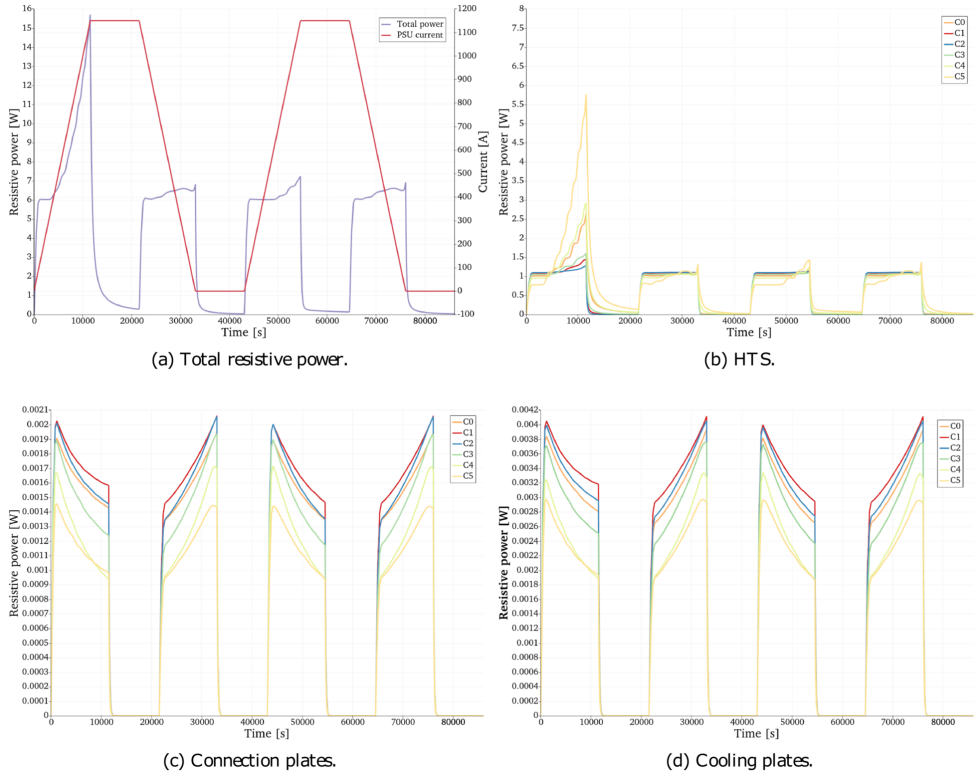
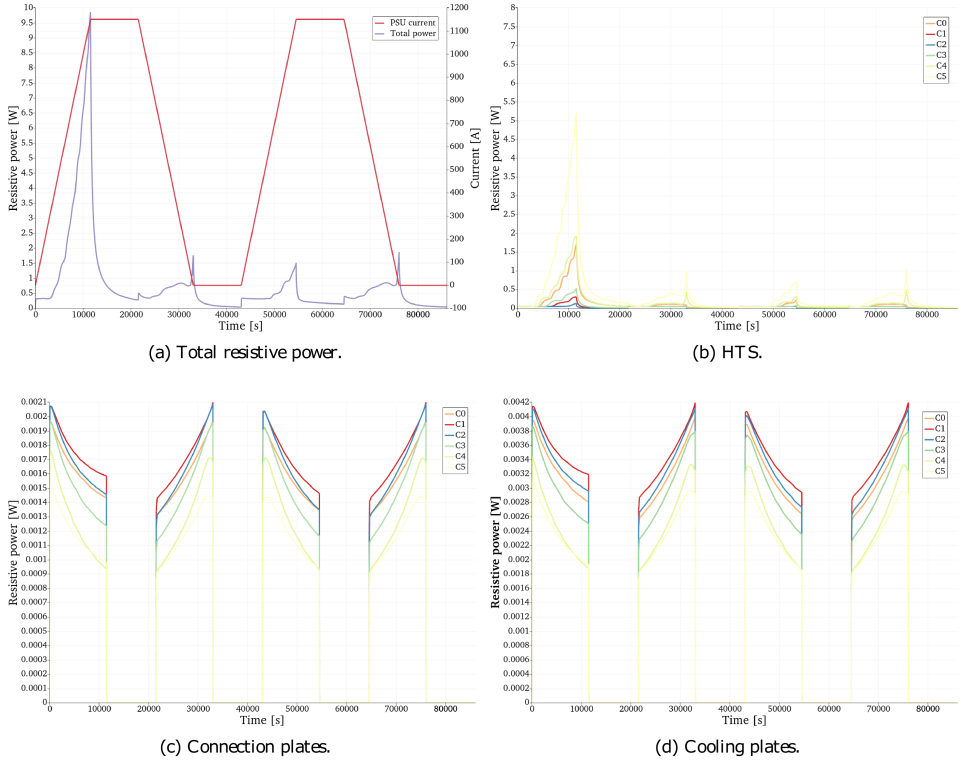


Figure 5.33: The total resistive power (top, left) and the total resistive power (bottom, left) as a function of time for the top half of the ESMA dipole with a contact resistivity of 0.092 $\Omega{\cdot}mm^2$. On the right section, the resistive power in the 1 mm thin copper connection plates (top, right), and the resistive power as a function of time in the 2 mm thick copper cooling plates (bottom, right), in both cases for the top half of the ESMA dipole

high value of $1.92{\cdot}10^4$ $\mu\Omega{\cdot}mm^2$. For the lowest resistivity case, the total resistive power generated in the top six pancakes is showed in the top left picture of Fig. 5.32, where the red curve represents the current supplied by the power supply. The power dissipated in each HTS coil is detailed in the bottom left graph of Fig. 5.32. The highest losses occur in coils C5 and C4, corresponding to the two uppermost racetracks of the dipole. This is attributed to the magnetic field orientation near these coils, which approaches an orientation almost parallel to the c-axis of the tape, thus maximizing the local coupling losses. The next most significant losses appear in coil C0, located in the central region where the magnetic field bends between the two coil stacks. The total resistive power peaks just before the current reaches its steady-state plateau at $1{,}15{\cdot}10^4$ s during the initial charging cycle. At that moment, the total power in the six modeled coils reaches approximately 32 W. During the second ramp, the peak total power decreases to 24 W, corresponding to about 48 W when considering the whole magnet. The top right panel of Fig. 5.32 presents the power dissipated in the six racetrack-shaped copper connection plates. Inductive currents generated during current ramping produce minor ohmic



(a) Total resistive power. (b) HTS.

(c) Connection plates. (d) Cooling plates.

Figure 5.34: The total resistive power (top, left) and the total resistive power (bottom, left) as a function of time for the top half of the ESMA dipole with a contact resistivity of 1.92 $\Omega{\cdot}mm^2$. On the right section, the resistive power in the 1 mm thin copper connection plates (top, right), and the resistive power as a function of time in the 2 mm thick copper cooling plates (bottom, right), in both cases for the top half of the ESMA dipole

losses, with peak power values around 0.01 W. Beyond this point, the resistive power decreases as a result of the magneto-resistance of copper, which increases with the magnetic field strength. Similarly, the power dissipated in the six racetrack-shaped cooling plates, each 2 mm thick (twice as thick as the connection plates), is illustrated in the bottom right graph of Fig. 5.32. The increased thickness leads to nearly double the ohmic losses compared to the connection plates. Nevertheless, the total power dissipated in the copper plates represents only about 0.08 % of the total system losses, indicating minimal induced currents and, consequently, low magnetic forces within these plates.
For comparison, Fig. 5.33 presents the same results for the intermediate contact resistivity of 920 $\mu\Omega{\cdot}mm^2$. As expected, the overall losses are lower than in the previous case, since a higher contact resistance favors current flow within the HTS path rather than through resistive turn-to-turn channels. Analogously, Fig. 5.34 shows the results for the highest simulated contact resistivity of $1.92{\cdot}10^4$ $\mu\Omega{\cdot}mm^2$, which produces the lowest overall AC losses among the three cases. Once again, the increasing resistivity between turns limits radial current sharing, thus reducing the total dissipated power.

5.4 Summary and achievements

The work described in this chapter aims at describing possible scenarios related to the operation of the ESMA magnet. In particular:

- A **non-linear optimal control model** was developed to exploit the temperature margins of HTS in order to **quicken the charging time** of metal insulated magnets, and primarly of ESMA.
- The optimization returns a **non-linear current ramp** including **current overshootin constrained** to a **fixed maximum heating allowed** for the magnet.

Different quench scenarios for ESMA where then simulated in order to identify the most and least critical conditions. To this aim the magnet geometry, the regions with the lowest operational margin, the analysis setup, the potential quench scenarios configurations, and material properties were provided to Little Beast Engineering as input, and the corresponding simulation results were returned. To this purpose, the main take-away messages can be summarized in the following highlights:

- **Is it likely for a quench to naturally occur during ESMA operation?**
  To successfully induce a quench an injected energy of about **200 J** is needed to be deposited locally in a single point, specifically in the **lowest margin** region. This value far exceeds what is typically required to trigger a quench in conventional LTS coils, thus making accidental quenches very unlikely to occur in ESMA.
- **What happens if a quench event is to be forced in ESMA?**
  The most critical aspect is the development of the **current shock-wave** which causes the electrical current to be inductively transferred from quenched turns to still-superconducting ones, causing them to quench. The phenomenon ultimately lead to the quench of the entire magnet within $\sim$ **1 s**, with the development of current densities the order of $\sim$ **1200 A/mm**^{2} and local region with temperature rising to $\sim$ **650 K**.
- **Is it easy to detect a quench early enough to avoid the shock wave?**
  Detecting such an event through voltage monitoring challenging, since once a turn quenches, the current rapidly redistributes away from that location, reducing the measurable normal-zone voltage. Quench detection strategies should consider **combining voltage and temperature sensing**.
- **Is it safe to sudden discharge the coil?**
  Both a sudden discharge of the magnet and controlled discharges at constant rates as low as **1 A/s** would cause the coil to quench with the development of a shock wave. For this reason, magnet operation must rely on ramp rates significantly slower than these values, on the order of the nominal rate of **0.1 A/s.** This may require a power dissipation monitoring system capable of slowing down, stopping, or gradually reversing the current ramp to allow the magnet to stabilize.

CHAPTER 6

Small-scale HTS coils: design and test

The handling of HTS tapes is considerably more delicate than that of conventional LTS wires and cables, as even non-visible damage can significantly impact their superconducting properties. To establish reliable handling procedures and to acquire practical experience with HTS winding, a small-scale coil test campaign was carried out at LASA laboratory. The objectives of this campaign were both to evaluate a winding technique procedure which could be well-endured by the tape and to validate numerical models through experimental data. Moreover, once set the procedure, the aim is to assess the repeatability of the process, thus determining the robustness of both the coil design and the winding process. These preliminary investigations directly support the production of the ESMA magnet and provide valuable insights into the practical behavior of HTS magnets. In turn, they represent an essential step toward scaling up the technology for the development of reliable large-scale magnets with potential applications in accelerators, medical technologies, and other societal domains. This chapter presents the first HTS winding experiments carried out at the LASA laboratory. Different winding technologies are introduced and discussed, followed by the design and fabrication of the prototype coils. Finally, the results of liquid nitrogen (LN_2) testing are presented and discussed.

6.1 First winding and test experiences

A small coil production and test campaign was started with the primary intention of enhancing the experience on the conductor behavior. The first design was aimed at being mostly flexible and re-usable, such that various configurations and types of windings could be investigated in the short term. The first set of coil, therefore, were circular and dimensioned such that feedback from literature could be found, as for [107]. Moreover it was designed to be flexible and consequently able to accommodate a variable number of turns. The design is showed in the left picture of Fig.6.1, and consists of a inner mandrel of 60 mm inner diameter, made of copper, to act as the inner current adductor, a stainless steel plate to support the winding and wide enough to accommodate up to tens of turns. Once the winding is finished the plate is equipped with a support able to rotate, which acted as the outer current adductor and received the HTS tape coming out tangent form the main winding, thus enabling the closing of the winding independently

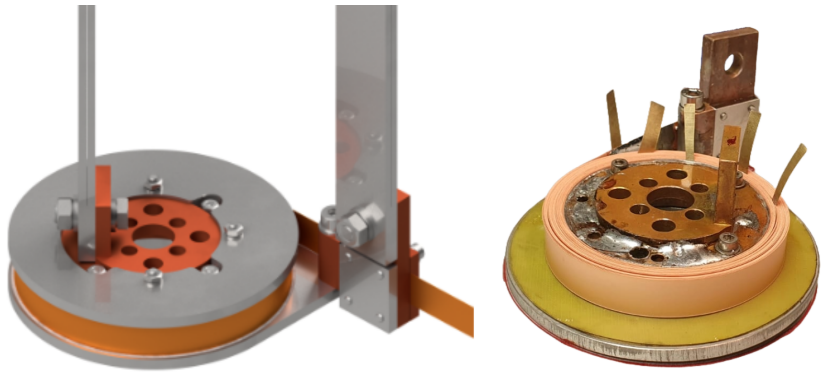


Figure 6.1: Visual representation of the design of the small circular coils (left) and manufactured NI circular coil C1 based on the design pictured aside.

from the number of turns.

Given this premises, the first family of coils wound focused on dry-wounded NI coil, such that the behavior of a in-house built NI coil could be assessed and since a single tape NI winding could be carried out even with a simple winding machine. Indeed, the winding was carried out through a manual process, this enabled a good control on the overall process, but suffered from a low repeatability. In particular the manufacturing process consisted of pre-brazing the HTS tape on half-circumference of the inner copper mandrel, top left panel of Fig. 6.2, using Sn(40%)Pb(60%) to enable the beginning of the winding process and to enhance the electrical contact with the mandrel which is acting also as current adductor. Such brazing had to be performed by hand since was to be performed on a curved geometry, thus excluding a possible use of the previously described brazing tools and introducing another source of uncertainty impacting the repeatability of the process. The winding was then performed manually, without an active tension control or recording system, as showed in the right panel of Fig. 6.2, and stopped every ten turns to insert voltage taps as in the bottom left panel of Fig. 6.2. The voltage taps consisted of a 0.025 mm thick brass sheet, which was initially brazed and then just inserted between every ten turns to avoid additional perturbations of the tape, since no difference was observed between the signals measured using soldered and dry-contact voltage taps. The voltage taps are referred to as Tn, with n increasing by 10 accordingly to the position of the voltage tap, the overall signal across the coil, i.e.: from the first to last turn, is referred to as SC. These signals were acquired using as reference the voltage tap immediately adjacent, for instance T20 is referred to as the signal measured between the 10th and the 20th- turn. The winding tension provided by the machine adopted was supplied with a mechanical friction mounted on the winding spool shaft, therefore allowing only a pre-set value of winding tension without an on-line control system. The process of stopping the winding to insert voltage taps was necessary to provide an instrumentation of the coil, however, tension losses could not be excluded in this process. A total of three different coils were produced as part of this first series using HTS tape from Bruker, details reported in Tab. 6.1. Coils were named as C0, C1, and C2 with

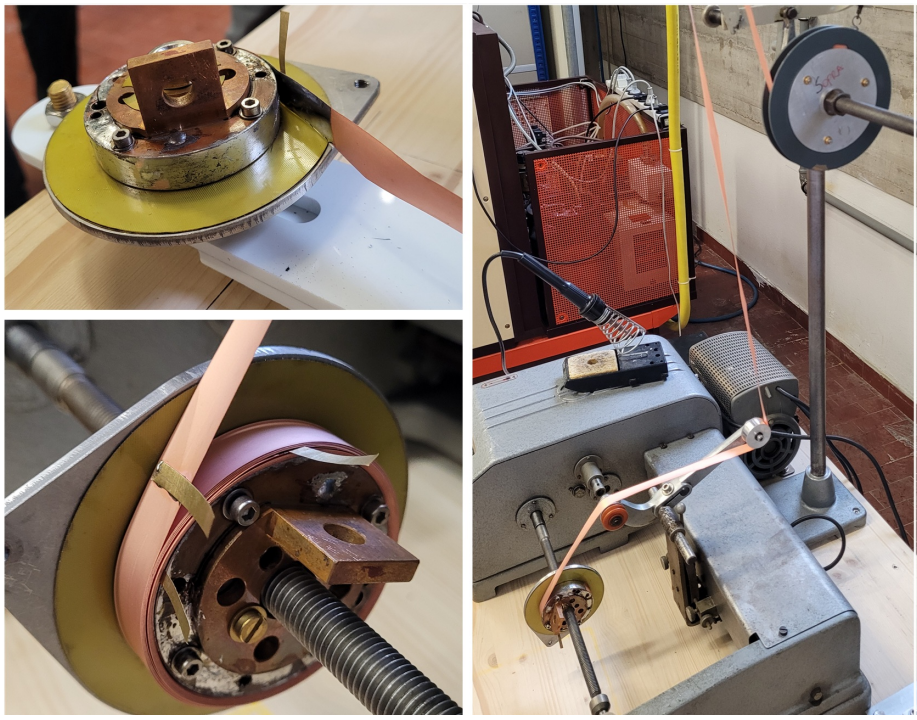


Figure 6.2: Manufacturing of the small circular coils: the top left picture represents the brazing of the first turn, the bottom left picture the placing of voltage taps, and the right picture shows the winding machine.

increasing number of turns coherently with their progressive number, and consisted in NI windings where both the number of turns and the winding tension were modified. A picture of C1 coil is represented in the right panel of Fig.6.1 and construction details are reported in Tab. 6.4. The coils were all tested at 77 K in LN_2, self-field with the aim of assessing the handling procedure, the effect of winding the tape at different tensions, and ultimately highlighting the first tier of issues in the processes, to feed further activities, as investigating different insulation and more complex geometries. The measures where carried out using the the same set up as described for critical current measurement, presented in Sec. 3.1, but instead of the nano-voltmeter a voltage acquisition system allowing for a high sampling frequency as well as multiple channels was required, therefore a Compact Field Point (CFP) from national instrument, equipped with an AI-118 analog input module was installed, allowing for the acquisition of eight channels at 100 Hz of sampling frequency, with a resolution of 100 µV in the range 0 - 1 V [108]. The test of each coil consisted in powering the winding using a staircase ramp performed with 5 A steps until the transition was observed via voltage taps signal, once the threshold imposed with the Ic_{100} criterion was surpassed. Around the transition the current steps where reduced to 2 A to better reconstruct the power law. For each step, the current was held constant, until a plateau of constant current the order of ten seconds was reached. In this particular case concerning NI winding a constant plateau appeared

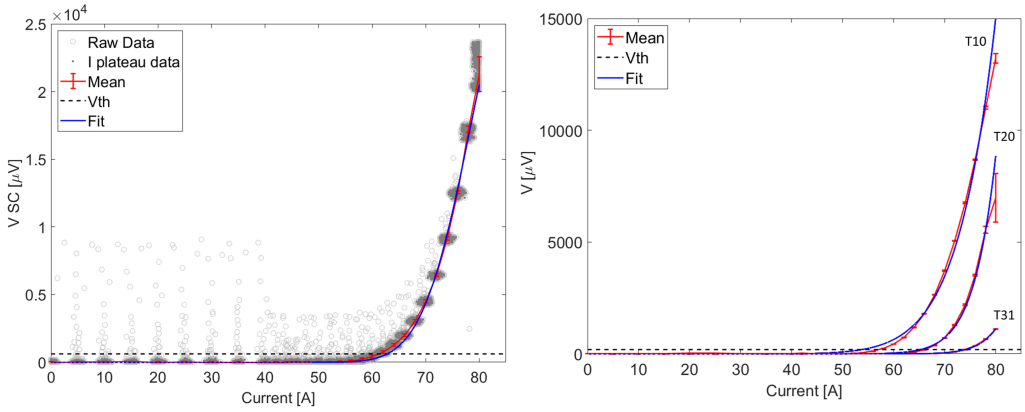


Figure 6.3: Voltage-current measured curves for C1 NI coil. The left panel shows the signal measured from the SC voltage tap across the whole coil, where the raw signal (gray circles), the plateau values (gray dots), their mean and standard deviations (red) are graphed together with the power law fit reconstruction of the signal. The right panel shows only the resulting mean, standard deviation and corresponding power law fit of the consecutive voltage taps every ten turns for coil C1.

upon completing the transient due to the electrical contact between adjacent turns. An example of the results produced by such measurement is showed in Fig.6.3: the left plot shows the resulting V-I curve for the SC voltage tap in case of the C1 coil test, where each point value and its corresponding error were calculated as the average of the points at plateau, together with the corresponding standard deviation. The data represented with gray circles, instead, represent the voltage signal during the electrical transient. In the right panel the consecutive transition measured by voltage taps T10, T20, and T30 of coil C1, corresponding to consecutive sets of ten turns, are showed. Here the effect of the peak field an the consequent decreasing of the magnetic field within the coil can be observed since the outer turns tend to surpass the 100 µV/m threshold later than inner turns. Once the last current step was fed to the tested coils, the current was reduced until all turns were superconducting and then reduced to zero in one step to maximize the signal resulting from the transient behavior that can be observed in the left figure of Fig. 6.4. The measured signal taken from the SC overall voltage tap was then reconstructed using an exponential fit, resulting form the solution of the parallel circuit between the radial resistance and the magnet inductance, as described in Sec. 1.2.4. To this purpose

Reference Bruker REBCO tape	
Substrate (material/Thickness)	Stainless steel / 50 μm
Cu stabilizer (type/thickness)	Electroplated / 20 μm per side
REBCO thickness	2.5 μm
Dimensions (width $\times$ thickness)	12.1 mm $\times$ 0.11 mm
I_c (77 K, self field)	100 A

Table 6.1: Specifications and properties of the HTS tape from Bruker.

the test of coil C2 was dedicated to assess the effect of the winding tension on the contact resistance, and ultimately on the charging time constant. Indeed, the last version of the first series of NI coils was wound with more turns and the winding tension was doubled. Given the inductance of the coil, the exponential fit would return the charging time constant τ and the contract resistance R_{ct} of the tested coil. The results of the critical current measured for all the tested coil of the first NI winding campaign, i.e.: for C0 and C1, are reported in Tab. 6.2, whereas the values of τ and R_{ct} for each coil are reported in the summary table regarding these small circular windings, Tab. 6.4. In case of the first C0 test coil, the charging time transient behavior was too fast to be appropriately recorded and only an estimation of its characteristic values is reported. On the other hand, the overall behavior of the coil could be estimated. Under the assumption of a magnetic field parallel to the tape *c*-axis, the simulated performance yields an expected critical current of 76.5 A, using the $I_{c_{100}}$ criterion, while when assuming a field perpendicular to the *c*-axis increases the predicted value to 85.5 A. These values should be compared with the experimentally measured critical current of 78 A, thus suggesting that the coil suffered no degradation caused by the winding procedure. The calculations were performed assuming current redistribution across the width of the tape. For what concerns the transient behavior, from the results reported in the table, it can be readily observed that the charging time constant of these windings is strongly dependent on the winding tension and, consequently, on the contact resistance R_{ct} between adjacent turns. In fact, the measured values of τ for each coil vary by more than one order of magnitude depending on the applied winding tension. This emphasizes the importance of performing NI windings under sufficient tension to ensure good electrical contact between turns, thus allowing the coil to fully exploit the intrinsic quench protection properties of this technology. Furthermore, a tension control system is required to continuously monitor the winding process, record its history, and promptly intervene in the event of localized tension variations, which would otherwise result into a non-uniform contact resistance.

Following the characterization of each coil in terms of I_c and τ, over-current tests were performed up to coil breakdown. Failure consistently occurred at the outer end of the winding, where the tape exits the coil tangentially to connect with the external current lead, as showed in Fig. 6.5. This was contrary to expectations, as the lowest I_c value, due to the peak magnetic field, was in the innermost section of the coil near the central

Coil	**Voltage taps**	**I_c [A]**
C0	SC	78 ± 2
C1	T10	53 ± 2
	T20	65 ± 2
	T30	73 ± 1
	SC	62 ± 1

Table 6.2: Critical current values of the first series of small circular NI coils wound and tested at LASA laboratory. The values are referred to the overall I_c value in case of the SC voltage tap and, where possible, for each consecutive set of ten turns in case of voltage taps T10, T20, and T30.

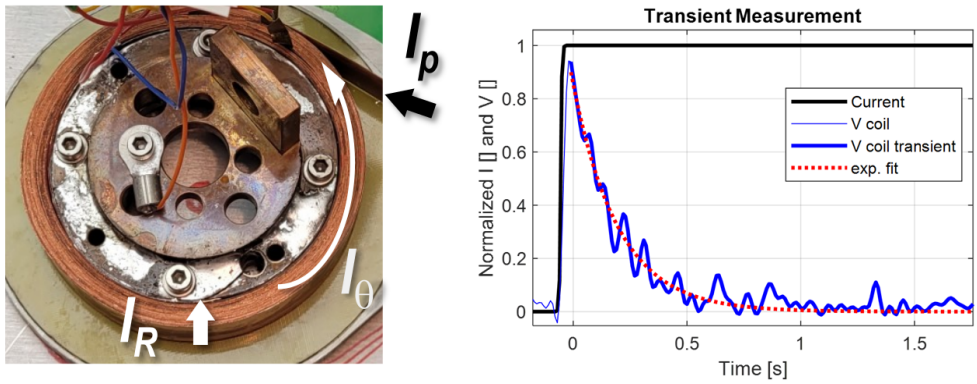


Figure 6.4: In the left panel is sketched the current behavior when powering a NI coil, i.e.: the presence of a parallel circuit between a radial resistance and an inductance generates both an azimuthal and a radial current for a time scale the order of τ. This behavior was measured as reported in the right panel where the exponential decrease of the measured voltage over time when the current was suddenly increased with a step is reported, together with an exponential fit reconstruction of the signal.

mandrel. These results demonstrate the robustness of NI windings in small, low-energy coils, confirming their self-protective behavior.

Two additional versions of coil C1, thus considering 30 turns of HTS tape, were produced following an insulated design. In particular the first version named C1-fiber resulted from a co-winding of HTS tape and a 0.13 mm thick and 12 mm wide fiberglass tape which was positioned at the beginning of the winding after the soldered part such that it could be dragged in between each tape by friction, thus avoiding the need of an additional tensioned winding winding spool support. The resulting coil is showed in the left panel of Fig. 6.6. This coil was initially tested to assess the effectiveness of the fiberglass insulating layer, following the same procedure as for the previous coils. Indeed, the measurement highlighted no measurable transient behavior. The same coil was then impregnated with paraffin wax leading to C1-wax coil, showed in the right panel of 6.6 after the LN_2 test. Impregnation was carried out with the same procedure as for the wax-impregnated sample prepared for thermal conductivity measurements in Sec. 4.1.1. The impregnation process, widely adopted in conventional LTS magnets, serves to ensure uniform mechanical contact throughout the entire winding, effectively allowing the coil to behave as a single, consolidated body, thus enhancing its mechanical stability. Traditionally, epoxy resin has been employed for this purpose, providing additional structural rigidity to the winding [109]. However, in the case of HTS tapes, the strong adhesion between the tape surface and the epoxy matrix, combined with the significant shear stresses experienced during operation, can lead to delamination of the superconducting layer[110]. This phenomenon causes irreversible damage to the conductor and can critically compromise the overall integrity and performance of the coil. To address this issue, paraffin wax was selected for the impregnation of the C1-fiber coil. Wax pro-

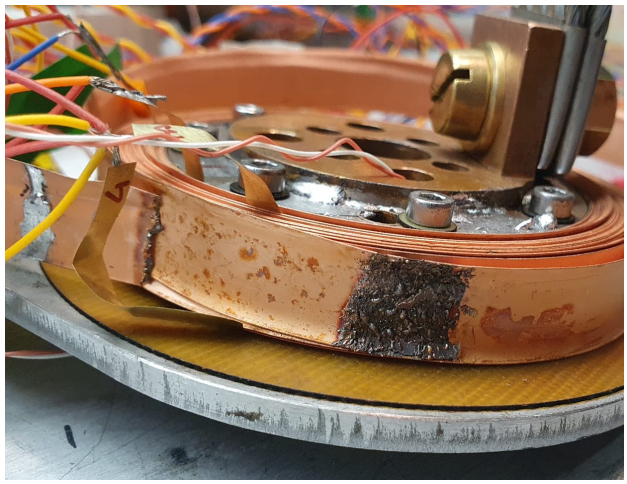


Figure 6.5: Breakdown region of C2 NI circular coil.

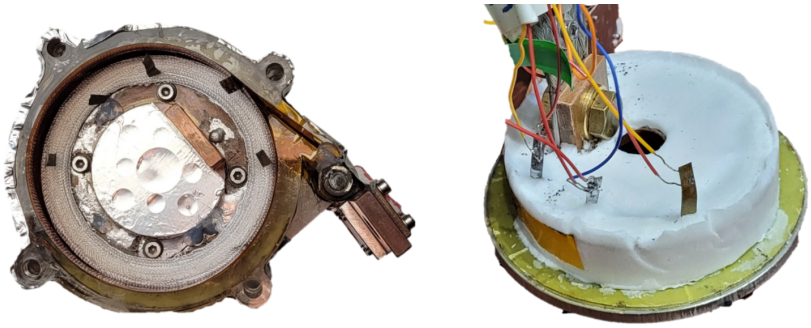


Figure 6.6: Small circular coil co-wound with fiberglass tape to insulate each turn (C1-fiber, left panel). The same coil was impregnated with paraffin wax and tested again (C1-wax, right panel).

vides both electrical insulation and ensures a uniform thermal contact between adjacent layers, while its relatively low mechanical rigidity minimizes the risk of inducing shear stresses. Although mechanically softer than traditional epoxy resins, this characteristic becomes beneficial in the context of HTS windings, as it helps to prevent delamination of the superconducting layer. For these reasons, wax may represent a promising candidate for the impregnation of HTS coils.

The paraffin wax impregnated C1-wax coil was tested in LN_2 following the same procedure as for the other tests, and measurements results are reported together with C1-fiber test measures in Tab. 6.3. As can be observed, the measured I_c values are consistent with those obtained in previous winding trials on NI coils, confirming that both the dry winding procedure for NI coils and the fiberglass co-winding ans subsequent impregnation process for insulated versions of C1 yielded reproducible results. Furthermore, the effect of the insulation was assessed by analyzing the coil response under current step excitation, during which no measurable transient behavior was detected. Over-current



Figure 6.7: Insulation test performed on C1-wax coil after LN_2 test at 2.5 kV.

tests were also performed, however the electrical breakdown of C1-wax coil could not be achieved due to the voltage saturation of the power supply. A further insulation test was carried out on C1-wax after LN_2 measurements. The coil was initially cut to visually assess the penetration of wax in between each turn on the fiberglass tape. Then the insulation quality was controlled by connecting a megger, insulator tester, between one turn and one voltage tap as showed in Fig. 6.7, resulting into a resistance of more than 150 GΩ at 2.5 kV, thus confirming the insulation reliability of fiberglass and paraffin wax impregnation.

Given the experience gained with the first set of small circular coils, both fully non-insulated and insulated with a wax-impregnated versions, a new prototype was developed to assess a geometry more representative of the final ESMA windings, namely a small racetrack coil. To this aim, a dedicated design was developed, as shown in the left panel of Fig.6.8. The coil features a central support made of 3D-printed polypropylene reinforced with glass fibers (PPGF), which serves both as the winding plate and the inner

Coil	Voltage taps	I_c [A]
C1-fiber	T10	59 ± 1
	T20	69 ± 1
	T30	73 ± 2
	SC	62 ± 1
C1-wax	T10	58 ± 1
	T20	67 ± 2
	T30	74 ± 2
	SC	62 ± 1

Table 6.3: Critical current values of the first series of small circular NI coils wound and tested at LASA laboratory. The values are referred to the overall I_c value in case of the SC voltage tap and, where possible, for each consecutive set of ten turns in case of voltage taps T10, T20, and T30.

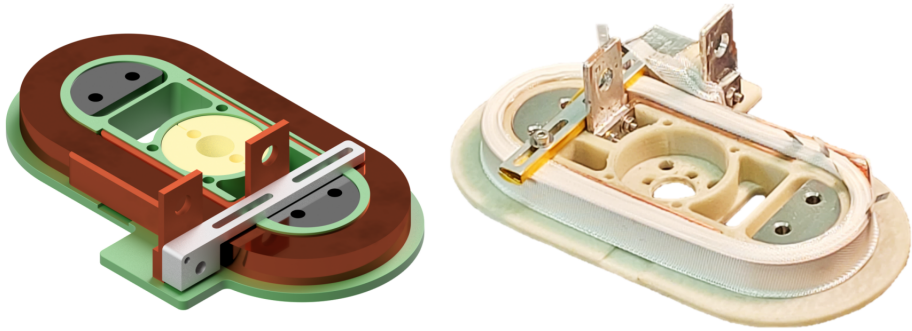


Figure 6.8: Rendered and real images of the first HTS ractrack coil

mandrel. The choice of PPGF provided greater design flexibility thanks to the versatility of additive manufacturing and was motivated by its relatively low thermal contraction among 3D-printed plastics, measured as an integral contraction of 6 mm/m, as reported in Sec. 4.2.1. Although PPGF exhibits lower mechanical strength compared to G10 or metallic mandrels, it was evaluated to be sufficiently robust to withstand stresses arising from both thermal contraction in liquid nitrogen and winding tension. Moreover, the mandrel was equipped with two D-shaped stainless steel inserts to counteract PPGF contraction on the curved sections, and a copper bar, together with the inner current lead, to limit deformation along the straight sides. The winding plate was designed to accommodate a variable number of turns, ensuring similar flexibility to that of the small circular coil design. In this configuration, however, the winding could be terminated near the coil itself, eliminating the need for the tape to exit tangentially from the main body as in previous designs. The closure of the winding was achieved through an adjustable aluminum clamp mounted on the PPGF mandrel, featuring two slots to adapt to the total thickness of the winding. Finally, the racetrack geometry allowed junctions to be positioned along the straight section, thus enabling the use of the brazing tool previously developed for the resistive splice experimental campaign. Key design parameters are reported in Tab. 6.5.

	C0	**C1**	**C1-fiber**	**C1-wax**	**C2**
Turns	5	30	30	30	45
Winding technology	NI	NI	INS	INS	NI
Winding Tension [N]	8	10	15	15	30
Tape length [m]	0.95	5.95	6.23	6.23	9.13
τ **[s]**	< 0.01	0.2 ± 0.020	N/A	N/A	45 ± 4
L [mH]	0.003	0.075	0.074	0.074	0.167
Rct [$\mu\Omega$cm^2]	>2000	319 ± 31	N/A	N/A	3.2 ± 0.3

Table 6.4: Construction details and physical properties of all the small round coils designed and tested at LASA laboratory.

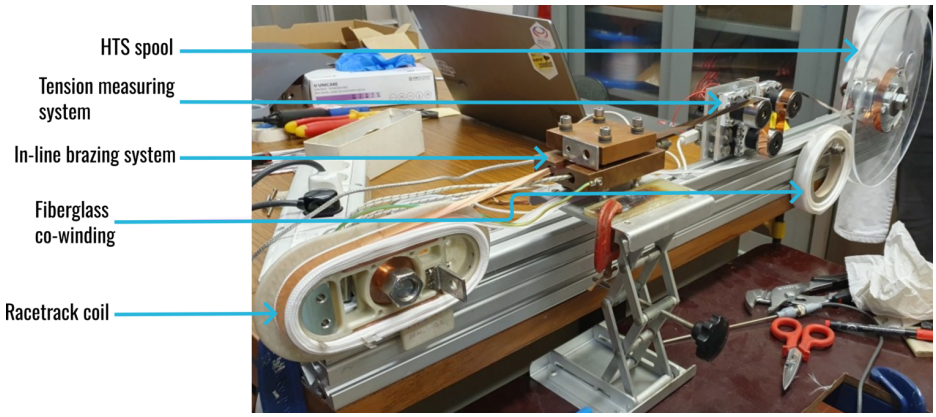


Figure 6.9: Improved version of the manual winding machine, used to wind the first HTS racetrack coil at LASA.

The winding procedure for this racetrack coil was performed using an ad hoc system, which, although still operated manually, was significantly improved based on the experience gained during the previous campaign involving circular windings. The upgraded manual winding tool is illustrated in Fig. 6.9. The winding tension was given through a mechanical friction device positioned on the spool axis. A second mechanical friction system, set to a lower resistance, was mounted on the axis of the racetrack coil mandrel to compensate for tension losses that occurred whenever the winding process was stopped. Similarly to the procedure adopted for the previous coils, the winding was interrupted every ten turns to insert brass strips serving as voltage taps. To monitor the winding tension, a passive measurement system was implemented in-line with the winding setup. This system consisted of two fixed pulleys and one mobile pulley, the latter being displaced toward a load cell by the tensioned tape, thus enabling a passive and continuous measurement of the applied tension. Upon completion of the winding, the brazing tool was inserted in-line to perform the brazing of the external adductor, allowing the winding to be finalized and the tape to be cut with minimal tension loss. Given that winding tension was identified as a key parameter for NI windings, this first racetrack coil was co-wound with a 12 mm wide and 0.13 mm thick fiberglass tape, and subsequently impregnated with paraffin wax following the same procedure used for the C1-wax coil. This approach was intended to reduce manufacturing uncertainties during

Racetrack coil parameters	
Mandrel material	PPGF
Curvature radius	25 mm
Straight side	90 mm
N turns	38
Expected Ic	230 A

Table 6.5: First HTS racetrack coil key design parameters

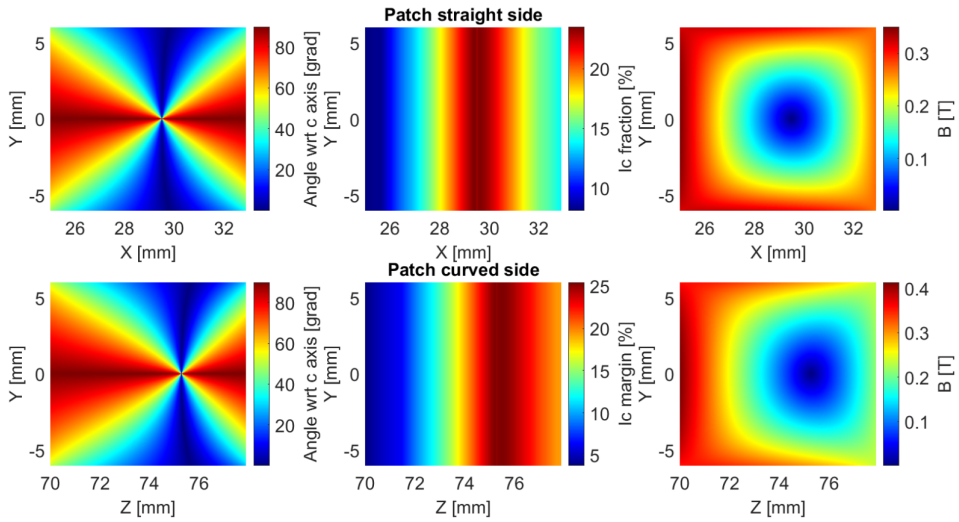


Figure 6.10: Simulation results of magnetic field angle and magnitude, and expected Ic margin at 230 A for the first HTS racetrack coil at two different sections of the coil: in the middle of the straight section (top) and of the curved side (bottom).

testing. Unlike the circular coils, the racetrack coil was wound using a 12 mm-wide HTS tape supplied by Faraday Factory Japan (FFJ), whose properties are well-characterized, allowing for a more accurate estimation of the expected performance of this design. The detailed characteristics of the specific FFJ HTS tape spool used for the winding are listed in Tab. 6.6. Given the expected critical surface of the FFJ tape at 77 K, as reported in [71], the average critical current provided by the manufacturer through Tapestar measurements at 77 K and self-field conditions, 590 A in this case, was used to rescale the critical surface. A three-dimensional magneto-static model of the coil was then developed in Opera 3D, and the resulting magnetic field magnitude and orientation were extracted to evaluate the I_c margin of the coil by interpolating the critical surface. The results are summarized in Fig. 6.10. Subsequently, the coil was discretized using a MATLAB code to compute the local electric field values according to the power-law equation, with the objective of integrating these values along a racetrack-like path to reconstruct the expected voltage-current expected signal. From this analysis, the estimated critical current of the coil was found to be approximately 230 A using the transition threshold defined by the I_{c100} criterion. Moreover, since Tapestar data provides a dense spatial resolution

FFJ HTS tape charatceristics	
Substrate thickness	40 μm
Cu thickness per side	10 μm
Average thickness	70 μm
Average Ic	590 A
Minimum Ic	419 A

Table 6.6: FFJ HTS tape characteristics used to wind the first HTS racetrack coil at LASA

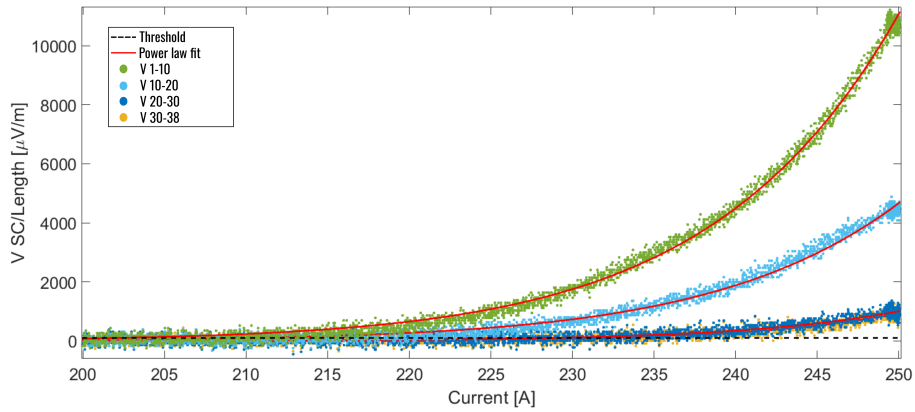


Figure 6.11: Voltage signal registered via voltage taps normalized on the length of tape between the taps themselves with respect to the powering current for the first HTS racetrack coil in LN_2 together with the reconstructed power law. The threshold correspond to the I_{c100} criterion, i.e.: 100 μV/m.

of roughly one measurement every 2 mm, a more precise performance estimation is currently under development. This refined approach involves using the exact portion of the tape employed in the winding, corresponding to the measured Tapestar section, to derive a local critical current profile. This localized I_c distribution will then be used to rescale the critical surface before performing the racetrack integration, enabling a more accurate reconstruction of the expected power-law transition. The racetrack coil was first energized using a staircase current ramp, and subsequently with linear ramps in LN_2 up to the transition of each set of turns. The resulting voltage–current measurements, normalized with respect to the conductor length, are reported in Fig.6.11, together with the reconstructed power-law fit from which the I_c values listed in Tab. 6.7 were extracted. A Hall probe was also installed at the coil center to measure the magnetic field at the maximum applied current. The measured central field reached 132 mT, in good agreement with the simulated value of 133 mT at the same current. The acquisition of such measurement was carried out using the same experimental set up disclosed previously. However, the overall simulated I_c slightly overestimates the experimentally measured critical current. This suggests that a more detailed analysis, currently underway, may be necessary to refine the prediction accuracy. Such an analysis could also help to exclude the possibility of performance degradation related to the manufacturing process.

Voltage taps	**I_c [A]**
V 1-10	202
V 10-20	210
V 20-30	228
V 30-38	232
Overall	212

Table 6.7: Measured I_c values for the first HTS racetrack coils in LN_2.

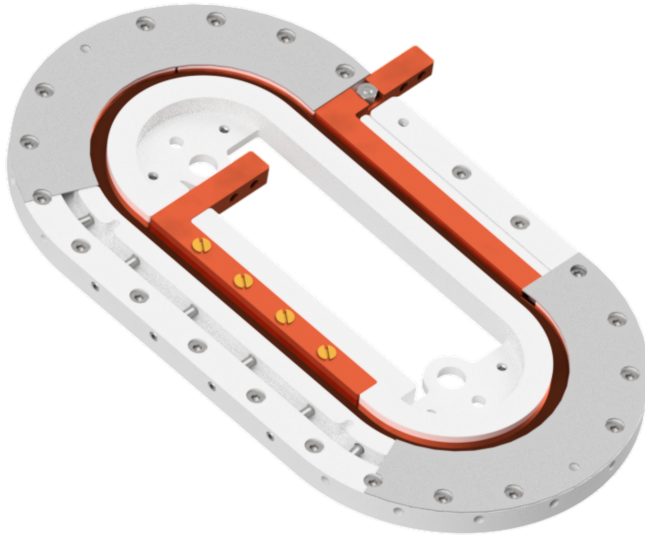


Figure 6.12: Visual representation of the improved design of the HTS small racetrack coil

6.2 Small-scale NI racetrack coils

The experience collected in the design, winding, and testing of small HTS coils, both insulated and without turn-to-turn insulation, led to the development of a new racetrack coil design. The new design aims to achieve a more controlled and repeatable coil manufacturing process, thus contributing in realizing and studying NI coil behavior without uncertainties related to the realization itself. The effort is carried out in synergy with the ESMA magnet development, with the dual objective of advancing the technological readiness level of REBCO conductors for future particle accelerator applications and building in-house expertise on HTS winding technologies to support upcoming projects. To this purpose two racetrack coils prototypes were designed, as showed in Fig. 6.12, manufactured and tested at LASA laboratory. The campaign focused on validating the electromechanical behavior of such coils via charging and discharging tests at different rates and transition measurements to the normal conducting state.

6.2.1 Small racetrack coils design

Each coil consists in a non-insulated 100 turn racetrack winding made of a single 4 mm wide HTS tape, wound under a controlled tension of 20 N. The manufactured coils are shown in Fig. 6.13 and their geometric parameters are summarized in Tab.6.8. The racetrack geometry was selected also in this case both for its synergy with the ESMA magnet project and as a representative configuration for long accelerator-type magnets. In addition, this geometry allows for simpler straight current leads, compatible with the developments of the dedicated brazing tool. Analogously to the first racetrack coil design, the mandrel was fabricated using 3D-printed PPGF. However, in this updated



Figure 6.13: The two coils produced with 3D-printed PPGF mandrel before the tests. The coils share the same design, and the only noticeable difference is that the mandrel of Coil 1 (left) is one bulk piece, while the one of Coil 2 (right) is in two pieces: extra screws are visible on top of it.

configuration, the mandrel assembly includes, in addition to the base plate, a coil pre-stress system consisting of a surrounding frame equipped with threaded holes for M3 grains used to apply uniform pressure around the coil. Given the dry-wound nature of this racetrack coil, the pre-stress system was implemented to prevent unforeseen variations in contact resistance and to maintain the structural integrity of the winding during cool-down, warm-up, and energization. Moreover, the use of pressers effectively mitigated the buckling effect observed along the straight sections, which typically arises from the loss of radial stress induced by the winding tension. The pressers were also 3D-printed in PPGF and designed to apply a uniform load along the entire coil perimeter. The coils were wound using FFJ HTS 4 mm tape from two different spools. The HTS tape expected performances measured with Tapestar technology are summarized in Tab. 6.9. In addition, critical current transport tests were performed in LN_2, self field,

Maximum central field B_0	mT	100
Peak field	T	0.6
Straight side length	mm	95
Curvature radius	mm	30
Number of turns	N/A	100
Estimated maximum current	A	70

Table 6.8: Small racetrack coil design parameters

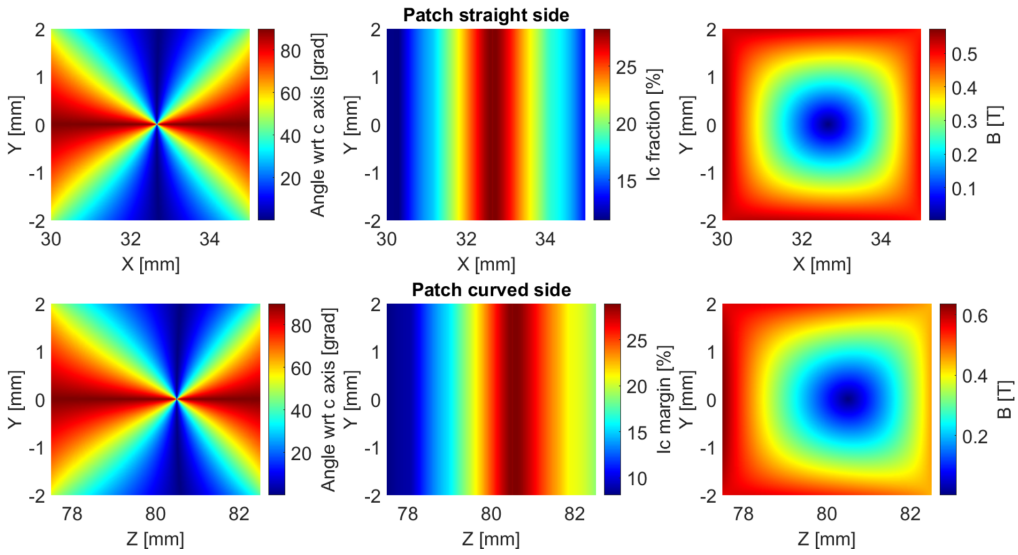


Figure 6.14: Simulation results of magnetic field angle and magnitude, and expected I_c margin at 70 A for the HTS racetrack coil wound with the higer performance tape at two different sections of the coil: in the middle of the straight section (top) and of the curved side (bottom).

on short samples taken at the beginning and end of each winding unit to validate I_c data provided from the manufacturer. The electromagnetic simulation of the racetrack configuration predicted a central field of 100 mT at 70 A, achieved by the coil wound with the higher performance tape. The corresponding field on the conductor is shown in Fig. 6.14 where the peak field is expected to reach 0.6 T in the curved section. The picture also reports the magnetic field orientation and the coil I_c margin. For what concerns the winding procedure, the machine was further improved to achieve an active tension control system, with the aim of realizing NI windings exhibiting a reproducible behavior. To this purpose, the winding was performed using the machine shown in Fig. 6.15, developed by SAES [111] for the Hi-Lumi High Order Correctors (HOC) project [112] and later upgraded to handle 4 mm HTS tape without twisting or introducing hard-way paths. The system features an active real-time tension control mechanism based on a

	Tape for Coil 1	Tape for coil 2
Thickness	50 μm	
Hastelloy	30 μm	
Cu (per side)	5±2 μm	
Ic average Tapestar	241 A	183 A
Minimum Ic Tapestar	174 A	154 A
Ic from transport current	231 A	184 A

Table 6.9: FFJ HTS 4 mm adopted tape characteristics

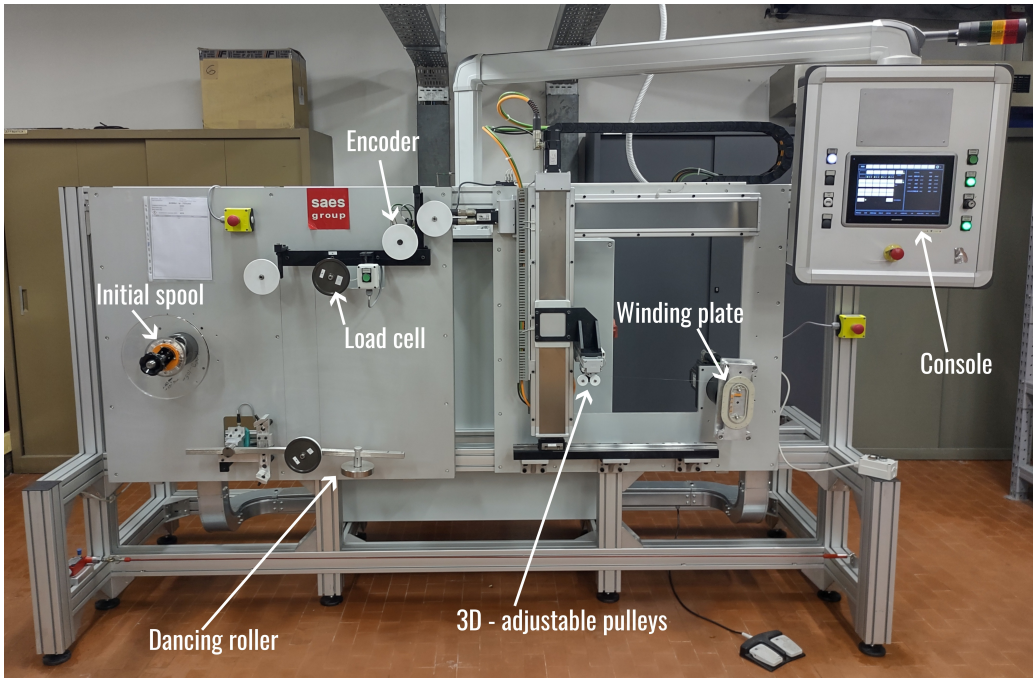


Figure 6.15: Winding machine from the Hi-Lumi HOC manufacturing [112], now upgraded to wind HTS coils.

dancer roller, ensuring consistent tape tension during winding. Tension measurements are acquired via a load cell (0.1 N resolution) and recorded during the entire process, while tape length is monitored using an encoder. Using this setup, two non-insulated racetrack coils were successfully wound as showed in Fig. 6.13, achieving tight layer alignment and uniform mechanical tension. Once the second current lead was brazed and secured to the mandrel base plate through a dedicated threaded hole, the external compression frame was mounted and the grains tightened to compensate for buckling along the straight sections.
In order to ensure repeatability of splicing and brazing of the current leads and potentially of internal joints, the thermal- and pressure-controlled system described in Sec. 3.3 was employed. The system was moved in-line with the winding machine to perform online splicing or brazing, as shown in Fig. 6.16. A 3-axis system allows the positioning of the tool.
The nominal performances of the racetrack coils expressed in terms of their transfer functions were evaluated as follows:

1. The same critical current functions used in previous simulations were adopted, with each coil assigned its own measurement-driven curve.

2. An average turn of the coil was considered, and a current divider was solved between the azimuthal (spiral) and radial (inter-turn) current paths. The azimuthal path follows a power-law resistivity, while the radial path resistance corresponds

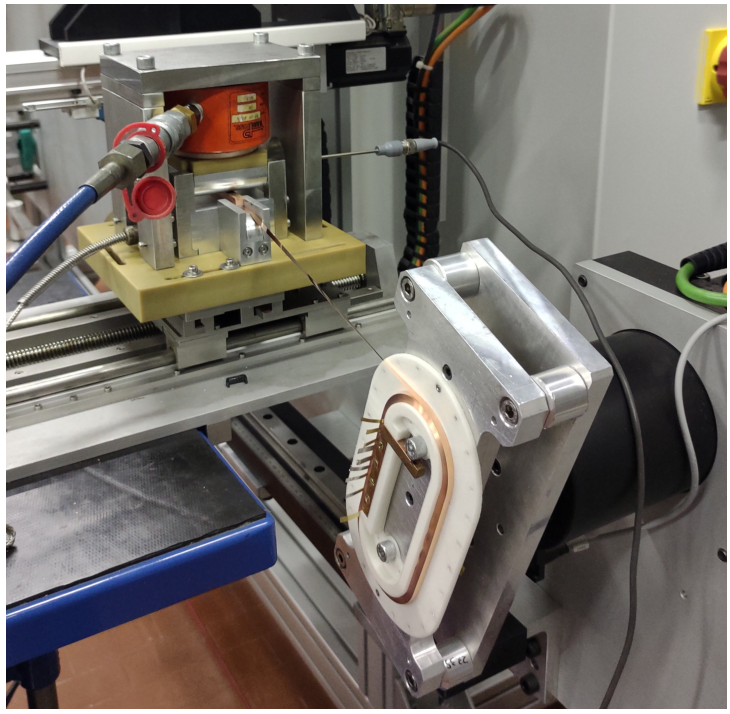


Figure 6.16: In-line current lead soldering using the temperature and pressure controlled brazing system.

to the measured turn-to-turn resistance (described later on in this section).

3. The system is described by the implicit equation:

$$I_\theta + \frac{V_\mathrm{c}}{\mathrm{R_{turn}}} \left(\frac{I_\theta}{I_\mathrm{c}} \right)^n = I_\mathrm{t}, \tag{6.1}$$

being I_θ the azimuthal current, V_c the threshold criterion for one turn, $\mathrm{R_{turn}}$ the turn radial resistance and I_t the transport current.

4. For each I_t value, the equation was solved for each turn block to obtain the equivalent ampere-turns generating the central magnetic field.

5. The field calculation was updated accordingly. Results are presented in Fig. 6.17.

This method provides a first-order estimation of the nominal performance of the magnet.

6.2.2 Small racetrack coils LN_2 test results

Both coils were tested in LN_2 using the same set-up as in the previous HTS coils tests and for transport current measurements on short samples. Voltage was measured both

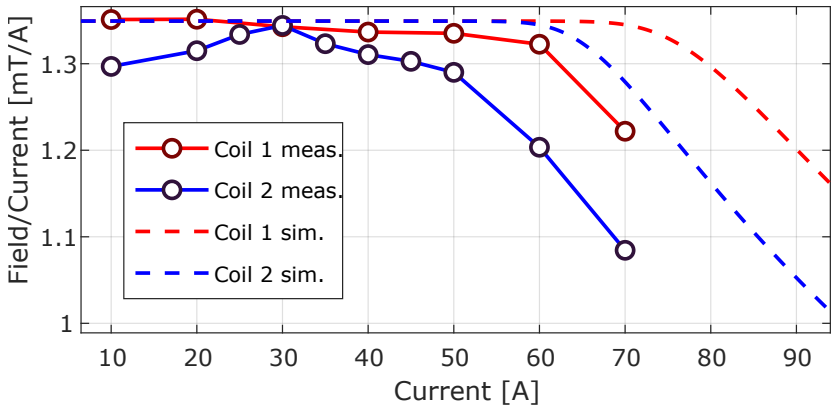


Figure 6.17: Transfer function of the flux density in the center for both coils. Both measured and simulated results are shown, highlighting that both coils are under-performing against the expectations. Both post-mortem analysis and improved models are needed to fully understand the gap.

across the entire coil (including copper leads) and locally across nine dry voltage taps installed approximately every 5 m, corresponding to $\sim$ 12 turns, as shown in Fig. 6.18. A Hall probe positioned at the coil center measured the magnetic field. All signals were acquired using a National Instruments Compact FieldPoint (cFP) system: current and field sampled at 3 kHz, and voltage taps at 2 Hz due to their low amplitude. The primary objectives of the test campaign were both to quantify performance degradation relative to nominal expectations and to characterize the time constant and current-bypass dynamics due to the completely NI design. To this purpose, the static transfer function of the central magnetic field was derived and compared with simulation results, as graphed in Fig. 6.17. For the second, the step-response behavior was fitted with an exponential decay, resulting from the RL circuit solution, as showed in Fig.6.19. The static transfer function was obtained via a staircase current cycle, consisting of 10 A steps every 150 s, approximately corresponding to a value of 10 measured charging time constants τ. The voltage across the taps for both coils is shown in Fig. 6.18, where coil 2 exhibits degradation in the inner turns. Overall, the lower performance of coil 2 compared to coil 1 is consistent with the reduced critical current of its corresponding short sample. It is worth to highlight how the measured transition of the various voltage taps graphed in Fig. 6.18, follows the I_c margins distribution in the central plot of Fig. 6.14, namely resulting in the innermost and outermost set of turns to surpass the threshold before the central turns, due to lower values of magnetic field. Transfer functions reported in Fig. 6.17 show that the field decay due to radial current flow occurs approximately 15 A earlier than predicted by simulation for both coils. Once the current corresponding to full superconductivity was determined, a step-down transient was analyzed. Field and voltage decays were fitted with exponential functions, as showed in Fig. 6.19, yielding τ values of 17.5 s and 13.2 s, corresponding to specific contact resistivity of 0.98 mΩ·mm^2 and 1.29 mΩ·mm^2 for the first and second coils, respectively. It is important to note from Fig. 6.19 that the observed transient behavior is consistent across all measurements from

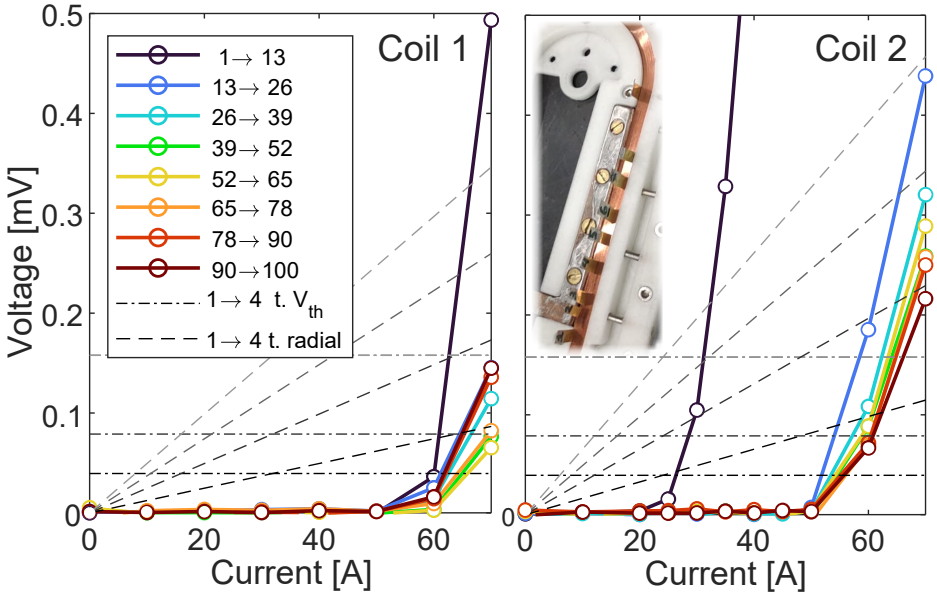


Figure 6.18: Voltage differences across the turns pack for both racetrack coils. The non-solid lines are the superconducting voltage thresholds (E= 0.1 mV/m) for 1 to 4 turns, together with the voltages arising if 100% of the current goes radially in one turn.

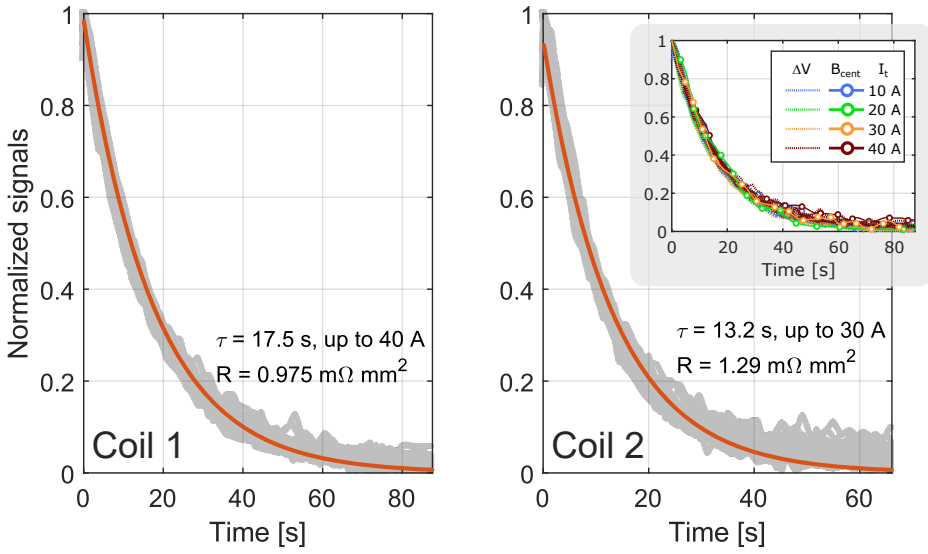


Figure 6.19: Step response of field sensors and of voltage differences. As shown in the floating panel, in the linear (i.e. full superconducting) regime, voltages and Hall experience the same decay. Higher-current transients are not shown for clarity, but they do differ.

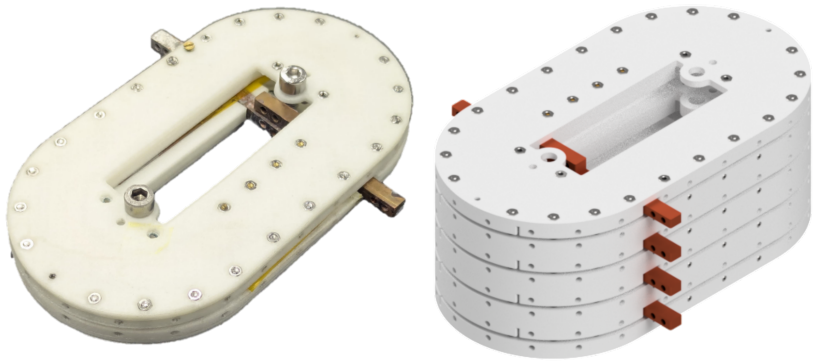


Figure 6.20: Mechanical assembly of the two manufactured and tested racetracks (left) and rendered prevision of a racetrack stack foreseen by this campaign (right).

both the partial voltage taps and the Hall probe. This indicates that voltage taps can reliably be used to investigate the characteristic charging time transient behavior of the coil, instead or complementary to the Hall probe, which provides a direct measure of the magnetic field and, consequently, of the azimuthal current flowing in the winding. Moreover, the observation of the same response across all voltage taps suggests that the turn-to-turn resistance is uniformly distributed throughout the coil. On the other hand, to establish statistically significant conclusions on reproducibility, additional coils of the same design are being manufactured and tested at LASA laboratory.
Within the IRIS Project, substantial progress was made toward the next generation of HTS accelerator magnets. Efforts toward repeatability include, semi-automatic brazing and splicing procedures, and precise control of winding parameters, all aimed at developing a robust quality control system for magnet fabrication. These developments operate synergistically with the modular construction approach, shared with ESMA, in which each coil is treated as an independent magnetic module. This enables individual testing, sorting, and acceptance, leading to a more reliable and reproducible magnet assembly. The first two modules of a possible stacked racetrack configuration, showed in Fig. 6.20, successfully manufactured and tested, with additional units in progress. Future work will aim to refine the process, better understand performance losses, and develop comprehensive coupled models to support both design and experimental characterization.

6.3 Summary and achievements

This final chapter describes the initial phase of the experimental campaign dedicated to the design, manufacturing, and testing of small-scale HTS coils. The experimental campaign achieved the following results:

- A **preliminary set of round coils** was successfully designed and tested, providing the basis for experience with both **non-insulated** windings and insulated coils impregnated with **paraffin wax**.
- A dedicated **winding machine** was adapted and validated for winding non-insulated HTS racetrack coils, featuring a **real-time tension control system**.
- A **winding procedure** was defined to wind HTS racetrack coils, capable of yielding **consistent charging time** constants once the winding tension is fixed.
- The **joint manufacturing tool** and procedure previously developed were successfully applied to perform in-line resistive splices without inducing tension loss.
- The experimental behavior of the coils was modeled to predict the **expected performance** of the manufactured coils based on available measurements and the Tapestar characterization of each spool. Ongoing upgrades aim to improve the accuracy of these predictions and achieve better agreement with experimental data.
- **Two equal racetrack coils** were wound with a **20 N** winding tension and tested in **liquid nitrogen** to assess the repeatability of the process. The measured charging time constant were **17.5 s** and **13.2 s**, corresponding to contact resistances of **9.75 $\mu\Omega\cdot cm^2$** and **12.9$\mu\Omega\cdot cm^2$** respectively. **Additional coils are planned** to improve the statistical significance of the results. Further refinement of the process is also required to avoid performance losses.
- The manufactured coils will ultimately be combined to realize a **racetrack stack** , in order to measure the overall behavior of the coil assembly and to further validate the preliminary simulations.

Conclusion

The study of the Energy Saving Magnet for Accelerator (ESMA) focused on developing a dipole demonstrator fully based on REBCO High Temperature Superconducting (HTS) tape, aimed at validating the technological readiness recently achieved through fusion-driven progresses in REBCO production. This research is part of the project IRIS, funded by NextGeneration EU, aimed at realizing an Innovative Research Infrastructure on applied Superconductivity in Italy. IRIS involves six technological poles already conducting research in superconductivity, cryogenics, or accelerator instrumentation which are being upgraded and assigned specific roles, promoting complementarity and collaboration across the network. Within IRIS, WP8 and WP9 are dedicated to the design and realization of two technological demonstrators, one of which is the ESMA magnet. In addition to serving as a technological demonstrator, ESMA has a second purpose: to provide INFN Genova with a variable magnetic field test facility for characterization of superconducting materials.

The dipole was designed to produce a maximum central field of 10 T and to operate cryogen-free at 20 K, a challenging feature because of the extremely limited thermal budget. On the other hand, the possibility to operate at higher temperatures offer an energy saving the order of a factor of five with respect to classical Low Temperature Superconducting (LTS) magnets operated at 4.2 K in a liquid helium bath, considering only thermal efficiency. ESMA therefore represents an early milestone toward a new generation of more sustainable, higher performance superconducting magnets for future particle accelerators such as the Future Circular Collider (FCC) and the Muon Collider (MuCol).

A primary challenge addressed in this work was designing a coil geometry suitable for tape conductors rather than for traditional round wire. In particular, the preferential bending direction of tapes discourage non-flat geometries as, for instance, solutions that cross the mid-plane as in the classical cos θ design. To this purpose an optimized geometry was developed that satisfies the project requirements while facilitating industrial scale manufacturing. The electromagnetic design was studied in depth and supported by extensive experimental campaigns to map tape electrical properties. These campaigns expanded the set of parameters available for future designs and motivated a novel junction concept intended to overcome the limitations of classical lap or bridge geometries without substantially lower cable performance.

Dedicated measurement campaigns were also carried out to characterize the thermal and mechanical properties of the tape. Thermal conductivity tests were performed on tape stacks in the dry configuration representative of ESMA and on a potential impregnated variant using paraffin wax, which appears promising as an impregnant that avoids delamination. Mechanical testing revealed a non-uniform cross section and a lower than expected Young's modulus. These studies are initial but important steps toward a more complete characterization of REBCO tapes and highlighted several primary issues whose discovery was driven by the study of ESMA.
Since conductor behavior during quench events remains an open point in the community, the design exploration included a metal-as-insulation winding technique. This approach helps quench protection by reducing localized hot-spot formation but introduces a finite charging transient during ramps, which could conflict with the role of ESMA as a variable-background testing facility. To address this trade-off, charging procedures were investigated and optimized, including ad-hoc non-linear current ramps intended to minimize charging time without inducing excessive dissipation that would trigger a quench. These studies also established preliminary limits on acceptable ramp rates. Although comprehensive quench modeling and protection remain open research topics, one insight from the experience gained with ESMA is that, given the large temperature margin of REBCO conductors, shifting the paradigm toward quench prevention, rather than relying on protection, may be advantageous. This fact is particularly when considering the destructive scenarios suggested by early quench simulations.
Concerning the applications of HTS tapes in particle accelerators, additional considerations remain, mostly due classical adoption of multi-filamentary, twisted cables to reduce AC losses and magnetization effects. These requirements are essential to reach the repeatable and homogeneous good field region needed for accelerator operation and to meet the machine ramping requirements defined by the duty cycle. Although these aspects were secondary for ESMA, given its more relaxed field-quality constraints and the possibility of performing slower current ramps, they must be addressed in future designs aiming at particle accelerators.
To capitalize on ESMA experience, a small-scale coil experimental campaign was initiated and is currently ongoing. These tests provide fundamental insight into handling and winding procedures and serve to validate conductor behavior against simulation predictions.
To sum up, as of mid-2025, the mechanical, electrical, and thermal subsystems and the winding tooling are in place at ASG; the cryostat and thermal shield are expected before the end of 2025. Winding procedure refinement is ongoing using full-scale mandrels. A prototype module is scheduled for fabrication in Q3 2025 and will be tested at LASA in a liquid helium environment as soon as it is available. The main objective of that test is to push the coil current to its mechanical limit: peak stress on the conductor is estimated near ~ 2200 A, and if that threshold is reached, even higher currents will be explored. Final testing of the full magnet in its operational cryostat, including cool-down and warm-up cycles, ramping sequences and stability checks, and magnetic field mapping with a fixed Hall-probe array, will follow to verify performance against design predictions and to probe operational limits.

Despite the tight schedule imposed by the IRIS timeline, milestones are generally on track: magnet assembly is expected by the end of 2025, followed by final tests. The 10 T HTS dipole being developed under IRIS is a first step toward sustainable high-field magnet technology, combining cryogen-free operation, all-HTS conductors, and novel approaches to quench management. The data, methods, and practical experience generated by ESMA will directly support future high-performance accelerator magnets and broader societal and medical applications.

Bibliography

[1] H.K. Onnes. *The Liquefaction of Helium*. Communication No. 108 from the Physical Laboratory at Leiden, 1908.

[2] H. Kamerlingh Onnes. Sur les Résistances Électriques. *Communications from the Physical Laboratory of the University of Leiden*, 1911.

[3] M. Hauschild. *Exploring the Large Hadron Collider – CERN and the accelerators : the world machine clearly explained*. Essentials. Springer, Wiesbaden, 2021.

[4] I. Bejar Alonso and L Rossi. HiLumi LHC Technical Design Report: Deliverable: D1.10. Technical report, CERN, 2015.

[5] F. Benedikt, M. Zimmermann et al. Future Circular Collider Feasibility Study Report Volume 2: Accelerators, technical infrastructure and safety. Technical report, CERN, Geneva, 2025. 627 pages. Please address any comment or request to fcc.secretariat@cern.ch.

[6] C. Accettura et al. Towards a muon collider. *Eur. Phys. J. C 83, 864 (2023)*, 2023.

[7] Martin N. Wilson. *Superconducting magnets / Martin N. Wilson*. Clarendon Press, Oxford, 1983.

[8] C. Wyss. LHC Arc Dipole Status Report, Technical report. Technical report, CERN, 2008.

[9] L. Rossi and Geneva Switzerland Accelerator Technology Division, CERN. THE LHC SUPERCONDUCTING MAGNETS. *JACoW*, 2023.

[10] G Ambrosio and G Bellomo. Magnetic field, multipole expansion and peak field in 2D for superconducting accelerator magnets. Technical report, INFN, Rome, 1996.

[11] W. Meissner and R. Ochsenfeld. Ein neuer effekt bei eintritt der supraleitfähigkeit. *Naturwissenschaften 21*, 1933.

[12] A.A. Abrikosov. The magnetic properties of superconducting alloys. *Journal of Physics and Chemistry of Solids*, 2(3):199–208, 1957.

[13] Teruo Matsushita. *Measurement Methods for Critical Current Density*, pages 209–231. Springer Berlin Heidelberg, Berlin, Heidelberg, 2007.

[14] David Kramer. Helium prices surge to record levels as shortage continues. *Physics Today*, 76(9):18–20, 09 2023.

[15] Wikipedia. Yttrium barium copper oxide. https://en.wikipedia.org/wiki/Yttrium_barium_copper_oxide.

[16] Michel Cyrot and Davor Pavuna. *Introduction to superconductivity and high-tc materials / Michel Cyrot, Davor Pavuna*. World Scientific, Singapore [etc, 1992.

[17] M. K. Wu et al. Superconductivity at 93 k in a new mixed-phase y-ba-cu-o compound system at ambient pressure. *Phys. Rev. Lett.*, 58:908–910, Mar 1987.

[18] K. K. Mehta, Prantik Mukhopadhyay, R. K. Mandal, and A. K. Singh. Mechanical properties anisotropy of cold-rolled and solution-annealed ni-based hastelloy c-276 alloy. *Metallurgical and Materials Transactions A*, 45(8):3493–3504, 2014.

[19] A. Goyal. Conductors with controlled grain boundaries: An approach to the next generation, high temperature superconducting wire. *Journal of Materials Research*, 1997.

[20] Y. Iijima, N. Tanabe, O. Kohno, and Y. Ikeno. In-plane aligned yba2cu3o7 x thin films deposited on polycrystalline metallic substrates. *Applied physics letters*, 60(6):769–771, 1992.

[21] Theva. Tapestar. https://www.theva.com/products/.

[22] G Grimaldi, M Bauer, H Kinder, W Prusseit, U Gambardella, and S Pace. Magnetic imaging of ybco coated conductors by hall probes. *Physica. C, Superconductivity*, 372(2):1009–1011, 2002.

[23] A. Molodyk. Manufacture of rebco tape for high field applications: present technology and future challenges. Short course on HTS - MT29: https://agenda.infn.it/event/47554/.

[24] L. Rossi et al. The eucard-2 future magnets european collaboration for accelerator-quality hts magnets. *IEEE transactions on applied superconductivity*, 25(3):1–7, 2015.

[25] Lucio Rossi et al. The eucard2 future magnets program for particle accelerator high-field dipoles: Review of results and next steps. *IEEE transactions on applied superconductivity*, 28(3):1–10, 2018.

[26] Etienne Rochepault et al. Fabrication and assembly of the nb3sn dipole magnet fresca2. *IEEE transactions on applied superconductivity*, 27(4):1–5, 2017.

[27] Wilfried Goldacker, Francesco Grilli, Enric Pardo, Anna Kario, Sonja I Schlachter, and Michal Vojenčiak. Roebel cables from rebco coated conductors: a one-century-old concept for the superconductivity of the future. *Superconductor Science and Technology*, 27(9):093001, aug 2014.

[28] H. W. Weijers et al. Progress in the development of a superconducting 32 t magnet with rebco high field coils. *IEEE transactions on applied superconductivity*, 24(3):1–5, 2014.

[29] Philippe Fazilleau et al. Metal-as-insulation sub-scale prototype tests under a high background magnetic field. *Superconductor science technology*, 31(9):95003–, 2018.

[30] Thibault Lécrevisse, Xavier Chaud, Philippe Fazilleau, Clément Genot, and Jung-Bin Song. Metal-as-insulation hts coils. *Superconductor science technology*, 35(7):74004–, 2022.

[31] Seungyong Hahn et al. 45.5-tesla direct-current magnetic field generated with a high-temperature superconducting magnet. *Nature (London)*, 570(7762):496–499, 2019.

[32] Rui F. Vieira et al. Design, fabrication, and assembly of the sparc toroidal field model coil. *IEEE Transactions on Applied Superconductivity*, 34(2):1–15, 2024.

[33] D. G. Whyte et al. Experimental assessment and model validation of the sparc toroidal field model coil. *IEEE transactions on applied superconductivity*, 34(2):1–18, 2024.

[34] Yufan Yan, Yi Li, and Timing Qu. Screening current induced magnetic field and stress in ultra-high-field magnets using rebco coated conductors. *Superconductor science technology*, 35(1):14003–, 2022.

[35] Y Suetomi et al. Quench and self-protecting behaviour of an intra-layer no-insulation (lni) rebco coil at 31.4 t. *Superconductor science technology*, 34(6):64003–, 2021.

[36] Yi Li et al. Magnetization and screening current in an 800 mhz (18.8 t) rebco nuclear magnetic resonance insert magnet: experimental results and numerical analysis. *Superconductor science technology*, 32(10):105007–, 2019.

[37] Zachary S Hartwig et al. Viper: an industrially scalable high-current high-temperature superconductor cable. *Superconductor science technology*, 33(11):11–, 2020.

[38] Eduard Galstyan et al. High critical current star® wires with rebco tapes by advanced mocvd. *Superconductor science technology*, 36(5):55007–, 2023.

[39] `https://www.advancedconductor.com/corccable`.

[40] Anders Christian Christian Wulff, Asger Bech Abrahamsen, and Andrea Insinga. Topical review: Multifilamentary coated conductors for ultra-high magnetic field applications. *Superconductor science technology*, 2021.

[41] T. H. Nes, G. Kirby, G. de Rijk, M. Canale, L. Gentini, J. van Nugteren, A. Kario, and H. H. J. ten Kate. Design of a cloverleaf-racetrack dipole demonstrator magnet with dual rebco conductor. *IEEE transactions on applied superconductivity*, 32(6):1–5, 2022.

[42] Y. Zhang, D. W. Hazelton, R. Kelley, M. Kasahara, R. Nakasaki, H. Sakamoto, and A. Polyanskii. Stress-strain relationship, critical strain (stress) and irreversible strain (stress) of ibad-mocvd-based 2g hts wires under uniaxial tension. *IEEE transactions on applied superconductivity*, 26(4):1–6, 2016.

[43] Jiamin Zhu, Shuiliang Zhen, and Zhijian Jin. Development of a novel method to efficiently measure critical bending diameter of 2g hts tapes. *IEEE transactions on applied superconductivity*, 32(7):1–7, 2022.

[44] M. V. Polikarpova et al. Bending strain effects on the critical current in cu and cu-nb-stabilized ybco-coated conductor tape. *IEEE transactions on applied superconductivity*, 24(3):1–4, 2014.

[45] Chia-Ming Yang, Qi-Fu Hong, Chi-Lei Chang, and In-Gann Chen. Effect of heating

and bending on localized critical current in 2g hts tapes with non-contact trapped field measurements. *Journal of materials research and technology*, 32:2022–2029, 2024.

[46] D C van der Laan, J W Ekin, C C Clickner, and T C Stauffer. Delamination strength of ybco coated conductors under transverse tensile stress. *Superconductor science technology*, 20(8):765–770, 2007.

[47] E. Ravaioli, V. I. Datskov, G. Kirby, M. Maciejewski, H. H. J. ten Kate, and A. P. Verweij. Cliq-based quench protection of a chain of high-field superconducting magnets. *IEEE transactions on applied superconductivity*, 26(4):1–5, 2016.

[48] J. van Nugteren, M. Dhallé, S. Wessel, E. Krooshoop, A. Nijhuis, and H. ten Kate. Measurement and analysis of normal zone propagation in a rebco coated conductor at temperatures below 50k. *Physics procedia*, 67:945–951, 2015.

[49] M. Bonura and C. Senatore. An equation for the quench propagation velocity valid for high field magnet use of rebco coated conductors. *Applied physics letters*, 108(24), 2016.

[50] Federico Scurti and Justin Schwartz. Optical fiber distributed sensing for high temperature superconductor magnets. In *2017 25th Optical Fiber Sensors Conference (OFS)*, pages 1–4, 2017.

[51] Bailey et al. Metallic insulation for superconducting coils. *US4760365A*, 1988.

[52] Seungyong Hahn, Dong Keun Park, J Bascunan, and Y Iwasa. Hts pancake coils without turn-to-turn insulation. *IEEE transactions on applied superconductivity*, 21(3):1592–1595, 2011.

[53] Jun Lu, Jeremy Levitan, Dustin McRae, and Robert Walsh. Contact resistance between two rebco tapes: the effects of cyclic loading and surface coating. *Superconductor Science and Technology*, 31(8):085006, jul 2018.

[54] Lucio Rossi et al. Iris - a new distributed research infrastructure on applied superconductivity. *IEEE transactions on applied superconductivity*, 34(3):1–9, 2024.

[55] L Rossi, L Balconi, P Campana, S Maffezzoli Felis, S Sorti, and M Statera. Iris - the italian research infrastructure on applied superconductivity for particle accelerators and societal applications. *Journal of physics. Conference series*, 2687(9):92012–, 2024.

[56] W. Altmannshofer et al. Fcc-ee: The lepton collider: Future circular collider conceptual design report volume 2. *The European physical journal. ST, Special topics*, 228(2):261–623, 2019.

[57] W. Altmannshofer et al. Fcc-hh: The hadron collider: Future circular collider conceptual design report volume 3. *The European physical journal. ST, Special topics*, 228(4):755–1107, 2019.

[58] E. Acerbi, F. Allessandria, G. Baccaglioni, C. Birattari, E. Fabrici, L. Rossi, and A. Sussetto. High field superconducting solenoid for the lasa in milan. *IEEE transactions on magnetics*, 24(2):1417–1420, 1988.

[59] S. Maffezzoli Felis, M. Statera, A. Chiuchiolo, D. D'Agostino, L. Rossi, C. Santini, A. Musso, G. Angeli, and M. Bocchi. Status of the iris superconducting line test

station and 1 gw green superconducting line design and procurement. *IEEE transactions on applied superconductivity*, 35(5):1–5, 2025.

[60] RAT-GUI. `https://www.rat-gui.com/`.

[61] MathWorks. `https://it.mathworks.com/help/optim/ug/fmincon.html`.

[62] L. Rossi and M. Sorbi. Qlasa: A computer code for quench simulation in adiabatic multicoil superconducting windings, 2004.

[63] T. Lecrevisse et al. Quench propagation in ybco pancake: Experimental and computational results. *IEEE transactions on applied superconductivity*, 23(3):4601805–4601805, 2013.

[64] Bluefors AL325 cryocooler model. `https://bluefors.com/products/gifford-mcmahon-cryocoolers/al325-gifford-mcmahon-cryocooler/`.

[65] Magnus Dam, William Jerome Burger, Rita Carpentiero, Enrico Chesta, Roberto Iuppa, Gijs de Rijk, and Lucio Rossi. Design and modeling of amased-2: A high temperature superconducting demonstrator coil for the space spectrometer arcos. *IEEE transactions on applied superconductivity*, 32(4):1–5, 2022.

[66] Magnus Dam et al. A high temperature superconducting demonstrator coil for arcos: A novel toroidal magnetic spectrometer for an astroparticle physics experiment in space. *Proc. 37th Int. Cosmic Ray Conf. PoS*, 395, 2021.

[67] Magnus Dam et al. Manufacturing and testing of amased-2: a no-insulation high-temperature superconducting demonstrator coil for the space spectrometer arcos. *Superconductor science technology*, 36(1):14007–, 2023.

[68] Carmine Senatore, Matteo Alessandrini, Andrea Lucarelli, Riccardo Tediosi, Davide Uglietti, and Yukikazu Iwasa. Progresses and challenges in the development of high-field solenoidal magnets based on re123 coated conductors. *Superconductor science technology*, 27(10):103001–26, 2014.

[69] Thomas W. Sederberg and Scott R. Parry. Free-form deformation of solid geometric models. *Computer graphics (New York, N.Y.)*, 20(4):151–160, 1986.

[70] L. Rossi et al. Design and plan of a 10 t hts energy saving dipole magnet for the italian facility iris. *IEEE transactions on applied superconductivity*, 34(5):1–6, 2024.

[71] Victoria University of Wellington HTS performances database. `https://htsdb.wimbush.eu/`.

[72] A. Molodyk et al. Development and large volume production of extremely high current density yba2cu3o7 superconducting wires for fusion. *Scientific reports*, 11(1):2084–11, 2021.

[73] A Molodyk et al. Development and large volume production of extremely high current density yba2cu3o7 superconducting wires for fusion. *Scientific reports*, 11(1):2084–11, 2021.

[74] S. Angius et al. *The Upgrade of MA.RI.S.A. Facility from 6.5 to 10 Tesla Design, Construction and Preliminary Test*, pages 218–222. Springer Netherlands, Dordrecht,

1990.

[75] MATLAB Patternsearch. https://it.mathworks.com/help/gads/patternsearch.html.

[76] Schnorr disc springs. https://www.schnorr.com/_files/ugd/c85325_bc9df82fc7144a1086b8d691a7d8401c.pdf?index=true.

[77] Fujifilm. https://www.fujifilm.com/it/it/business/inspection/measurement-film/prescale.

[78] Yu Chen, Pengfei Zheng, Tong Che, Wei Qian, Xiaoyuan Chen, Shan Jiang, and Boyang Shen. Hts joint resistance for high-field magnets: Experiment and temperature-dependent modeling. *Journal of superconductivity and novel magnetism*, 35(5):1089–1098, 2022.

[79] Ziyi Huang et al. Study on the electrical performances of soldered joints between hts coated-conductors. *Cryogenics (Guildford)*, 122:103422–, 2022.

[80] Youngjae Kim, J. Bascunan, T. Lecrevisse, S. Hahn, J. Voccio, Dong Keun Park, and Y. Iwasa. Ybco and bi2223 coils for high field lts/hts nmr magnets: Hts-hts joint resistivity. *IEEE transactions on applied superconductivity*, 23(3):6800704–6800704, 2013.

[81] L. Balconi et al. Optimization of internal splicing for non-insulated hts magnets. *IEEE transactions on applied superconductivity*, 35(5):1–5, 2025.

[82] 'FARO Arm'. https://www.faro.com/it-IT/Products/Hardware/Quantum-FaroArms.

[83] Little Beast Engineering. https://littlebeastengineering.com/.

[84] R B Sims and J A Place. The stresses in the reels of cold reduction mills. *British journal of applied physics*, 4(7):213–216, 1953.

[85] J E Huber, D Nowell, and D. A Hills. On the stress analysis of a wound coil with application to electromagnet manufacture. *The Journal of Strain Analysis for Engineering Design*, 42(6):447–460, 2007.

[86] Jeonghwan Park, Jaemin Kim, Yufan Yan, and Seungyong Hahn. Diameter change of dry wound rebco solenoid pancake coil by winding tension. *IEEE transactions on applied superconductivity*, 34(5):1–5, 2024.

[87] Yong-hui Park, Kyutae Park, Sung-yeun Won, Wan-kee Hong, and Hyun-chul Park. Stress analysis model of strip winding system with a sleeve for a coil of thin stainless steel. *Journal of iron and steel research, international*, 24(1):1–7, 2017.

[88] V. Arp. Stresses in superconducting solenoids. *J. Appl. Phys.; (United States)*, 48(5):2026–2036, 1977.

[89] Maha Rhandi, S Bischof, B Iwamoto, Patrícia Borges de Sousa, and Torsten Koettig. Design and construction of an enhanced thermal conductivity measurement set-up in the temperature range of 1.8 k to 50 k at cern. *IOP Conference Series: Materials Science and Engineering*, 1327:012149, 05 2025.

[90] V.I. Datskov and J.G. Weisend. Characteristics of russian carbon resistance (tvo)

cryogenic thermometers. *Cryogenics (Guildford)*, 34:425–428, 1994.

[91] Robert J. Moffat. Describing the uncertainties in experimental results. *Experimental Thermal and Fluid Science*, 1(1):3–17, 1988.

[92] LakeShore 120CS manual. `https://www.lakeshore.com/docs/default-source/product-downloads/manuals/120cs_manual.pdf`.

[93] Keithley 2182A manual. `https://assets.testequity.com/te1/Documents/pdf/keithley/2182A.pdf`.

[94] Seungcheol Ryu, Changhyung Lee, Youngjun Choi, Kideok Sim, Seungyong Hahn, and Seokho Kim. Deformation behavior of stacked rebco tapes under compressive loads. *IEEE transactions on applied superconductivity*, 34(5):1–5, 2024.

[95] D Abraimov, A Ballarino, C Barth, L Bottura, R Dietrich, A Francis, J Jaroszynski, G S Majkic, J McCallister, A Polyanskii, L Rossi, A Rutt, M Santos, K Schlenga, V Selvamanickam, C Senatore, A Usoskin, and Y L Viouchkov. Double disordered ybco coated conductors of industrial scale: high currents in high magnetic field. *Superconductor science technology*, 28(11):114007–8, 2015.

[96] Y Zhao et al. Progress in fabrication of second generation high temperature superconducting tape at shanghai superconductor technology. *Superconductor science technology*, 32(4):44004–, 2019.

[97] Insung Park et al. Development of continuous thickness measurement system for long-length hts ccs. *IEEE transactions on applied superconductivity*, 35(5):1–5, 2025.

[98] Seungcheol Ryu et al. Deformation behavior of stacked rebco tapes under compressive loads. *IEEE transactions on applied superconductivity*, 34(5):1–5, 2024.

[99] Donald E. Kirk. *Optimal control theory : an introduction / Donald E. Kirk*. Dover Publications, New York, 2004.

[100] Seokho Kim, Seungyong Hahn, Kwangmin Kim, and David Larbalestier. Method for generating linear current-field characteristics and eliminating charging delay in no-insulation superconducting magnets. *Superconductor science technology*, 30(3):35020–, 2017.

[101] Matanya B. Horowitz, Anil Damle, and Joel W. Burdick. Linear hamilton jacobi bellman equations in high dimensions. In *53rd IEEE Conference on Decision and Control*, pages 5880–5887. IEEE, 2014.

[102] Jérôme Darbon and Stanley Osher. Algorithms for overcoming the curse of dimensionality for certain hamilton–jacobi equations arising in control theory and elsewhere. *Research in the mathematical sciences*, 3(1):1–26, 2016.

[103] B.D.O. Anderson and J.B. Moore. *Optimal Control: Linear Quadratic Methods*. Dover Books on Engineering. Dover Publications, 2007.

[104] Mohinder S. Grewal and Angus P. Andrews. Kalman filtering: Theory and practice using matlab, 4th edition. *ProtoView*, 2(11), 2015.

[105] L Rossi and M Sorbi. MATPRO. Technical report, CARE, 2005.

[106] R. Batulin et al. The physical properties of hastelloy® c-276tm and hastelloy®

c-276tm with al2o3/y2o3/mgo/lamno3 buffer layers down to cryogenic temperatures for applications in superconducting magnets. *Cryogenics (Guildford)*, 137:103776–, 2024.

[107] S. Choi et al. A study on the no insulation winding method of the hts coil. *IEEE transactions on applied superconductivity*, 22(3):4904004–4904004, 2012.

[108] National Instrument Compact Field Point AI 118. `https://download.ni.com/support/manuals/372056b.pdf`.

[109] David Evans. Resins for superconducting magnet construction - an overview of requirements, processing and properties. *IOP conference series. Materials Science and Engineering*, 756(1):12003–, 2020.

[110] Joshua Feldman, Wolfgang Stautner, Christopher Kovacs, Nenad Miljkovic, and Kiruba S Haran. Review of materials for hts magnet impregnation. *Superconductor science technology*, 37(3):33001–, 2024.

[111] SAES Rial Vacuum. `https://saesrial.com/`.

[112] M. Statera et al. The hl-lhc high order correctors series production and powering tests status. *IEEE transactions on applied superconductivity*, 32(6):1–5, 2022.

List of Publications

Refereed publications:

- Experimental measurements on small-scale HTS racetrack coils at INFN for future particle accelerators.
  Authors: L. Balconi et al.
  Journal: IEEE Transactions on Applied Superconductivity.
  Year: 2025.
  DOI: `https://doi.org/10.1109/TASC.2025.3636498`

- Final design and production of a 10 T HTS energy saving dipole magnet for the Italian facility IRIS.
  Authors: S. Sorti et al.
  Journal: IEEE Transactions on Applied Superconductivity.
  Year: 2025.
  DOI: `https://doi.org/10.1109/TASC.2025.3628303`

- The Role of High Temperature Superconductors for a 10 TeV Muon Collider.
  Authors: S. Mariotto et al.
  Journal: IEEE Transactions on Applied Superconductivity.
  Year: 2025.
  DOI: `https://doi.org/10.1109/TASC.2025.3624724`

- Optimization of Internal Splicing for Non-Insulated HTS Magnets.
  Authors: L. Balconi et al.
  Journal: IEEE Transactions on Applied Superconductivity.
  Year: 2025.
  DOI: `https://doi.org/10.1109/TASC.2024.3517552`

- Magnetic and Mechanical Design of the Large Aperture HTS Superconducting Dipoles for the Accelerator Ring of the Muon Collider.
  Authors: F. Levi et al.
  Journal: IEEE Transactions on Applied Superconductivity.
  Year: 2025.
  DOI: `https://doi.org/10.1109/TASC.2024.3520073`

- Enhanced Model for Non-Insulated HTS Coils.
  Authors: S. Sorti et al.
  Journal: IEEE Transactions on Applied Superconductivity.
  Year: 2025.
  DOI: `https://doi.org/10.1109/TASC.2025.3546873`

- Toward Real-Time Electromagnetic Simulations of HTS Non-Insulated Coils Through Proper Orthogonal Decomposition.
  Authors: S. Sorti et al.
  Journal: IEEE Transactions on Applied Superconductivity.
  Year: 2025.
  DOI: `https://doi.org/10.1109/TASC.2025.3526741`

- Nonlinear Optimal Control of No-Insulation and Controlled-Insulation HTS Coils and Magnets.
  Authors: L. Balconi et al.
  Journal: IEEE Transactions on Applied Superconductivity
  Year: 2024.
  DOI: `https://doi.org/10.1109/TASC.2024.3369009`

- IRIS - The Italian research infrastructure on Applied Superconductivity for Particle Accelerators and Societal Applications.
  Authors: L. Rossi et al.
  Journal: Journal of Physics: Conference Series.
  Year: 2024.
  DOI: `https://doi.org/10.1088/1742-6596/2687/9/092012`

- Design and Plan of a 10 T HTS Energy Saving Dipole Magnet for the Italian Facility IRIS.
  Authors: L. Rossi et al.
  Journal: IEEE Transactions on Applied Superconductivity
  Year: 2024.
  DOI: `https://doi.org/10.1109/TASC.2024.3355357`

- IRIS-A New Distributed Research Infrastructure on Applied Superconductivity.
  Authors: L. Rossi et al.
  Journal: IEEE Transactions on Applied Superconductivity
  Year: 2024.
  DOI: `https://doi.org/10.1109/TASC.2023.3341984`

- Towards a muon collider.
  Authors: C. Accettura et al.
  Journal: European Physical Journal
  Year: 2023.
  DOI: `https://doi.org/10.1140/epjc/s10052-023-11889-x`